

Piotr Ślęczkowski  
**Chirality under Confinement –  
Multidimensional Constraints in  
Liquid Crystalline Materials**

CHIRALITY UNDER CONFINEMENT –  
MULTIDIMENSIONAL CONSTRAINTS IN  
LIQUID CRYSTALLINE MATERIALS

Piotr Ślęczkowski

**Members of the committee:**

<b>Chairman:</b>	Prof.dr.ir. J.W.M. Hilgenkamp	(University of Twente)
<b>Promotor:</b>	Prof. dr. J.J.L.M. Cornelissen	(University of Twente)
<b>Promotor:</b>	Dr. E. Lacaze	(Université Pierre et Marie Curie (France))
<b>Co-promotor:</b>	Dr. N. Katsonis	(University of Twente)
<b>Members:</b>	Prof. S. De Feyter	(Katholieke Universiteit Leuven (Belgium))
	Dr. F. Charra	(CEA Saclay (France))
	Prof. C. Petit	(Université Pierre et Marie Curie (France))
	Prof.dr.ir. H. Zandvliet	(University of Twente)
	Prof.dr.ir. J. H. Snoeijer	(University of Twente)

The research described in this thesis was performed within the laboratories of the Institut des NanoSciences de Paris (INSP – UMR 7588, France) and the laboratories of the Biomolecular Nanotechnology (BNT) group, the Mesa+ Institute for Nanotechnology and the Department of Science and Technology of the University of Twente. This research was supported by the French Ministry of Higher Education and Research and the European Research Council through a Starting Grant (Photo-engineered helices in chiral liquid crystals, PHELIX, number 307784).

**Chirality under Confinement – Multidimensional Constraints in Liquid Crystalline Materials**

Copyright © 2014, Piotr Ślęczkowski.

All rights reserved. No part of this thesis may be reproduced or transmitted in any form, by any means, electronic or mechanical without prior written permission of the author.

**ISBN:** 978-90-365-3795-7

**DOI:** 10.3990/1.9789036537957

**Cover art:** Agnieszka Zalewska-Dziwoki

**Printed by:** Gildeprint Drukkerijen - Enschede (The Netherlands)

Université Pierre et Marie Curie  
University of Twente

**Chirality under confinement – multidimensional constraints  
in liquid crystalline materials**

By Piotr Ślęczkowski

PhD Thesis Dissertation

Supervised by Dr. Emmanuelle Lacaze and Prof. dr. Jeroen Cornelissen

Presented and defended on Thursday 11.12.2014 at 12:45

**Members of the graduation committee:**

<b>Chairman:</b>	Prof. dr. ir. J. W. M. Hilgenkamp	(University of Twente)
<b>Promotor:</b>	Prof. dr. J. J. L. M. Cornelissen	(University of Twente)
<b>Promotor:</b>	Dr. E. Lacaze	(Université Pierre et Marie Curie (France))
<b>Co-promotor:</b>	Dr. N. Katsonis	(University of Twente)
<b>Members:</b>	Prof. S. De Feyter	(KU Leuven (Belgium))
	Dr. F. Charra	(CEA Saclay (France))
	Prof. C. Petit	(Université Pierre et Marie Curie (France))
	Prof.dr.ir. H. Zandvliet	(University of Twente)
	Prof.dr.ir. J. H. Snoeijer	(University of Twente)



# CHIRALITY UNDER CONFINEMENT – MULTIDIMENSIONAL CONSTRAINTS IN LIQUID CRYSTALLINE MATERIALS

## DISSERTATION

to obtain

the degree of doctor at the University of Twente

on the authority of the rector magnificus,

Prof. dr. H. Brinksma,

on account of the decision of the graduation committee,

to be publicly defended

on Thursday December 11, 2014, at 12.45 h

by

Piotr Bronisław Ślęczkowski

born on May 5, 1984

in Knurów, Poland

This dissertation has been approved by:

**Promotor:** Prof. dr. J.J.L.M. Cornelissen

**Promotor:** Dr. E. Lacaze

**Co-promotor:** Dr. N. Katsonis

„Twenty years from now you will be more disappointed by the things you didn't do  
than by the ones you did do. So throw off the bowlines.  
Sail away from the safe harbor. Catch the trade winds in your sails.  
Explore. Dream. Discover.”

H. Jackson Brown, Jr.

This thesis is dedicated to my parents.





# TABLE OF CONTENTS

<b>Chapter 1: General introduction</b>	<b>1</b>
1.1 References	3
<b>Chapter 2: Two-dimensional confinement of discotic liquid crystals: a diverse role of the substrate</b>	<b>5</b>
2.1 Introduction to discotic liquid crystals: a historical sketch	6
2.2 Structural features of discotic molecules possessing thermotropic mesogenic character	7
2.3 Thermotropic mesophases originating from the planar anisometry of molecules	8
2.3.1 Types of columnar mesophases	10
2.4 Triphenylene-based discotic liquid crystals	12
2.5 Columnar mesophases as one-dimensional semiconductors	14
2.6 Scanning tunneling microscopy at the liquid/solid interface	17
2.6.1 Beyond optical microscopy	17
2.6.2 Physics behind STM	18
2.7 Experimental setup	18
2.8 Description of the substrate used	20
2.8.1 Introduction to surface crystallography	21
2.8.2 Chirality of achiral units upon surface confinement	22
2.8.3 Triphenylenes on Highly-Oriented Pyrolytic Graphite (HOPG)	24
2.8.4 Triphenylenes on Au(111)	29
2.8.5 Hexabenzocoronenes	31
2.9 Conclusions	38
2.10 References	39
<b>Chapter 3: An unexpected chirality in hexagonally packed monolayers of hexapentyloxytriphenylene on Au(111)</b>	<b>45</b>
3.1 Introduction	46
3.2 STM of H5T at the <i>n</i> -tetradecane/Au(111) interface	47
3.2.1 Hexagonal structure of H5T on Au(111)	47
3.2.2 Two-fold orientation of H5T domains on Au(111)	51

3.3 Theoretical approach to the H5T/Au(111) system	53
3.3.1 H5T molecule <i>in vacuo</i> : structure optimization	54
3.3.2 Computation of intermolecular interactions (12-6 LJ Potential)	55
3.3.3 Validation of intermolecular interactions model by a simplified interfacial potential	61
3.4 Conclusions	64
3.5 Experimental section	65
3.5.1 Materials	65
3.5.2 Sample preparation	65
3.5.3 Equipment: scanning tunneling microscope	65
3.6 Acknowledgements	66
3.7 References	66
<b>Chapter 4: Stabilizing 2D hexagonal self-assemblies of discotic liquid crystals: a potential role for azobenzenes</b>	<b>69</b>
4.1 Introduction	70
4.1.1 Azobenzene molecules on surfaces	71
4.1.2 Switching of azobenzenes immobilized on surfaces	71
4.2 A hybrid triphenylene-azobenzene mesogenic system: C-12	73
4.3 STM of C-12 at the 1,2,4-trichlorobenzene/Au(111) interface	76
4.3.1 Hexagonal packing of domains and intermolecular azobezene-coupling	76
4.3.2 Investigation of the z-direction of the system by varying the tunneling parameters	79
4.3.3 The twofold mesh orientation of C-21 at the TCB/Au(111) interface	80
4.3.4 Azobenzene pairing as the driving force of C-12 mesh dual directionality	84
4.3.5 Substrate-promoted assembling for the azobenzene/Au(111) system	86
4.4 Specificity of the probed azobenzene interactions: STM of C-12/HOPG system	89
4.5 Conclusions	91
4.6 Experimental section	93
4.6.1 Materials	93
4.6.2 Sample preparation	93
4.6.3 Equipment: scanning tunneling microscope	93
4.7 Acknowledgements	94
4.8 References	94

<b>Chapter 5: Self-assembly and dynamics in the self-assembled monolayers of C-12 at the TCB/Au(111) interface</b>	<b>97</b>
5.1 Introduction	98
5.2 Resolving the 'up'-'up' and 'down'-'down' C-12 dimer structure	99
5.3 STM observations of the local dynamic changes within C-12 monolayers	101
5.3.1 Probing of 'up'/'down' contrast changes within C-12 monolayers	101
5.3.2 Proposed mechanism of 'up'/'down' contrast changes at the submolecular level	104
5.3.3 Conclusions on the dynamics of C-12 molecules on Au(111)	107
5.4 C-12 self-assemblies on Au(111) as a function of droplet concentration, role of inter-azobenzene interactions	108
5.5 Conclusions	115
5.6 Experimental section	117
5.6.1 Materials	117
5.6.2 Sample preparation	117
5.6.3 Equipment: scanning tunneling microscope	117
5.7 Acknowledgements	118
5.8 References	118
<b>Chapter 6: Cholesteric liquid crystal droplets: three-dimensional confinement of chirality</b>	<b>119</b>
6.1 Introduction to thermotropic liquid crystals of rod-like molecules	120
6.1.1 Chirality induction in nematic liquid crystals by doping with chiral dopants	121
6.1.2 Photo-responsive chiral liquid crystals	122
6.1.3 Polarized Light Microscopy (PLM)	123
6.1.4 Bulk elasticity of nematic and cholesteric liquid crystals	125
6.1.5 Surface anchoring in nematic liquid crystals	126
6.2 Studies of dispersed systems of liquid crystals	127
6.2.1 Droplets of nematic liquid crystals	127
6.2.2 Appearance of chirality: twisted bipolar droplets from achiral nematic LCs	131
6.2.3 Droplets of cholesteric liquid crystals	133
6.2.4 Geometrical factor determining the structure of cholesteric droplets	134
6.2.5 Cholesteric droplets of planar anchoring – theoretical approach	134
6.2.6 Cholesteric droplets of planar anchoring – experimental validation	138
6.2.7 Negative-to-positive monopole transitions in cholesteric droplets	140
6.3 Conclusions	142
6.4 References	143

<b>Chapter 7: Photo-switching the structures of cholesteric liquid crystal droplets with planar surface anchoring</b>	<b>145</b>
7.1 Introduction	146
7.1.1 Overcrowded alkenes – molecular motors as dopants for photo-responsive cholesteric liquid crystals	147
7.1.2 Determination of the cholesteric pitch	148
7.2 Droplets of photo-responsive cholesteric liquid crystals in a glycerol matrix	151
7.2.1 Low concentration of chiral dopant	151
7.2.2 High concentration of chiral dopant	152
7.3 Effect of geometrical confinement on the cholesteric textures	153
7.4 Photo-induced structural changes in the cholesteric droplets	158
7.5 Discussion and conclusions	165
7.6 Experimental section	168
7.7 Acknowledgements	168
7.8 References	169
Summary and perspectives	171
Samenvatting en perspectieven	175
Résumé et perspectives	179
Acknowledgements	181
Curriculum Vitae	185

# Chapter 1

## General introduction

### 1. Introduction

It is undoubtedly true that surface (or interface) science lies at the foundation of what we nowadays call nanotechnology.<sup>1</sup> Since interfacial phenomena play a crucial role in the most important industrial processes like heterogeneous catalysis<sup>2</sup> or semiconductor processing<sup>3</sup> it is of the highest importance to search for the improvement of existing technologies – especially by continual stimulation of the research in surface science. Metal-organic material interface is one of the special types of interfaces, again, from the point of view of catalysis, but also from the point of view of the emerging organic electronics devices<sup>4</sup> and photovoltaic cells.<sup>5</sup> Another important phenomena that may be related to metal-organic interfaces are adhesion and lubrication, among many others.

The research described in this thesis focuses on the special group of organic molecules, namely thermotropic liquid crystals (LCs), and their response to the multidimensional confinement. Knowledge about structure of mesophases, i.e. bulk structures of liquid crystalline materials, is continuously growing since decades.<sup>6</sup> What is more recent in the liquid crystals research is the massive tendency for studies of peculiarities: domain boundaries/interfaces, bulk and surface defects, or frustrated systems. Since one of the necessary conditions for an organic molecule to exhibit mesomorphism is the high anisotropy of intermolecular interactions (in first approximation as a consequence of the anisotropy of the molecular shape), one may expect that the interfacial phenomena of highly anisotropic molecules should be more complex. The plot of presented manuscript comprising Chapters 2 to 5 is the study of interfacial behavior and self-assembly of a specific type of mesogens: discotic liquid crystals (DLCs). Those molecules, that are flat in shape (resemble *discs*) possess an interesting property – in bulk they form columns which have semiconducting properties of high anisotropy.<sup>7</sup> Examination of their 2D self-assembly properties on a metallic substrate (Au(111)), geometrical analysis of monolayers that they potentially form, is an important step in the design and fabrication of controllable interfaces that should further result in the development of valuable ‘smart’ materials. The Chapters 6 and 7 concern the study of the structural evolution of cholesteric (chiral nematic) droplets, for which the surface influence increases when the droplet size decreases. We evidence in Chapter 7, that using photo-switchable chiral motors we can monitor, under irradiation, the evolution of the droplets texture.

Chapter 2 contains a comprehensive introduction to the surface crystallography and the chirality in 2D. Moreover, it provides an overview of the literature related to self-assembled monolayers of discotic molecules at the liquid/solid interface. The quoted bibliographic positions are specified to those describing the DLC/substrate systems where the interfacial interactions are limited to physical adsorption and the molecules are lying flat on the substrate (homeotropic configuration). Several factors influencing the self-assembly are discussed, including the substrate and solvent used, temperature variations and the influence of the buffer monolayer.

Chapter 3 describes the combined experimental and theoretical investigations of a model (archetypal) DLC molecule, H5T, at the Au(111) substrate. The most straightforward result, namely the coexistence of two types of commensurate domains of hexagonal symmetry, was evidenced experimentally by STM. However, the inconclusive intramolecular contrast resulted in need of employment of complementary techniques to explain two-fold orientation of 2D crystals of H5T. While both of them belong to a hexagonal space group, analogical to the triangular symmetry of the molecule and the hexagonal symmetry of the substrate surface, they reveal a 2D chiral character which origin is unraveled through the use of a theoretical model.

Chapter 4 provides an extensive analysis of the self-assembly of a novel hybrid molecule: C-12, which contains the triphenylene core decorated with six azobenzene units. Initially obtained results regarding the formation of hexagonally packed domains of a large lattice parameter were followed by the discovery of a specific type of interactions between neighbors in the hexagonal network, directly promoted by Au(111). Obtaining the intramolecular resolution enabled to establish that the C-12 self-assembly on Au(111) is particularly dependent on coupling between the azobenzene groups from the neighboring molecules. The existence of two distinct stable configurations of a couple of azobenzenes and the appearance of the two mirror-like types of domains resulted in confirmation of the fact that intermolecular azobenzene dimerization plays a crucial role for the studied system, in particular for the establishment of clockwise and counter-clockwise chirality in the two types of adsorbed domains.

The work presented in Chapter 5 is related to the dynamic character of the monolayers of C-12 molecule described in Chapter 4. The observed dynamics appears directly related to the interactions between azobenzene units, strongly suggesting a hydrogen bonding between them, which can be modified according to the orientation of C-12 molecules in the ordered network. In a second part, we describe how concentration of C-12 molecules in the droplet on top of the substrate influences the growth of the ordered networks. We evidence formation of more stable networks for large C-12 concentration in the droplets, in contrast with usual growth phenomenon associated with evaporation of organic molecules.

Chapter 6 provides an introduction to the topic of dispersed systems of liquid crystals. An introduction to previous studies of nematic liquid crystal droplets is presented, both theoretical and experimental. A very important fact of arising of chirality in the systems composed of non-chiral molecules is underlined and explained.<sup>8</sup> Special attention is focused on the cholesteric liquid crystal droplets and the different expressions of chirality in those confined systems, depending on the geometrical confinement as a main parameter.<sup>9</sup> It is shown that liquid crystal droplets show a variety of structures with particularly different director field, usually possessing some stable topological defects. Previous studies of dynamics within the director field, and connected with it dynamics of defects, is shown for various types of stimuli. We also present a brief state of the art concerning photo-switchable motors and their role to control cholesteric textures under irradiation.

Studies of photo-switching of droplets of cholesteric liquid crystals are main topic of Chapter 7. We show for the first time the transition between the different textures of cholesteric droplets with the use of light as switching stimulus. Moreover, we evidence the helix inversion appearing in the system for sufficiently long irradiation, and we study the role of the confinement on the dynamical texture evolution of the droplets.

## 1.1. References

1. Kolasinski, K. W. *Surface Science: Foundations of Catalysis and Nanoscience*, 1<sup>st</sup> Edition, John Wiley & Sons (2002).
2. Ertl, G.; Knözingerand, H. & Weitkamp, J. *Handbook of Heterogeneous Catalysis*, 1<sup>st</sup> Edition, Wiley-VCH (1997).
3. Moriarty, P. *Rep. Prog. Phys.* **64**, 297-383 (2001).
4. Shimizu, Y.; Oikawa, K.; Nakayama, K.-i. & Guillon, D. *J. Mater. Chem.* **17**, 4223–4229 (2007).
5. Schmidt-Mende, L.; Fechtenkötter, A.; Müllen, K.; Moons, E.; Friend, R. H. & MacKenzie, J. D. *Science* **293**, 1119–1122 (2001).
6. Cammidge, A. N. & Bushby, R. J. *Handbook of Liquid Crystals*, vol. **2B**, Chap. VII, Wiley-VCH (1998).
7. Sergeyev, S.; Pisula, W. & Geerts, Y. H. *Chem. Soc. Rev.* **36**, 1902-1929 (2007).
8. Drzaic, P. S. *Liq. Cryst.* **26**, 623–627 (1999).
9. Sec, D.; Porenta, T.; Ravnik, M. & Zumer, S. *Soft Matter* **8**, 11982-11988 (2012).





## Chapter 2

### Two-dimensional confinement of discotic liquid crystals: a diverse role of the substrate

This chapter introduces the reader to a distinct class of thermotropic mesomorphic materials: discotic liquid crystals (DLCs). Those compounds, as a result of their molecular shape and associated intermolecular interactions, often form the specific long-range arrangements called columnar mesophases. These peculiar supramolecular architectures are well-known to possess very good one-dimensional charge transport characteristics, making them a promising alternative to the already existing solid-state inorganic devices where the active layers are based on silicon. Despite the ongoing optimization of their semiconductive properties and the performance of DLC-based devices, much less attention has been paid to the exploration of the processes that occur at the interface between the solid state electrode material and the DLC-organic layer. Main part of this chapter deals with the previous investigations of the self-assembly of discotic molecules on atomically flat substrates with the use of scanning tunneling microscopy at the liquid/solid interface. We have decided to limit to one of the two main adsorption geometry modes, the face-on arrangement with respect to substrate, thus limiting the potential applicative solutions to the light-emitting diodes (LEDs) or photovoltaic cells (PVs). The examples presented within this chapter consist of the main physisorbed systems for which the dominating interactions arise from various non-covalent forces, e.g. van der Waals-type.

## 2.1 Introduction to discotic liquid crystals: a historical sketch

One of the primary features for any organic molecule to display mesomorphic character is the shape anisotropy. This fact has been established by the pioneering work of a German chemist Daniel Vorländer, who has performed probably the first series of systematic syntheses of liquid crystalline molecules at a considerable scale. The consequences of derivation of his 'rule of the most extended molecular shape' were further numerous investigations regarding calamitic (rod-like) molecules as precursors of mesophases.<sup>1</sup> Moreover, none other than Vorländer has supposed, as soon as 1924, the possibility of mesogenic character of non-rod-like molecules, as suggests the title of a chapter of his book.<sup>2</sup> 'From star-like, cross-like and plate-like molecules to liquid crystals?' - also being a title of PhD thesis of one of his students.<sup>3</sup> Nonetheless, his attempts on obtaining any liquid crystalline derivatives of gallic acid and triphenyl-benzene, triphenylene, perylene among others had not been successful. The reason was probably the fact that the molecules he looked at did not contain enough of the flexible chains, or the substituents were too short (i.e. methyl or ethyl). However, the idea of flat molecules that could be packed in analogy to Volta's column or battery should be noticed in the rich scientific output of the 'father of liquid crystal chemistry'.<sup>1</sup>

Long before the discovery of discotics, it has been already shown with the use of theoretical approach that, in principle, a transition from the isotropic to the anisotropic (nematic) phase is possible in an assembly of plate-like particles.<sup>4</sup> Although the work of Isihara *et al.* has been followed by further studies of biaxial particles, none of them has envisaged the appearance of columnar structure.<sup>5</sup> Yet, Landau and Lifshitz have formulated the problem of a three-dimensional system 'melted' in one dimension, but such a structure was regarded as improbable.<sup>6</sup> In addition to theoretical approach, it is possible to elaborate some results from the experimental side. Brooks and Taylor, for instance, have observed a mesophase occurrence during the pyrolysis of certain graphitizable organic materials like petroleum and coal tar. They communicated on the irreversible reaction which proceeds from the isotropic melt to a nematic type of mesophase with increasing temperature. The mesophase, referred to as the 'carbonaceous' phase, is a multicomponent system composed of large plate-like polynuclear aromatic molecules having a wide range of molecular weights.<sup>7</sup> However, due to its complexity in composition, transient existence and limited lifetime (caused by subsequent hardening to a semicoke), the carbonaceous phase is not considered as stable liquid crystalline system. Skoulios and Luzzati investigated alkali and alkaline earth salts of long chain fatty acids. In salts of potassium and rubidium they found ribbon-like structures that are similar to columnar mesophase to some extent. Each 'disc' consists of double sheet of molecules that form the 'core' and molten alkyl groups filling the space between the discs.<sup>8</sup>

It has been well established among the liquid crystal community, that the symbolic birth of the discotic liquid crystals (DLCs) coincides with the release of the famous paper by Chandrasekhar *et al.* published in 1977,<sup>9</sup> where authors reported on “...what is probably the first observation of thermotropic mesomorphism in pure, single component systems of relatively simple plate like, or more appropriately disc-like molecules”. A family of benzene hexa-*n*-alkanoates that has been synthesized and thereafter examined by thermodynamic, optical and X-ray methods, has exhibited a peculiar supramolecular architecture. It was confirmed that those materials did form a new class of liquid crystals in which molecules were stacked one on the top of another in columns that constitute a hexagonal arrangement. This discovery has opened the new sub-field of fascinating liquid crystal research.

It is worth to underline at this point that some of the compounds have been already synthesized about 40 years before, by the Dutch chemists at the University of Groningen.<sup>10</sup> However, despite of the fact of describing synthesis and some basic physico-chemical properties of 14 homologues of ‘plano-radiate’ compounds (author’s terminology) no mesogenic character of those compounds have been detected. A slightly different series of hexavalent benzene esters have been reported couple of years later by Neifert *et al.*,<sup>11</sup> again without pointing the liquid crystalline properties. Shortly after the work of Chandrasekhar *et al.*, another series of discotic compounds have been synthesized: hexaalkoxy- and hexaalkanoyloxytriphenylenes,<sup>12,13</sup> which represent a second subclass of the discotic mesogens: polycyclic aromatic hydrocarbons (PAHs), characterized by the extended aromatic core. Columnar hexagonal structure bearing translational order in two dimensions (but not in the third) has been confirmed for those compounds with the X-ray studies by Levelut.<sup>14,15</sup> Detailed crystallographic measurements enabled to gain the knowledge about the unique geometry of the system, and soon it was recognized that columnar mesophases should become one of the hot topics in materials chemistry.

## **2.2 Structural features of discotic molecules possessing thermotropic mesogenic character**

Discotic liquid crystal mesogen is generally built of a (poly)aromatic core, that is surrounded by several aliphatic tails. The conjugation of aromatic core, in other words: the repetition of multiple and single bonds between subsequent carbon atoms, makes the core flat (or nearly flat) and rigid with  $sp^2$  configuration of carbon atoms. The number of flexible side-chains that are symmetrically attached to the central part most commonly via ether or ester groups is generally determined by the symmetry of the core, with the 6 or 8 being most popular, and 3 and 4 less common. As evidenced by numerous experimental studies, the presence of alkyl tails is crucial for the mesogenic character of the molecule.<sup>16</sup> Typical peripheral substituents are schematically shown on Figure 2.1(a).

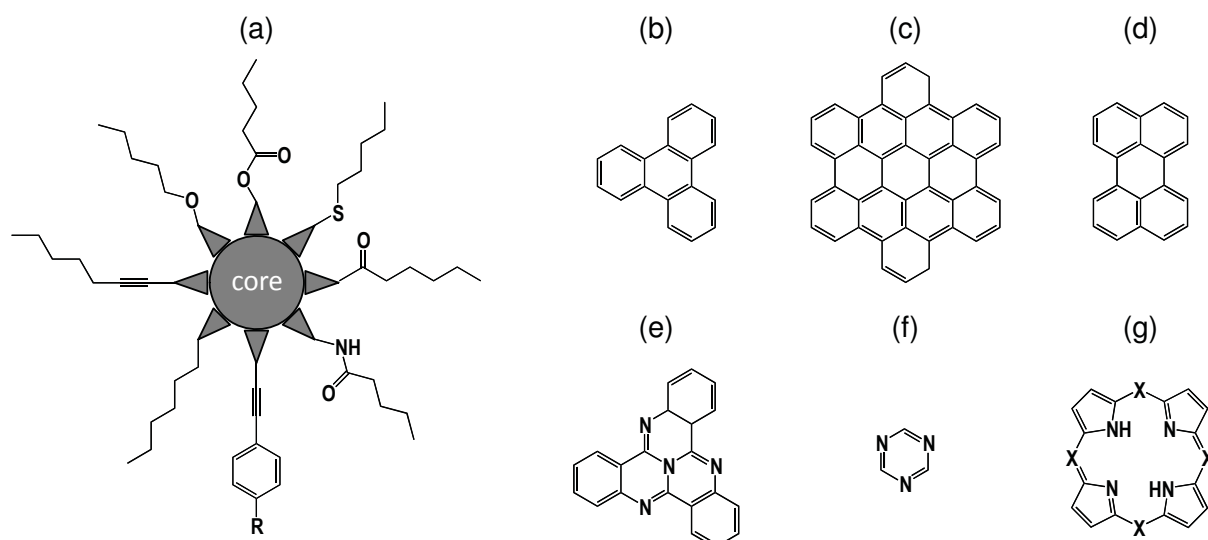


**Figure 2.1** (a) A general molecular architecture of a disc-like mesogen. Among the most frequently present ether, ester and thioether bonds, also more complex linkers may be found. (b) to (g) represent some of the most commonly met discoid cores: (b) triphenylene, (c) hexa-*peri*-hexabenzocoronene, (d) perylene, (e) tricycloquinoxaline, (f) triazine, (g) porphyrin (X = CH) or phthalocyanine (X = N).

Among more than 3000 disc-like compounds that exhibit various types of thermotropic mesomorphism, roughly 50 different subgroups are known, depending on the chemical structure of the central core, of which major part are: aromatic hydrocarbons (e.g. benzene, perylene, triphenylene, hexabenzocoronene), heterocyclic cores (e.g. hexaazotriphenylene), metallomesogens (e.g. porphyrin, phthalocyanine), and even saturated cores (like cyclohexane or pyranose sugars). Additionally, a number of discotic cores generated through non-covalent hydrogen-bonding are also known to display columnar mesophases.<sup>17</sup> Precursors of some of the most widely studied systems are presented on the Figure 2.1(b) to (g).

### 2.3 Thermotropic mesophases originating from the planar anisometry of molecules

Similarly to their calamitic (rod-like) counterparts, discotics are capable to form manifold anisotropic phases. The simplest case, analogous in the symmetry frame to the 'regular' nematic mesophase is the discotic nematic mesophase, denoted often ( $N_D$ ) and depicted by Figure 2.2(a).<sup>18</sup> For a disc-like mesogen the molecular symmetry axis that coincides with the director points perpendicularly to the molecular plane, thus resulting in the negative birefringence of the system. Unlike the calamitic nematics, its discotic analogues are not so often met, however, due to the abovementioned optical properties the polymerized discotic nematic phases have been well commercialized as compensation films that enhance the viewing angle of conventional liquid-crystal

displays.<sup>19</sup> Accordingly, a chiral nematic phase of disc-like mesogen will be normally formed, when the molecule is chiral, or when a chiral dopant is added to the discotic nematic matrix.<sup>20</sup> In both cases the director is progressively rotated along the screw axis, creating a helical structure with the parameter called pitch which is a distance equal to one complete ( $2\pi$ ) turn of the local director.<sup>21</sup> Figure 2.2(b) is a simplistic portrayal of ( $N_D^*$ ), exaggerating the twist of the director, for better clarity. Director that is initially parallel to the plane of the image (*black*) rotates of about  $\frac{\pi}{2}$  to point towards the reader (*white*).

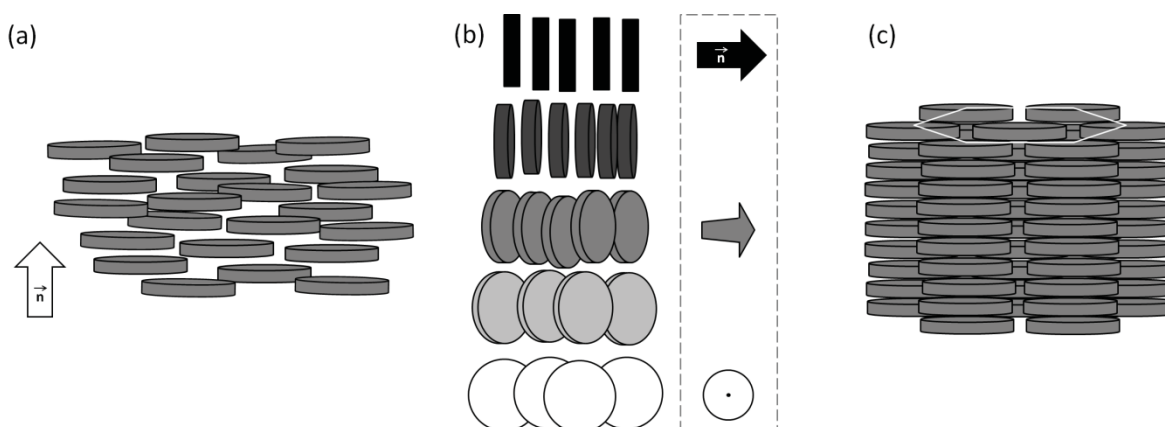


**Figure 2.2** Schematic representation of (a) discotic nematic ( $N_D$ ), (b) chiral discotic nematic ( $N_D^*$ ) and (c) columnar hexagonal ( $Col_h$ ) mesophases. (a) Vertical arrow points the local direction of symmetry axis of molecules – the director,  $n$ . (b) Director rotation inherent to the chiral mesophase is underlined in the dashed box. Starting from the state parallel to the plane of the image it horizontally rotates to the normal orientation. (c) White hexagon underlines the lateral symmetry of depicted mesophase occurring between the vertical supramolecular columns. Hexagonal arrangement is the most common among the various columnar systems.

Expansion of the averaged molecular geometry to the second dimension and the flat structure of discotics create novelty in comparison to 1D anisometric rod-like building blocks. Difference in the molecular shape has a direct influence on the change of the anisotropy of intermolecular interactions what is further manifested in unusual structural features of mesophases composed of discotic molecules. As a result of miscellaneous non-covalent forces (mainly steric and dispersion interactions) molecules tend to stack one onto another and create supramolecular wires that further arrange themselves in extended arrays called columnar mesophases. Regular packing of columns may exhibit several geometries, with a hexagonal arrangement of columns, presented on Figure 2.2(c) being most frequently met. Columnar mesophases are also the most characteristic systems of discotic liquid crystals that discern them from the calamitics.<sup>21</sup>

### 2.3.1 Types of columnar mesophases

Several subclasses of columnar mesophases exist, according to the spatial arrangement of molecular wires. What distinguishes among different representatives is the packing symmetry that is defined by three components:

- the arrangement of columns in space,
- the orientation of the molecular planes with respect to the columnar axis,
- the degree of stacking order within the columns.

As already mentioned, the columns may be arranged in close-packed architecture, where cross-section perpendicular to the column axis reveals hexagonal symmetry. In this case the molecular planes remain perpendicular to the columnar axes. This is one of the most commonly met types of mesophases formed by discotics: the columnar hexagonal ( $\text{Col}_h$ ) mesophase. Its plan view is presented on Figure 2.3(a), together with the respective unit cell. The associated space group:  $P6/mmm$  (equivalent to the  $D_{6h}$  point group in Schoenflies notation) is the one of the highest symmetry. However, the columnar hexagonal, although often met, is only one of the possible arrangements for columnar mesophases of discotic molecules. The other typical examples are therefore presented on Figure 2.3(b) and (c), which consist of rectangular and oblique space groups, respectively. Worth to be underlined is the fact, that those plan views represent not only the 2D hexagonal symmetry breaking of the centers of masses of building blocks. All of the presented columnar mesophases (besides hexagonal) contain molecules with their planes tilted from the plane of the image, as indicated by the oval shapes. Such loss of coplanarity may be an important factor in the incompatibility of bulk mesophase with the 2D crystal adsorbed on the surface.

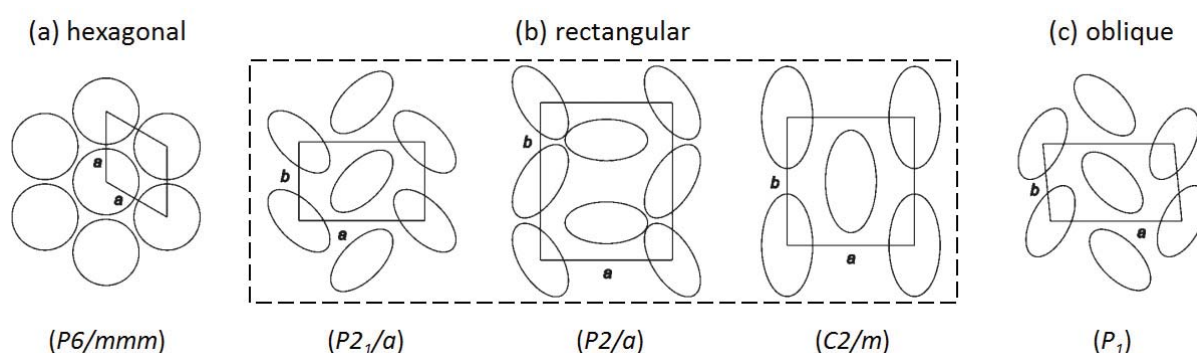


**Figure 2.3** Plan views of the 2D lattices of: (a) hexagonal, (b) different subclasses of rectangular and (c) oblique columnar mesophases. Point-group symmetries according to the Hermann-Mauguin notation are shown in parentheses underneath each lattice. Circles in the case of columnar hexagonal (a) illustrate planarity of molecules with respect to columnar axis. In other cases, ellipses emphasize that molecular planes are not coplanar with the plane of the image, thus molecular axes are tilted from the columnar axes (from Ref. 21).

The classification of columnar mesophases according to the degree of stacking is presented by Figure 2.4. So far, it is commonly accepted to distinguish between at least four states of intracolumnar order. The disordered ( $Col_d$ ) and ordered ( $Col_o$ ) types of stacks may be distinguished based on X-ray diffraction data, but the transition between the two is not strictly defined. A further increase in orientational and/or positional order leads to the plastic columnar phase ( $Col_p$ ) in which molecules preserve possibility of in-plane-rotation (1D orientational and 3D positional order). The helical columnar phase (H) possessing crystal-like set of degrees of freedom (3D orientational and 3D positional order) have been also identified.<sup>22</sup> An illustrative example of variation of intracolumnar degree of order among close derivatives of discotic mesogens is the sequence of hexa-substituted triphenylenes (core presented on Figure 2.1(b)), with pentyloxy- and butyloxy-substituents. The X-ray diffraction data of a triphenylene possessing six  $-OC_5H_{11}$  tails reveals a hexagonal ordered state.<sup>23</sup> Decrease the length of each side-chain by only one carbon atom, that is substitution with  $-OC_4H_9$ , changes the situation significantly, as may be seen on Figure 2.4(b) with lower and upper curve, respectively. The occurrence of additional narrow reflections at intermediate scattering angles in the case of hexabutyloxy-homologue are in perfect agreement with the data reported previously for plastic columnar phase,  $Col_p$ .<sup>24</sup>

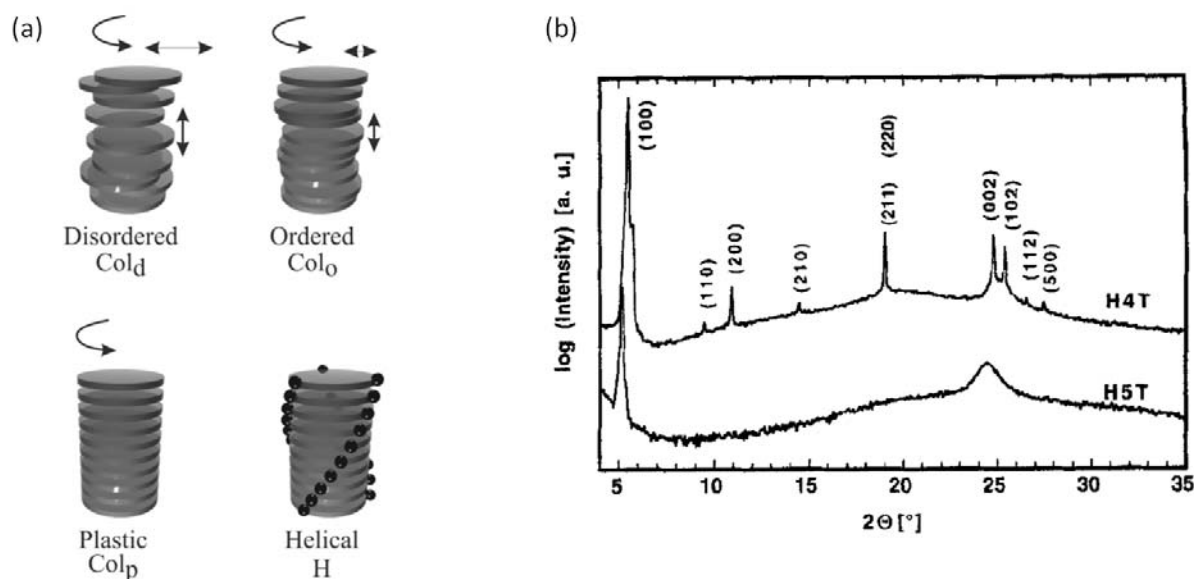


**Figure 2.4** Schematic representation of classification of columnar mesophases according to the intracolumnar degree of order and the dynamics of the molecules within the column: disordered columnar phase ( $Col_d$ ), ordered columnar phase ( $Col_o$ ), plastic columnar phase ( $Col_p$ ) and helical columnar phase (H) (from Ref. 22). Wide angle X-ray diffraction data for hexapentyloxy- (lower curve,  $T = 100$  °C) and hexabutyloxytriphenylene (upper curve,  $T = 115$  °C), revealing the increase of intracolumnar order for the latter one (from Ref. 23).



## 2.4 Triphenylene-based discotic liquid crystals

One of the most widely studied groups of discotic molecules are derivatives of triphenylene. Chemical literature recognizes symmetrical fused aromatic hydrocarbon 'triphenylene' for more than a century. It was Schultz who has isolated it from the pyrolytic products of benzene and to whom it owes its name.<sup>25</sup> The synthesis from cyclohexanone and following studies of various physical properties were performed at the beginning of twentieth century. Electrophilic aromatic substitution in bare triphenylene is directed by steric and electronic effect. Substitution at the  $\beta$ - or 2-position is favored over the one at the  $\alpha$ - or 1-position (please refer to the triphenylene core nomenclature depicted by Figure 2.5(a)), presumably due to a steric hindrance effect.<sup>25</sup>

The potential disc-like mesogenic properties of triphenylene were found in 1978,<sup>13</sup> and since that moment triphenylene derivatives have attracted attention of a numerous liquid crystals researchers. Triphenylene derivatives are thermally and chemically stable, their chemistry is fairly accessible, they show variety of mesophases and their one-dimensional charge and energy migration properties may be employed in wide group of potentially commercializable applications.<sup>17</sup> Those features have stimulated lots of synthetic chemists to challenge the efforts of preparing miscellaneous triphenylene-based DLCs that were later examined for their electroluminescence,<sup>26,27</sup> ferroelectric switching,<sup>28</sup> one-dimensional charge<sup>29-34</sup> and energy<sup>35-37</sup> migration. Up to date, more than 500 triphenylene-based discotic liquid crystals have been reported. Variety of possible substitutions (symmetrical, unsymmetrical or even hepta-substitutions) of the triphenylene core gives a wide range of changes in thermal and structural complexity, what is the topic of comprehensive reviews by Kumar.<sup>38,39</sup> The symmetrically 2,3,6,7,10,11-hexasubstituted derivatives of triphenylene are the most commonly studied DLCs.<sup>40</sup> Hexaethers, thioethers, selenoethers, esters (e.g. benzoates and cyclohexanoates) and hexaalkynes are examples most often met in the literature,<sup>41</sup> however, in recent years, research has focused primarily on improving the synthesis of triphenylene ethers, as these materials were reported to have interesting conducting<sup>42</sup> and photoconducting<sup>43</sup> properties. In the group of hexaether derivatives of triphenylene, the mesomorphic character of molecule is present only when the all six peripheral alkoxy chains have a minimum of three carbon atoms, i.e. propyloxy chains. This was actually discovered quite recently by Bushby *et al.*<sup>44</sup>

An example of widely studied hexa-substituted triphenylene: 2,3,6,7,10,11-hexapentyloxytriphenylene is depicted by Figure 2.5(b). This molecule is usually abbreviated "H5T" or "HAT5" in the literature, and very often plays a role of a model molecule in the comparative studies of newly synthesized mesogens.

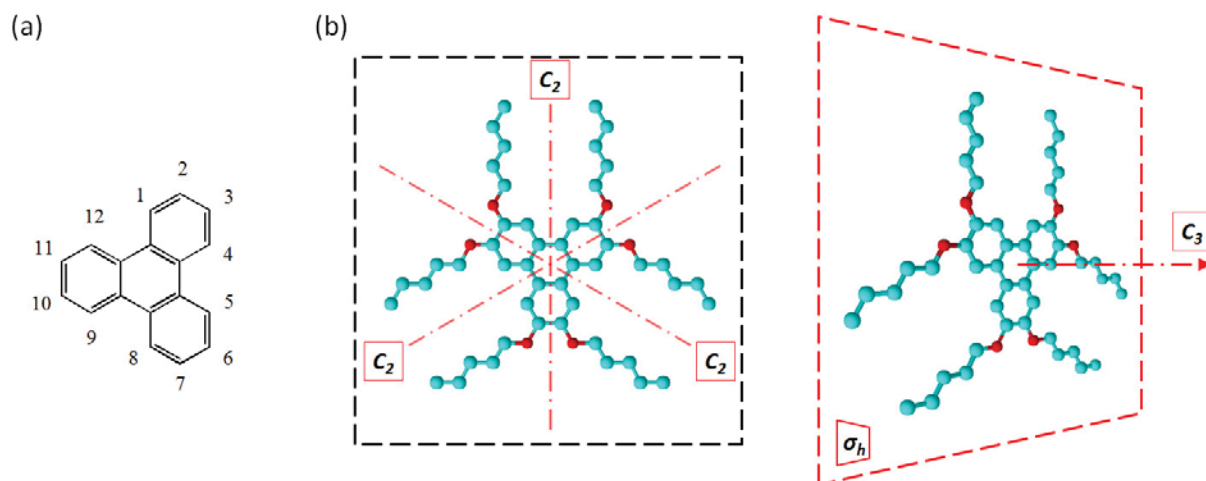


**Figure 2.5** (a) Structure of triphenylene polyaromatic core with denoted positions available for the side chain substitution. (b) Schematic presentation of symmetry elements on an example of hexasubstituted triphenylene that possesses the mesogenic properties. The molecule of 2,3,6,7,10,11-hexapentyl oxytriphenylene (H5T) represents the  $D_{3h}$  symmetry group, accordingly to possessed symmetry elements, presented here:  $3C_2$  proper symmetry axes,  $C_3$  principal axis and horizontal symmetry plane ( $\sigma_h$ ).

In terms of its crystallographic point group, the symmetry of triphenylene is classified as  $D_{3h}$  in Schoenflies notation. Symmetrically 2,3,6,7,10,11-hexa-substituted molecules keep the same symmetry and thus they possess following set of symmetry elements:  $C_1$ ,  $3C_2$ ,  $3\sigma_h$ ,  $\sigma_h$ ,  $\pm C_3$  and  $\pm S_6$ . The first one,  $C_1$ , represents a proper symmetry axis connected with an identity transformation (denoted as  $E$ , coming from the German *Einheit*, meaning 'unity'), for  $n = 1$  in association with  $\frac{2\pi}{1}$  radians rotation. The three  $C_2$  axes marked on Figure 2.5(b) by red dash-dot lines represent another proper symmetry axes. They lie within the plane of the molecule and the symmetry operation associated with them is a rotation by  $\frac{2\pi}{2}$  radians, equal  $180^\circ$ . The following symmetry element depicted on Figure 2.5(b) is the  $C_3$  axis, pointing out of the plane of the molecule (right panel). We call this axis the *principle axis*, since it represents the highest  $n$  for this particular molecule. For triphenylene molecule it is connected with a rotation by  $\frac{2\pi}{3}$  radians (i.e.  $120^\circ$ ) symmetry operation. The remaining axes of rotation,  $S_6$ , that is the improper rotation axes are not shown on the scheme. They represent a regular rotation followed by a reflection in the plane perpendicular to the axis of rotation, here the plane of the image. Another subgroup of symmetry elements are reflection planes, with *horizontal* reflection plane ( $\sigma_h$ ) - passing through the origin and perpendicular to the axis with the 'highest' symmetry. The three *vertical* reflection planes ( $\sigma_v$ ) are perpendicular to the plane of the image and they contain each of the  $C_2$  proper symmetry axes (not shown for clarity).

## 2.5 Columnar mesophases as one-dimensional semiconductors

The main reason of a large interest of scientific community in exploration of DLCs and in particular in tailoring of the columnar mesophases are their highly anisotropic charge and energy transport characteristics. Vast amount of DLCs form columnar mesophases probably due to intense  $\pi$ - $\pi$  interactions between polyaromatic cores. Typical inter-core distance for two neighboring molecules in a single column is usually approximately 3.5 Å what means that there exists a net overlap between the  $\pi$ -orbitals. Due to the presence of long aliphatic chains around the core, the inter-columnar distance is of the order of 20÷40 Å, depending on the chain length.<sup>17</sup> Therefore, interactions between subsequent molecules within the same column are much stronger than interactions between the molecules of different columns. The peripherally spaced aliphatic tails create an isolating shell that, firstly, stabilizes the mesophase by the microsegregation of chemically alike moieties, and secondly isolates the inner region of the column. The latter fact results in virtual confinement of the charge in a single column connected with a drastic decrease in probability for it to traverse in the direction other than perpendicular to axis of column. Conductivity along the columns for those types of mesophases has been reported to be greater for several orders of magnitude comparing to the perpendicular direction.<sup>45</sup> Prior to a seminal paper of Adam *et al.*,<sup>43</sup> electronic conductivity in liquid crystals was generally assumed to be of ionic nature. This statement is in agreement with the inherent liquid-like fluidity of liquid crystals and the high sensitivity of electronic conduction to the chemical impurities that are capable of terminating it, being present in the amounts as small as ppm.<sup>46</sup> As a consequence of creating the energetic traps, i.e. additional energetic levels in the existing HOMO-LUMO gap of the material, chemical impurities are responsible for trapping of charge and the successive drift as ionic species. The latter is possible especially in the low-viscosity phases like e.g. nematics.<sup>47</sup> In fact, a first pure liquid crystalline system for which non-ionic conduction has been shown was a discotic hexapentyloxytriphenylene (H5T). Until that moment several research groups have reported electronic conductivity achieved as a result of chemical doping of hexahexyloxytriphenylene (H6T) with iodine<sup>48</sup> or AlCl<sub>3</sub>.<sup>49</sup> Results published by Adam *et al.*<sup>43</sup> have evidenced that mobility of positive electronic charge carriers (holes) in the columnar hexagonal mesophase range may reach values as high as  $10^{-3} \text{ cm}^2 \text{ V}^{-1} \text{ s}^{-1}$ . A development of time-of-flight (TOF) method basing on the (photo)injection of charges into the cell filled with the well-aligned material facilitated further understanding of charge transport within discotic liquid crystals, and resulted in finding of electronic mobility values comparable to the amorphous silicon ( $\sim 10^{-1} \text{ cm}^2 \text{ V}^{-1} \text{ s}^{-1}$ ), obtained for hexa-hexylthiotriphenylene (HHTT).<sup>50</sup> Extensive examinations of this material, enabled to achieve the ambipolar charge transport of the same order of magnitude, what normally remain more challenging since the detrimental influence of the oxygen on the electron mobility.<sup>51</sup> The latter fact is

directly connected with the appearance of additional degrees of order within the material that specifically occurs for HHTT and is referred to as the *helical order*. This alternatively called *H-phase* may be effectively treated as 3D ordered system with a rotational freedom of molecules. According to the X-ray diffraction experiments the associated formation of triangular superlattice of columns is a manifestation of increase of the stiffness of the terminal alkyl tails.<sup>52</sup> In addition to the helical phase, the hexabutyloxytriphenylene (H4T) has shown the plastic crystal order for which intercolumnar and intracolumnar distances are more tight in comparison to H5T homologue. From X-ray diffraction data, the phase behavior of H4T can be described as ordered in three dimensions, but with the rotation of the molecular units within the ordered columns still being allowed. Comparison of the low-angle sides of the peaks revealed that the intracolumnar order is significantly greater in H4T than in H5T, what has a direct reflection in the high charge carrier mobility for H4T, which equals  $10^{-2} \text{ cm}^2 \text{ V}^{-1} \text{ s}^{-1}$ .<sup>23</sup> As easily noticed, symmetrically hexa-substituted triphenylenes used to prevail the beginning of the studies of self-organizing low-molecular weight semiconductors.<sup>53,54</sup> However, besides triphenylenes several other central polyaromatic motifs have attracted attention of researchers, e.g. hexabenzocoronenes,<sup>55,56</sup> perylenes<sup>57,58</sup> or heterocyclic macrocycles like porphyrin and phthalocyanine<sup>59,60</sup> (Figure 2.1(c), (d) and (g), respectively). Some of the most promising discotic liquid crystal semiconductors are hexabenzocoronenes for which room temperature mobility values exceeded  $1 \text{ cm}^2 \text{ V}^{-1} \text{ s}^{-1}$ .<sup>61</sup> High values of charge carrier mobility in DLC materials caused increasing interest in the applicative type of research. As a result, discotic liquid crystals have been implemented in various types of organic electronic devices like Organic Light-Emitting Diodes (OLEDs),<sup>27,62,63</sup> Organic Field-Effect Transistors (OFETs)<sup>64</sup> and Organic Photovoltaic Devices (OPVs)<sup>65–67</sup> in order to verify their usability as active layers.

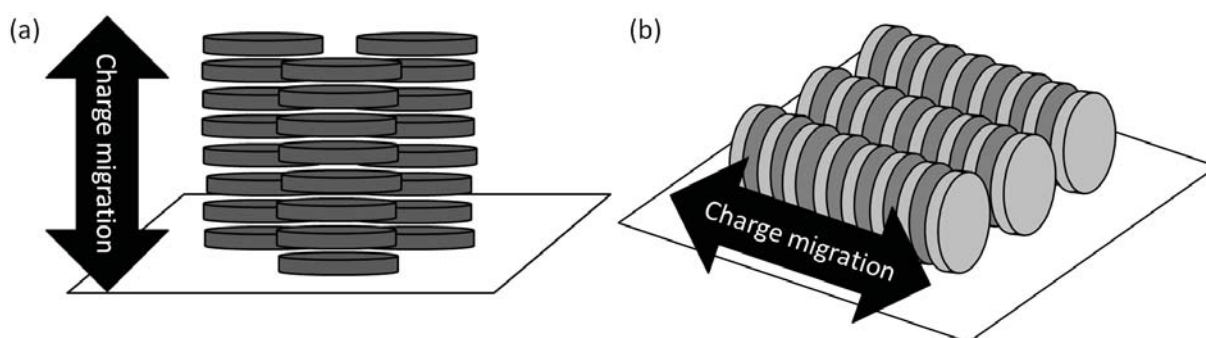


**Figure 2.6** Schematic representation of two main anchoring modes: (a) homeotropic, and (b) planar alignment of columns formed by discotic liquid crystals. Black arrows point the direction of charge transport which is perpendicular or parallel to the surface, respectively.

Another important feature is that depending on the type of the device there is a fundamental difference in the preferable orientation of the columnar meso-structure.<sup>68</sup> While for the OLEDs or OPVs the desirable column orientation is normal to the substrate, i.e. *homeotropic* (Figure 2.6(a)), architecture of OFETs requires parallel column orientation with respect to the substrate, i.e. *planar* (Figure 2.6(b)). Those two basic anchoring modes of molecules can be controlled by various ways including chemical treatment,<sup>69</sup> photoalignment,<sup>70,71</sup> or even by the rate of annealing process.<sup>72</sup> In general there is one consistent need for the proper performance of a semiconducting layer, i.e. assurance of a non-disturbed charge carrier drift by uniformity of alignment and lack of structural defects. This is one of the most prominent features of liquid crystalline materials, since their well-known property of self-healing. Considering high demand on the clean and renewable energy we especially observe an increasing need of improvement of state of the art organic photovoltaic devices, which implement the columnar mesophases in the orthogonal orientation. Majority of the research on homeotropic alignment of discotic liquid crystals has been almost exclusively devoted to LC films confined between two surfaces. This is of primary importance, since a good definition of the interface between the DLC material and the supporting solid is necessary, especially in the case of substrates of technological interest, like indium tin-oxide.<sup>73</sup> However, since OPV devices are generally made by deposition of the organic active layer on one of the electrodes followed by deposition of the second electrode, it is necessary to obtain homeotropic orientation in open films as well.<sup>74</sup> Massive amount of studies has been performed in order to relate the molecular structure of discotics with the extent of supramolecular order and its influence on the charge transport properties.<sup>55,75,76</sup> However, much less attention has been paid to the interfacial region and the geometry of the physisorbed discotic molecules and its modification as a result of presence of solid substrate. One way to start the discussion of this topic is to try to observe if the molecules of interest do form two-dimensional self-assemblies at surfaces of considerable interest, i.e. metallic or semiconductive crystals. Formation of monolayers of DLCs on various substrates, especially highly-oriented pyrolytic graphite (HOPG) and one of the main crystallographic faces of gold: Au(111), will be discussed in the following section. Several surface-promoted events will be underlined, one of the most important being the symmetry breaking and the appearance of the 2D chirality for the non-chiral organic molecules. An interesting strategy of introduction of a buffer monolayer consisting of *n*-hydrocarbons will also be shown. In addition, the influence of the temperature as a controlling parameter will be discussed.

## 2.6 Scanning tunneling microscopy at the liquid/solid interface

Equipment and procedures described in this section, including preparation of materials and deposition of solution onto the substrate, are identical for all measurements included in this thesis, regardless the molecule of analyte. All of those aspects, including the experimental setup will be presented here, but they apply uniformly to the results contained in Chapters 3, 4 and 5.

### 2.6.1 Beyond optical microscopy

Scanning tunneling microscopy (STM) was invented in the second to last decade of the XXth century, thanks to the scientists working in the IBM laboratories in Zurich. The first scanning tunneling microscope has been constructed by Gerd Binnig and Heinrich Rohrer, who have performed research on the thin films of oxides, at the end of seventies.<sup>77</sup> The limitations of the apparatus of that time have actuated the discovery by both physicists of a new experimental tool which enabled to explore the solid surfaces in the nanometric scale.<sup>78</sup> This invention may be considered as a first response for the discussion initiated by the Richard Feynman in his lecture *There's plenty of room at the bottom*, regarded until today as a symbolic moment of birth of the field of nanotechnology.<sup>79</sup> STM was the first instrument which allowed for imaging of surfaces with atomic resolution in a real space, without the applying of diffraction.<sup>80,81</sup> The great importance of STM has been soon appreciated, since just 4 years after the presentation – in 1986 – Binnig and Rohrer have been awarded the Noble Prize in Physics.

STM has been initially used for obtaining the information about the structure of surfaces of different semiconducting and metallic materials, mainly in the controlled environment of ultra-high vacuum (UHV).<sup>82</sup> After completion of characterization of most technologically important surfaces (i.e. silicon), their reconstructions and common defects, there was a second phase to begin: observation of the other objects already deposited onto the surface. On one hand, the development of the apparatus enabled to visualize single molecules together with exploration of their 'behavior', e.g. preferential adsorption on the vicinal surfaces (also the possibility of stimulation of those objects by the scanning probe). On the other hand, it was established that on the less reactive substrates (e.g. graphite), work in ambient conditions or in the liquid environment is possible, what gives the possibility of monitoring of self-assembly processes of the low-molecular weight compounds, like liquid crystals.<sup>83</sup> This last mentioned branch of scanning probe microscopy is actually the main experimental method employed throughout first of the two main parts of this thesis, which comprise Chapters 3, 4 and 5.

## 2.6.2 Physics behind STM

The idea of scanning tunneling microscopy is based on the quantum tunneling effect, which has consequences in formation of the so-called tunneling current, which in other words is the passage (*tunneling*) of the electron through the potential barrier in vacuum. Such situation is a violation of classical mechanics, being at the same moment a manifestation of a quantum theory. Although the tunneling effect was theoretically predicted as soon as 1920s,<sup>84</sup> its first experimental evidence dates for the 1958, when Leo Esaki reported on the ‘new phenomenon in narrow Germanium  $p-n$  junctions’.<sup>85</sup> In STM the tunneling of electrons takes place between two biased electrodes, through an insulating medium that is vacuum, air or carefully chosen liquid.<sup>86</sup> One of the polarized electrodes is an atomically flat surface, while the other (called *probe*) is a thin wire (usually made of Pt/Ir alloy or tungsten). As soon as the two are placed in a close proximity (*ca.* 1 nm) the wave-functions of both electrodes overlap and the tunneling may occur. The polarity of bias is determining the direction of tunneling current flow, i.e. if the electrons will tunnel from the probe to the sample or in reverse direction. The exponential relation between the inter-electrode gap and the tunneling current magnitude makes the STM an extremely sensitive tool.<sup>87,88</sup> Another parameter very decisive on the quality of measurements is the sharpness of the tip, since for the conditions normally used in high resolution STM about 90% of the tunneling current is carried by the apical atom because of the difference in distance between it and the atoms at its base.<sup>89</sup>

## 2.7 Experimental setup

The STM is schematically presented on Figure 2.7(a). A crucial element of each type of scanning probe microscope is the piezoelectric scanner, which enables an extremely precise movement of either the probe, or the sample (as in the case presented by Figure 2.7(a)), in the x-y plane. When the properly cut wire is placed in the probe-holder (Figure 2.7(b)), and the latter is fixed above the sample, the following step is a coarse approach, which is performed manually, with a designed screw-system (Figure 2.7(c)). Before the fine-approach of the tip is made – with the aid of an automated step motor, the system is to be isolated from the surroundings to diminish the unwanted noise. This is achieved by (i) damping the mechanical vibrations by means of e.g. hanging the microscope head on a special mounting (see the three black ropes on the Figure 2.7(d)) and also by (ii) separating the microscope from the sonic noise (e.g. covering the microscope head with the vessel, Figure 2.7(d)).

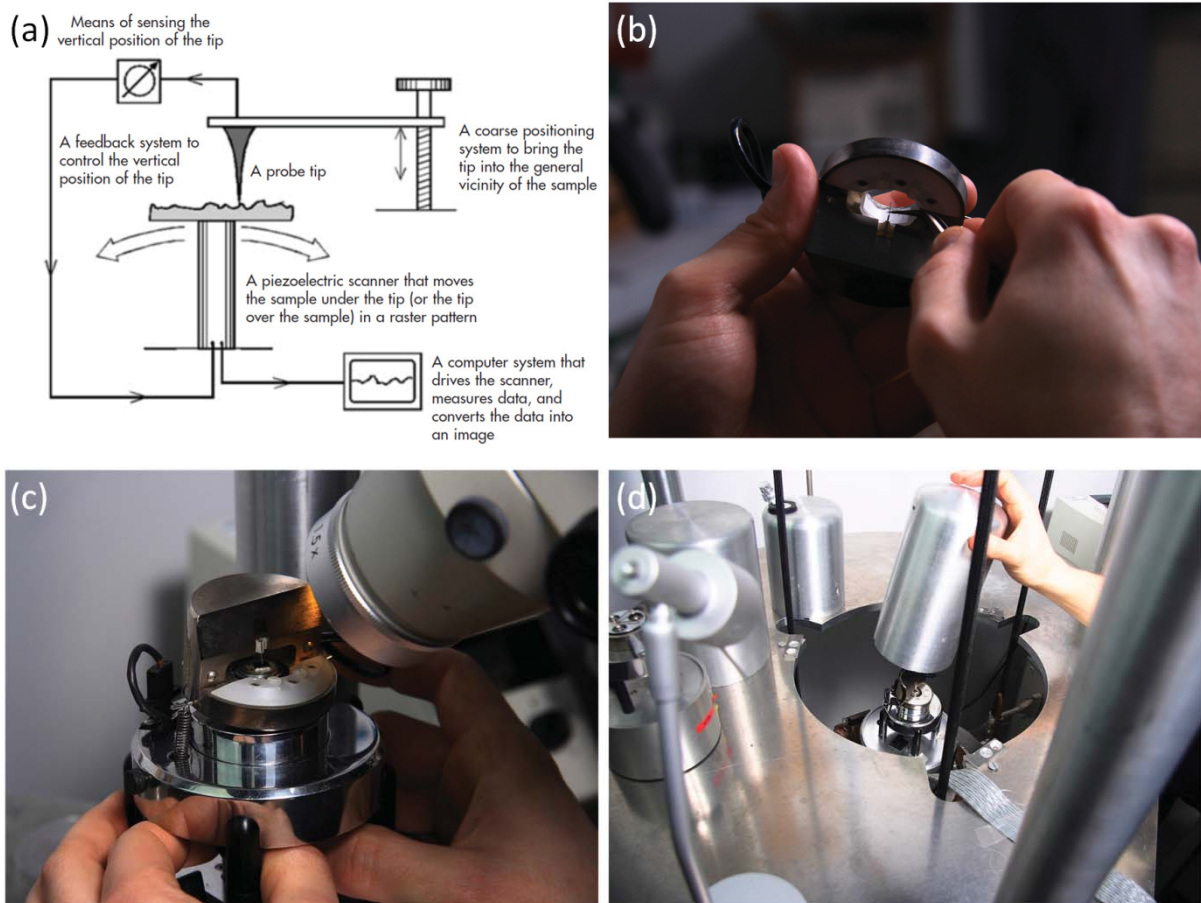


**Figure 2.7** (a) A general scheme of the scanning probe microscope, with the explanation of basic principles including scanning process and the feedback. (b) placing of the STM tip (Pt/Ir wire) in the tip-holder. (c) coarse positioning of the tip over the sample surface. (d) covering of the microscope head with the metallic cylinder in order to isolate it from the ambience.

All of the measurements presented in this thesis were performed in the so-called constant-current mode (CCM), which is employing the negative-feedback (an increase in the tunneling current causes the increase in the sample-probe gap). The scanning probe is registering the tunneling current for each measuring point and subsequently compares its value to the set-point at the each step, in order to establish the offset and either approach or retract the probe. What should be underlined at this point is that the STM data should not be treated as information on the exact topography of the sample, but rather an envelope of electronic and topological features. For the applied bias, the scanning tip probes the amount of occupied and non-occupied electronic states in the proximity of the Fermi level, so it rather maps the surface of a constant probability of tunneling, which is dependent in a first approximation on the local density of states (LDOS) of the surface.



## 2.8 Description of the substrate used

Bulk crystal of gold corresponds to a face-centered cubic (fcc) crystallographic structure. The (111) face of gold, denoted as Au(111), is one of its three low-index planes and represents the situation when surface atoms are hexagonally packed with the distance between the centers of closest neighbors equal to 0.288 nm (Figure 2.8(a)). However, this ideally flat facet is a highly unfavorable state. Since surface atoms are lacking of neighbors – in order to minimize the surface energy - they reorganize the bonding among themselves. This leads to formation of reconstructions of periodicities different from bulk-terminated surface, namely the appearance of a ( $p \times 1$ ) superstructure with  $p = 22 \div 23$  along the  $\langle 110 \rangle$  direction corresponding to an overall contraction of about 4%.<sup>90</sup> Appearance of a  $23 \times 3$  reconstruction (Figure 2.8(b)) is, firstly, the evidence of purity of the surface which is crucial for self-assembled monolayers (SAMs) formation. Secondly, it is well-established that lines of surface reconstructions on Au(111) are formed along  $\langle 112 \rangle$  crystallographic direction,<sup>91</sup> thus making them a good reference for finding orientation of molecules of adsorbates with respect to underneath substrate. In the following section, lines of reconstruction will help us to answer the question if the self-assemblies of molecules of a model discotic liquid crystal on gold reveal any features of commensurability with Au(111).

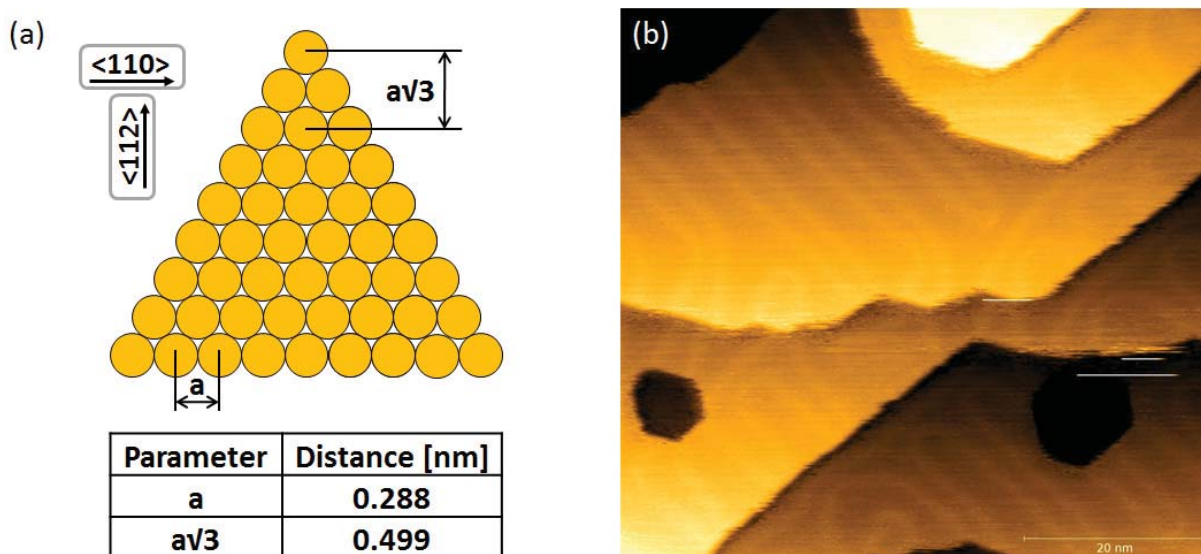


**Figure 2.8** (a) Hard-sphere representation of non-reconstructed Au(111) surface with indicated crystallographic directions and distance parameters. (b) UHV-STM constant current image showing several terraces of bare, reconstructed Au(111) surface. Bright linear features that always go in pairs represent the relaxation of the surface of gold. The sample has been flame annealed in propane gas flame in ambient conditions, prior to the transfer into the STM chamber.  $I_t = 40$  pA,  $V_t = 500$  mV.

Among the full panoply of experimental methods most frequently implemented for studying surfaces and processes related to surfaces one may distinguish the direct space techniques and reciprocal space techniques. One of the most classical methods regarding the surface studies in the reciprocal space – low-energy electron diffraction (LEED), uses electron beams of energies of about 20÷500 eV, so that only the first few atomic layers are penetrated. This enables to examine the species physisorbed on the surface, including organic compounds like DLCs.<sup>92</sup> Another group of techniques consist of electron spectroscopy techniques, like X-ray photoelectron spectroscopy (XPS) which probes the electronic states associated with core levels.<sup>93</sup> Also vibrational spectroscopies have been employed to study anchoring and alignment of DLCs, e.g. infrared (IR) spectroscopy.<sup>94,95</sup> Nevertheless, the most revolutionary class of surface science techniques remain the scanning probe microscopies (SPM), that started in 1980s with the invention of a scanning tunneling microscope (STM).<sup>80,82</sup> The basis of all scanning probe or proximal techniques is that an extremely sharp tip is brought to the close vicinity of the analyzed surface. The heart of every kind of SPM setup is the scanning system that employs the piezoelectric elements for the extremely precise motion of the probe. Depending on the type of SPM technique – different parameter is monitored and mapped onto the 2D space that reflects the spatial variations of a given property of system. Beside the protoplast method - scanning tunneling microscopy, for which the tunneling current is measured, a lot of studies of liquid crystals have been conducted by atomic force microscopy (AFM)<sup>96,97</sup> and near-field scanning optical microscopy (NSOM).<sup>98</sup> However, due to the fact that the following chapters of this thesis present experimental results obtained by STM measurements at the liquid/solid interface (which is, by far, the technique of highest resolution for surface studies of such systems) quoted literature examples are limited to those obtained by this technique. In other words, the highlighted results describe the self-assembly behavior of discotic molecules at the interface between the tunneling liquid (solvent) and a crystalline solid (electrode). During the process of collecting the data a scanning probe (STM tip) remains immersed in the solution.

### 2.8.1 Introduction to surface crystallography

Since I study the following ordered 2D networks of DLC molecules, organized thanks to the influence of the crystalline substrate, a brief introduction to 2D crystallography may be useful. Presence of surface for regular crystalline material is connected with breaking of the three-dimensional symmetry of a crystal. Consequently, the 14 Bravais lattices present in the bulk crystal, are reduced to the 5 Bravais nets on the surface. The corresponding structures of unit cells in 2D (also called unit meshes) are presented on Figure 2.9. The least symmetric one is the *oblique* structure, for which the two unit vectors of different length form a non-right angle. If the angle between the unit vectors is equal to 90°, one of the two *rectangular* lattices is present, *p* stands for

primitive rectangular lattice, and *c* stands for centered rectangular lattice that is the only non-primitive lattice. The latter one is also called *rhombic*, since the existing other possibility of constructing the unit cell is a diamond (two edges of equal length and the angle between them which is different than 90° and 60° degrees). The two latter cases, namely when two unit vectors of similar length form an angle of 90° or 60° degrees, represent the *square* and *hexagonal* lattices, respectively.

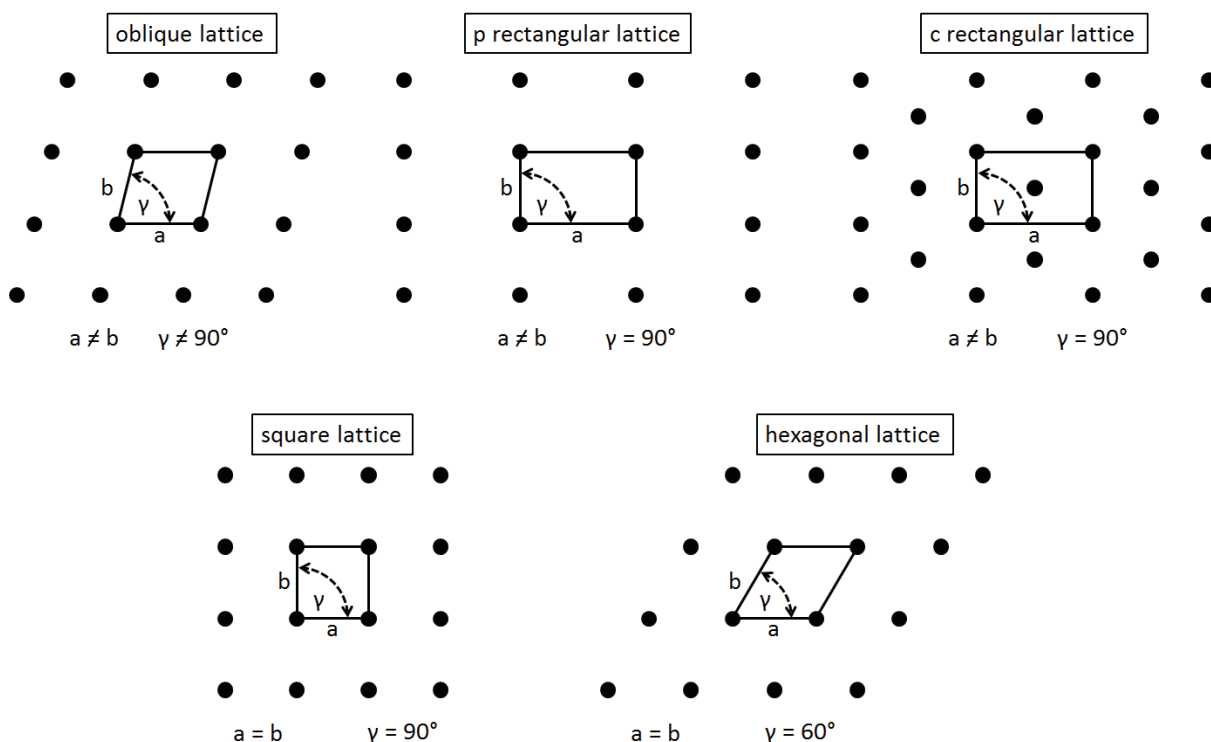


**Figure 2.9** Schematic representation of the five two-dimensional Bravais nets, together with their geometrical parameters. The centered *rectangular* lattice is the only non-primitive system, sometimes called *rhombic*.

## 2.8.2 Chirality of achiral units upon surface confinement

Unambiguously a reduction of systems dimensionality from 3D to 2D, (regardless the nature of studied interface: ultra-high vacuum/solid, liquid/solid, air/solid), creates a new situation from the symmetry point of view. Upon confinement by the substrate (2D) a single molecule may create a chiral motif, even if in solution (3D) it is achiral. It is a consequence of the fact that interface cannot possess a center of symmetry and the only preserved reflection planes are those perpendicular to the surface. Surface chirality of achiral molecules can be of twofold nature, but in both cases it is locally only expressed and vanishes at the global level.<sup>99</sup> In the first case, a single adsorption event of an achiral molecule may drive to a local chirality, defined as *point chirality*, depicted by Figure 2.10(a). It may happen when the molecule adsorption symmetry locally destroys all surface mirror

planes, e.g. when the reflection planes of the adsorbed molecule are not aligned with the surface mirror planes. In the second type of chirality, called the *organizational* chirality and schematically shown on Figure 2.10(b) – the ordered domains are formed in which organization of molecules destroys the reflection planes of the underlying surface.

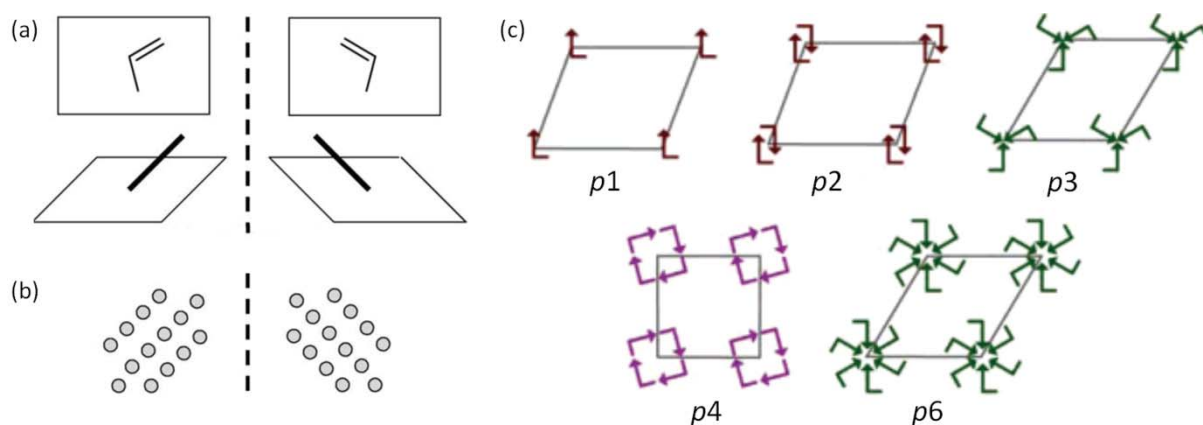


**Figure 2.10** Schematic representation of (a) point chirality (connected with either flat or out-of-plane arrangement of the molecule) and (b) organizational chirality – the ordered domains possess a chiral space group (here: *plane* group, according with the systems dimensionality). Dashed lines represent the mirrors (from Ref. 99). (c) Unit meshes of five chiral plane groups in 2D consisting of the asymmetric building blocks. Maroon color ( $p1$  and  $p2$  unit meshes) depicts an oblique symmetry of arrangement. Green color ( $p3$  and  $p6$  unit meshes) stands for a hexagonal spacing of lattice nodes. Violet color ( $p4$  unit mesh) represents the square symmetry (from Ref. 100).

The combination of the 5 Bravais nets representing the translational symmetry of lattice points with the 10 different point groups existing in 2D leads to 17 space groups appearing on surface.<sup>101</sup> Out of those 17 structures – called *plane groups* – only 5 support chirality (i.e. have no mirror symmetry perpendicular to the surface), namely  $p1$ ,  $p2$ ,  $p3$ ,  $p4$  and  $p6$ , which are schematically presented on Figure 2.10(c). Interestingly, the extensive studies evidence that in the case of physisorption at the liquid/solid interface roughly 80% of achiral molecules pack into the chiral plane groups.<sup>100</sup>

### 2.8.3 Triphenylenes on Highly-Oriented Pyrolytic Graphite (HOPG)

One of the first reports regarding the physisorption of complex organic molecules onto atomically flat substrates using scanning tunneling microscopy at a liquid/solid interface are papers of Rabe *et al.*<sup>102,103</sup> Among several types of objects examined from the point of view of potential self-assembly a distinct subgroup was represented by the hexa-substituted triphenylenes -  $HnT$ <sup>103,104</sup> (where 'n' denotes the number of carbon atoms in the single peripheral chain, attached to the positions 2, 3, 6, 7, 10 and 11 of the triphenylene core). First successful trials of self-assembled monolayers of hexakis-alkoxytriphenylenes on HOPG have been demonstrated by STM, and whereas in both  $H7T$ <sup>105</sup> and  $H16T$ <sup>104</sup> cases the 2D crystallites have been reported, the structures exhibited different geometry. Authors point out that the packing of hexakis-hexadecyloxytriphenylenes ( $n = 16$ ) allows the side-chain crystallization, whereas in the case of previously studied shorter heptyl-substituted-derivative ( $n = 7$ ) it was not the case.<sup>105</sup> STM image and proposed model of arrangement of  $H16T$  molecules are depicted by Figure 2.11. Regularly spaced linear features (among the brighter areas of higher STM contrast originating from triphenylene cores) represent the alkyl tails that are preferentially oriented parallel to each other, while in the case of  $H7T$  the arrangement exhibited three-fold symmetry, i.e. somehow preserved the molecular symmetry imposed by the core.

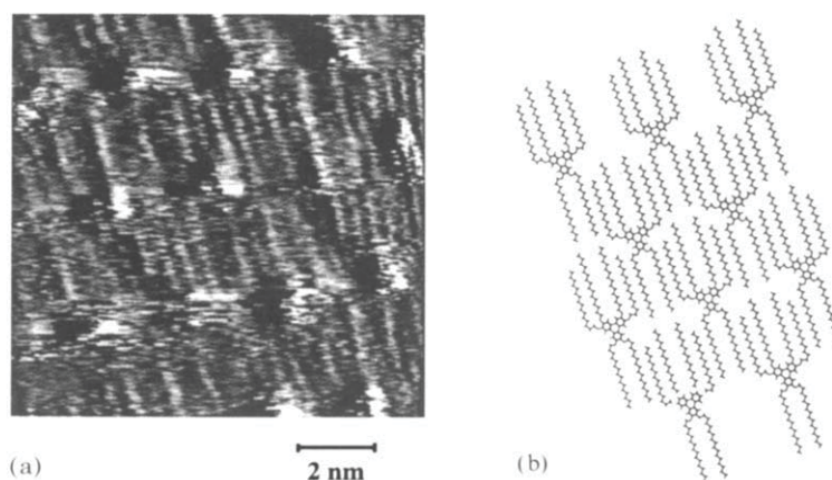


**Figure 2.11** (a) STM image and (b) the corresponding model of a hexakis-hexadecyloxytriphenylene ( $H16T$ ) monolayer on HOPG (from Ref. 104). Noticeable parallel orientation of terminal alkyl tails distinguishes the  $H16T$  structure from the  $H7T$ .<sup>105</sup>

Subsequently, the family of hexa-substituted triphenylene analogues having  $n = 5; 7; 9$  or  $11$  carbon atoms in the side chain has been studied by Charra *et al.*<sup>107</sup> For all four compounds authors report formation of monodomains of size bigger than  $100$  nm that show reproducible results of

geometrical features. Hexagonal organization of bright spots is evidently visible on Figure 2.12(a-d), respectively to each of four  $HnT$  molecules. Again, these regions correspond to the areas of higher electron density, thus to the  $\pi$ -conjugated cores of the single  $HnT$  molecules.<sup>107–109</sup> The common thing for those pictures (besides the hexagonal pattern) is the fact that in all the cases packing between the nearest neighbors is smaller than the corresponding distance between columns in the bulk columnar mesophase (with respect to literature<sup>110</sup>) However, as going from the molecules of shorter alkoxy chains:  $n = 5$  and  $7$  [(a) and (b) at Figure 2.12, respectively] to the mesogens of  $n = 9$  and  $n = 11$  [(c) and (d) at Figure 2.12, respectively] an interesting change in pattern may be noticed. In case of (a) and (b) all the spots are of equal size and brightness, while pictures (c) and (d) reveal the existence of a superlattice. Every third molecule appears brighter in H9T and H11T monolayers, while nothing similar happens for H5T and H7T monodomains – all the molecules are equivalent. For H9T intramolecular resolution may be achieved, what is not the case for e.g. H5T which is simply visible as a slightly diffused disc. Authors propose two different molecules conformations in the case of H9T and H11T, first of  $C_3$  and second of  $C_6$  symmetry. They claim that this difference is the answer for the non-equivalent appearance within the single domain. Intriguing is the fact that according to this point of view, a non-chiral  $HnT$  molecule (dissolved in a non-chiral solvent) can produce a chiral structure on a non-chiral substrate. This situation is illustrated by Figure 2.12(e). The molecule possessing  $C_6$  symmetry is said to have a rotational degree of freedom which enables alternation between more than one configuration with a rate faster than the STM scanning. However, theoretical predictions performed in accordance to the model of frustrated anti-ferromagnetic-like triangular Ising net is not so easily related to the experimentally evidenced differences.

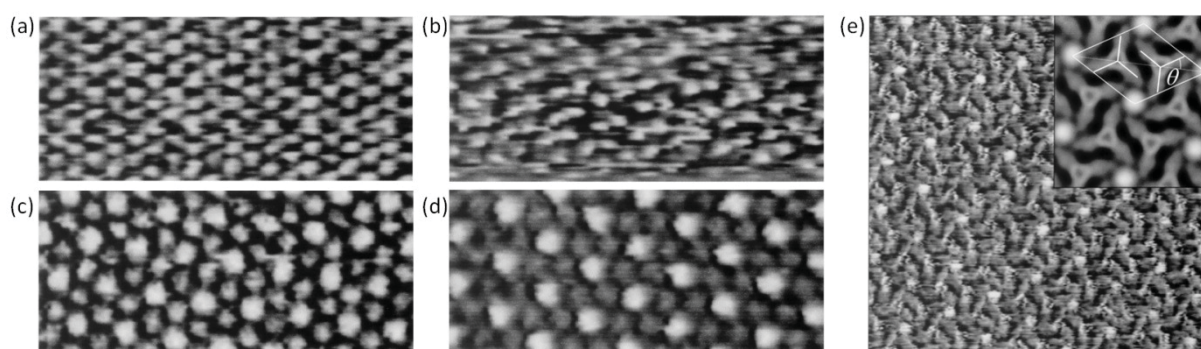


**Figure 2.12** STM images ( $29 \times 13 \text{ nm}^2$ ) of single domains of  $HnT$  monolayers, at the interface between the graphite and  $n$ -tetradecane solutions. (a) H5T, (b) H7T, (c) H9T and (d) H11T. (e) High-resolution STM image ( $29 \times 28 \text{ nm}^2$ ) of H11T monolayer. The inset shows the corresponding symmetrized correlation averaged image together with the unit cell (from Ref. 107).

Hexaalkoxytriphenylenes have been exploited on HOPG even further. Wu *et al.*<sup>111</sup> have performed experiments on H12T, H14T, H16T, H18T and H20T following procedure similar to the one used by Charra *et al.* As in the previous case, extended monolayer domains were obtained and individual molecules were highly resolved, with the conjugated cores consisting of three adjacent rings corresponding to the aromatic moiety. In the case of H12T surrounding alkoxy tails have been resolved precisely enough for authors to propose a model - geometrically similar to the one outlined by Charra *et al.* for H11T. Moreover, the triangular character of the core which may be seen on Figure 2.13(a), enabled to assess the orientation of the triphenylene part with respect to the monolayer. The model that consists of a central H12T molecule in the  $C_6$ -symmetry conformation surrounded by another six molecules in the  $C_3$ -symmetry conformation forming a regular hexagon is presented on Figure 2.13(b).

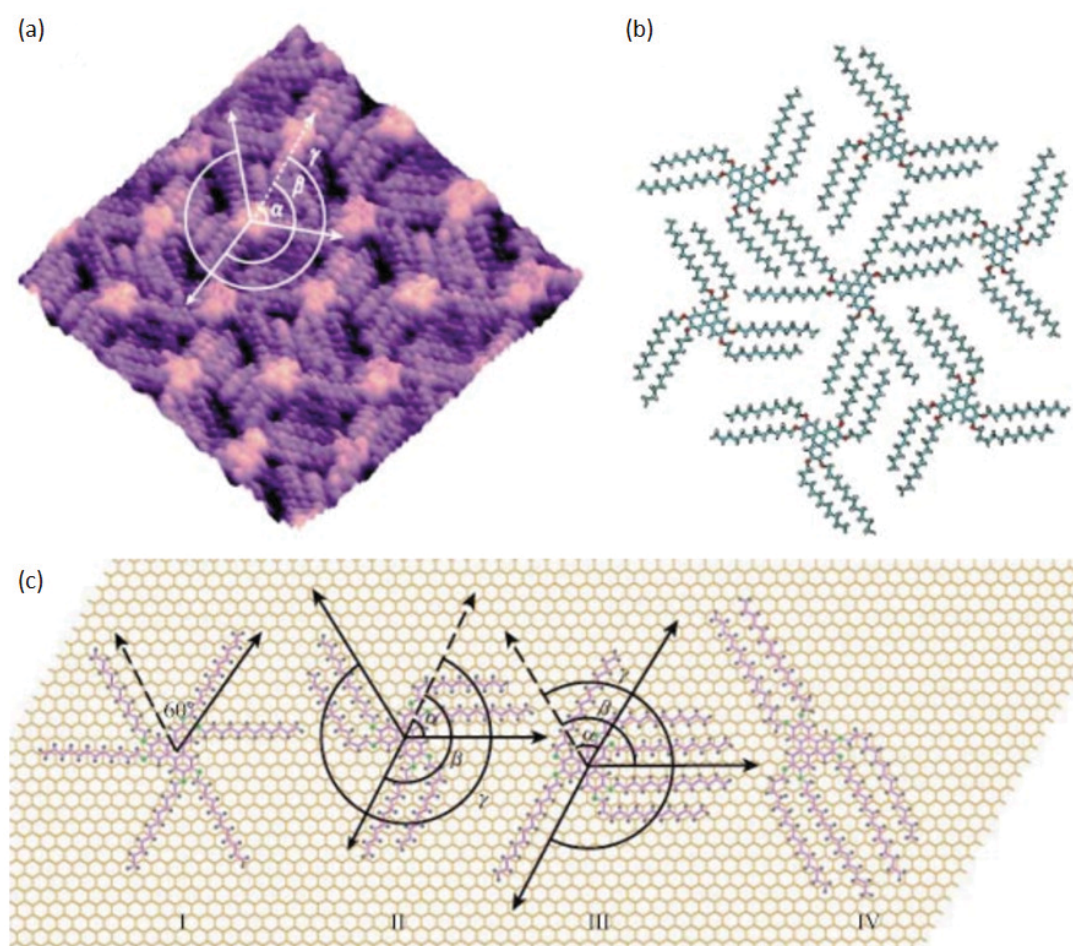


**Figure 2.13** (a) High-resolution STM image ( $10 \times 10 \text{ nm}^2$ ) of a H12T monolayer on HOPG and (b) the respective molecular packing model (from Ref. 111). (c) Schematic representation of 4 different molecular conformations corresponding to: H12T (I and II), H14T (III) and H16T and higher order derivatives (IV). Both triphenylene cores and alkoxy chains are commensurate with the HOPG lattice. Solid arrows represent orientations of flexible tails and dashed ones the midline of the triangle formed by aromatic core (from Ref. 111).

Situation changes drastically when two methylene groups are added to each of alkyl tails (i.e. for H14T). Self-assembly of this system is shown on Figure 2.14(a) and (b). Formation of dimers persistent on large areas may be clearly seen on Figure 2.14(a). High-resolution images reveal the antiparallel orientation of triphenylene cores within each dimer and the fact that alkyl chains are divided into two oriented groups (4 + 2) what leads to the loss of original symmetry of the molecule as depicted on Figure 2.14(b). When the alkoxy tails are extended further by additional two methylene units (H16T) the molecular arrangement changes again and another type of two-dimensional lattice is formed (Figure 2.14(c)). Although the arrangement of bright spots exhibits dimerization also in this case, it is assumed to have different origin. Firstly, due to the fact that the distance between two molecules increased (from 1.57 nm for H14T to 2.01 nm for H16T), interaction between the cores within the dimer is probably of a lesser extent. Moreover, intramolecular resolution evidently shows that although the antiparallel orientation of triphenylene cores is preserved, the alkyl tails changed their arrangement (Figure 2.14(d)). This appearance of the H16T system with all of the alkyl tails within one domain pointing the same direction is with good agreement to previously reported work (Rabe *et al.*<sup>105</sup>).

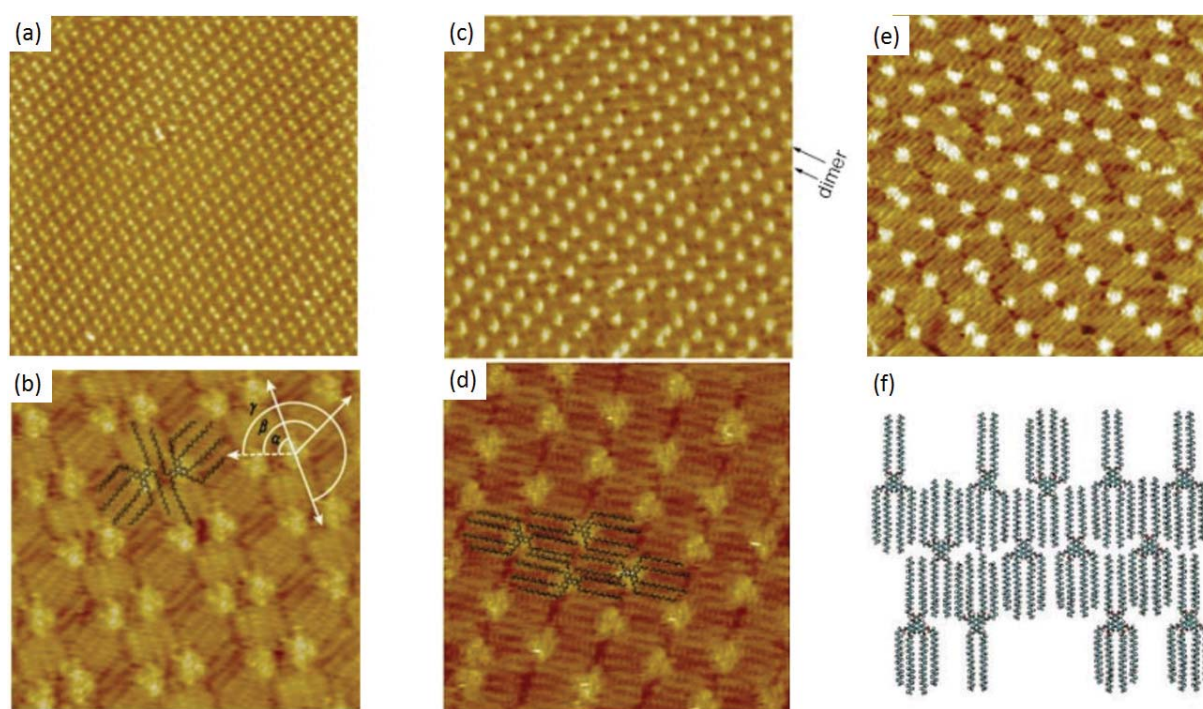


**Figure 2.14** (a) STM image ( $75.6 \times 75.6 \text{ nm}^2$ ) of a H14T monolayer and (b) high-resolution STM image ( $12.9 \times 12.9 \text{ nm}^2$ ) of a H14T with proposed dimer conformation. (c) STM image ( $48.2 \times 48.2 \text{ nm}^2$ ) of a H16T monolayer and (d) high-resolution STM image ( $18.7 \times 18.7 \text{ nm}^2$ ) of a H16T with proposed model of molecular arrangement. (e) High-resolution STM image ( $29.8 \times 29.8 \text{ nm}^2$ ) of a H20T and (f) proposed model of molecular packing of the monolayer of H20T underlying decrease in the regularity of the mesh (from Ref. 111).



According to authors no drastic changes are observed for the subsequently studied homologues, H18T and H20T, besides increase of spacing between the nearest neighbors and decrease in the uniformity in the intermolecular spacing. This is accounted for the reason that the steric hindrance of aromatic cores becomes less important as alkyl chains become longer and the 2D crystallization dominates. For better comparison of all the mesogens examined by Wu and co-workers, an idealized model of the molecules conformations proposed for the  $n = 12; 14; 16; 18$  and 20 series is shown on Figure 2.13(c). In the presented model the commensurability with underlying graphite lattice is assumed for both, the triphenylene cores and the alkoxy tails. An indisputable achievement of discernibility between different submolecular parts for the higher homologues of  $HnT$ , and associated probing of chirality of monolayers, e.g. in the case of H9T and H11T, have opened a new field of interfacial phenomena. Although the exact mechanism of formation of monolayers and the appearance of chirality were not explained, works of Charra *et al.* and Wu *et al.* have risen many questions and stimulated further research of discotic molecules on surfaces, including non-chiral and symmetrically substituted DLCs, for which the generated output was found to be not trivial.

Besides the alkoxy-substituted triphenylenes, the well-known thio-ether derivative: 2,3,6,7,10,11-hexakis(hexylthio)triphenylene (HHTT) has been studied on HOPG by Gabriel *et al.*<sup>112</sup> The ordered long-range self-associates of HHTT molecules in face-one configuration were found, that resembled those reported for the hexa-ethers of comparable molecular size. The main difference underlined by the authors was that due to the more extended triangular shape of the bright central motif, it was assumed that the higher conductivity zone includes also the sulfur atoms. This is in particularly good agreement with the high STM contrast of sulfur-containing functional groups of various organic compounds on HOPG.<sup>113,114</sup> Also in the case of higher homologues, e.g. hexakis(decylthio)triphenylene (HDTT) the intra-molecular contrast in the STM images showed a large contribution of electronic levels localized on the sulfur atoms bridging the conjugated core with the aliphatic side-chains.<sup>115</sup> Interestingly, the structure of 2D-self-assemblies of HDTT depends on the solvent used for the dissolution, deposition and observation of the material. In both cases the monolayers consist of unit cells possessing an oblique symmetry, but for phenyloctane solution HDTT molecules tend to form dimers with the antiparallel orientation of high-conductivity regions (Figure 2.15(a)). On the contrary, uniformly oriented features are observed for the HDTT/ $n$ -tetradecane solution casted onto HOPG, and no signs of dimerization are observed (Figure 2.15(b)). Moreover, since the domains containing the antiparallel-oriented dimers (phenyloctane cast) represent higher degree of surface density one would expect them to be thermodynamically more stable. On the contrary, what is observed is that the uniformly packed domains ( $n$ -tetradecane cast) tend to grow with time, at the expense of the more tightly packed ones. According to Palma *et al.* it is assumed to

originate from the fact that both surface polymorphs involve different arrangement of the alkyl chains, what is probably characterized by a higher degree of interdigitation in the case of less dense structure. This results in the increased extent of interfacial and intermolecular interactions, which has a further consequence that the less dense mesh is thermodynamically more stable structure.

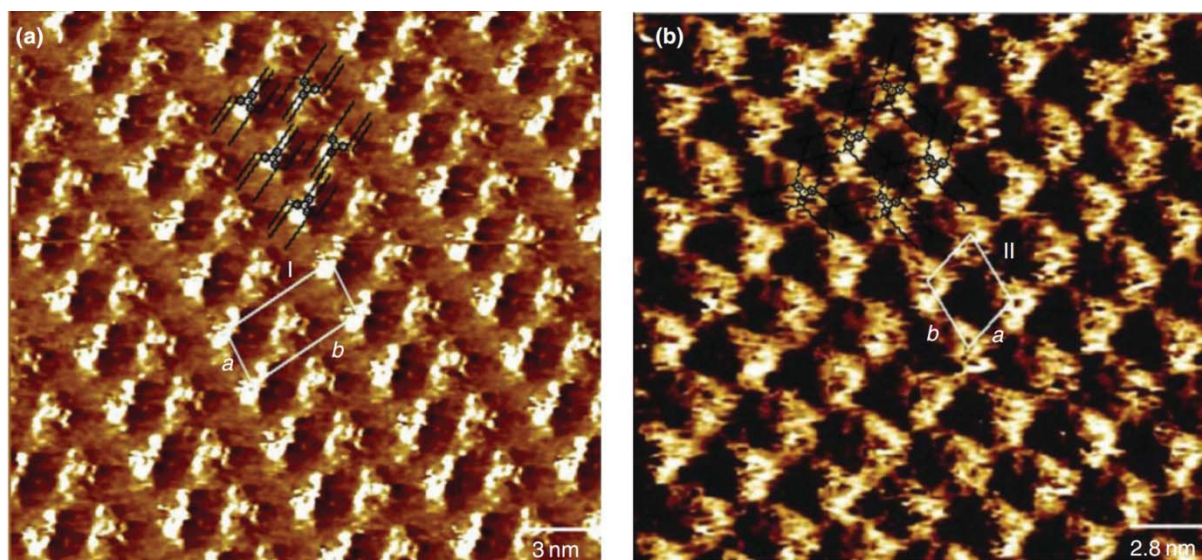


**Figure 2.15** STM images of HDTT recorded at the interface between HOPG and a solution in (a) phenyloctane or (b) *n*-tetradecane. While in the case of phenyloctane antiparallel orientation of molecules may be remarked and associated dimer formation, such behavior is not encountered when the *n*-tetradecane is used as a solvent (from Ref. 115).

#### 2.8.4 Triphenylenes on Au(111)

An important step in further understanding of two-dimensional self-assembly of discotic molecules was exploration of surfaces different than HOPG and examining the potential influence of the substrate on the formation of the monolayer. Regarding the discussed hexakis-alkoxytriphenylenes, one of the first examples of successful probing of discotic mesogens physisorbed on metallic substrates was reported by Katsonis *et al.*<sup>105</sup> Particularly, the H11T analogue have been studied on gold, namely on one of its main crystallographic planes, Au(111). The results of room-temperature STM experiments have evidenced well-organized monolayers of molecules of analyte. However, in comparison to H11T/HOPG system, H11T molecules when deposited onto Au(111) exhibit formation of self-assemblies with parallel rows of molecules, rather than 2D crystals of hexagonal symmetry. Figure 2.16 contains STM image and the corresponding schematic model of molecular packing of H11T mesogens. Intramolecular resolution reveals an omnipresent anti-parallel orientation of triphenylene cores for each dimer (schematically presented as ellipses - Figure 2.16).

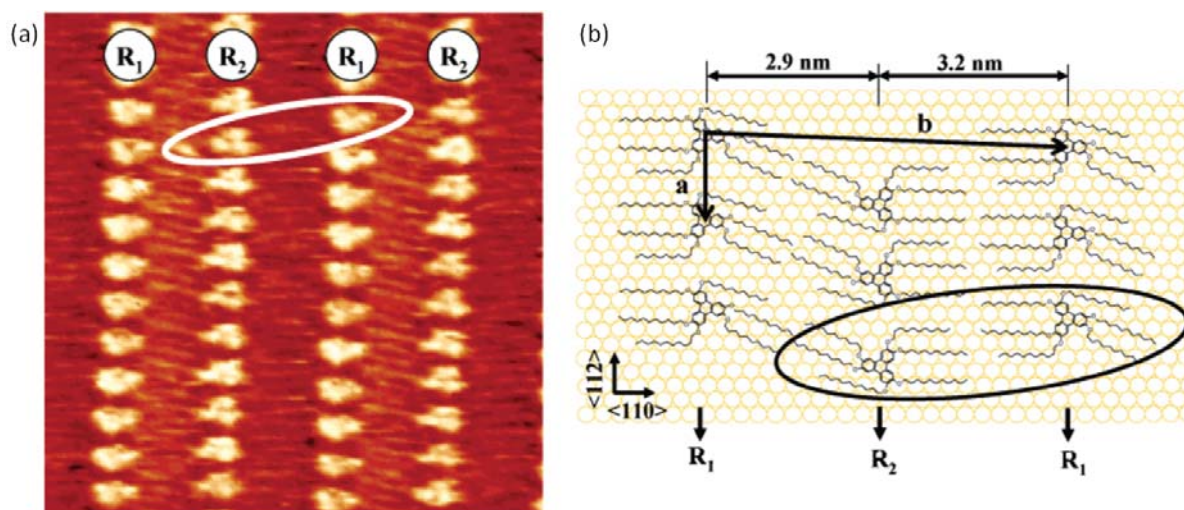


**Figure 2.16** (a) High-resolution STM image ( $17 \times 17 \text{ nm}^2$ ) of a H11T monolayer revealing the triangular shape of aromatic core and alkyl tails positions and (b) proposed model for packing of H11T on Au(111). In both cases ellipses represent H11T dimer (from Ref. 105).

Surprisingly encountered hexagonal symmetry breaking of H11T monolayer on Au(111) was a reason of several comparative studies regarding the substrate influence on the monolayer geometry in the case of triphenylenes. Perronet *et al.* have examined H5T and H11T on the basal plane of graphite, and on Au(111).<sup>117</sup> The authors pointed the fundamental difference in the molecular arrangements for H11T on both substrates that confirmed previous results.<sup>107,116</sup> Due to the drastic change in the geometry of the monolayer, the H11T molecule remains a classical example of studies of the substrate influence on the self-assembly process. At the origin of such state stands the tendency of relaxation of Au-surface atoms what results in the so-called surface reconstruction and in consequence arising of non-compatibility of substrate potential field symmetry with the molecule threefold symmetry. On the contrary, the lack of intramolecular resolution, due to diffusivity of the molecular features in the case of H5T, and consistence of the hexagonal symmetry of the monolayer on both HOPG and Au(111) resulted in the less clear nature of the self-assembly for this case. Main findings, formulated on the basis of surface density calculations stated that the hexagonal symmetry breaking for H11T/Au(111) system was a result of the change of mutual affinity of aromatic and aliphatic parts of the adsorbate while changing the substrate (namely the increased affinity to gold of the triphenylene core). In related studies, Katsonis *et al.*<sup>118</sup> referred to the different strength of the 'lever arm effect', as the mechanistic analogy to the surface-induced aligning of alkyl tails. For triphenylenes symmetrically substituted with short alkyl tails, like, H5T and H7T molecules adopt a hexagonal packing instead of H11T forming twin rows. Interestingly, for an intermediate H9T both types of packing coexist within the same monolayer: hexagonally arranged and row-like structures. In conclusion, tuning the length of the alkyl chain appears as an efficient way to precisely control the surface arrangement of triphenylenes.<sup>119</sup>

## 2.8.5 Hexabenzocoronenes

Another important group of discotic molecules possessing very good charge transport characteristics,<sup>61</sup> and thus potentially applicable as active layers, are hexa-*peri*-hexabenzocoronenes (HBC). Representing also all-benzenoid PAHs, unsubstituted HBC is roughly three times larger than the bare triphenylene, what may be noticed comparing Figures 2.1(b) and (c). It has been well-established, on group of numerous derivatives, that this is the direct reason of higher charge carrier mobility values for hexabenzocoronenes in comparison to triphenylenes and other discoid molecules.<sup>120</sup> One of the first HBC-derivatives studied by STM was the symmetrical hexakis(*n*-dodecyl)-*peri*-hexabenzocoronene (HBC-C<sub>12</sub>).<sup>121</sup> Stabel *et al.* have reported on the rhombic symmetry of the self-assemblies at a 1,2,4-trichlorobenzene/HOPG interface. STM image and corresponding molecular packing of the unit cell is presented on Figure 2.17(a) and (b). As may be seen, the adsorbed alkyl chains have a preferential direction parallel to one of the main axes of the underlying graphite lattice. Because the depicted packing results in some free volume, the alkyl chains fill this space dynamically by utilizing the thermal energy  $kT$  at room temperature. The unit cell drawn in Figure 2.17(b) ( $a = 1.94$  nm,  $b = 2.64$  nm,  $\gamma = 80^\circ$ ) reveals that the six-fold symmetry of the molecule has been reduced to a twofold symmetry of the adsorbate lattice. This phenomenon of symmetry reduction was previously known from the system H16T/HOPG.<sup>104</sup>

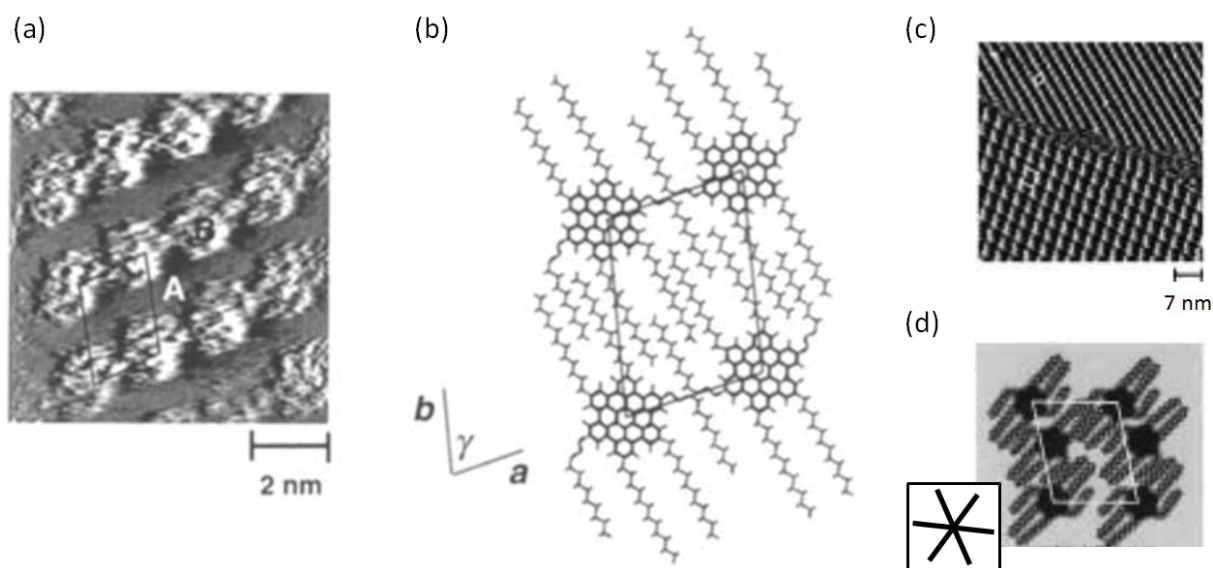


**Figure 2.17** (a) STM image of a HBC-C<sub>12</sub> monolayer at a 1,2,4-trichlorobenzene/HOPG interface with the schematically shown unit cell. (b) The proposed close-packed model of a 2D crystal of rhombic symmetry (from Ref. 121). (c) STM image of coexisting two types of self-assemblies of HBC-C<sub>12</sub> at a 1,2,4-trichlorobenzene/HOPG interface, rhombic (*top*) and dimer rows (*bottom*). (d) Proposed close-packed model of the dimer rows type of HBC-C<sub>12</sub> crystal. The inset represents the graphite lattice axes (from Ref. 122).

Surprisingly, the following studies by Ito *et al.*<sup>122</sup> have evidenced the appearance of two types of monolayers for identical HBC-C<sub>12</sub>/HOPG system. Besides the previously reported rhombic lattice, STM images provide a direct proof for coexisting of structure in which molecules are dimerized, forming molecular rows. Both molecular patterns are shown on the Figure 2.17(c), where the rhombic and 'dimer rows' are present respectively on the top and at the bottom of the image. Between the two domains, the area of domain boundary is present where the molecules are disordered. In addition, the molecular packing of the unit cell for the case of 'dimer rows' monolayer is shown on Figure 2.17(d), together with schematic directions of graphite lattice underneath. The molecular surface density calculated for rhombic and 'dimer rows' structures and equal to  $4.96 \pm 0.48 \text{ nm}^2$  per molecule and  $6.63 \pm 0.75 \text{ nm}^2$  per molecule indicate the more tightly packed monolayer of the rhombic structure. It is in agreement with the increased stability of this type of molecular packing since the areas of rhombic lattice-type tend to increase their size, at the cost of the 'dimer rows' expense that are the more loosely packed type of domains.<sup>122</sup> As a result, the rhombic type of monolayer was assumed to represent the most stable surface polymorph, while the existence of 'dimer rows' corresponded to the metastable one. What should be noticed, that symmetrically substituted HBC-derivatives, although representing the  $D_{6h}$  symmetry group, behave similarly to HnT molecules, and lose the property of the hexagonal symmetry present in the bulk, considering the arrangement of the columnar stacks. This fact is strongly dependent on the breaking of the mirror symmetry of interactions present in the bulk, and in consequence it is a direct manifestation of the appearance of additional intermolecular interactions, activated by the surface confinement. The already mentioned influence of the solvent on the monolayer arrangement (see the HHTT molecule deposited onto HOPG from either phenyloctane or *n*-tetradecane solutions,<sup>115</sup> Figure 2.15) is another factor that plays a role also in the case of HBC-C<sub>12</sub>/HOPG system. As reported by Piot *et al.*,<sup>123</sup> when the *n*-tetradecane is used as a tunneling liquid, the HBC-C<sub>12</sub> molecules tend to form molecular patterns that do not resemble any of the two types of arrangements found by Ito and co-workers. Another rhombic phase is formed, possessing different crystallographic parameters, namely:  $a = 3.5 \pm 0.05 \text{ nm}$ ,  $b = 3.2 \pm 0.05 \text{ nm}$ , and  $\gamma = 87 \pm 1^\circ$ , and the average area per molecule equal  $5.6 \pm 0.1 \text{ nm}^2$ . Contrary to previous results, STM data clearly demonstrate that the peripheral alkyl chains of HBC-C<sub>12</sub> form an angle of  $\sim 120^\circ$  reflecting the symmetry of the underlying HOPG substrate. In contrast to nonpolar and chemically inert *n*-tetradecane, 1,2,4-trichlorobenzene (TCB) possesses a dipole moment, three (bulky) chlorine atoms, and a planar conjugated core. Therefore, interactions between HBC-C<sub>12</sub> and 1,2,4-trichlorobenzene molecules are expected to take place and influence the packing arrangement. Since no significant evolution in either the location of the molecules or the 2D structure was observed, authors conclude that the HBC-C<sub>12</sub> molecules are irreversibly physisorbed on the HOPG surface and that the surface mobility of individual molecules inside the islands is suppressed.

Stability and dynamics of HBC-C<sub>12</sub> monolayers were further explored by the implementation of the 2D buffer adlayer, constituting of another (inert) chemical species physisorbed onto the bare graphite. Namely, prior the deposition of the molecules of analyte, the surface of HOPG has been exposed to the solution containing the long aliphatic compound *n*-C<sub>50</sub>H<sub>102</sub>. It has been well established, that due to the good registry between the graphite lattice and inter-methyl group spacing, various *n*-alkanes self-assemble readily on HOPG as large domains of parallel lamellae, even at room temperature.<sup>124–126</sup> Similarly to shorter homologues, the *n*-C<sub>50</sub>H<sub>102</sub> form closely packed lamellae, in a way that each row constitutes of molecules oriented perpendicular to the lamellae direction and parallel to the <100> direction of the HOPG lattice. Results of the experiments of self-assembly of hexakis(*n*-dodecyl)-*peri*-hexabenzocoronene on the *n*-pentacontane decorated surface of highly oriented pyrolytic graphite are presented on Figure 2.18.

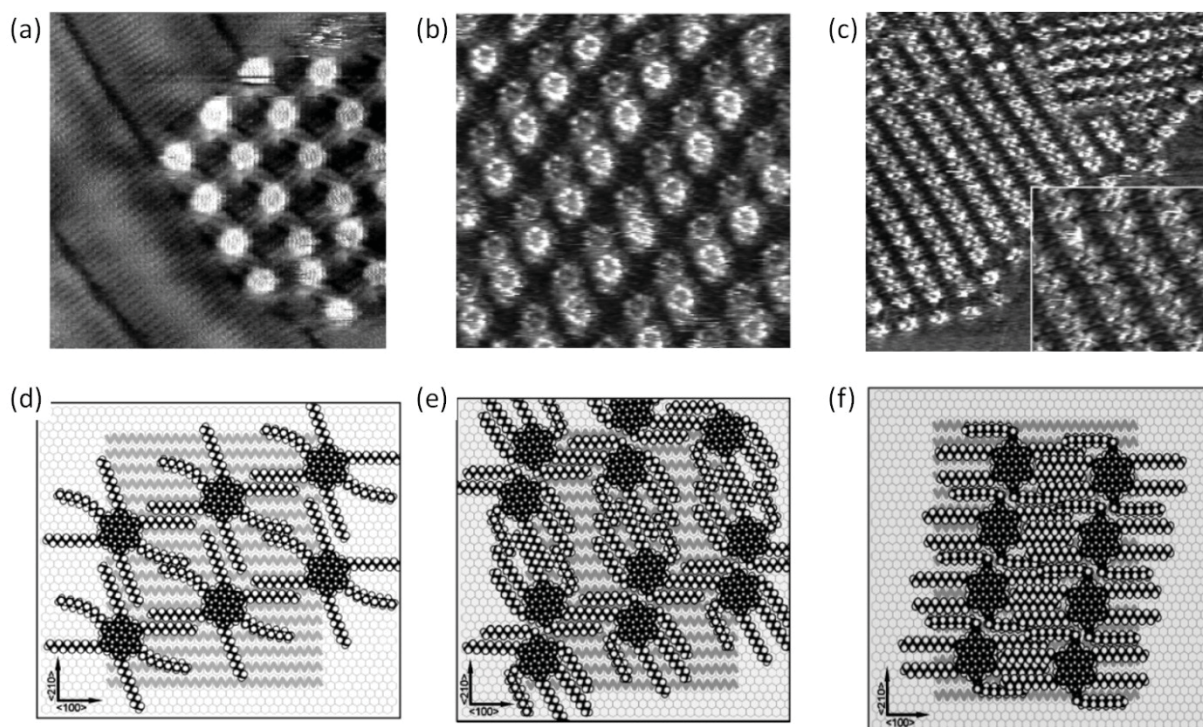


**Figure 2.18** (a) STM image ( $18.7 \times 18.7 \text{ nm}^2$ ) showing an HBC-C<sub>12</sub> island having the  $\alpha$ -phase adsorbed on top of the  $\{n\text{-C}_{50}\text{H}_{102} \text{ monolayer/graphite}\}$  system. (b) STM image ( $23.1 \times 23.1 \text{ nm}^2$ ) of  $\beta$ -phase (dimer structure) on top of the *n*-C<sub>50</sub>H<sub>102</sub> monolayer. Two molecules within the dimer are not equivalent and have different STM contrast. Dodecyl chains of HBC-C<sub>12</sub> occupy the space between the dimers and are aligned along preferential directions. (c) STM image ( $37 \times 37 \text{ nm}^2$ ) of the final  $\gamma$ -phase with a row structure. HBC-C<sub>12</sub> cores form parallel rows on top of the *n*-C<sub>50</sub>H<sub>102</sub> template. Inset shows details of packing ( $12 \times 12 \text{ nm}^2$ ). Images (d), (e) and (f) represent possible packing model of the  $\alpha$ -,  $\beta$ -, and  $\gamma$ -phase, respectively. On (d), (e) and (f) *n*-C<sub>50</sub>H<sub>102</sub> molecules are depicted by gray zigzag lines on top of hexagonal graphite lattice (from Ref. 123).

Upon the deposition of HBC-C<sub>12</sub> molecules, bright spots start to appear on the top of areas of crystallized domains of *n*-pentacontane. The latter, represented on Figure 2.18(a) by the regular lamellae of closely-packed linear features, act as a template for the self-assembly of discotic molecules. HBC-C<sub>12</sub> form regular arrays of almost square packing ( $a = 3.5 \pm 0.05$  nm,  $b = 3.2 \pm 0.05$  nm, and  $\gamma = 84 \pm 1^\circ$ ) and the average area per molecule equal  $5.4 \pm 0.1$  nm<sup>2</sup>, thus slightly diminished in comparison with bare HOPG case. Proposed model of molecular packing is shown on Figure 2.18(d), underlining the orientation of two dodecyl chains along the *n*-C<sub>50</sub>H<sub>102</sub> template, and two other dodecyl chains forming an angle close to 12° with <210>. Contrary to HBC-C<sub>12</sub>/HOPG system, for which nucleation takes place in the middle of the terraces, the nucleation of the oblique structure from Figure 2.18(a) takes place either at the step-edges or at the areas close to the morphological defects of underlying *n*-C<sub>50</sub>H<sub>102</sub> monolayer. In comparison with the stable and time-invariant domains of hexakis(*n*-dodecyl)-*peri*-hexabenzocoronene on bare graphite, the self-assemblies of HBC-C<sub>12</sub> molecules physisorbed on the top of the *n*-C<sub>50</sub>H<sub>102</sub>-modified HOPG reveal more dynamic behavior. Therefore, the oblique structure from Figure 2.18(a) and (d), hereinafter called the  $\alpha$ -phase, gradually undergoes the transformation into a 'dimer structure' depicted by Figure 2.18(b). This phase transition, that is totally accomplished roughly 2÷3 hours after the HBC-C<sub>12</sub> deposition, gives the origin to the  $\beta$ -phase. Interestingly, the aromatic cores within each dimer have different tunneling contrast and although the unit cell parameters changed ( $a = 5.6 \pm 0.05$  nm,  $b = 3.6 \pm 0.05$  nm, and  $\gamma = 68 \pm 1^\circ$ ), the alkyl tails are assumed to orient along roughly the same directions like in the  $\alpha$ -phase (Figure 2.18(e)).<sup>123</sup> Another consequence of changed geometry of the  $\beta$ -phase is the increased density of molecular packing ( $4.7 \pm 0.1$  nm<sup>2</sup>), which ultimately achieves the value as small as  $3.2 \pm 0.1$  nm<sup>2</sup>, after consecutive  $\beta \rightarrow \gamma$  phase transition. The latter transition, completed within 6 hours after the hexabenzocoronene deposition, originates in the 'row structure' of self-assemblies, depicted by Figure 2.18(c). Tightly packed HBC-C<sub>12</sub> molecules in the  $\gamma$ -phase, form molecular rows that create an angle close to 18° with the lamellae direction and all of the dodecyl chains are aligned by the adlayer template. Due to the time evolution of the HBC-C<sub>12</sub>/*n*-C<sub>50</sub>H<sub>102</sub>/HOPG system the global minimum of potential energy is represented by the  $\gamma$ -phase, while  $\alpha$  and  $\beta$  are metastable states. Such strategy of incorporation of a decoupling layer became one of the alternatives for controlling of molecular self-assembly. In the example extensively studied by Piot and co-workers<sup>123</sup> higher mobility of HBC-C<sub>12</sub> on top of *n*-C<sub>50</sub>H<sub>102</sub> than on bare HOPG induced a sequence of phase transitions, additionally influenced by templating effect. None of the registered structures of HBC-C<sub>12</sub> represented a direct translation of either  $D_{6h}$  symmetry group of the molecular building block or hexagonal symmetry of packing present in the bulk.<sup>127,128</sup> Moreover, the system with *n*-C<sub>50</sub>H<sub>102</sub> adlayer was shown to be directed towards the increased density of packing, what was manifested by the decrease in the average area per molecule for spontaneously taking place  $\alpha \rightarrow \beta \rightarrow \gamma$  transitions.

Besides (1) structural incompatibility of the HBC-C<sub>12</sub> monolayer geometry on HOPG with the respective inter-columnar spacing in the bulk,<sup>121,122</sup> and (2) kinetically controlled sequence of transitions of the self-assemblies occurring on *n*-alkane passivated graphite<sup>123</sup> there exist other premises that HBC-homologues may not be the best option for the vertical charge transport. As reported by Piot *et al.*, the hierarchical self-assembly of HBC-C<sub>12</sub> takes place at *n*-tetradecane/HOPG interface, for sufficiently high concentrations of discotic molecule (>10<sup>-6</sup> mol/L). The situation is depicted on Figure 2.19, where linear STM contrast features represent the supra-molecular columns anchored in the edge-on mode on the top of the planar monolayer of HBC-C<sub>12</sub>. Figure 2.19(b) schematically shows the face-on arrangement of the first adsorbed monolayer depicted by blue discs, and the successive layer in the edge-on arrangement depicted by red discs.

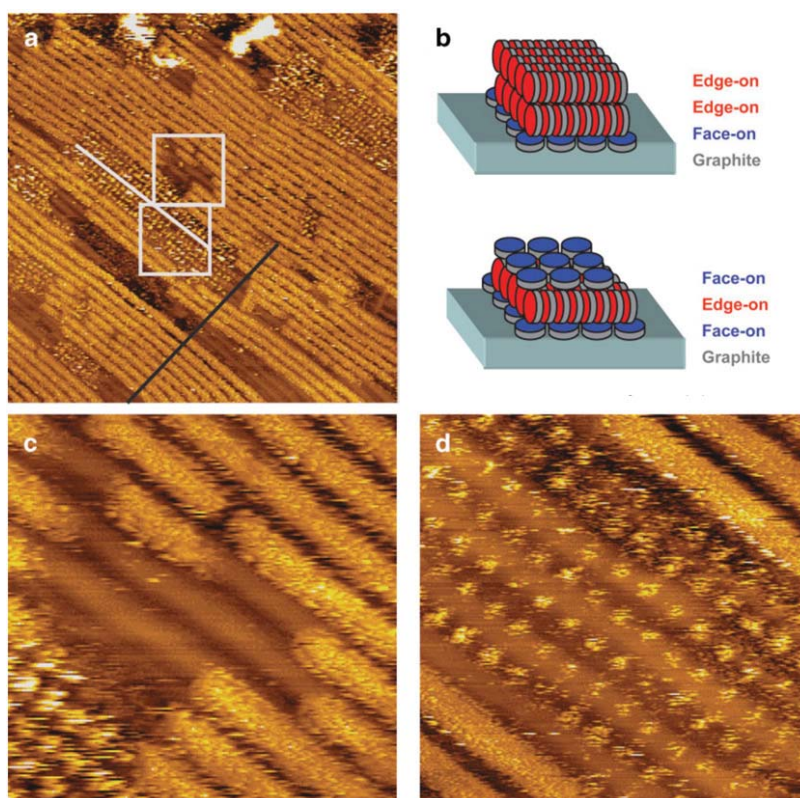


**Figure 2.19** (a) STM image (215 x 215 nm<sup>2</sup>) of a multilayer HBC-C<sub>12</sub> superstructure showing the coexistence of superimposed edge-on and face-on self-organized domains. (b) Schematic representations of the {HOPG/face-on/edge-on/edge-on} (*top*) and {HOPG/face-on/edge-on/face-on} (*bottom*) multilayered self-organized superstructures. (c) and (d) represent high resolution STM images (36 x 36 nm<sup>2</sup>) of the {HOPG/face-on/edge-on/edge-on} superstructure appearing in the upper white square of Figure 2.19(a) and the {HOPG/face-on/edge-on/face-on} stack in the lower white square. Top face-on molecules are embedded in the edge-on overlayer and adsorbed on top of columns of the second layer, which can be distinguished through the upper face-on domain (from Ref. 129).



Moreover, for carefully controlled measurement parameters the visualization of third layer of molecules was attained. The third layer may adopt either edge-on or face-on configurations, characterized by bright linear features or fuzzy spots (Figure 2.19(c) and (d), respectively). Interestingly, the well-organized planar columns, that may achieve lateral size of hundreds of nanometers, were never observed when the non-*n*-alkane solvents such as phenyloctane or dichlorobenzene were used as tunneling liquids. Another reason for lack of horizontal supramolecular columns is too small concentration (i.e.  $< 10^{-6}$  mol/L) of disc-shaped molecules. Authors explain the appearance of hierarchical self-assemblies owing to the relatively poor solubility of HBC-C<sub>12</sub> in *n*-C<sub>14</sub>H<sub>30</sub> that results in aggregation of the discotic molecules through the  $\pi$ -interactions.<sup>129</sup>

This is another indication of the impact that the type of solvent may have on the self-assembly at a liquid/solid interface, here directing the growth of the long edge-on oriented columns of HBC-C<sub>12</sub>. Such nonhomogeneous arrangement of successive layers of molecules is undesirable from the supramolecular point of view since it does not provide the continuity of electronic coupling what may have detrimental impact on charge transport properties.

Exploration of self-assembly properties of HBC-C<sub>12</sub> molecules on Au(111) has been conducted by Marie *et al.*<sup>130</sup> who have demonstrated occurrence of a monolayer ( $\alpha$ -phase) possessing rhombic unit cell of lattice parameters equal:  $a = b = 3.6$  nm, and  $\gamma = 70^\circ$ . STM image of the  $\alpha$ -phase and the associated model of molecular packing are presented on Figure 2.20(a). The low packing density (i.e.  $12.2$  nm<sup>2</sup> per molecule) is in agreement with a noticeable trend of co-adsorption of four molecules of *n*-tetradecane solvent per each unit cell. This open  $\alpha$ -phase was demonstrated to possess kinetically controlled character, since 1 hour after deposition the phase transition into  $\beta$ -phase was evidenced. The appearance of the latter phase, that possesses rhombic unit cell of modified geometry ( $a = b = 3.0$  nm, and  $\gamma = 87^\circ$ , Figure 2.20(b)) and represents more dense packing of HBC-C<sub>12</sub> molecules (i.e.  $9.0$  nm<sup>2</sup> per molecule) is connected with two changes. First of them is completion of the physisorption of peripheral alkyl tails, and second is the decrease of solvent co-adsorption by half. Most striking results are represented by Figures 2.20(c) and (d) which show two consecutive phases:  $\gamma$  and  $\delta$ , which appearance is stimulated by precise change of temperature of substrate. The  $\beta$ -phase stable at room temperature is irreversibly transformed into  $\gamma$ -phase at  $30$  °C, that has oblique unit cell ( $a = 2.9$  nm,  $b = 1.6$  nm, and  $\gamma = 75^\circ$ , Figure 2.20(c)). The phase transition is proceeding with desorption of three out of six peripheral tails per molecule, and the monolayer does not contain any solvent molecules. The ultimate  $\delta$ -phase that starts to appear at around  $35$  °C, results in the densely packed ( $2.81$  nm<sup>2</sup> per molecule) domains of hexagonal symmetry with physisorbed HBC-cores and all alkyl subunits pointing away from the substrate. The whole process being a textbook example of the tuning of 2D self-assemblies by adjusting the temperature of solid substrate is in agreement with minimization of Gibbs free energy. The system, on one hand tends to minimize the enthalpy and

promotes the maximized density at the interface, what is congruent with consecutively increasing packing density. On the other hand, to maximize the entropy, the adsorption of larger and more rigid molecules/units is promoted, since less of the translational and conformational entropy is lost in such way. At the end of the day, the thermodynamically stable  $\delta$ -phase is entirely covering the surface, since the T-induced transitions are irreversible, what was confirmed by further annealing of the substrate. Although hexagonal symmetry of packing of HBC-C<sub>12</sub> in planar anchoring mode was successfully achieved, the lattice parameter ( $a = b = 1.8$  nm,  $\gamma = 60^\circ$ , Figure 2.20(d)) and vertical arrangement of C<sub>12</sub>H<sub>25</sub>-tails does not correspond well to the bulk structure of examined compound.

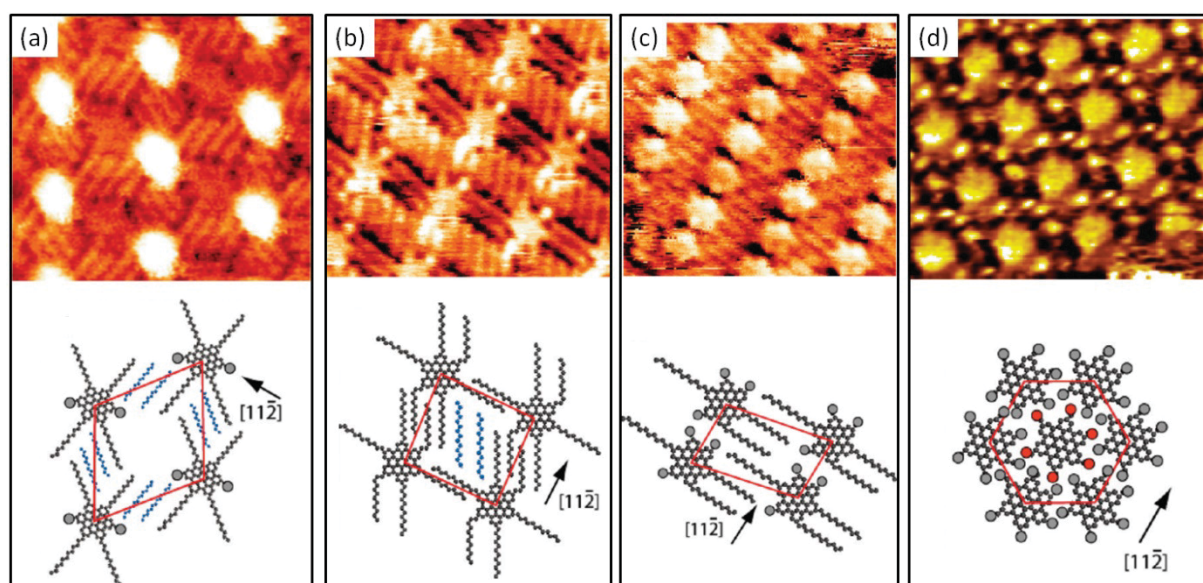


**Figure 2.20** STM images ( $10 \times 9$  nm<sup>2</sup>) and corresponding models of molecular packing of various phases of HBC-C<sub>12</sub> at *n*-tetradecane/Au(111) interface. (a) The kinetically controlled  $\alpha$ -network that undergoes phase transition into  $\beta$ -phase, shown on (b). The gray circles represent out-of-plane *n*-dodecyl chains. Co-adsorbed *n*-tetradecane molecules appear in blue. (c) The following phase transition  $\beta \rightarrow \gamma$  is connected with unidirectional adsorption of peripheral C<sub>12</sub>-tails and lack of the co-adsorption of solvent molecules. (d) The most compacted and thermodynamically stable  $\delta$ -phase, none of the alkyl tails are physisorbed on the substrate, and the solely repetitive units are the central HBC-moieties. The arrows indicate the  $\langle 112 \rangle$  direction of gold (from Ref. 130).

## 2.9 Conclusions

Two-dimensional self-assembly of the most prominent groups of discotic molecules have been summarized in this chapter. Many symmetric discotic molecules possessing mesogenic character and belonging to different point groups have been already extensively studied with varying molecular (core-to-tail) aspect ratio and using various substrates as adsorbing surface. Additional parameters, like passivating (buffer) monolayers or controlling the substrate temperature have been used. In the first instance, to evidence the existence of self-assembly and secondly to gain the knowledge about possible control of first adsorbed monolayer. Literature quoted in this chapter is a small part on the existing entirety of knowledge about flat-shaped molecules that are able to form columnar mesophases. However, set of different results mentioned in this chapter consist of the most adequate examples according to the following experimental chapters of this thesis. Due to limited space, mesogenic derivatives of only few of the (poly)aromatic cores are classified. Moreover, symmetrical substitution is another provision, since unsymmetrical substitution creates enormous number of possibilities, what is out of the scope of this thesis. Finally, since phthalocyanines and porphyrins are not the main object of studies, the rich literature in surface studies of those (metallo)mesogenic compounds is limited to the simples systems. In other words, many of the derivatives are omitted, including the double- and triple-decker systems, which constantly increase the scientific attention.

The composition of the group selected and emphasized in this introductory part, was determined mostly by the potential in the application as active layers in organic electronic devices, which are one of the hot-topics nowadays. In other words, most often materials were already studied according to their charge transport properties, in few examples only some of their photophysical properties are known up till now. Almost all of the listed examples show the complexity in the problem of fabrication and control of the well-ordered face-on arrangement domains, which preserve the geometrical parameters from the bulk discotic mesophase. The origin of two-dimensional crystals formed after deposition of the mesogenic discotic molecules is governed by complex set of forces, which (basing on the knowledge included here) is partially deciphered further in the following part of this thesis: Chapter 3, Chapter 4 and Chapter 5.

## 2.10 References

1. Demus, D. *Mol. Cryst. Liq. Cryst.* **364**, 25–91 (2001).
2. Vorländer, D. *Chemische Kristallographie der Flüssigkeiten*. Akademische Verlagsgesellschaft, Leipzig (1924).
3. Voigt, H. PhD Thesis, Halle (1924).
4. Isihara, A. *J. Chem. Phys.* **19**, 1142-1147 (1951).
5. Alben, R. *Phys. Rev. Lett.* **30**, 778-781 (1973).
6. Landau, L. D. & Lifshitz, L. M. *Statistical Physics*, Oxford: Pergamon (1970).
7. Brooks, J. D. & Taylor, G. H. *Carbon* **3**, 185-193 (1965).
8. Skoulios, A. E. & Luzzati, V. *Acta Cryst.* **14**, 278-286 (1961).
9. Chandrasekhar, S.; Sadashiva, B. K. & Suresh, K. A. *Pranama* **9**, 471-480 (1977).
10. van der Baan, S. PhD Thesis, Groningen (1937).
11. Neifert, I. E. & Bartow, E. *J. Am. Chem. Soc.* **65**, 1770–1772 (1943).
12. Destrade, C.; Mondon, M. C. & Malthete, J. *J. Phys. (Paris)* **40**, C3 17-22 (1979).
13. Billard, J.; Dubois, J. C.; Tinh, N. H. & Zann, A. *Nouv. J. Chim.* **2**, 535–540 (1978).
14. Levelut, A. M. *J. Chim. Phys.* **80**, 149-161 (1983).
15. Levelut, A. M. *J. Physique Lett.* **40**, 81-84 (1979).
16. Chandrasekhar, S. & Ranganath, G. *Rep. Prog. Phys.* **53**, 57-84 (1990).
17. Kumar, S. *Chem. Soc. Rev.* **35**, 83–109 (2006).
18. Tinh, N. H.; Destrade, C. & Gasparoux, H. *Physics Letters* **72A**, 251-254 (1979).
19. Bisoyi, H. K. & Kumar, S. *Chem. Soc. Rev.* **39**, 264–285 (2010).
20. Destrade, C.; Tinh, N. H.; Malthete, J. & Jacques, J. *Phys. Lett. A* **79**, 189-192 (1980).
21. Laschat, S.; Baro, A.; Steinke, N.; Giesselmann, F.; Hagele, C.; Scalia, G.; Judele, R.; Kapatsina, E.; Sauer, S.; Schreivogel, A. & Tosoni, M. *Angew. Chem. Int. Ed.* **46**, 4832–4887 (2007).
22. Bushby, R. J. & Lozman, O. R. *Curr. Opin. Colloid In.* **7**, 343-354 (2002).
23. Simmerer, J.; Glüsen, B.; Paulus, W.; Kettner, A.; Schuhmacher, P.; Adam, D.; Etzbach, K.-H.; Siemensmeyer, K.; Wendorff, J. H.; Ringsdorf, H. & Haarer, D. *Adv. Mater.* **8**, 815–819 (1996).

24. Glösen, B.; Kettner, A. & Wendorff, J. *Mol. Cryst. Liq. Cryst.* **303**, 115–120 (1997).
25. Buess, C. M. & Lawson, D. D. *Chem. Rev.* **60**, 313-330 (1960).
26. Bacher, A.; Bleyl, I.; Erdelen, C. H.; Haarer, D.; Paulus, W. & Schmidt, H.-W. *Adv. Mater.* **9**, 1031–1035 (1997).
27. Christ, T.; Glösen, B.; Greiner, A.; Kettner, A.; Sander, R.; Stumpfen, V.; Tsukruk, V. V. & Wendorff, J. H. *Adv. Mater.* **9**, 48–52 (1997).
28. Heppke, G.; Kruerke, D.; Lohning, C.; Lotzsch, D.; Moro, D.; Müller, M. & Sawade, H. *J. Mater. Chem.* **10**, 2657-2661 (2000).
29. Kats, E. *Mol. Cryst. Liq. Cryst.* **396**, 23–34 (2003).
30. Donovan, K. J.; Kreouzis, T.; Scott, K.; Bunning, J. C.; Bushby, R. J.; Boden, N.; Lozman, O. R. & Movaghar, B. *Mol. Cryst. Liq. Cryst.* **396**, 91–112 (2003).
31. Warman, J. M. & van de Craats, A. M. *Mol. Cryst. Liq. Cryst.* **396**, 41–72 (2003).
32. Roussel, O.; Kestemont, G.; Tant, J.; de Halleux, V.; Gomez Aspe, R.; Levin, J.; Remacle, A.; Lehmann, M. & Geerts, Y. H. *Mol. Cryst. Liq. Cryst.* **396**, 35–39 (2003).
33. Sandhya, K.; Prasad, S. K.; Nair, G. G. & Prasad, V. *Mol. Cryst. Liq. Cryst.* **396**, 113–119 (2003).
34. Schmidt-Mende, L.; Watson, M.; Müllen, K. & Friend, R. H. *Mol. Cryst. Liq. Cryst.* **396**, 73–90 (2003).
35. Marguet, S.; Markovitsi, D.; Millie, P.; Sigal, H. & Kumar, S. *J. Phys. Chem. B* **102**, 4697–4710 (1998).
36. Markovitsi, D.; Marguet, S.; Bondkowski, J. & Kumar, S. *J. Phys. Chem. B* **105**, 1299–1306 (2001).
37. Markovitsi, D.; Marguet, S.; Gallos, L. K.; Sigal, H.; Millie, P.; Argyrakis, P.; Ringsdorf, H. & Kumar S. *Chem. Phys. Lett.* **306**, 163–167 (1999).
38. Kumar, S. *Liq. Cryst.* **32**, 1089–1113 (2005).
39. Kumar, S. *Liq. Cryst.* **31**, 1037–1059 (2004).
40. Bengs, H.; Closs, F.; Frey, T.; Funhoff, D.; Ringsdorf, H. & Siemensmeyer, K. *Liq. Cryst.* **15**, 565-574 (1993).
41. Cammidge, A. N. & Bushby, R. J. *Handbook of Liquid Crystals*, vol. **2B**, Chap. VII, Wiley-VCH (1998).
42. Markovitsi, D.; Rigaut, F.; Mouallem, M. & Malthête, J. *Chem. Phys. Lett.* **135**, 236–242 (1987).
43. Adam, D.; Closs, F.; Frey, T.; Funhoff, D.; Haarer, D.; Schuhmacher, P. & Siemensmeyer, K. *Phys. Rev. Lett.* **70**, 457 (1993).

44. Bushby, R. J.; Boden, N.; Kilner, C. A.; Lozman, O. R.; Lu, Z.; Liu, Q. & Thornton-Pett, M. A. *J. Mater. Chem.* **13**, 470–474 (2003).
45. Boden, N.; Bushby, R. J.; Clements, J.; Movaghar, B.; Donovan, K. J. & Kreouzis, T. *Phys. Rev. B* **52**, 13274-13280 (1995).
46. Funahashi, M. & Hanna, J. *Chem. Phys. Lett.* **397**, 319–323 (2004).
47. Hanna, J. *Opto-electron. Rev.* **13**, 259-267 (2005).
48. van Keulen, J.; Warmerdam, T. W.; Nolte, R. J. M. & Drenth, W. *Recl. Trav. Chim. Pays-Bas* **106**, 534–536 (1987).
49. Boden, N.; Bushby, R. J.; Clements, J.; Jesudason, M. V.; Knowles, P. F. & Williams, G. *Chem. Phys. Lett.* **152**, 94–99 (1988).
50. Adam, D.; Schuhmacher, P.; Simmerer, J.; Haussling, L.; Siemensmeyer, K.; Eitzbach, K. H.; Ringsdorf, H. & Haarer, D. *Nature* **371**, 141–143 (1994).
51. Iino, H.; Takayashiki, Y.; Hanna, J.; Bushby, R. J. & Haarer, D. *Appl. Phys. Lett.* **87**, 192105 (2005).
52. Fontes, E.; Heiney, P. A. & de Jeu, W. H. *Phys. Rev. Lett.* **61**, 1202-1205 (1988).
53. Iino, H.; Hanna, J.-i. & Haarer, D. *Phys. Rev. B* **72**, 193203 (2005).
54. Bushby, R. J. & Lozman, O. R. *Curr. Opin. Solid State Mater. Sci.* **6**, 569–578 (2002).
55. Pisula, W.; Feng, X. & Müllen, K. *Adv. Mater.* **22**, 3634–3649 (2010).
56. van de Craats, A. M.; Warman, J. M.; Müllen, K.; Geerts, Y. & Brand, J. D. *Adv. Mater.* **10**, 36–38 (1998).
57. Benning, S.; Kitzerow, H.-S.; Bock, H. & Achard, M.-F. *Liq. Cryst.* **27**, 901-906 (2000).
58. An, Z.; Yu, J.; Jones, S. C.; Barlow, S.; Yoo, S.; Domercq, B.; Prins, P.; Siebbeles, L. D. A.; Kippelen, B. & Marder, S. R. *Adv. Mater.* **17**, 2580–2583 (2005).
59. Li, L.; Kang, S. W.; Harden, J.; Sun, Q.; Zhou, X.; Dai, L.; Jakli, A.; Kumar, S. & Li, Q. *Liq. Cryst.* **35**, 233–239 (2008).
60. Eichhorn, H. *J. Porphyr. Phthalocyanines* **4**, 88–102 (2000).
61. van de Craats, A. M.; Warman, J. M.; Fechtenkötter, A.; Brand, J. D.; Harbison, M. A. & Müllen, K. *Adv. Mater.* **11**, 1469–1472 (1999).
62. Bayer, A.; Zimmermann, S. & Wendorff, J. H. *Mol. Cryst. Liq. Cryst.* **396**, 1–22 (2003).
63. Seguy, I.; Jolinat, P.; Destruel, P.; Farenc, J.; Mamy, R.; Bock, H.; Ip, J. & Nguyen, T. P. *J. Appl. Phys.* **89**, 5442–5448 (2001).
64. Shimizu, Y.; Oikawa, K.; Nakayama, K.-i. & Guillon, D. *J. Mater. Chem.* **17**, 4223–4229 (2007).

65. Schmidt-Mende, L.; Fechtenkötter, A.; Müllen, K.; Friend, R. H. & MacKenzie, J. D. *Physica E* **14**, 263–267 (2002).
66. Schmidt-Mende, L.; Fechtenkötter, A.; Müllen, K.; Moons, E.; Friend, R. H. & MacKenzie, J. D. *Science* **293**, 1119–1122 (2001).
67. Oukachmih, M.; Destruel, P.; Seguy, I.; Ablart, G.; Jolinat, P.; Archambeau, S.; Mabilia, M.; Fouet, S. & Bock, H. *Sol. Energ. Mat. Sol. Cells* **85**, 535–543 (2005).
68. Kastler, M.; Pisula, W.; Laquai, F.; Kumar, A.; Davies, J. R.; Balushev, S.; Garcia-Gutierrez, M.-C.; Wasserfallen, D.; Butt, H.-J.; Riekel, C.; Wegner, G. & Müllen, K. *Adv. Mater.* **18**, 2255 (2006).
69. van de Craats, A. M.; Stutzmann, N.; Bunk, O.; Nielsen, M. M.; Watson, M.; Müllen, K.; Chanzy, H. D.; Sirringhaus, H. & Friend, R. H. *Adv. Mater.* **15**, 495-499 (2003).
70. Monobe, H.; Awazu, K. & Shimizu, Y. *Adv. Mater.* **18**, 607–610 (2006).
71. Monobe, H.; Hori, H.; Heya, M.; Awazu, K. & Shimizu, Y. *Thin Solid Films* **499**, 259–262 (2006).
72. Grelet, E. & Bock, H. *Europhys. Lett.* **73**, 712-718 (2006).
73. Charlet, E.; Grelet, E.; Brettes, P.; Bock, H.; Saadaoui, H.; Cisse, L.; Destruel, P.; Gherardi, N. & Seguy, I. *Appl. Phys. Lett.* **92**, 024107 (2008).
74. Gearba, R. I.; Anokhin, D. V.; Bondar, A. I.; Bras, W.; Jahr, M.; Lehmann, M. Ivanov, D. A. *Adv. Mater.* **19**, 815–820 (2007).
75. Simpson, C. D.; Wu, J.; Watson, M. D. & Müllen, K. *J. Mater. Chem.* **14**, 494–504 (2004).
76. Piris, J.; Debije, M. G.; Watson, M. D.; Müllen, K. & Warman, J. M. *Adv. Funct. Mater.* **14**, 1047-1052 (2004).
77. Binnig, G.; Rohrer, H.; Gerber, Ch. & Weibel, E. Tunneling through a controllable vacuum gap. *Appl. Phys. Lett.* **40**, 178-180 (1982).
78. Binnig, G.; Rohrer, H.; Gerber, Ch. & Weibel, E. *Phys. Rev. Lett.* **49**, 57-61 (1982).
79. Feynman, R. P. *There's Plenty of Room at the Bottom: An Invitation to Enter a New Field of Physics*. Lecture at an 1959 APS meeting. The Archives, California Institute of Technology, see [www.its.caltech.edu/~feynman/plenty.html](http://www.its.caltech.edu/~feynman/plenty.html) (1959).
80. Binnig, G. & Rohrer, H. *Rev. Mod. Phys.* **59**, 615-625 (1987).
81. Binnig, G. & Rohrer, H. *Rev. Mod. Phys.* **71**, S324-S330 (1999).
82. Binnig, G. & Rohrer, H. *Surf. Sci.* **126**, 236-244 (1983).
83. Smith, D. P. E.; Horber, J. K. H.; Binnig, G. & Nejh, H. *Nature* **344**, 641-644 (1990).
84. Gamow, G. Z. *Physik* **51**, 204-213 (1928).
85. Esaki, L. *Phys. Rev.* **109**, 603-604 (1958).

86. Binnig, G. & Rohrer, H. *Angew. Chem. Int. Ed.* **26**, 606-614 (1987).
87. Tersoff, J. & Hamann, R. D. *Phys. Rev. Lett.* **50**, 1998-2001 (1983).
88. Tersoff, J. & Hamann, R. D. *Phys. Rev. B* **31**, 805-813 (1985).
89. Hippias, K.W. Scanning Tunneling Spectroscopy. In *Handbook of Applied Solid State Spectroscopy*, D. R. Vij, , Ed. Springer Verlag (2006).
90. Harten, U.; Lahee, A. M.; Peter Toennies, J. & Woll, Ch. *Phys. Rev. Lett.*; **54**, 2619-2622 (1985).
91. Barth, J. V.; Brune, H.; Ertl, G. & Behm, R. J. *Phys. Rev. B*, **42**, 9307-9318 (1990).
92. Buchholz, J. C. & Somorjai, G. A. *J. Chem. Phys.* **66**, 573-580 (1977).
93. Archambeau, A.; Seguy, I.; Jolinet, P.; Farenc, J.; Destruel, P.; Nguyen, T. P.; Bock, H. & Grelet, E. *Appl.Surf. Sci.* **253**, 2078-2086 (2006).
94. Orgasińska, B.; Kocotn, a.; Merkel, K.; Wrzalik, R.; Ziolo, J.; Perova, T. & Vij, J. K. *J. Mol. Struct.* **511**, 271–276 (1999).
95. Yang, X.; Nitzsche, S. A.; Hsu, S. L.; Collard, D.; Thakur, R.; Lillya, C. P. & Stidham, H. D. *Macromolecules* **22**, 2611–2617 (1989).
96. Zasadzinski, J. A.; Viswanathan, R.; Schwartz, D. K.; Garnæs, J.; Madsen, L.; Chiruvolu, S.; Woodward, J. T. & Longo, M. L. *Colloids Surf.; A* **93**, 305–333 (1994).
97. Frommer, J. *Angew. Chem. Int. Ed.* **31**, 1298–1328 (1992).
98. Rosenblatt, C. *ChemPhysChem* **15**, 1261–1269 (2014).
99. Barlow, S. M. & Raval, R. *Surf. Sci. Rep.* **50**, 201–341 (2003).
100. Plass, K. E.; Grzesiak, A. L. & Matzger, A. J. *Acc. Chem. Res.* **40**, 287–293 (2007).
101. Cracknell, A. P. *Thin Solid Films* **21**, 107–127 (1974).
102. Rabe, J. P. & Buchholz, S. *Science* **253**, 424-427 (1991).
103. Rabe, J. P. & Buchholz, S. *Phys. Rev. Lett.* **66**, 2096-2099 (1991).
104. Askadskaya, L.; Boeffel, C. & Rabe, J. P. *Ber. Bunsenges. Phys. Chem.* **97**, 517–521 (1993).
105. Rabe, J. P.; Buchholz, S. & Askadskaya, L. *Synth. Metals* **54**, 339-349 (1993).
106. Rabe, J. P.; Buchholz, S. & Askadskaya, L. *ACS Polym. Prepr.* **33**, 798-799 (1992).
107. Charra, F. & Cousty, J. *Phys. Rev. Lett.* **80**, 1682–1685 (1998).
108. Fisher, A. J. & Blöchl, P. E. *Phys. Rev. Lett.* **70**, 3263–3266 (1993).



109. Sautet, P. & Joachim, C. *Chem. Phys. Lett.* **185**, 23-30 (1991).
110. Markovitsi, D.; Germain, A.; Millie, P.; Lecuyer, P.; Gallos, L.; Argyrakis, P.; Bengs, H. & Ringsdorf, H. *J. Phys. Chem.* **99**, 1005-1017 (1995).
111. Wu, P.; Zeng, Q.; Xu, S.; Wang, C.; Yin, S. & Bai, C.-L. *ChemPhysChem* **2**, 750-754 (2001).
112. Gabriel, J. C.; Larsen, N. B.; Larsen, M.; Harrit, N.; Pedersen, J. S.; Schaumburg, K. & Bechgaard, K. *Langmuir* **12**, 1690–1692 (1996).
113. Claypool, C.L.; Faglioni, F.; Goddard III, W. A.; Gray, H. B.; Lewis, N. S. & Marcus, R. A. *J. Phys. Chem. B* **101**, 5978–5995 (1997).
114. Venkataraman, B.; Flynn, G. W.; Wilbur, J. L.; Folkers, J. P. & Whitesides, G. M. *J. Phys. Chem.* **99**, 8684–8689 (1995).
115. Palma, M.; Pace, G.; Roussel, O.; Geerts, Y. H. & Samori, P. *Aust. J. Chem.* **59**, 376–380 (2006).
116. Katsonis, N.; Marchenko, A. & Fichou, D. *J. Am. Chem. Soc.* **125**, 13682–13683 (2003).
117. Perronet, K. & Charra, F. *Surf. Sci.* **551**, 213–218 (2004).
118. Katsonis, N.; Marchenko, A. & Fichou, D. *Synth. Metals* **147**, 73–77 (2004).
119. Katsonis, N. PhD thesis, Universite Pierre et Marie Curie - Paris 6. (2004).
120. van de Craats, A. M. & Warman, J. M. *Adv. Mater.* **13**, 130–133 (2001).
121. Stabel, A.; Herwig, P.; Müllen, K. & Rabe, J. P. *Angew. Chem. Int. Ed.* **34**, 1609–1611 (1995).
122. Ito, S.; Wehmeier, M.; Brand, D.; Kübel, C.; Epsch, R.; Rabe, J. P. and Müllen, K. *Chem. Eur. J.* **6**, 4327–4342 (2000).
123. Piot, L.; Marchenko, A.; Wu, J.; Müllen, K. & Fichou, D. *J. Am. Chem. Soc.* **127**, 16245–16250 (2005).
124. Askadskaya, L. & Rabe, J. P. *Phys. Rev. Lett.* **69**, 1395-1398 (1992).
125. McGonigal, G. C.; Bernhardt, R. H. & Thomson, D. J. *Appl. Phys. Lett.* **57**, 28–30 (1990).
126. Wawkuszewski, A.; Cantow, H. J. & Magonov, S. N. *Langmuir* **9**, 2778–2781 (1993).
127. Herwig, P.; Kayser, C. W.; Müllen, K. & Spiess, H. W. *Adv. Mater.* **8**, 510–513 (1996).
128. Fechtenkötter, A.; Saalwächter, K.; Harbison, M. A.; Müllen, K. & Spiess, H. W. *Angew. Chem. Int. Ed.* **38**, 3039–3042 (1999).
129. Piot, L.; Marie, C.; Feng, X.; Müllen, K. & Fichou, D. *Adv. Mater.* **20**, 3854–3858 (2008).
130. Marie, C.; Silly, F.; Tortech, L.; Müllen, K. & Fichou, D. *ACS Nano* **4**, 1288–1292 (2010).

## Chapter 3

### An unexpected chirality in hexagonally packed monolayers of hexapentyloxytriphenylene on Au(111)

In this chapter, the unusual expression of chirality in a monolayer formed spontaneously by 2,3,6,7,10,11-pentyloxytriphenylene (H5T) on Au(111) is investigated. The morphology of the interface is determined by combining a scanning tunneling microscopy (STM) and theoretical calculations of intermolecular and interfacial interaction potentials. Two commensurate structures are observed, which both belong to the hexagonal space group – analogical to the triangular symmetry of the molecule and the hexagonal symmetry of the substrate surface. Surprisingly in case of both of the structures their chiral character is revealed. It is shown that the corresponding breaking of symmetry arises for two reasons. First of them is the maximization of a molecular density on the substrate, which leads to a rotation of the molecules with respect to the crystallographic axes of the molecular network – to avoid steric repulsion between the neighboring alkoxy chains. Second is due to the interfacial interactions, which lead to commensurable large crystallographic cells associated with the large size of the molecule. In consequence, molecular networks that are disoriented with respect to the high symmetry directions of the substrate are induced. Due to the high simplicity of both intermolecular and molecule-substrate van der Waals interactions that lead to these observations – a generic character for this kind of symmetry breaking is proposed. Furthermore it is demonstrated that, for similar molecular densities, only two kinds of molecular networks are effectively stabilized by the molecule-substrate interactions. While the most stable network favors the interfacial interactions between terminal alkoxy tails and Au(111), the metastable one benefits from the orientation of the triphenylene core with its symmetry axes parallel to Au<110>. This specific orientation of the triphenylene core with respect to Au(111) appears associated with an energy advantage larger by at least 0.26 eV with respect to the disoriented one.

Part of this chapter has been published in: Sleczkowski, P., Katsonis, N., Marchenko, A. and Lacaze, E. *Mol. Cryst. Liq. Cryst.* **558**, 102-108 (2012), Sleczkowski, P., Katsonis, N., Kapitanchuk, O., Marchenko, A., Mathevet, F., Croset, B. and Lacaze, E. *Langmuir* (2014), *accepted*.

### 3.1 Introduction

It is well known that many achiral molecules adsorbed on crystalline substrates can form 2D chiral structures.<sup>1,2</sup> This emergence of 2D chirality corresponds to a symmetry breaking induced by interactions with the substrate underlying the molecular monolayers. However, in the large majority of 2D systems reported to date, the chiral domains remain of limited extension and mirror image domains are formed. Therefore the surface-monolayer system remains racemic at the macroscopic scale. More recently a lot of attention was paid to chiral induction and amplification in 2D systems<sup>3</sup> and number of studies evidenced the possibility to favor specific 2D monolayers chiral plane groups, either by using chiral solvents,<sup>3,4</sup> a sergeant-and-soldiers approach<sup>3,5-7</sup> or chiral auxiliaries.<sup>8-11</sup> As a consequence, a precise understanding of how the interplay between molecule-substrate and molecule-molecule interactions allows the emergence of extended chiral domains in 2D, becomes of importance. Many STM investigations concerning supramolecular chirality at the liquid/solid interface have focused either on the influence of the substrate<sup>1</sup> or on the influence of specific molecule-molecule interactions, for example hydrogen bonding<sup>12-17</sup> or covalent bonding.<sup>18</sup> Antiferromagnetic-like coupling between molecules has also been demonstrated.<sup>19</sup> One system however displayed chirality for simple steric and van der Waals molecule-substrate and molecule-molecule interactions, HtB-HBC on Cu(110).<sup>20,21</sup>

In this chapter, it will be shown that the balance between steric and van der Waals molecule-substrate and intermolecular interactions can promote the formation of 2D chiral domains, thanks to the necessity for the molecular system to increase its density on the substrate. This is shown for 2,3,6,7,10,11-hexapentyloxytriphenylene (H5T), a model (archetypal) molecule - composed by an aromatic core that is symmetrically substituted by six alkoxy chains containing five carbons each. This achiral molecule presents a 3-fold symmetry, analogical to the 6-fold symmetry of the underlying gold surface. Upon self-assembly, a hexagonal network is formed, leading to an STM contrast without any sign of chirality.<sup>22</sup> However, using the observation of metastable domains by STM, together with calculations of steric van der Waals interactions between molecules, we establish the symmetry breaking associated with the presence of two kinds of domains, a stable and a metastable one. By analyzing the molecular orientations within the two domains, it will be demonstrated that the Au(111)/triphenylene core interaction is more favorable for a specific orientation of the core, close to be parallel to the Au<110> direction and it will be evidenced that it is responsible for the appearance of the metastable domain. Estimation of the corresponding energetic advantages will be then used further to reveal the induced chirality of the two domains. The observation of density-driven symmetry breaking with simple symmetric molecules suggests that a large number of physisorbed molecules are likely to present a similar behavior.

### 3.2 STM of H5T at the *n*-tetradecane/Au(111) interface

A molecule of interest: 2,3,6,7,10,11-hexapentyloxytriphenylene (H5T) is a discotic liquid crystal, that exhibits a hexagonal columnar mesophase between 69°C and 122°C.<sup>23</sup> It has been synthesized and characterized within the Laboratoire de Chimie des Polymères, Université Pierre et Marie Curie (Paris, France). Additional purification by the column chromatography has been performed, and material from several batches has been used for further studies.

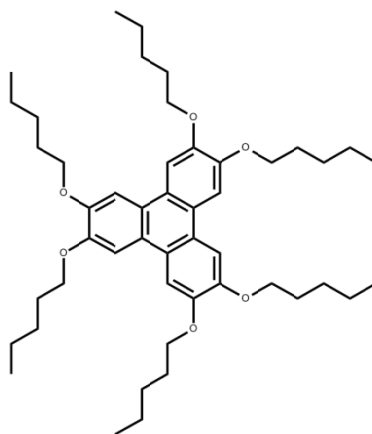


**Figure 3.1** Chemical structure of investigated 2,3,6,7,10,11-hexapentyloxytriphenylene (H5T), a molecule belonging to the  $D_{3h}$  point-symmetry group and a classical example of discotic liquid crystal.

#### 3.2.1 Hexagonal structure of H5T on Au(111)

Upon deposition of H5T/*n*-tetradecane solution onto heated Au(111) sample (just after the flame-annealing of substrate), the molecules self-organize into well-ordered domains on the large atomically flat gold terraces,<sup>22</sup> as shown on Figure 3.2(a). Such monolayers are stable for several days, within a large voltage range (-0.5; 0.5)V associated with STM measurements. This observation is in agreement with previous reports on the two-dimensional self-assembly of H5T on graphite (HOPG)<sup>19</sup> and on Au(111).<sup>22,24</sup> On Figure 3.2(a), first feature that should be noticed are the bright stripes of gold reconstruction, oriented with a slight anti-clockwise deflection from the vertical, which corresponds to the  $\langle 112 \rangle$  crystallographic axis on the gold surface. The fact that Au(111) reconstruction is not lifted as a result of monolayer formation suggests that the discotic molecules are physisorbed. On the STM image, each bright spot is attributed to a triphenylene aromatic core since it is well-known that conjugated  $\pi$ -electron systems exhibit a large contribution to the STM contrast.<sup>25</sup> Those spots form ordered domains of hexagonal symmetry, which is seen more clearly in higher resolution images (Figure 3.2(b) and (c)). Lack of any periodic variation of STM contrast within observed monolayers suggests that the physisorption has occurred at energetically equal adsorption

sites. Such situation was preserved throughout subsequent scans, for different scan directions, tip-sample polarities and tunneling current parameters and could constitute an indirect evidence of commensurability of the adlayer with respect to the symmetry of substrate.

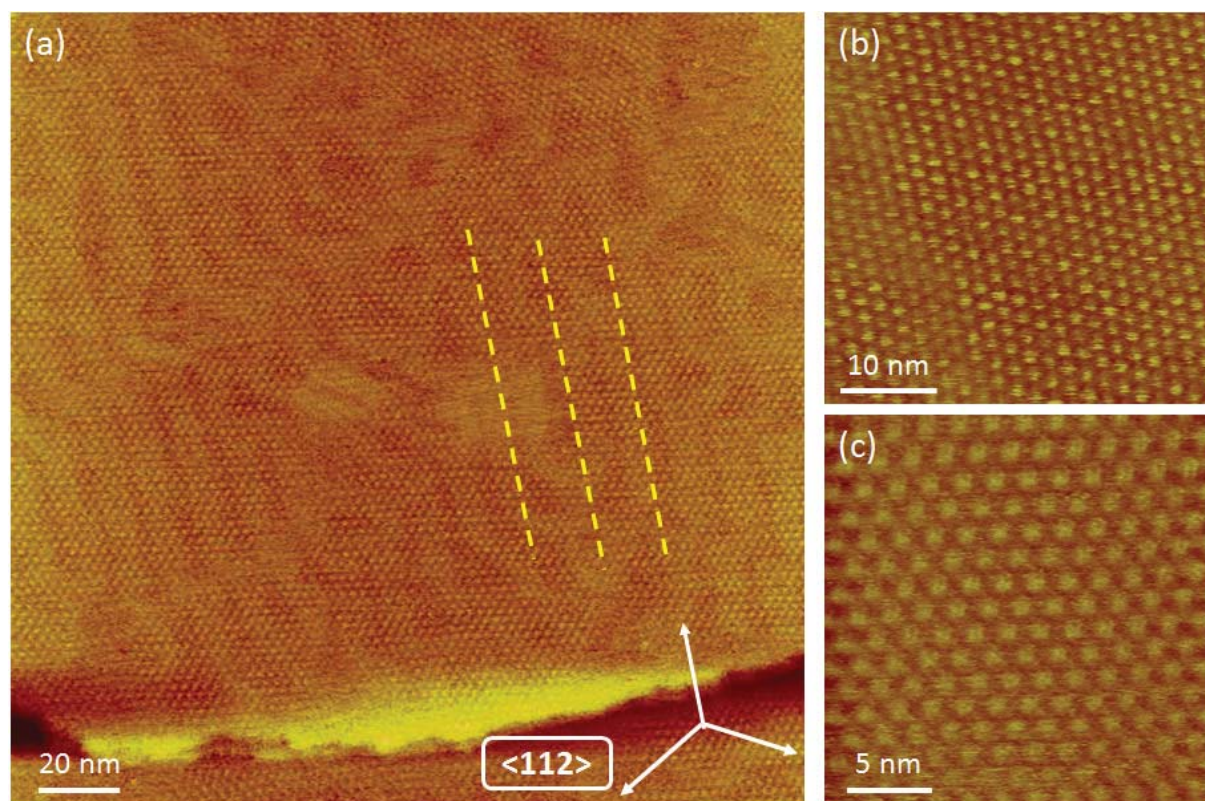


**Figure 3.2** STM images of H5T molecules self-assembled at the *n*-tetradecane/Au(111) interface. Yellow dashed-lines (a) highlight the main direction of Au(111) reconstruction. The brighter spots that are clearly organized into hexagonal mesh, and in accordance with a well-known fact of strong contribution of polyaromatic motifs to the STM contrast, resemble the central triphenylene cores. Even for small scale images, e.g. (c) hexagonal mesh nodes remain diffusive and no clear view on the alkyl tails was obtained. (a)  $I_t = 5$  pA,  $V_t = 100$  mV; (b)  $I_t = 5$  pA,  $V_t = 100$  mV; (c)  $I_t = 20$  pA,  $V_t = 280$  mV.

H5T has been involved previously in reports where the influence of the alkyl chain length was systematically investigated. However, no structural details of its self-assemblies on gold have been underlined. This is partially due to the fact that H5T molecules are usually visualized as diffuse spots, with hardly obtainable intra-molecular resolution, which is not the case for e.g. H11T and other long-tail analogues. The reason lies in the fact that interdigitation of side-chains from neighboring molecules occurs for the mesogens with peripheral alkyl-tails longer than five carbon atoms, what results in increased monolayer stability.<sup>12,24</sup>

Using the data which provided the precision necessary for accurate measurements, the center-to-center distance between two spots has been calculated to be  $2.0 \pm 0.1$  nm for several samples. This value, together with the fact of possible commensurability of H5T monolayer has driven us to study this system in details. If one recalls the lattice parameters of Au(111) defined on Figure 3.2(a), it is straightforward to construct two possible ways of simple hexagonal packing along main crystallographic directions that fulfill the condition of periodicity of about 2.0 nm. Both of the structures are schematically presented on Figure 3.3. The two black hexagons correspond to two possible geometric arrangements for which H5T molecular rows follow either the  $\langle 110 \rangle$  or the  $\langle 112 \rangle$  crystallographic direction (left and right structure, respectively).

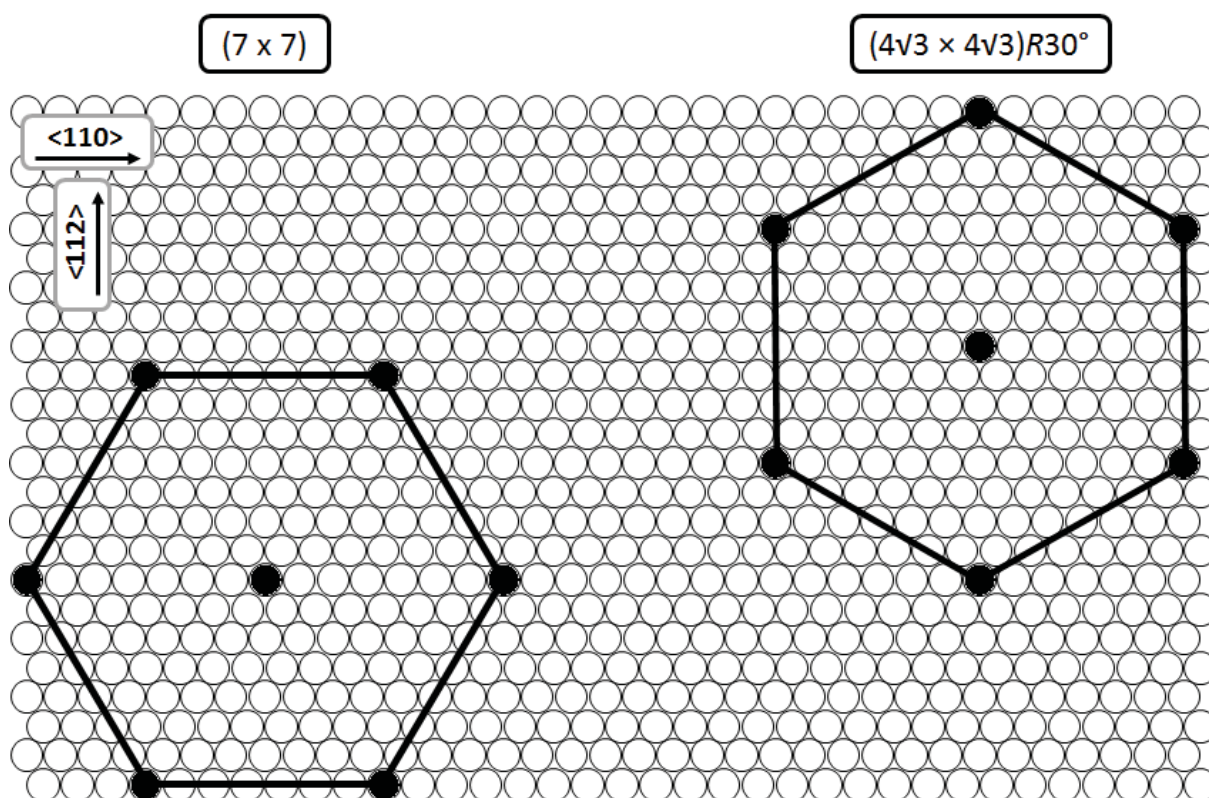


**Figure 3.3** Schematic view of hexagons of two possible packing models of H5T on Au(111) with lattice parameters equal to: 2.016 nm and 1.995 nm for  $(7 \times 7)$  and  $(4\sqrt{3} \times 4\sqrt{3})R30^\circ$  domains, respectively.

Theoretical spacing between the nearest neighbors that was calculated on the basis of distance between gold atoms in Au(111) is equal to 2.016 nm for the  $(7 \times 7)$  case and to 1.995 nm for the  $(4\sqrt{3} \times 4\sqrt{3})R30^\circ$  case. Relative spatial difference between those two values equals to  $\sim 1\%$ , which is not a sufficiently small difference to distinguish between the two structures experimentally. In consequence, it is impossible to exclude the appearance of both types of self-assemblies taking into account the internode distance of the monolayer as the only parameter.

However, when analyzing STM images we have never found molecules aligned along the Au(111) reconstruction lines, which suggests that  $(4\sqrt{3} \times 4\sqrt{3})R30^\circ$  structures are not formed. In contrast, what may be noticed on Figure 3.2(a), and is highlighted on Figure 3.4 is the fact that the molecular rows are aligned along  $\langle 110 \rangle$  crystallographic direction, as they form  $\pm 30^\circ$  angle with the gold  $2\sqrt{3} \times \sqrt{3}$  reconstruction (featured by yellow-dashed line). The value of distance between two nearest neighbors, equal  $2.0 \pm 0.1$  nm, is obtained from the analysis of STM images. The molecular rows being oriented along  $\langle 110 \rangle$ , this value must be compared to the corresponding Au(111) period, equal to 0.288 nm. This leads to the conclusion that the distance between two neighboring H5T molecules is equal to seven times the distance between two gold atoms along the  $\langle 110 \rangle$  crystallographic direction of Au(111). It is worth noticing that the observed period value of 2 nm is very close to the bulk columnar period of the liquid crystal phase<sup>23</sup> and thus the 2D monolayer presents a compactness comparable to the bulk one. This latter characteristics appears in contrast with the H5T 2D monolayers on graphite, which display smaller period than the bulk one.<sup>19</sup>

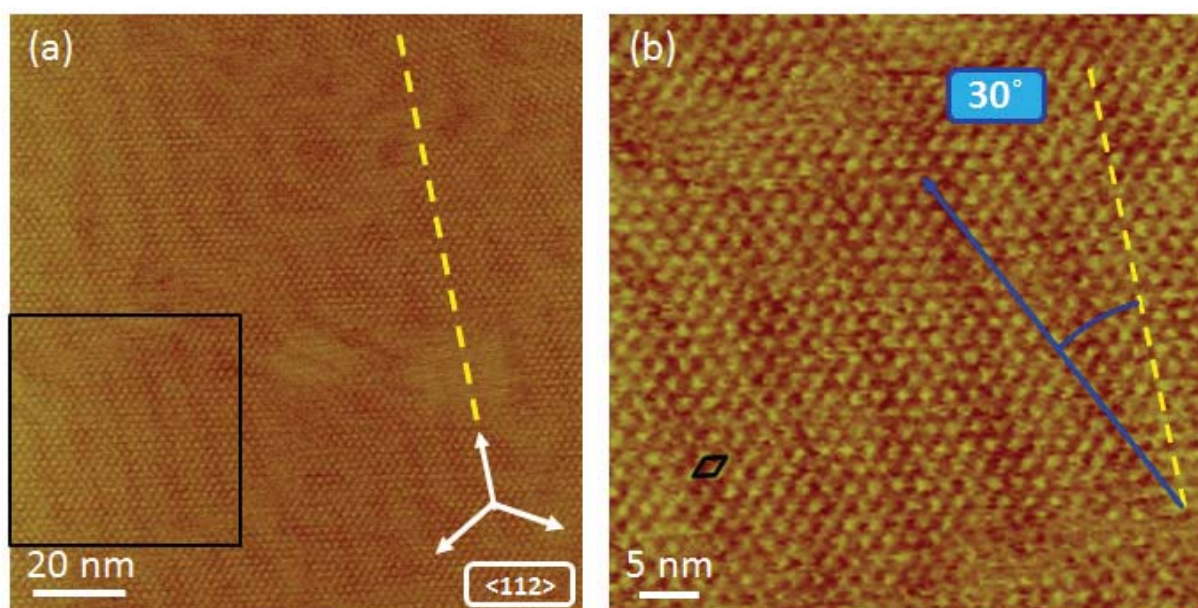


**Figure 3.4** STM image of H5T molecules self-assembled at the *n*-tetradecane/Au(111) interface. Yellow dashed-lines highlight the main direction of Au(111) reconstruction at presented image. Black square at (a) represents zoomed area of (b). Black diamond at (b) represent the primitive unit cell of H5T monolayer physisorbed at Au(111);  $I_t = 5$  pA,  $V_t = 100$  mV.

### 3.2.2 Two-fold orientation of H5T domains on Au(111)

Surprisingly, when deposition of H5T/*n*-tetradecane solution is performed onto a cold substrate, i.e. not directly after its flame-annealing, STM images also reveal that another type of domain usually coexists with (7 × 7) domains on Au(111). The situation is depicted by Figure 3.5, where (7 × 7) domain areas (A), and the ‘cold-deposition’ domain areas (B) are emphasized by blue and red lines, respectively. The black dotted-lines (on Figure 3.5(a) and (b)) highlight the boundaries between A and B domains, and yellow dashed-lines correspond to directions of gold 23xv3 reconstruction that again served as a reference. Also for STM data analyzed here, the good visibility of reconstruction lines (that often crosses both kinds of domains, as on the Figure 3.5(b)) suggests the physisorption of the molecules on the substrate. What may be further noticed is the stability of the monolayer, confirmed by its occurrence just at the visible “screw-dislocation” defect in the top-left corner of the Figure 3.5(c) (small blue-bordered domain).

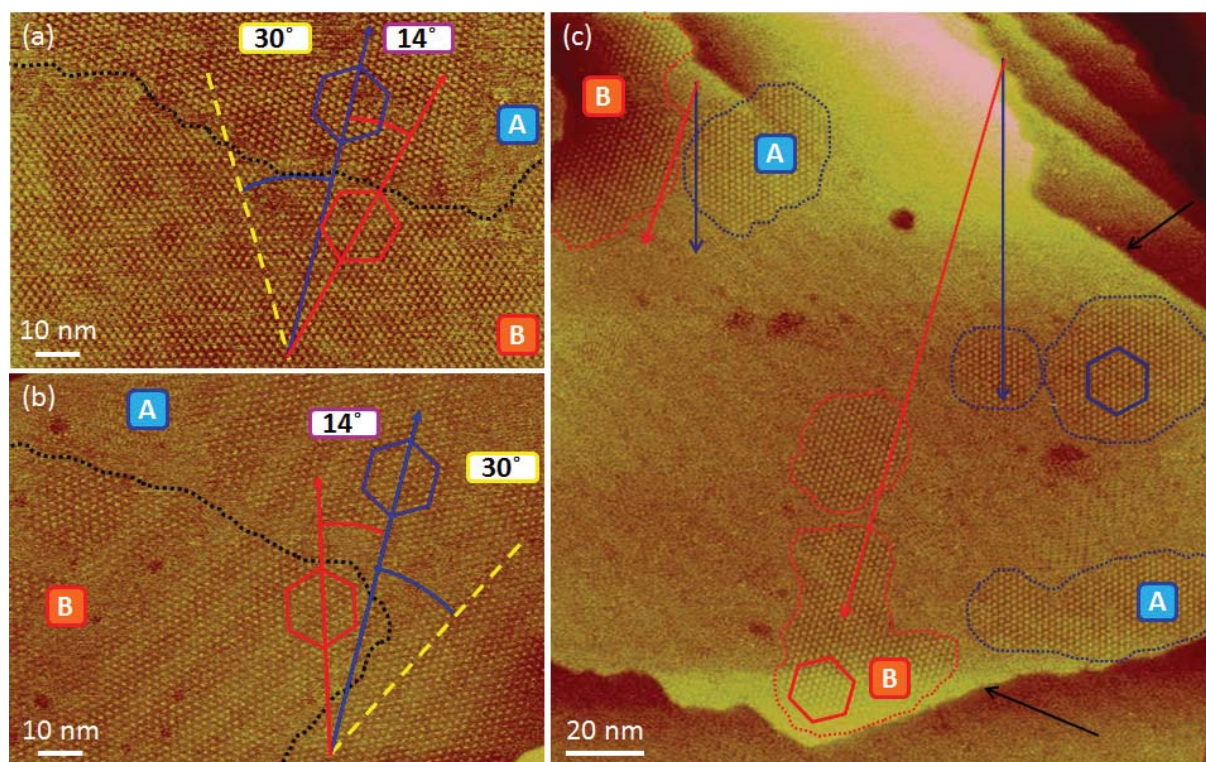


**Figure 3.5** STM images of twofold orientation of H5T molecules self-assembled at the *n*-tetradecane/Au(111) interface. (7 × 7) domains (A) and ( $\sqrt{52} \times \sqrt{52}$ )R13.9° domains (B) are depicted by blue and red graphics, respectively. Yellow dashed-lines at (a) and (b) highlight the main direction of Au(111) reconstruction, black dotted-lines at (a) and (b) highlight the domain boundaries. (a) and (b) STM pictures are taken on the same Au(111) monocrystal and evidence the two possible orientations of (B) domains, rotated by  $\pm 13.9^\circ$  from the (A) ones. Black arrows at (c) show the stepedges of Au(111) substrate;  $I_t = 10$  pA,  $V_t = 100$  mV.



After detailed study of lateral distance between triphenylene cores in A and B areas of monolayers, value of  $2.0 \pm 0.1$  nm has been established as periodicity of lattice nodes in both kinds of domains. Similarly to the ‘hot-deposition’ case, no sign of periodic variation of STM contrast of probed self-assemblies was observed suggesting commensurability of both two-dimensional crystals. Repeatedly appearing  $30^\circ$ -tilt between the reconstruction lines and molecular rows within one of the families of domains (marked with blue color, top of Figure 3.5(a) and (b)) suggests the re-appearance of the  $(7 \times 7)$  structure. Additionally, the drift-corrected image analysis resulted in determination of the angle between respective vectors of A and B unit cells to be equal  $14 \pm 1^\circ$ . Taking into account all geometrical features of A- and B-type domains obtained from STM measurements, it is possible to construct a model that theoretically corresponds to the observed monolayers. Figure 3.6 depicts schematically both meshes of two-dimensional crystals formed on Au(111). The blue color refers to the previously found  $(7 \times 7)$  structure, and the red color represents the second type of domain, found only after ‘cold-deposition’. Its theoretical nearest neighbor distance value equals 2.077 nm, with the unit cell vectors rotated by  $13.9^\circ$  from  $(7 \times 7)$  domain, and it may be denoted as  $(\sqrt{52} \times \sqrt{52})R13.9^\circ$  in Woods terminology. Comparison of Figure 3.5(a) and Figure 3.5(b) obtained on the same sample evidences the two possible orientations of B domains, i.e.  $13.9^\circ$  and  $-13.9^\circ$ .

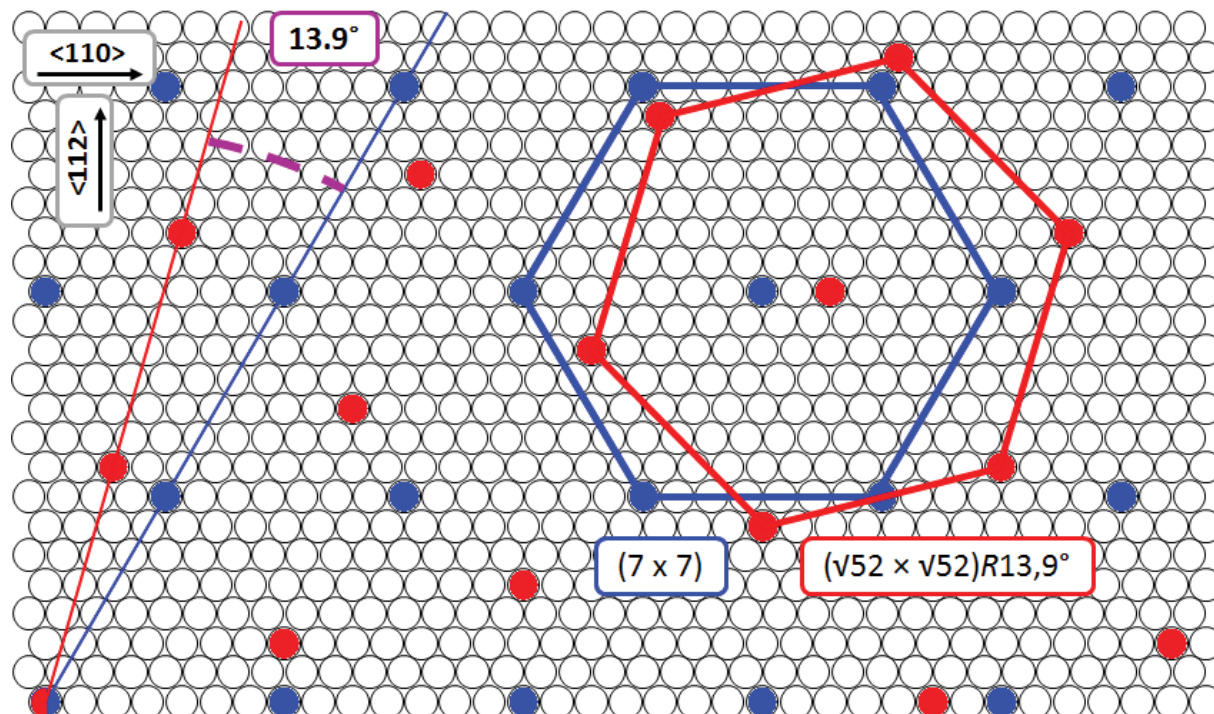


**Figure 3.6** Proposed model of packing of molecular centers of H5T species at a *n*-tetradecane/Au(111) interface for  $(7 \times 7)$  and  $(\sqrt{52} \times \sqrt{52})R13.9^\circ$  domains, indicated by blue- and red-color mesh, respectively. The two models correspond to the experimental data obtained with the assumption of the commensurability of the system.

It should be underlined, that due to the thermal drift and non-instantaneous response of piezoelectric element of the microscope scanner, both 2.016 nm and 2.077 nm mesh parameter values lie within the experimental error for STM measurements performed in the ambient conditions. Nevertheless, the structural features described here have been repeatedly obtained as result of multiple experimental trials and appear not to be connected with any abnormalities of measurements procedure, whatsoever. The appearance of such two-fold orientation of a hexagonally packed self-assemblies has never been reported for triphenylene molecules, neither on Au(111), nor on the basal plane of graphite. Extensive comparative studies of H5T performed at the *n*-tetradecane/HOPG interface have not evidenced multiorientation or any kind of polymorphism of molecular networks formed, what indirectly suggest a special role of the Au(111) substrate in the origin of described phenomenon. This experimentally obtained peculiarity was a subject of further research, this time with the use of computational methods, described in the section 3.3.

### **3.3 Theoretical approach to the H5T/Au(111) system**

Knowledge about particular commensurability of two-dimensional crystals formed by the H5T mesogens does not give clear view on the driving force behind the self-assembly process, since no information can be obtained concerning the mutual orientation of molecules within the monolayer, with respect to the surface. It should be recalled that physisorbed self-assemblies find their origin in the subtle interplay between intermolecular and interfacial interactions.<sup>1</sup> Due to structural dichotomy of H5T one may expect competition between the two components: triphenylene core and pentyloxy tails, since they may possess different relative affinities to the substrate, as it was stated before for H11T.<sup>24</sup> The obstacle in analysis of H5T monolayers on Au(111) results from the fact that molecules are visualized as blurred spots, as soon as the scale that normally should enable intramolecular resolution is attained. In particular alkyl chains are never visible, in connection with their mobility despite the fact that they may also present a well-defined average location on the substrate. However, combining several observations may facilitate to tackle the problem and should give an insight into fundamental knowledge on the surface phenomena of DLC/metal systems, especially those representing the branch of Polycyclic Aromatic Hydrocarbons (PAHs), since in some of heterocyclic macrocycles additional interactions may occur.<sup>26,27</sup>

### 3.3.1 H5T molecule *in vacuo*: structure optimization

We have started our approach by considering a single H5T molecule with no influence coming from the substrate, and also neglecting any intermolecular interactions coming from the neighboring H5T or solvent molecules. The primary goal was to estimate the orientation of alkoxy chains in average with respect to the central triphenylene core, since the situation depicted by Figure 3.1 is highly idealized. In reality, we would not expect the  $-C_5$  tails to point in one of the three directions exactly perpendicular to the edges of a triangular motif of triphenylene moiety. Planarity and symmetry of the molecule are other important issues that should have the impact on the structure of the monolayer, and any singularities should be underlined.

Figure 3.7 represents the optimized geometry of an isolated H5T molecule (i.e. related to gas phase) calculated by Density Functional Theory (DFT/B3Lyp/6-31G\*). As may be noticed H5T retains its tri-fold symmetry and central triphenylene core, as expected for polyconjugated moiety, remains flat. What should be further perceived is that each of the three equivalent sides of triphenylene motif remains in the plane of the central part of the molecule, but is associated with both alkyl tails bent apart by approximately  $15 \pm 1^\circ$ . This minimized energy conformation will serve us as a first approximation of model molecular structure in physisorbed monolayers.

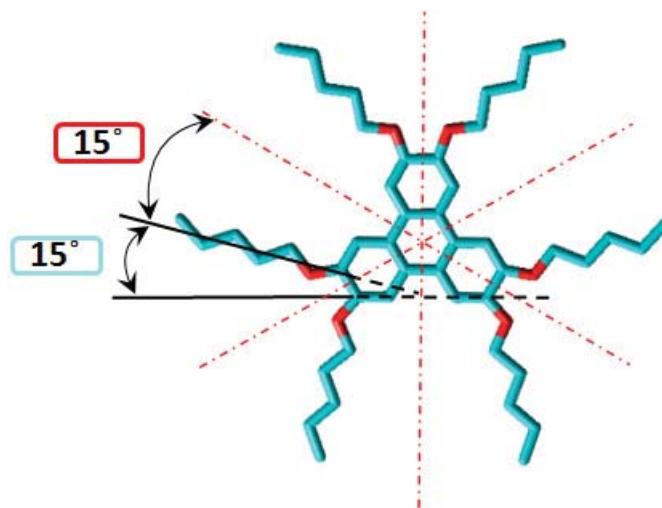


**Figure 3.7** Optimized geometry of H5T molecule calculated by Density Functional Theory (DFT/B3Lyp/6-31G\*). Red dash-dotted lines that represent symmetry axes of molecule underline its affiliation to the  $D_{3h}$  symmetry group. The planar character of the molecule is well noticeable, with an important alkoxy chains deflection by  $15^\circ$  from the respective symmetry axis.

### 3.3.2 Computation of intermolecular interactions (12-6 LJ potential)

In addition to the commensurability of the monolayer taken for granted, for further investigations two main assumptions have been made:

- on one hand, molecules should tend to maximize their packing density (together with alkyl chains lying flat on the surface, as they tend to preserve internal molecular planarity, Figure 3.7) and thus minimize the adsorption energy of the system.
- on the other hand, what need to be taken into account is the steric repulsion between each building block - associated with the peripheral alkyl parts.

Bearing in mind those facts, a more general model of the H5T/Au(111) system will be now built, transcending the two structures evidenced experimentally. Let us start with a black mesh from Figure 3.8(a) that represents the (7 x 7) 2D crystal. Due to the fact that molecules of analyte form a (7 x 7) structure – regardless of the preparation procedure - it may be considered as the thermodynamically stable configuration. Hence, the '0' notation is used, since this structure will serve as a reference one. The first important step would be now obtaining a more detailed energetic profile of the reference monolayer, what may be achieved by placing the DFT-optimized H5T molecules on the nodes of a hexagonal mesh with a reference lattice parameter. Such procedure will draw a picture of the intermolecular interactions, while, for the time being, neglecting the influence of substrate.

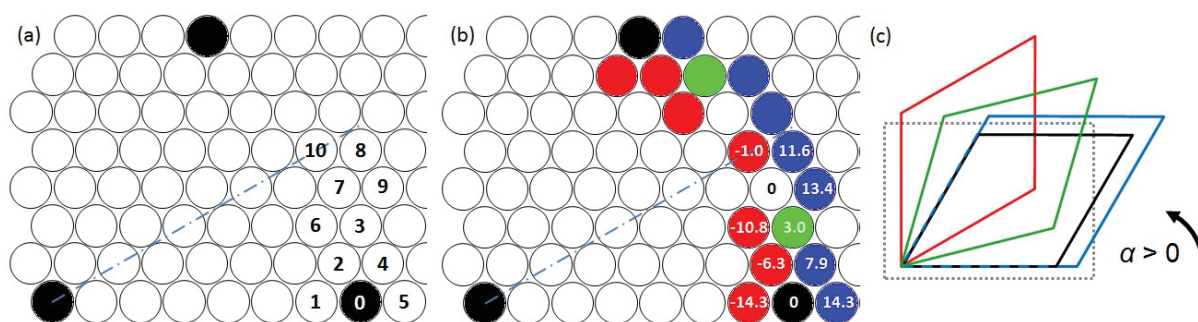


**Figure 3.8** (a) Schematic representation of the reference (7 x 7) structure (black atomic sites,  $M_0$ ). Alternative meshes ( $M_1$ ...  $M_{10}$ ) are created on the basis of a unit vector of absolute value close to the one of the (7 x 7) mesh. Each mesh is hooked at the center of the atom in the left-bottom corner and spans to the respective atomic site (numbered). Numerical values on (b) indicate difference (in %) in distance from the origin (black atom in left-bottom corner), to each atomic site, referred to (7 x 7) mesh. Blue dash-dotted line points the mirror symmetry axis. (c) Illustrative view of hexagonal unit cell size and orientation evolution for series:  $M_0$ ,  $M_3$ ,  $M_5$  and  $M_{10}$ , represented by black, green, blue and red diamonds, respectively. Black arrow points the direction for positive values of the mesh rotation. Dashed-line grey rectangle depicts area shown at (a) and (b).

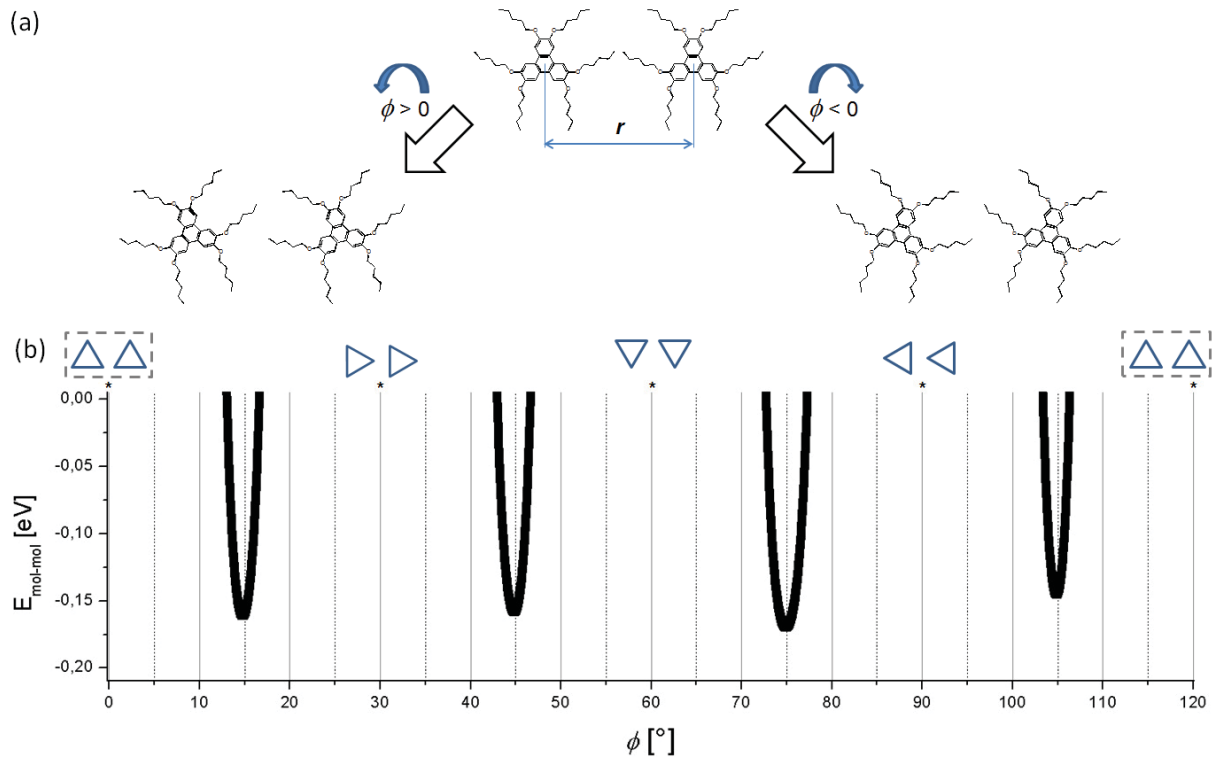


**Figure 3.9** (a) Two parallel oriented H5T molecules and their schematic unidirectional in-plane rotation of angle  $\pm\phi$ .  $r$  stands for the distance between the centers of their masses (varying for different meshes, see: Table 1). (b) Angular dependence of the energy of interaction for the dimers shown at Figure 5a with  $M0$  mesh parameter (i.e.  $r = 2.016$  nm). Since H5T belongs to  $D_{3h}$  symmetry group energetically allowed regions appear periodically and exhibit a mirror symmetry about each  $(2k + 1) \cdot 30^\circ$  value ( $k$  being an integer). Pairs of blue triangles show symbolically the orientation the corresponding aromatic cores (angles marked with asterisks).

We start with the intermolecular interaction,  $E_{\text{mol-mol}}$  and consider a pair of molecules uniformly oriented in one plane [as depicted on the top of Figure 3.9(a)] with a separation distance between centers of their masses,  $r$ , the lattice parameter. Possessing exact atomic coordinates, it is possible, by summing the Lennard-Jones (12-6 LJ) potential between each methylene group of the alkyl chains, to calculate the interaction between two molecules and probe the evolution of this interaction for unidirectional in-plane rotation of a molecular couple [Figure 3.9(a)]. The Lennard-Jones potential between two methyl group is  $E_{\text{L}} = 4 \epsilon [(\sigma/d)^{12} - (\sigma/d)^6]$ ,  $\epsilon = 1.03 \times 10^{-2}$  eV and  $\sigma = 0.398$  nm from Ref. 28. Angular dependence of this interaction is presented on the Figure 3.9(b) for  $(7 \times 7)$  mesh. The energetically allowed range (i.e.  $E < 0$ ), appears as a rather narrow angular regions which strictly defines the molecule orientation in the reference mesh. The interaction value, of the order of 0.15 eV appears smaller than the interaction between Au(111) and a  $\langle 110 \rangle$ -oriented  $C_5$ -carbon chain, equal to -0.53 eV.<sup>29</sup> Taking into account the value,  $\phi^0 = 13.6^\circ$ , corresponding to the energy

minimum, and the alkoxy chain deflection by  $15^\circ$  from the molecule's symmetry axis, we obtain, that three out of six  $-C_5H_{11}$  chains of each H5T molecule would be roughly oriented parallel to the Au<110>, similarly as shown on Figure 3.10(a). It is well-known that <110> is the preferred crystallographic direction for physisorption of alkanes on Au(111).<sup>30-32</sup> Alkyl chains may thus strongly contribute to the adsorption energy of (7 x 7) domains, as schematically indicated by their green color on Figure 3.10(c). This result evidences the unexpected chirality of the (7 x 7) mesh, associated with the rotation around  $\pm 13.6^\circ$  of the molecule with respect to the Au<110> direction. This is in the same time a point and an organizational chirality, the molecules being disoriented with respect to the 2D array as well. This chirality, in other word the  $13.6^\circ$  rotation of the molecule, could not be detected through the STM contrast only due to the "invisibility" of the alkoxy chains. It appears of very different nature with respect to the chirality demonstrated for the same molecules adsorbed on HOPG, this latter one being associated with different adsorption geometry of one molecule out of two.<sup>19</sup>

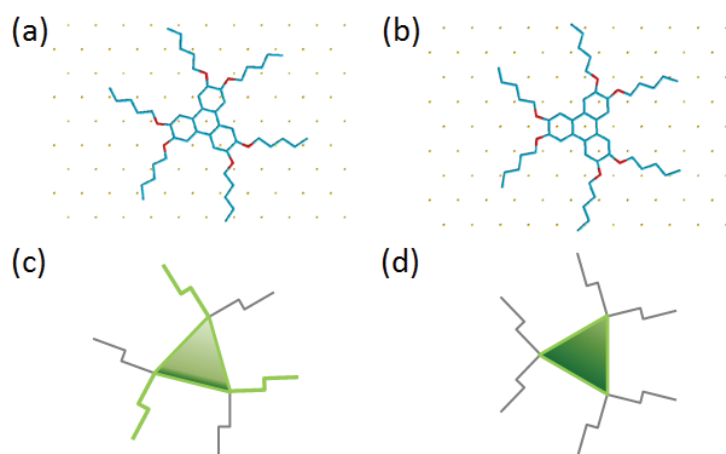


**Figure 3.10** (a) and (b) represent two orientations of minimized energy H5T molecule on Au(111):  $14^\circ$  and  $30^\circ$ -rotated, associated with (7 x 7) and  $(\sqrt{52} \times \sqrt{52})R13.9^\circ$  structures, respectively. Green features on (c) and (d) emphasize the input into adsorption energy for corresponding configurations. What should be noticed is the diversification of interactions in the case of  $14^\circ$ -rotated molecule, where both core and tails greatly contribute, contrary to the concentric character for the  $30^\circ$ -rotated one.

In contrast to the (7 x 7) mesh, the lattice nodes of  $(\sqrt{52} \times \sqrt{52})R13.9^\circ$  mesh follow neither Au<112>, nor Au<110> and assuming closely related intermolecular interactions profile each triangular triphenylene moiety is oriented in a way that its apexes are roughly pointing Au<110> directions, therefore excluding orientation of alkyl subunits parallel to the latter – preferable direction [Figure 3.10(b)]. Since the interfacial interactions between alkyl substituents and substrate

are diminished with respect to (7 x 7) mesh, the dominating term in the adsorption energy of the  $(\sqrt{52} \times \sqrt{52})R13.9^\circ$  structure is thus expected to be the interaction between the core and the substrate [Figure 3.10(d)]. In addition, as in the case of (7 x 7) mesh, chirality of domains arises, however, here as a reason of disorientation of the monolayer's lattice with respect to any of substrate's main crystallographic directions.

Alternative two-dimensional commensurate hexagonally packed meshes with near cell parameters must be considered. Altogether with the reference mesh (7 x 7), signified from now on  $M0$ , we denote these structures  $M1, \dots, M10$ , according to numbered atomic sites shown on Figure 3.8(a). Part of a whole set of hexagonal unit cells is schematically shown on Figure 3.8(c), and the idea was to hook unit vector at the origin (black atom in the left-bottom corner) and span it to the atom with a respective number. Numerical values on Figure 3.8(b) represent the relative percentage difference between inter-site distance for each mesh and the reference  $M0$ . Sites are color-coded, with unit cells smaller than the reference one marked on red, and those bigger than the reference marked on blue. The metastable  $(\sqrt{52} \times \sqrt{52})R13.9^\circ$  structure ( $M3$ ) is represented by green-colored features [position '3' on Figure 3.8(b)].

What should be stressed at this point is that meshes  $M0$  and  $M7$  possess exactly identical lattice parameters, despite both of them being rotated by non-trivial angular value (i.e.  $R21.8^\circ$ ). This obviously takes place as a result of peculiar property of hexagonal geometry of packing. Lack of experimental evidence of monolayer created by  $M7$  unit vector gives us a direct proof of the substrate influence on the self-assembly process, since for minor contribution of interfacial interactions, we would expect both  $M0$  and  $M7$  to be observable in the similar extent. The fact of the nonobservation of  $M7$  mesh combined with the noticeable difference in the interfacial energy distribution for the two model structures that reflect the experimental data ( $M0$  and  $M3$ ), results in the need of essaying the remaining meshes accordingly, in order to judge their hypothetical existence.

All of the characteristics of the constructed set of meshes, including the lattice parameter, are summarized in Table 3.1. Relative surface density specifies the ratio of a surface density for each mesh vs the value of  $^{M0}\delta$ , the thermodynamically stable structure ( $M0$ ). It should be noticed that the metastable  $(\sqrt{52} \times \sqrt{52})R13.9^\circ$  structure ( $M3$ ) appears slightly less dense than  $M0$ .

**Table 3.1** Comparison of 2D model lattices illustrated on Figure 3.8 \*with their geometrical parameters related to the thermodynamically stable (7 x 7) mesh (*M0*). †Final orientations of the central triphenylene cores within *M*[0,1...10] model lattices with respect to Au<110> crystallographic direction of substrate ( $\beta = 0^\circ$  stands for molecular symmetry axes (see Figure 3.7) pointing along Au<112>). For each mesh its corresponding angular value of interaction energy minimum ( $\phi^0$ ) is considered. Sterically forbidden (*M1*, *M6* and *M2*) and low-surface density structures (*M4*, *M8*, *M9* and *M5*) are omitted. Alkyl chains orientations vs Au<110> are also indicated.

Mesh	Lattice parameter <i>r</i> [nm]	Relative surface density*	Mesh rotation angle vs Au<110> $\alpha$ [°]	Intermol. rotation minima $\phi^0$ [°]	Triphenylene orientation† $\beta$ [°]		Alkyl chain orientation vs Au<110> [°]	
<i>M1</i>	1.728	1.361	0.0	-	-		-	
<i>M6</i>	1.799	1.256	16.1	-	-	-	-	-
<i>M2</i>	1.889	1.140	7.6	-	-	-	-	-
<i>M10</i>	1.995	1.021	30.0	13.6	16.4	-16.4	1.4 -28.6	-1.4 28.6
<i>M0</i>	2.016	[-]	0.0	13.6	13.6	-13.6	-1.4 28.6	1.4 -28.6
<i>M7</i>	2.016	1.000	21.8	13.6	24.6	8.2	-6.8 23.2	9.6 -20.4
<i>M3</i>	2.077	0.942	13.9	13.5	27.4	0.4	-14.6 15.4	12.4 -17.6
<i>M4</i>	2.174	0.860	6.6	n/a	n/a	n/a	n/a	n/a
<i>M8</i>	2.249	0.803	26.3	n/a	n/a	n/a	n/a	n/a
<i>M9</i>	2.286	0.778	19.1	n/a	n/a	n/a	n/a	n/a
<i>M5</i>	2.304	0.766	0.0	n/a	n/a	n/a	n/a	n/a



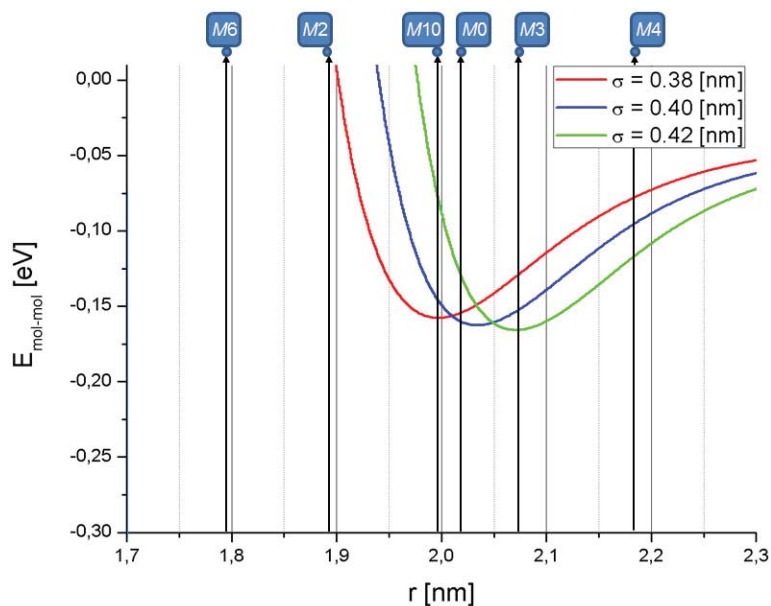


**Figure 3.11** Lennard-Jones intermolecular interactions ( $E_{\text{mol-mol}}$ ) as a function of intermolecular distance,  $r$ , for different values of  $\sigma$  parameter,  $\phi$  being optimized for each  $r$ . Lack of the non-negative part of the plot enables to exclude  $M6$  and  $M2$  meshes from further considerations.

Computations of Lennard-Jones interactions are shown on Figure 3.11, for molecule-molecule distances varying between 1.7 nm and 2.3 nm according to the variation of cell parameter from  $M0$  to  $M10$  (Table 3.1),  $\phi$  has been optimized for each  $r$ . To take into account the imprecise knowledge of the phenomenological parameter  $\sigma$ , we used three different values 0.38, 0.40 and 0.42 nm. Figure 3.11 shows that steric considerations exclude clearly structure  $M1$ ,  $M6$  and that for  $M2$  structure not to be completely excluded we need a  $\sigma$  value smaller than 0.38 nm, which is significantly lower than the standard value 0.398 nm.<sup>28</sup> At this stage, it is possible to eliminate  $M1$ ,  $M6$  and  $M2$  structures for steric reasons and  $M4$ ,  $M8$ ,  $M9$  and  $M5$  structures because their low surface densities lead to a remarkable loss in molecule-surface interactions.

In order to gain more knowledge about the molecular orientations of H5T molecules within the domains considered in the constructed model, some additional calculations of 12-6 LJ potential were performed. Figure 3.12 reveals another important result, regarding the  $\sigma$  parameter.

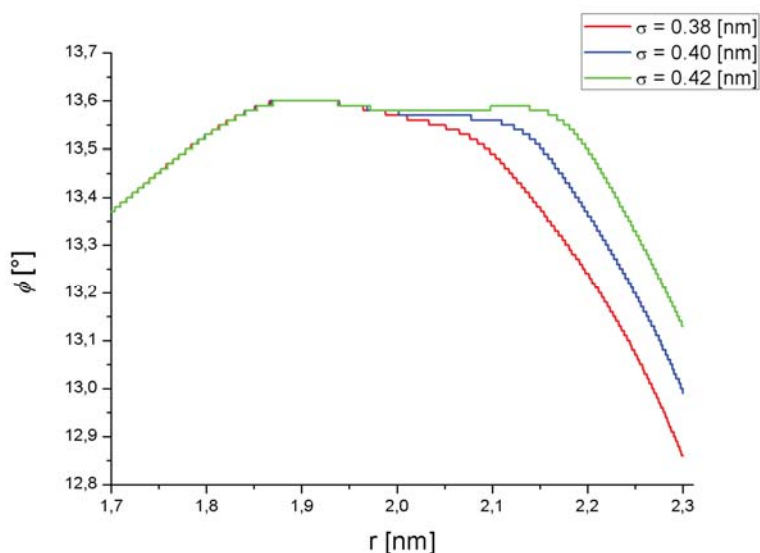


**Figure 3.12** The plot of  $\phi^0$  angle as a function of intermolecular distance, showing robustness with respect to  $\sigma$  variations. The rotation angle of a dimer equal  $13.6^\circ$  is a global maximum for the considered  $\sigma$  values.

Figure 3.12 reveals another important result, the value of the angle  $\phi^0$  around  $14^\circ$  determined by steric consideration is common to all the structures, this result being robust with respect to  $\sigma$  variations. Like *M0* mesh, *M10*, *M3* and *M7* mesh exhibit the molecule disorientation around  $14^\circ$  (exactly  $13.6^\circ$ ) with respect to the mesh crystallographic axis. All of the  $\phi^0$  values for meshes considered in further investigations are also indicated in Table 3.1, together with the triphenylene core orientation with respect to the substrate, denoted  $\beta$ . For conventional reasons:  $\beta = 0^\circ$  stands for H5T molecular symmetry axes (emphasized on Figure 3.7) pointing along Au<112>, and  $\beta = 30^\circ$  is presented on Figure 3.10(b), i.e. when H5T symmetry axes pointing along Au<110>.

### 3.3.3 Validation of intermolecular interactions model by a simplified interfacial potential

It is important now to find the reason for observation of *M0* and *M3* structures together with the non-observation of *M7* and *M10* structures. Table 3.1 shows that the orientations of the molecules with respect to the substrate are close for *M0* - which is observed, and *M10* - which is not observed, on one hand, and for *M3* - which is observed - and *M7* - which is not observed, on the other hand. In the case of *M0* and *M10*, the molecule orientation allows three of the alkyl chains to be parallel (*M10* case) or almost parallel (*M0* case, misfit angle of  $3^\circ$ ) to the Au <110> direction which is known to be an energetically favourable direction. On the contrary, all the six alkyl chains are misoriented for *M3* and *M7* structures.

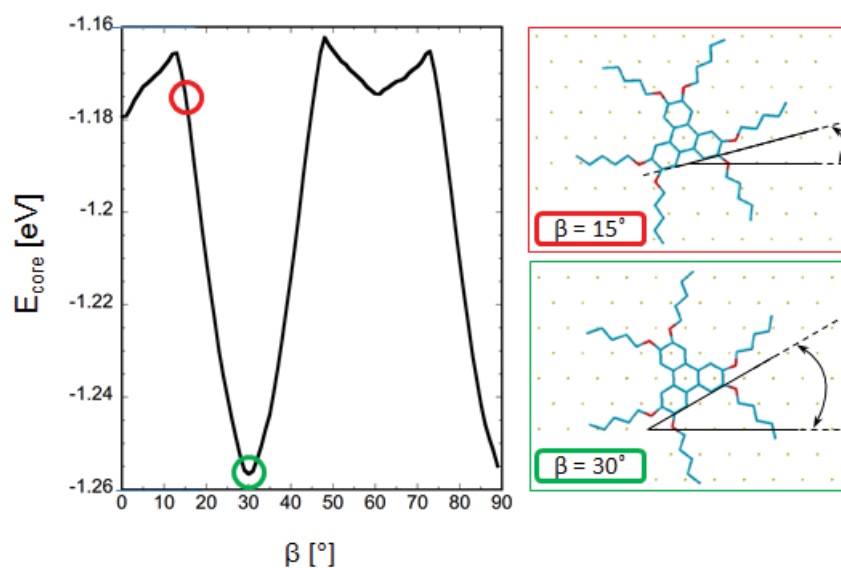


**Figure 3.13** Energy plot of molecule-substrate interactions based on a 12-6 LJ potential, as a function of the molecule rotation angle  $\beta$ . For presented results only the central triphenylene core has been taken into consideration (alkoxy tails excluded). Schemes in red and green boxes indicate the actual orientations of the core with respect to the substrate for the  $+15^\circ$  and  $+30^\circ$  rotations, respectively (the latter one being visibly favorable, since occupying the energetic minimum).

In order to evaluate the interaction energy between the triphenylene core and the substrate,  $E_{\text{core}}$ , a summation of Lennard-Jones term between the carbon atoms of the core and the Au atoms of the surface was performed. The required parameters were taken on the basis of previous studies, and they were equal:  $\sigma_{\text{C-Au}} = 3.0 \text{ \AA}$  and  $\epsilon = 0.013 \text{ eV}$ .<sup>33</sup> The summation being done for all the distances between interacting atoms superior to  $2.5 \sigma_{\text{C-Au}}$ . Respective results are shown on Figure 3.13, where  $E_{\text{core}}$  is presented as a function of the core orientation with respect to the substrate, and the position of the molecule has been optimised for each value of this orientation. A strong minimum is observed for  $\beta = 30^\circ$ . This is consistent with the stabilization of the *M3* structure which is in agreement with STM data, despite the non-favourable orientation of the alkyl chains, and the lower density for *M3* in comparison to *M0* network. One of the initially allowed  $\beta$  value for *M3* of  $0.4^\circ$  may be finally not observed, as inferred from Figure 3.13 (Table 3.1). The other  $\beta$  value is not exactly  $30^\circ$ , but  $27.4^\circ$ . However, the width of the potential well in Figure 3.9(b) (i.e.  $4^\circ$ ) authorizes the disorientation between  $27.4^\circ$  and  $30^\circ$  for the *M3* mesh. The value  $\beta = 24.6^\circ$  associated with *M7* may appear in contrast too far from the minimum of Figure 3.13 to allow for the stabilization of *M7* mesh in agreement with experimental non-observations of *M7* by STM. On the other hand, no sensible differences in  $E_{\text{core}}$  are visible on Figure 3.13 for the orientation corresponding to *M0* and *M10*. The origin of the non-observation of *M10* mesh is thus not clear. We may postulate that the core/Au potential may exhibit rapid variation with  $\beta$  not accounted by our model. This suggests that the

flexibility of the molecule should be taken into account to refine the model. Accordingly the numerical values of Figure 3.13 do not quantitatively describe the experimental data. The potential well at 30° is not deep enough to account for the stabilization of *M3* with a density lower by 6% with respect to *M0*. Taking into account the known energy of adsorption for <110>-oriented C<sub>5</sub>-carbon chain, equal to -0.53 eV,<sup>29</sup> together with a <sup>*M0*</sup>E<sub>core</sub> value equal to -1.17 eV (Figure 3.13), we would expect <sup>*M3*</sup>E<sub>core</sub> - <sup>*M0*</sup>E<sub>core</sub> to be larger than 0.26 eV, i.e. 3 times more than the calculated potential well.

A major conclusion arising from the scenario depicted above is thus the dual origin of both H5T domains on Au(111), driven by specific interaction of the substrate with either the polyaromatic core or the alkoxy chains and leading to a 2D chirality of both structures. *M0* is associated with organizational chirality, but *M3* is chiral as well, whatever corresponding to a different type of chirality. It is worth noticing that, generally speaking, for large molecules, if the molecule-substrate interactions are strong enough to impose commensurate structure, we expect emergence of point chirality structures. They correspond to meshes disoriented with respect to the dense crystallographic directions of the substrate, which must exist if the intermolecular distance is significantly large with respect to the substrate period. This is here the case of *M10* and *M3*. However, the molecule-substrate interactions being strong enough to impose commensurability, usually it also leads to selection of specific chiral structure among all possible ones, here *M3* only. For one given selected mesh, it also leads to selection of only a limited number of diastereoisomers among the possible ones, as already shown for HtB-HBC molecules on Cu(110).<sup>20,21</sup> For *M3*, combining point chirality together with the same chirality than *M0*, four diastereoisomers are expected.<sup>20,21</sup> We expect clockwise and anticlockwise orientation of the mesh, which are indeed observed as shown on Figure 3. Moreover, for each of these two meshes orientations, as shown in Table 1, we would expect a molecular disorientation of ±13.6° to fulfill the observed large adsorbed density. However, we finally show that, due to specific triphenylene core-Au(111) interactions, only two diastereoisomers may exist instead of four, corresponding to β = ±27.4°. The *M0* and *M3* chirality, deduced on a basis of twofold orientation of domains consisting of equidistant lattice nodes residing on the surface sites of similar potential, could not be directly evidenced from STM images. A theoretical analysis finally appears instrumental in elucidating the chiral character of the structures.

Two meshes over a number of eleven commensurate structures are finally selected: in the first one, *M3*, the interactions between triphenylene core and substrate are dominating, while the second one, *M0*, benefits from the stabilizing alkyl chains. We discovered the specificity for the triphenylene core/Au substrate interaction, leading to a favorable interaction for the orientation of the triangular motif of triphenylene core with its apexes pointing the Au<110> directions. For triphenylene molecules with C<sub>5</sub>H<sub>11</sub> alkyl chains, this latter geometry appears of similar energy to the one with

three over six chains oriented parallel to the Au<110>. Consequently our results also suggest that for alkoxy chains shorter than pentyloxy, the core may be oriented parallel to the Au<110> for all molecules. For chains longer than C<sub>5</sub>H<sub>11</sub>, we expect in contrast disoriented triphenylene cores. This finally suggests that increasing the alkoxy chains length would also select only one kind of adsorbed mesh, the latter one. Ultimately (for increasing *n* further), we can even expect that the monolayer loses the hexagonal symmetry, which would definitely allow a larger number of alkoxy chains in epitaxy with respect to Au(111). This last event has been well described previously, with the H11T forming row-like structures on Au(111),<sup>24,34</sup> or on graphite for alkoxy chains of length longer than 12 carbons.<sup>35</sup>

### 3.4 Conclusions

In this chapter a detailed description of the self-assembly of H5T, a discotic molecule, on Au(111), is presented. Although H5T and its several homologues have been studied previously on different substrates, here we evidence the emergence of chirality in two structures that coexist in the monolayer. By combining both experimental and theoretical approach we evidence the commensurability of the two structures, respectively (7 x 7) and ( $\sqrt{52} \times \sqrt{52}$ )R13.9°. Our calculations show that the maximization of molecular density on the substrate leads to a rotation of the molecules with respect to the crystallographic axes of the molecular network – to avoid steric repulsion between neighboring alkoxy chains. This rotation plays a major role in the emergence of chirality together with the induced commensurability of the adsorbed molecular structures. For large adsorbed molecules, commensurability implies large structures and therefore potential disorientations of the molecular network with respect to the high symmetry directions of the underlying substrate. Moreover, we evidence that the Au(111) substrate stabilizes only few of the potentially allowed adsorbed structures, as a result of the dual nature of interfacial interactions. ( $\sqrt{52} \times \sqrt{52}$ )R13.9° domains benefit from the triphenylene (aromatic) core interactions with gold while the (7 x 7) structure is stabilized by the three out of six pentyl chains for each molecule. We thus evidence a specifically stabilized orientation for the triphenylene core with its symmetry axes parallel to Au<110>. This orientation represents an energy advantage at least larger than 0.26 eV with respect to disoriented core. Moreover, we demonstrate that H5T constitutes an interesting example where balanced contributions from both aromatic and aliphatic counterparts are present. This appears in contrast with longer peripheral substituents, i.e. H11T, for which alkyl part dominates the organization of the monolayer what is manifested by the hexagonal symmetry breaking.<sup>24,34</sup>

## 3.5 Experimental section

### 3.5.1 Materials

**Analyte.** 2,3,6,7,10,11-hexapentyloxytriphenylene (H5T) has been synthesized and characterized within the Laboratoire de Chimie des Polymères, Université Pierre et Marie Curie (Paris, France). Additional purification by the column chromatography has been performed, and material from several batches has been used for further studies.

**Solvent.** H5T was dissolved in *n*-tetradecane (Sigma Aldrich, pure >99%, used as received) with a concentration of 1.67 mmol/L. Solution was heated up to ~70°C for 15 min prior to deposition onto the substrate.

**Substrate.** The Au(111) substrates were purchased from Neyco (Structure Probe, Inc. supplier for France). The raw samples consisted of mica plates of thickness between 50 and 75 µm, onto which thin (~100 nm) layer of gold has been evaporated. Details about the crystallographic structure of Au(111) will be presented in the another section.

**Probe.** The STM tip was mechanically cut from a Pt/Ir wire (90/10 wt%) that was purchased from Goodfellow SARL. During the measurement the probe was immersed in the droplet of solution.

### 3.5.2 Sample preparation

A crucial step for ensuring the most favorable conditions for the self-assembly of molecules into the physisorption-driven monolayer is preparation of a high quality surface, i.e. composed of atomically flat terraces of large size (100s of nm in 2D). The procedure of preparing of Au(111) consist normally of short (~1 min) flame annealing in a hydrogen or propane gas flame. The latter one has been used for experiments described in this thesis. The gently heated (~70°C) solution of H5T has been deposited onto freshly flamed Au/mica sample, either straight after the flaming process was ceased ('hot deposition'), or 15 minutes afterwards ('cold deposition').

### 3.5.3 Equipment: scanning tunneling microscope

The monolayers were investigated using a commercial STM equipped by low current head (Veeco, Digital Instruments, Inc. USA). For each monolayer, several STM-images recorded in constant current mode with current ranging from 1 to 100 pA and tip bias from ±100 to ±1000 mV were obtained with different samples and tips to check reproducibility and to ensure that results are free from artifacts. All STM images presented here were recorded under ambient conditions without any further image processing.

### 3.6 Acknowledgments

Dr. Fabrice Mathevet is gratefully acknowledged for the supplying the H5T molecule of good purity. Dr. Bernard Croset (INSP-CNRS, Paris) is gratefully acknowledged for the help with construction and improvement of the theoretical model used in this chapter and for many fruitful discussions. Dr. Oleksiy Kapitanchuk (Bogolyubov Institute for Theoretical Physics, Kiev, Ukraine) is acknowledged for the development of interfacial potential profile of the aromatic part of the molecule.

### 3.7 References

1. Katsonis, N.; Lacaze, E. & Feringa B. L. *J. Mater. Chem.* **18**, 2065–2073 (2008).
2. Ernst, K.-H. *Top. Curr. Chem.* **265**, 209–252 (2006).
3. Xu, H.; Ghijsens, E.; George, S. J.; Wolffs, M.; Tomovic, Z.; Schenning, A. P. H. J. & De Feyter, S. *ChemPhysChem* **14**, 1583–1590 (2013).
4. Katsonis, N.; Xu, H.; Haak, R. M.; Kudernac, T.; Tomovic, Z.; George, S.; van der Auweraer, M.; Schenning, A. P. H. J.; Meijer, E. W.; Feringa, B. L. & De Feyter, S. *Angew. Chem., Int. Ed.* **47**, 4997–5001 (2008).
5. Tahara, K.; Yamaga, H.; Ghijsens, E.; Inukai, K.; Adisojojoso, J.; Blunt, M. O.; De Feyter, S. & Tobe, Y. *Nat. Chem.* **3**, 714–719 (2011).
6. Masini, F.; Kalashnyk, N.; Knudsen, M. M.; Cramer, J. R.; Lægsgaard, E.; Besenbacher, F.; Gothelf, K. V. & Linderoth, T. R. *J. Am. Chem. Soc.* **133**, 13910–13913 (2011).
7. Parschau, M.; Romer, S. & Ernst, K.-H. *J. Am. Chem. Soc.* **126**, 15398–15399 (2004).
8. De Feyter, S.; Grim, P. C. M.; Rücker, M.; Vanoppen, P.; Meiners, C.; Sieffert, M.; Valiyaveettil, S. Müllen, K. & De Schryver, F. C. *Angew. Chem., Int. Ed.* **37**, 1223–1226 (1998).
9. De Cat, I.; Guo, Z.; George, S. J.; Meijer, E. W.; Schenning, A. P. H. J. & De Feyter, S. *J. Am. Chem. Soc.* **134**, 3171–3177 (2012).
10. Zhao, J.-S.; Ruan, Y.-B.; Zhou, R. & Jiang, Y.-B. *Chem. Sci.* **2**, 937–944 (2011).
11. Guo, Z.; De Cat, I.; van Averbek, B.; Lin, J.; Wang, G.; Xu, H.; Lazzaroni, R.; Beljonne, D.; Meijer, E. W.; Schenning, A. P. H. J. & De Feyter, S. *J. Am. Chem. Soc.* **133**, 17764–17771 (2011).
12. Samori, P & Rabe, J. P. *J. Phys.: Condens. Matter* **14**, 9955–9973 (2002).
13. De Feyter, S.; Uji-i, H.; Mamdouh, W.; Miura, A.; Zhang, J.; Jonkheijm, P.; Schenning, A. P. H. J.; Meijer, E. W.; Chen, Z.; Wurthner, F. Schuurmans, N.; van Esch, J. & Feringa, B. L. *Int. J. Nanotechnol.* **3**, 462–479 (2006).

14. Frommer, J. *Angew. Chem., Int. Ed.* **31**, 1298–1328 (1992).
15. Weckesser, J.; De Vita, A.; Barth, J. V.; Cai, C. & Kern, K. *Phys. Rev. Lett.* **87**, 096101 (2001).
16. De Feyter, S. & De Schryver, F. C. *Chem. Soc. Rev.* **32**, 139–150 (2003).
17. Hermann, B. A.; Scherer, L. J.; Housecroft, C. E. & Constable, E. C. *Adv. Funct. Mater.* **16**, 221–235 (2006).
18. Humblot, V.; Ortega Lorenzo, M.; Baddeley, C. J.; Haq, S. & Raval, R. *J. Am. Chem. Soc.* **126**, 6460–6469 (2004).
19. Charra, F. & Cousty, J. *Phys. Rev. Lett.* **80**, 1682–1685 (1998).
20. Richardson, N. V. *New J. Phys.* **9**, 395–410 (2007).
21. Schöck, M.; Otero, R.; Stojkovic, S.; Hümmelink, F.; Gourdon, A.; Lægsgaard, E.; Stensgaard, I.; Joachim, C. & Besenbacher, F. *J. Phys. Chem. B* **110**, 12835–12838 (2006).
22. Sleczkowski, P.; Katsonis, N.; Marchenko, A. & Lacaze, E. *Mol. Cryst. Liq. Cryst.* **558**, 102–108 (2012).
23. Billard, J.; Dubois, J. C.; Tinh, N. H. & Zann, A. *Nouv. J. Chim.* **2**, 535–540 (1978).
24. Perronet, K. & Charra, F. *Surf. Sci.* **551**, 213–218 (2004).
25. Fisher, A. J. & Blöchl, P. E. *Phys. Rev. Lett.* **70**, 3263–3266 (1993).
26. Hulsken, B.; van Hameren, R.; Thordarson, P.; Gerritsen, J. W.; Nolte, R. J. M.; Rowan, A. E.; Crossley, M. J.; Elemans, J. A. A. W. & Speller, S. *Jpn. J. Appl. Phys.* **45**, 1953–1955 (2006).
27. Katsonis, N.; Vicario, J.; Kudernac, T.; Visser, J.; Pollard, M. M. & Feringa, B. L. *J. Am. Chem. Soc.* **128**, 15537–15541 (2006).
28. A. I. Kitaigorodskii, *Organic Chemical Crystallography*, Consultants Bureau (1962).
29. Libuda, J. & Scoles, G. *J. Chem. Phys.* **112**, 1522–1531 (2000).
30. Uosaki, K. & Yamada, R. *J. Am. Chem. Soc.* **121**, 4090–4091 (1999).
31. Yamada, R. & Uosaki, K. *J. Phys. Chem. B* **104**, 6021–6027 (2000).
32. Marchenko, O. & Cousty, J. *Phys. Rev. Lett.* **84**, 5363–5366 (2000).
33. Yoon, B.; Luedtke, W. D.; Gao, J. & Landman, U. *J. Phys. Chem. B* **107**, 5882–5891 (2003).
34. Katsonis, N.; Marchenko, A. & Fichou, D. *J. Am. Chem. Soc.* **125**, 13682–13683 (2003).
35. Wu, P.; Zeng, Q.; Xu, S.; Wang, C.; Yin, S. & Bai, C.-L. *ChemPhysChem* **2**, 750–754 (2001).





## Chapter 4

### Stabilizing 2D hexagonal self-assemblies of discotic liquid crystals: a potential role for azobenzenes

Azobenzenes are well known for their reversible *trans-to-cis* photo-isomerization that is associated with geometrical and electronic changes between the two forms. A lot of efforts have been made in order to immobilize various azobenzene molecular switches onto different metallic substrates while preserving their switching behavior. It was particularly challenging to preserve the photo-switching behavior of molecules in planar geometry (i.e. when the plane of diphenyldiazene core is parallel to the substrate), because this conformation is detrimental to photoisomerization. Here, we show that besides their potential photo-switching properties, azobenzenes could be employed to provide additional stability to self-assembled monolayers, specifically, hexagonally self-assembled monolayers of discotic liquid crystals, such as triphenylenes functionalized by long alkyl chains, where an azobenzene can be inserted. A dominant character of intermolecular coupling via the azobenzene-azobenzene bridge is manifested by the orientation of the molecular mesh of studied (**C-12**) molecule with respect to substrate. Furthermore, the described dimerization between azobenzene moieties was shown to occur exclusively on Au(111) and not on HOPG, which we attribute to specific interfacial interactions, mediated by metallic orbitals.

## 4.1 Introduction

Self-assembled monolayers of molecules physisorbed on atomically flat surfaces - either metallic or semiconducting, are relevant to the development of nanotechnologies. Indeed, by combining molecular design and a careful choice of the substrate, high quality organic/inorganic interfaces could constitute the heart of prospective organic electronic devices like: light-emitting diodes, field-effect transistors, photovoltaic cells and sensors that would be more cost-effective in comparison to their inorganic counterparts. The subtle balance between interfacial and intermolecular forces driving to the desired self-assembly becomes even more sophisticated, as soon as one considers the presence of additional spectators, e.g. solvent molecules, or other chemical species. As a reason of complexity of the process, there has been a great stress laid upon finding of the surface-programmable molecular motifs. Extensive and systematic studies of compounds of different backbone and complexity have resulted in formulation of several 'golden rules' of physisorption-type self-assembly. One of the most important among them is the strong tendency for the aliphatic hydrocarbons to physisorb along the  $\langle 100 \rangle$  crystallographic direction of graphite. There are two reasons for such state of things. First lies in the good registry between spatial periodicity of the substrate along this direction (2.46 Å), and the length of the C-C bond between two successive methylene units of the alkyl chain (2.51 Å). Second comes from the attractive lateral interactions, which result either in (a) close-molecular packing of simple alkanes into lamellae, or (b) interdigitation of the alkyl side-chains of neighboring molecules in case of more complex systems. Both cases may be perfectly represented by so-called Groszek model.<sup>1</sup> However, whereas the alkanes are no more favorably oriented along the  $\langle 110 \rangle$  direction of the metallic Au(111), as also shown in the preceding chapter and leading to an absorption energy of 0.53 eV for  $-C_5$  alkyl chain correctly oriented, the situation is somewhat different from the HOPG case due to two kinds of geometrical reasons. First of them is the incompatibility between the unit vector along closed packed Au $\langle 110 \rangle$  direction and  $-CH_2-$  group period, that has a consequence in the non-complete spectrum of  $n$ -alkyl homologues successfully physisorbed on Au(111).<sup>2,3</sup> Second comes from the fact that surface reconstruction resulting from unsaturation of gold surface atoms and equivalent to a compression along one of the three Au $\langle 110 \rangle$  directions, can facilitate physisorption only along two non-parallel closed-packed directions, leaving one of them unfavorable for alkane-lamellae formation.<sup>4</sup> Since gold remains one of the most important substrates in the field of surface science, it would be useful to possess new building block for promoting orientational-specific interactions that drive to the self-assembly. This chapter is devoted to studies of the molecular self-assembly driven by the azobenzene groups present in the peripheral chains

### 4.1.1 Azobenzene molecules on surfaces

Azobenzenes are molecular switches, that undergo a photoinduced isomerization from the thermodynamically stable *trans* form to the *cis* form.<sup>5</sup> As a result of their unique characteristics, they have attracted great scientific attention throughout last decades,<sup>6,7</sup> including numerous trials of their immobilization onto metallic surfaces.<sup>8</sup> Vast amount of studies were devoted to the vertical systems in which the azobenzene molecules form self-assembled monolayers on a basis of chemisorption via the thiol-noble metal bond formation. However, these systems will not be discussed in this chapter. Here, we will focus on the behavior of azobenzene molecules and their derivatives in physisorbed systems, in which at least one of the two phenyl rings adopt the orientation coplanar with the surface underneath and interacts with it directly or is at the proximity of the surface. The possible geometries are schematically presented Figure 4.1.

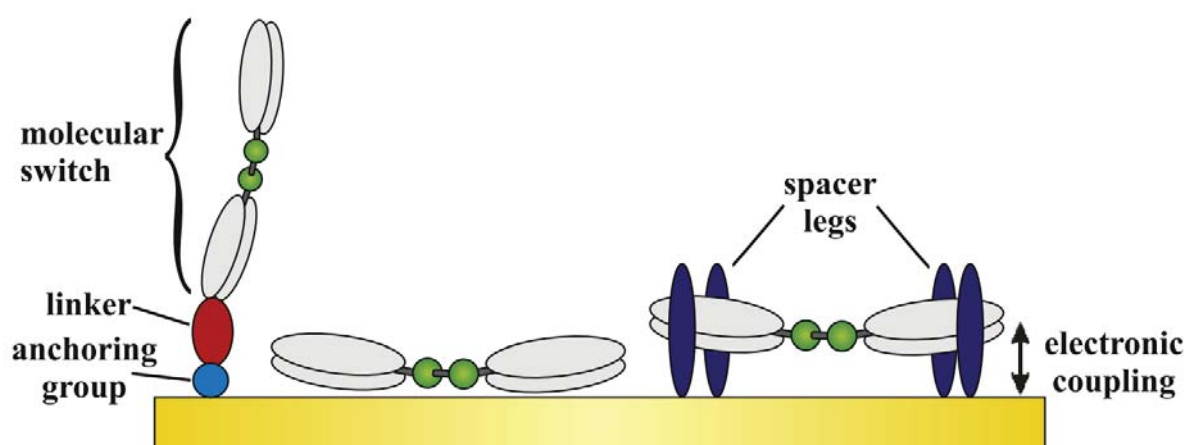


**Figure 4.1** Adsorption of molecular switches via an anchoring group, leading to a vertical orientation and physisorbed systems in which the molecules are in direct contact with the substrate. Spacer groups yield a reduced electronic coupling between the molecules and the substrate (from Ref. 9).

### 4.1.2 Switching of azobenzenes immobilized on surfaces

Studies on discrete molecular systems, covalently bonded or physisorbed monolayers of either protoplast or diversely substituted diphenyldiazenes were usually focused on their possible response to a variety of external stimuli.<sup>9,10</sup> Beside UV-irradiation that initiates *trans* to *cis* conversion and a reverse process that is thermally driven, and can be accelerated by irradiation with visible light, it has been well established that switching may occur also as a result of an electric field.<sup>11,12</sup> Vast amount of studies performed in this area have been conducted with the aid of scanning tunneling microscope. Initially it has been shown, that (1) the probe may be used either to slide the molecules in order to create molecular chains, and that (2) the tip voltage pulses may repeatedly switch the

molecule between two stable orientational configurations.<sup>13</sup> For a long time, reversible *trans-cis* isomerization of a native azobenzene physisorbed on metallic surfaces was not successful. Among various reasons, the strong electronic coupling with the substrate that potentially reduces the lifetime of excited states of the molecule and blocks the photoisomerization has been reported.<sup>14</sup> In addition, for too densely packed monolayers, the motion of the molecule can be sterically constrained by the presence of neighboring molecules and substrate,<sup>15</sup> what may be detrimental for the space-demanding *trans* to *cis* photoisomerization of azobenzene. Several investigations on the actual mechanisms of these processes have been reported,<sup>16-18</sup> and multiple strategies have been employed in order to understand the 'on-surface' behavior of molecules containing azobenzene motives. The most prominent include a very efficient decoupling approach by bulky *tert*-butyl substituents<sup>19</sup> or by a thin insulating layer on the top of metallic substrate.<sup>20</sup> As a consequence of strong geometrical and electronic changes accompanying the isomerization process, majority of experimental investigations have been concentrated on triggering the molecular shape, and some properties of azobenzenes might have not have been used. From the 2D-supramolecular point of view, there have been reported successful trials of designing multi-shaped small oligomers of azo-compounds by tuning the strength and position of C-H...N hydrogen bonds, but obtained systems consisted of rather small and discrete clusters.<sup>21</sup> Bleger *et al.*<sup>22</sup> have reported on successful decoupling of individual azobenzenes in a multi-switch design, so that they operate independently. That was achieved by an introduction of a large dihedral angle between the two subunits of a symmetric bisazobenzene.

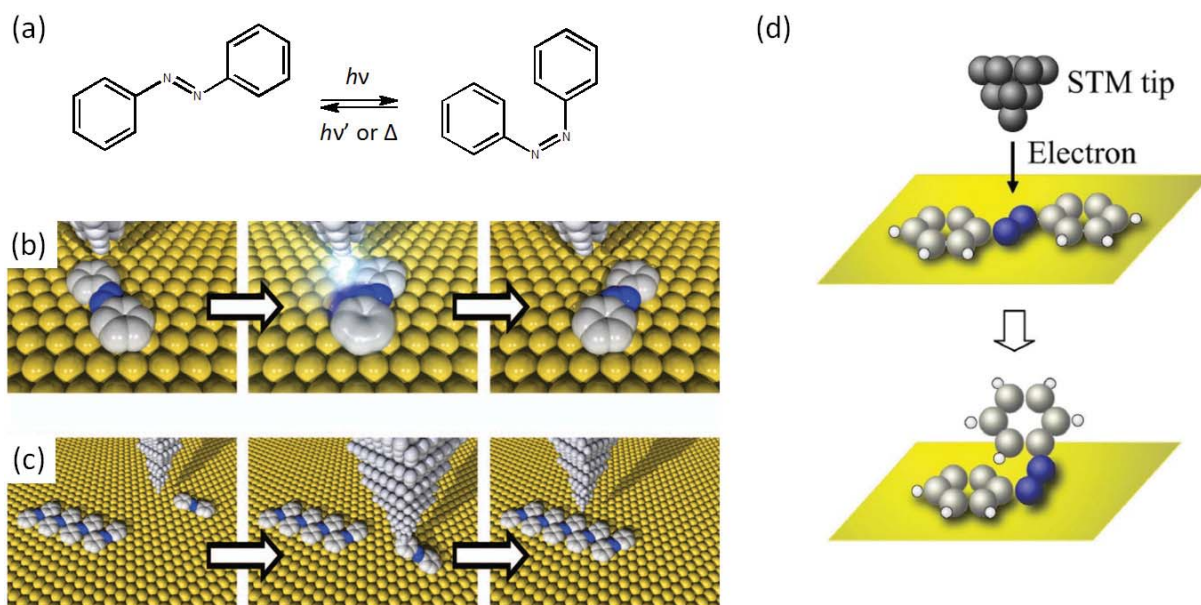


**Figure 4.2** (a) Scheme of a gas-phase and liquid-phase azobenzene photoisomerization reaction. It should be underlined that unlike the *trans*-isomer (*left*), the *cis*-isomer (*right*) is non-planar. The following two sketches illustrate the on-surface-azobenzene manipulation techniques: (b) bistable rotational switching where a single azobenzene molecule is induced by a tip voltage pulse to rotate clockwise by 60°; (c) lateral translation where an isolated azobenzene molecule is bound to the STM tip and slid to join a four-member azobenzene chain (from Ref. 13). (d) A concept of electron-induced isomerization of an azobenzene molecule adsorbed onto a metallic surface with a scanning tunneling microscope (from Ref. 11).

#### 4.2 A hybrid triphenylene-azobenzene mesogenic system: C-12

One of the directions in the liquid crystals research particularly devoted to exploration of the occurrence of liquid crystallinity is the molecular engineering of combined disc-like and rod-like counterparts. Although for most thermotropic liquid-crystalline systems, molecular shape and mesophase structure is closely linked, there are several exceptions, as e.g. some rod-shaped mesogens that self-organize into columnar phases. Such peculiar mesomorphic behavior may be often observed for polycatenars,<sup>23</sup> or dendritic structures in which layered organization is penalized by steric factors.<sup>24</sup> Kouwer and Mehl have reported, that the discotic-calamitic hybrid molecules in form of a pitchfork or a trident are capable to form nematic<sup>25</sup> or even smectic (SmA and SmC) mesophases,<sup>26</sup> respectively. Shimizu *et al.* have demonstrated the first disc-rod alternating system that exhibits kinetically controlled bimesomorphism. A triphenylene derivative which has six 4-dodecyloxyazobenzene units connected with ethylene carbonyloxy groups was synthesized,

portrayed by the stick-and-balls model on Figure 4.3(a). Magenta, red and blue spheres correspond to the carbon, oxygen and nitrogen atoms, respectively. The scheme on Figure 4.3(c) shows that in bulk the mesogen, hereinafter referred to as **C-12**, exhibits a thermodynamically stable columnar (Col) mesophase, and a metastable smectic (Sm) mesophase, by alternating the dominant molecular shape from disc-like to rod-like.<sup>27</sup> Moreover, in addition to the previously reported thermotropic phase transitions, **C-12**-analogue has been recently proven to undergo successive phase transitions under the UV-photoirradiation, with a possibility of the process control by the light intensity.<sup>28</sup>

Incorporation of azobenzenes not only introduces the interesting photophysical properties manifested in bulk, but also causes the inherent change in molecular symmetry to the substituted triphenylene molecules - as the azobenzene groups convey the property of prochirality. This is a significant difference with respect to the H5T molecule studied in the preceding chapter. Figure 4.3(b) shows the molecular arrangement of **C-12** for which all of the carbonyl group oxygens and -N=N- bonds in neighboring azobenzene moieties are oriented counter-clockwise. This creates the chiral  $C_{3v}$  symmetry group. Figure 4.3(d) illustrates, on the contrary, another possible planar conformation of **C-12** molecule, which represents the  $D_{3h}$  symmetry group and directly reflects the triangular symmetry of the inner triphenylene core. This is the high symmetry conformation since it possesses more symmetry elements than the previously mentioned  $C_{3v}$ . In comparison to the  $C_{3v}$  case, the  $D_{3h}$  possess three proper symmetry axes  $C_2$  and three *vertical* reflection planes ( $\sigma_v$ ) that are perpendicular to the plane of the image (not shown). Upon transition from  $D_{3h}$  to  $C_{3v}$  and associated reduction of symmetry the three proper symmetry axes  $C_2$  axes become  $C_1$  axes, and the originally present *vertical* reflection planes ( $\sigma_v$ ) - vanish. This in turn means that while adsorption for the  $D_{3h}$  molecular conformation is an identical event in terms of symmetry, whatsoever is the enantiotopic face of a molecule, the  $C_{3v}$  molecular conformation distinguishes between the two enantiotopic faces and as a result produces two chiral forms – surface enantiomers. The presented two scenarios of the 2D conformation of a single **C-12** molecule open a discussion on the possible self-assembly and surface conformation of an ensemble of **C-12** molecules. The following part of this chapter is aimed to present more deeply the investigated surface behavior of the hybrid mesogen, the chirality character of the self-assemblies and the intermolecular interactions which arise due to the presence of the azobenzene groups as well. These interactions will be shown as decisive for a stable and well-defined molecular 2D assembly.

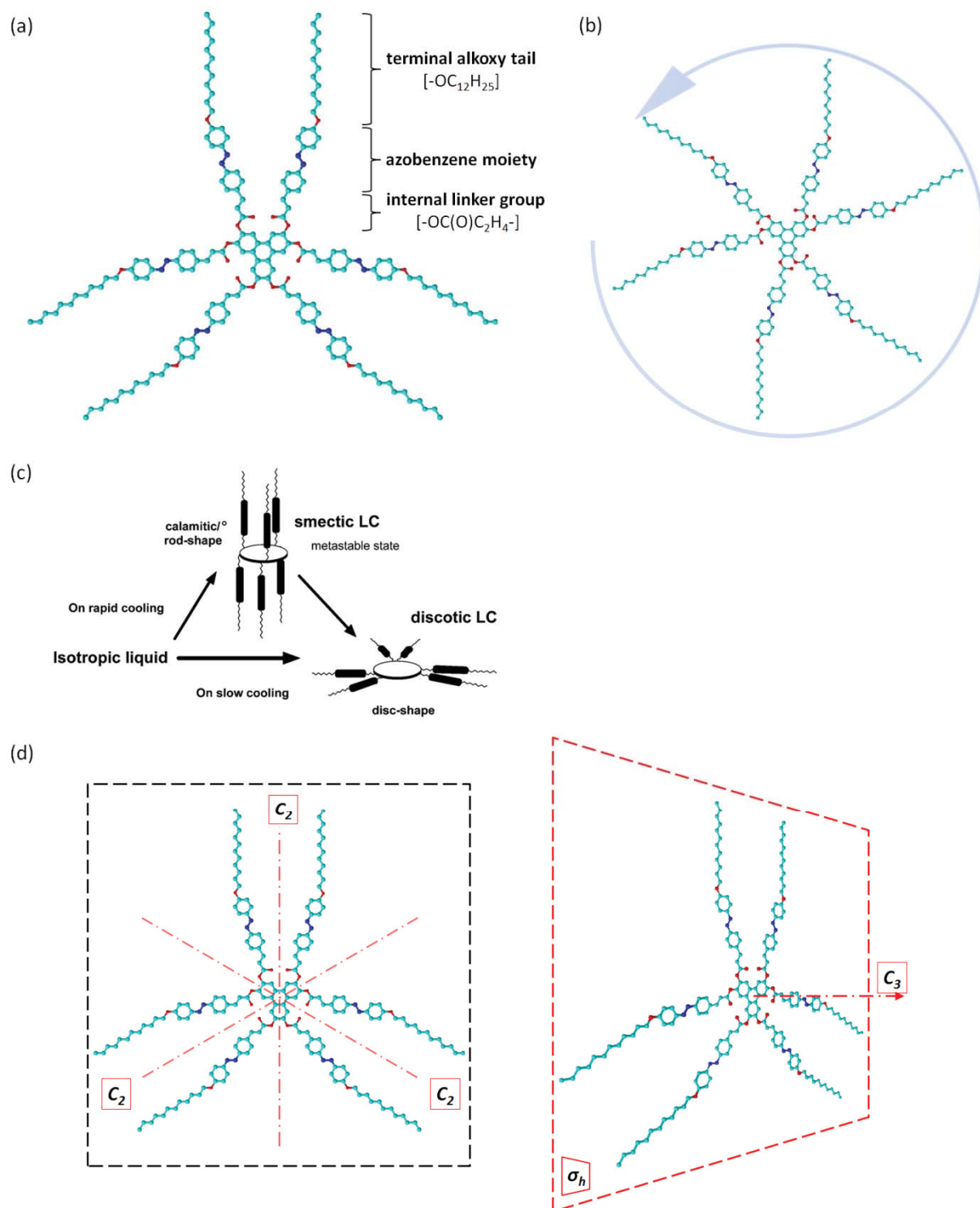


**Figure 4.3** (a) Chemical structure of **C-12** molecule, together with a description of its consecutive radial components. (b) Possible chiral arrangement of **C-12** molecule. (c) Interesting bulk property of Sm-Col bimesomorphism due to a change in molecular shape depending on the cooling rate.<sup>27</sup> (d) Illustration of symmetry elements of **C-12** molecule in one of the possible spatial conformations:  $3C_2$  proper symmetry axes,  $C_3$  principal axis and horizontal symmetry plane ( $\sigma_h$ ).



### 4.3 STM of C-12 at the 1,2,4-trichlorobenzene/Au(111) interface

#### 4.3.1 Hexagonal packing of domains and intermolecular azobenzene-coupling

The goal of the following studies is to investigate the behavior of the disc-rod hybrid system on the surface, in particular at the solid-liquid interface. Due to the problems with dissolution of the **C-12** compound in *n*-tetradecane and phenyloctane solvents, the 1,2,4-trichlorobenzene (TCB) has been used as a tunneling liquid. Drop casting of **C-12**/1,2,4-trichlorobenzene solution onto flame-annealed Au(111) substrate results in formation of hexagonally packed self-assemblies, as may be encountered on Figures 4.4(a) and (b). Those STM images show well-defined domains - represented by the equidistant bright dots that on Figure 4.4(b) are enhanced by red/blue color. In addition, the regularly packed associations are locally separated by imperfect areas that consist of fuzzy regions near the edges of domains. From the analysis of drift-corrected images, we conclude that bright spots are indeed organized into hexagonal mesh with a lattice parameter  $a_{\text{Au}} = 3.5 \pm 0.1$  nm. In accordance with their size and the well-known fact of strong contribution of polyaromatic motifs to the STM contrast,<sup>29</sup> we infer them being the central triphenylene cores lying flat on the substrate. Since no visible periodic variation of STM contrast within the monolayers may be encountered, we deduce that the molecules are physisorbed at energetically equal adsorption sites. Such situation has remained invariable throughout subsequent scans, for different scanning directions, tip-sample polarities and tunneling current parameters.

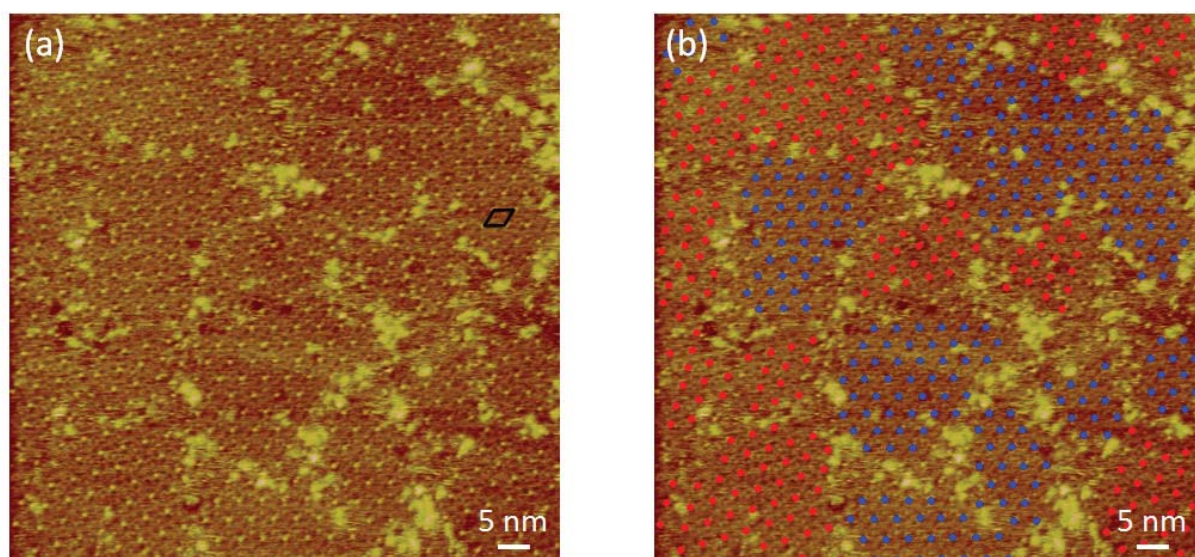


**Figure 4.4** STM constant-current images of **C-12** self-assemblies at the TCB/Au(111) interface. Black diamond at (a) represent the primitive unit cell of **C-12** monolayer physisorbed at Au(111). Blue and red dots on (b) schematically represent two types of domains formed;  $I_t = 9$  pA,  $V_t = 150$  mV.

Figure 4.5 shows the high-resolution STM images of Au-physisorbed **C-12** and thus provides more information, by revealing the intramolecular details of the monolayer. The image on the left (Figure 4.5(a)) depicts the area of specimen with seven homeotropically adsorbed **C-12** molecules that form a regular hexagon with horizontal rows. In addition to the central polyaromatic cores, visible on the large-scale images, and represented by the brighter spots in the apexes of the hexagon and in its center, one may find a peculiar motif present between every two neighboring triphenylene moieties. This motif consists of a four protrusions of the enhanced tunneling contrast that form a rhombic shape. The longer diagonal of this virtual structure is pointing the direction close to the line joining the centers of both molecules (*cf.* Figure 4.5(c) cyan line).

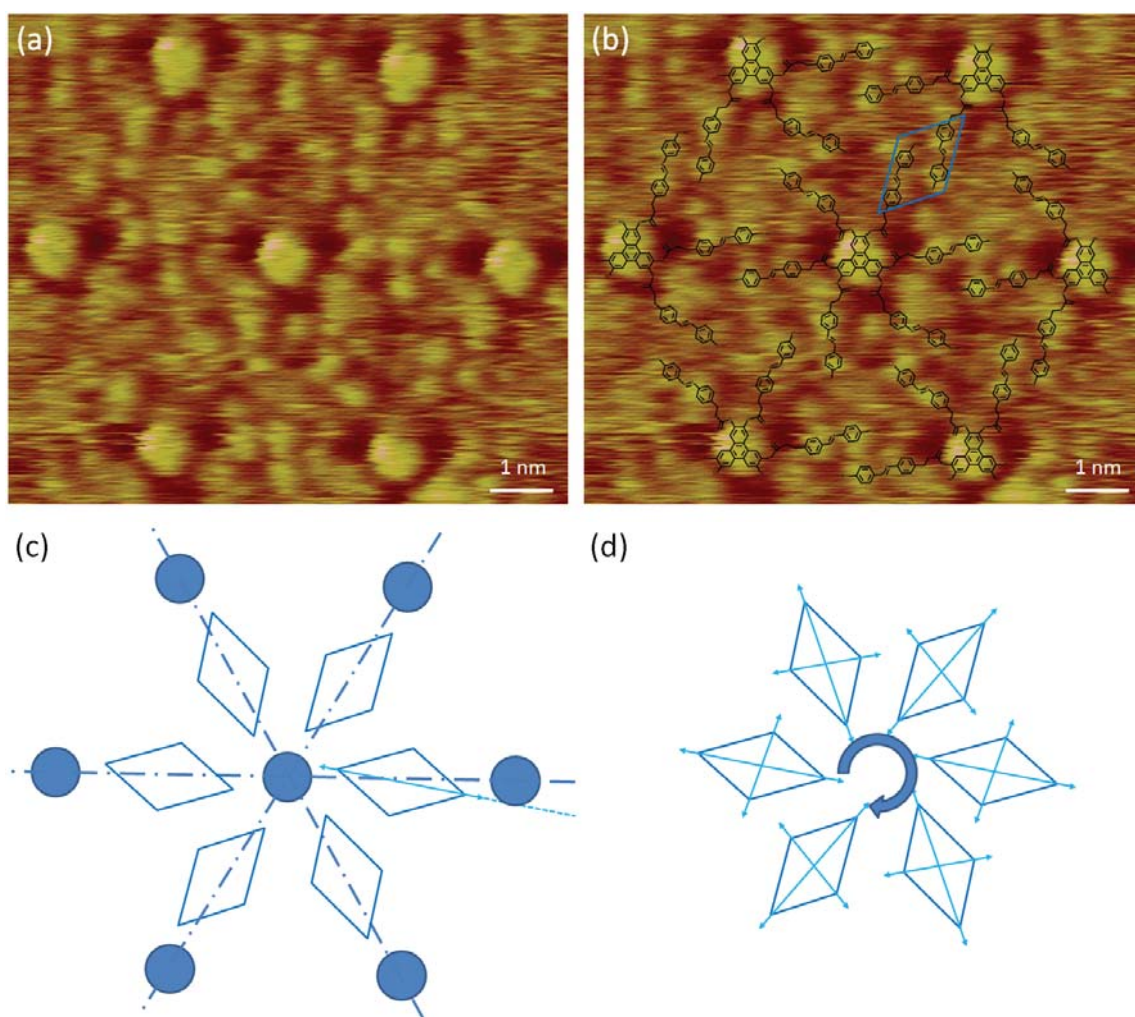


**Figure 4.5** (a) and (b) high-resolution STM images of **C-12** self-assemblies at the TCB/Au(111) interface. In addition to the hexagonally packed central triphenylene cores, some intramolecular details may be perceived, e.g. dumbbell-shaped protrusions that represent azobenzene groups forming intermolecular dimers. (b) shows the same area, with the proposed model of molecular packing, and one of the azobenzene-dimers enlighten by a blue rhombus. (c) and (d) schematical representation of the system enhancing its chirality, with highlighted triphenylene moieties (circles), and intermolecular azobenzene-dimers (diamonds);  $I_t = 3.93$  pA,  $V_t = 315.3$  mV.

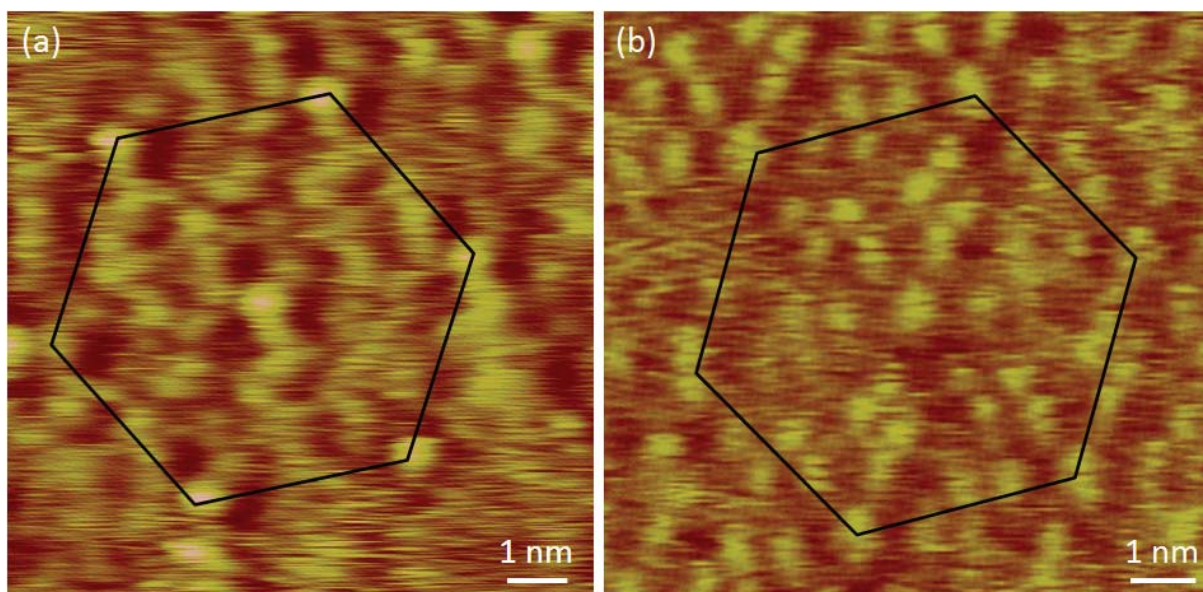
From careful analysis of those superstructures, we conclude that each of the four protrusions represent a single phenyl ring of an azobenzene. This means that one rhombic feature displayed on Figure 4.4(b) consists of two *trans*-azobenzene moieties, one for each of the neighbors. One of those 'sub-molecular' azobenzene-dimers is enhanced by a blue diamond shape on Figure 4.5(b), in addition to a proposed model of molecular packing overlaid therein. Similarly to the central core of **C-12**, azobenzene subunits quasi-lie flat on Au(111), likewise to the well-known affinity of aromatic species to metallic substrates. There exists several bases for us to claim that this intermolecular azobenzene-coupling is a relatively strong interaction, and, moreover, fundamental for the origin of self-assembly of **C-12** at a 1,2,4-trichlorobenzene/Au(111) interface and the monolayer stability.

Figure 4.5(b) contains in addition a schematic model of packing of C-12 monolayer presented on the Figure 4.5(a). Construction of this model was a multistep process for which finding of on the orientation of the central triphenylene core with respect to the molecular network was a milestone. The first factor was the peculiar triangular contrast of the central motif, visible on Figure 4.5(a) and also underlined on Figure 4.7. According to previous STM studies on differentiating between various chemical groups, oxygen is, most often, responsible for the low tunneling current probability and thus appears darker than many other groups and hydrocarbon backbone areas.<sup>30,31</sup> Although the areas of carbonyl oxygen atoms are not well resolved on Figure 4.4(a), they may be easily noticed on Figure 4.5(a). As shown on Figure 4.7(a), they form a tripod that is always oriented in one of the two possibilities with respect to the molecular lattice of **C-12**: 'up' or 'down'. First of all it enabled to orient triphenylene properly with respect to molecular mesh of **C-12**, in particular the triangular feature of triphenylene was kept oriented with its symmetry axes roughly perpendicular to the molecular rows of **C-12**. Secondly, a tripod of dark features (low tunneling probability) was a premise to keep the  $D_{3h}$  symmetry of the central part of the molecule (Figure 4.3(a)), where carbonyl oxygens from ester group point themselves, forming three pairs - analogically to the three regions of poor tunneling probability. The second main factor was deciphering a consistent trend in the intermolecular interactions based on azobenzenes, namely homochirality of azobenzene-azobenzene dimers within a single domain. This ensemble of assumptions enabled finally to construct a model of molecular packing, based on fixed position of triphenylene cores and azobenzenes associated with the observed STM contrast. The exact position and orientation of linkers between triphenylene and azobenzene motifs was not determined, but after superposition of STM contrast and molecular model, we evidence a limited evolution from the observed one and a *trans* conformation. The terminal alkyl tails were actually ignored, since there is no experimental evidence on their contribution to the 2D-structure stabilization.

In addition to the introductory presentation of the structure of **C-12**/TCB/Au(111) system few facts should be listed. First of all, as it may be noticed from Figures 4.4 and 4.5, there is no evidence on the Au-reconstruction lying underneath the hexagonally packed monolayers of **C-12**. This may be a sign that as a result of strong interaction between the organic molecules adsorbed on Au(111), the reconstruction is lifted. At this point it is hard to estimate the extent of excess of interaction energy in comparison to H5T/Au(111) system, but it is clear that the molecule-substrate interactions for those two systems are different. Since alkyl tails in the case of **C-12** are rather bystanders, i.e. they are not physisorbed on the surface of Au(111), we may postulate that the main energetical advantage comes from the azobenzene-Au interactions. Moreover, it is worth to mention, that bare triphenylene molecules possessing similar peripheral chains like **C-12** (i.e. H12T with six  $-C_{12}H_{25}$  chains) do not form self-assemblies of hexagonal packing. Incorporation of azobenzene groups between the terminal alkyl tails and the central core results in preservation of the hexagonal symmetry of packing within the self-assembled monolayers of **C-12**. Moreover, according to the model of Figure 5b, it appears that the adsorbed molecular structure is neither of  $D_{3h}$ , nor of  $C_{3v}$ . Indeed orientation of oxygens around the triphenylene core appears similar to the  $D_{3h}$  model, but adsorbed **C-12** molecules appear to convey intrinsic chirality, from the point of view of azo-benzene orientation, either clockwise or counter-clockwise. The adsorbed molecular structure is finally a mixture between the two models of Figure 4.3 and presents a molecular chirality.

#### 4.3.2 Investigating of the z-direction of the system by varying the tunneling parameters

An important information on the origin of self-assembly of **C-12** on Au(111), and the specific character of interfacial interaction between the substrate and the azobenzene moieties of studied molecules could be attained by careful modulation of the scanning parameters, e.g. the tunneling current ( $I_t$ ) and the bias ( $V_t$ ) applied between the probe and the surface. Figure 4.6 shows two high-resolution STM images taken at different tunneling parameters:  $I_t = 4.4$  pA and  $V_t = 315$  mV in the case of (a) and  $I_t = 11$  pA and  $V_t = 150$  mV in the case of (b). It is commonly recognized that the increase of tunneling current (and also lowering the bias) results in the sweeping of the scanning tip in the closer proximity to the studied interface, in comparison to the lower tunneling current.



**Figure 4.6** High-resolution STM images of **C-12** self-assembled at the TCB/HOPG interface, taken at different scanning parameters: (a)  $I_t = 4.4$  pA,  $V_t = 315$  mV; (b)  $I_t = 11$  pA,  $V_t = 150$  mV.

It is straightforward to notice that in the case of lower tunneling currents - (a) the central triphenylene motifs (which positions are emphasized by the black hexagon) exhibit a dominating tunneling contrast, with the other sub-molecular features often visualized. Moreover, the dark tripod feature around it additionally emphasizes each of the triphenylene cores. This is particularly general for the tunneling parameters in the range of  $I_t$  between 4 and 4.5 pA and  $V_t$  between 250 and 350 mV. Visualization of azobenzene groups in such conditions is possible and often they are well resolvable, but the electronic density is large on top of triphenylene for a large energetical range, whereas on the azobenzene, only specific energetic states may exist. In the case of the tunneling parameters in the range of  $I_t = 10 \div 11$  pA and  $V_t = 150 \div 200$  mV, the situation is more uniform, like depicted on Figure 4.6(b). In other words, the triphenylene central core becomes less bright with respect to the other parts and the dark tripod orientation becomes occasionally only prominent. At the same time, the azobenzene dimers become very well resolvable, i.e. their contrast rises to the level similar to the triphenylene moieties. This suggests that the electronic density is large on top of triphenylene for a large energetical range, whereas on the azobenzene, only specific energy states may exist.

### 4.3.3 The twofold mesh orientation of C-12 at the TCB/Au(111) interface

First of all, aforementioned nearest neighbor distance of  $3.5 \pm 0.1$  nm, confronted with the molecular dimensions (approximately 7 nm between the ends of two opposite in-plane alkyl tails) excludes the situation when all of the molecular subunits lie flat on the surface. Since it has been

already evidenced by high STM contrast, that azobenzene moieties occupy well-defined positions within internode areas of self-assembled monolayers, we conclude that the terminal alkyl tails are, if not completely desorbed, at least partially jutting upwards. This confirms that the intermolecular azobenzene-pairing is indeed considerably strong interaction, since the tendency for physisorption of aliphatic hydrocarbons on Au(111), could have resulted in theory in adsorption energy input close to 6 eV per molecule.<sup>32</sup> However, the self-assembly occurs, as evidenced by the regular meshes of triphenylene and azobenzene-dimer motifs. The system we studied exhibits a hexagonal symmetry which orientation with respect to the underlying substrate can vary. Globally, one may distinguish two types of domains mutually rotated of about  $16 \pm 1^\circ$ , hereafter named  $\alpha$  and  $\beta$  and marked by red and blue attributes, respectively. Similar lattice parameter and STM contrast of corresponding building blocks within both domains, suggest their twin-like character and energetically similar interaction with the substrate.

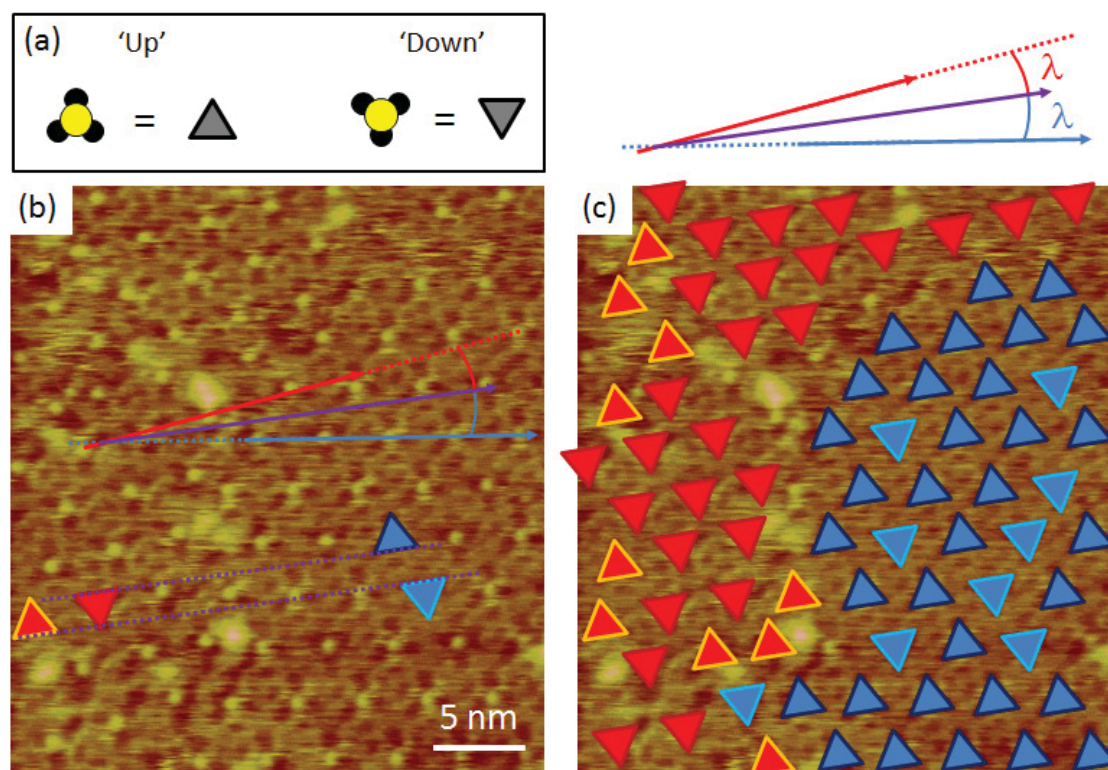
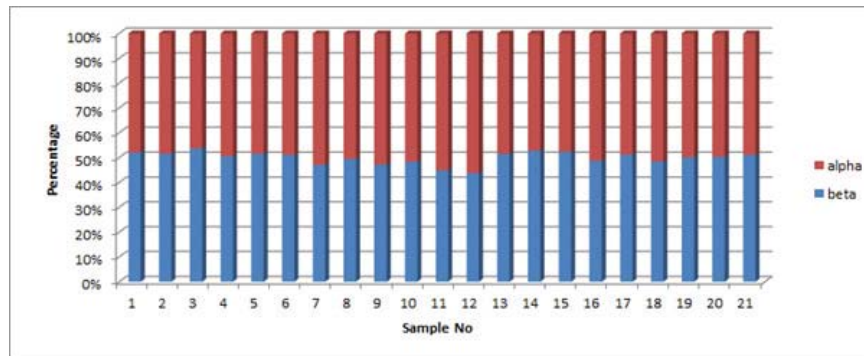


**Figure 4.7** (a) Schematic representation of 'up' and 'down' types of STM contrast of central part of **C-12**. (b) and (c) STM images showing the same area that contains two kinds of domains,  $\alpha$  and  $\beta$ . The triphenylene triangles are overlaid onto the STM image (c), and they are color-coded (red/blue - respectively to the domain they belong). Lack of correlation between the 'up/down' contrast and the mesh orientation suggests the minor role of triphenylene in the multiorientation of domains. This is further confirmed by similar triangle orientation in both domains (violet dashed-lines joining the collinear edges of red and blue triangles, (b)), what shows that two conformations of central part are invariant, regardless the orientation of **C-12** mesh;  $I_t = 9$  pA,  $V_t = 220$  mV.

Concerning the 'up' and 'down' orientations of the molecules, none of the two domains is homogeneous, although there seem to be a slight tendency towards 'down' and 'up' orientations, in case of red- and blue-labeled areas, respectively. For better clarity, red triangles pointing up were marked with the orange edges, and blue triangles pointing down were marked with the azure edges. No regular patterns or superstructures on larger spatial scales suggest that the (up/down) 'value' of the triangular contrast feature at each of the lattice nodes is rather a statistical event that is probably equally likely to occur for both 'up' and 'down' orientations. What should additionally attract the reader's attention is the similar orientation of central parts of molecules in both types of domains. In order to underline this fact, 4 molecules (2 from each domain type and up/down orientation) were highlighted on Figure 4.7(b) and the corresponding edges of triangles from both red and blue areas were joined by two purple dotted lines. It is clear to see that the edges are collinear and, moreover the direction creates an angle bisector for the angle between the domains molecular rows (red/blue). This allows us to state that the two molecular rows are rotated by around  $\lambda = \pm 8^\circ$  from the third axis (violet) representing the orientation of a central motif contrast feature. The situation is well-illustrated by three vectors on Figure 4.7(b).

The obstacle in determination of the orientations of the two hexagonal meshes of **C-12** is the fact that, in contrast to the case of H5T on Au(111), it is impossible to detect the orientation of the reconstructions lines. First of all, it is a manifestation of a different type or strength of interaction between the self-assemblies of **C-12** and the underlying substrate, with respect the H5T/Au(111) system. Even though it complicates the analysis of the orientation of molecular networks of **C-12** at the TCB/Au(111) interface, several facts should be underlined:

- the lattice parameter in both types of **C-12** domains is similar and equals  $a_{Au} = 3.5 \pm 0.1$  nm,
- both  $\alpha$  and  $\beta$  domains are always encountered while analyzing the STM images, contrary to the H5T/Au(111) system where one of the two types of domains was always present and the other (metastable) one appeared exclusively for a certain experimental conditions,
- the numerousness of both kinds of **C-12** domains is similar, as may be seen from Figure 4.8,
- the tunneling contrast in both structures is similar (the only variation from site to site is the up/down change, but globally the central core contrast and the azobenzene features possess comparable tunneling contrast in both domains).



alpha vs beta (4343 counts)

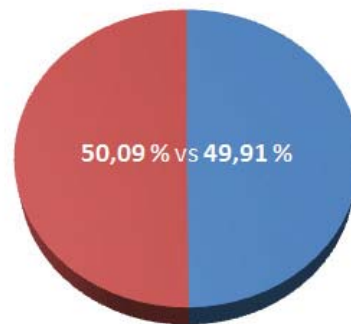


**Figure 4.8** Statistical analysis shows that both types of domains:  $\alpha$  (red) and  $\beta$  (blue) are equally-likely formed. (50.09 % vs 49.91 % for  $\alpha$  (red) and  $\beta$  (blue) domains, respectively). Equal probability of finding either of mesh orientations suggests, together with identical lattice parameter and similar contrast features, a twin-like character of both meshes.

All abovementioned facts suggest that the  $\alpha$  and  $\beta$  domains are commensurate and energetically equivalent, thus could exhibit a mirror-like character. Moreover, the fact that, on a given zone of Au(111), we always evidence only two orientations suggests that these two orientations are fixed with respect to the Au(111) crystallographic directions. We can thus examine the possibility that they are mutually rotated by an angle  $16^\circ$ , thereby they are rotated by  $\pm 8^\circ$ , either from Au<112> or from Au<110> high symmetry axes. Let us perform a crude analysis on the possible. Figure 4.9 illustrates the set of unit vectors of alternative meshes with the closest possible lattice parameter ( $a_{Au} = 3.5 \pm 0.1$  nm) and mirror-like molecular mesh orientation ( $\sim \pm 8^\circ$  from main crystallographic axis). The origin is in the bottom left-corner of the schematic Au(111) mesh. As may be seen, none of the several closely related meshes rotated from Au<112> fulfils both conditions and in each case the incorrect parameter is marked on red. However, there is a possibility to create a mesh rotated by  $8.2^\circ$  from Au<110>, which together with its lattice parameter (3.49 nm) fits well to the STM data. It is marked by green color, which symbolizes its validity.



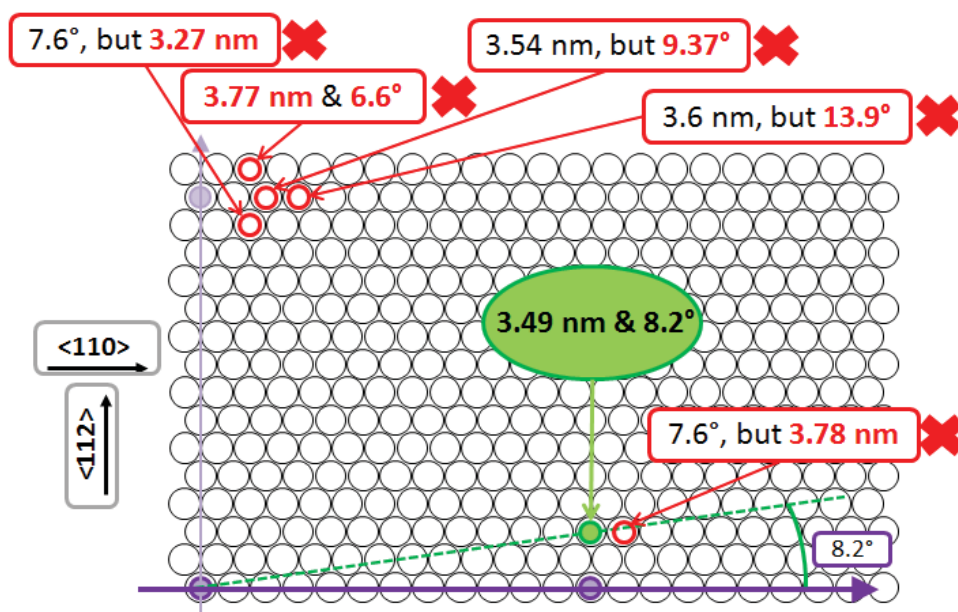


**Figure 4.9** Schematically shown basis for unit vectors for molecular meshes with parameters closely related to the  $a_{Au} = 3.5 \pm 0.1$  nm and rotation by  $\pm 8^\circ$ , from one of the two high symmetry axes, evidenced by STM.

#### 4.3.4 Azobenzene pairing as the driving force of C-12 mesh dual directionality

Contrary to physisorbed triphenylene units, that due to the favorable tunneling conditions for wide range of parameters may serve as a litmus test for the fulfilling self-assembly, visualization of the azobenzene moieties is more subtle. General trend of enhanced electronic interactions within the virtually decreased tip-substrate tunneling gap is manifested by the appearance and sharpening of dumbbell features, for smaller amplitudes of voltage bias and higher tunneling current values. Figure 4.10 presents the successful visualization of both triphenylene and azobenzene parts for the two mesh orientations. In the two corresponding insets (b) and (c), showing domains  $\alpha$  and  $\beta$ , the abovementioned pairing between azobenzenes coming from neighboring molecules is enhanced by the red and blue diamonds, respectively. As mentioned before, the direction of the longer diagonal of the azo-dimer feature (i.e. red/blue dashed line) is not collinear with the direction defined by the corresponding unit cell vector (i.e. orange/azure dashed line). Moreover, there is a consistent trend of rotation between the two, being equal  $10 \pm 1^\circ$ , and found either counter-clockwise, or clockwise within the entire  $\alpha$ - and  $\beta$ -domain families, respectively. As a consequence, the azo-dimer network creates rosette-like superstructures of shape-chirality, as depicted on Figures 4.10(b) and (c). Geometrical correlation between the mesh orientation and the four-lobe motif representing the intermolecular azobenzene coupling, suggests that the latter may be responsible for the dual orientation of self-assemblies of C-12 at the 1,2,4-trichlorobenzene/Au(111) interface.

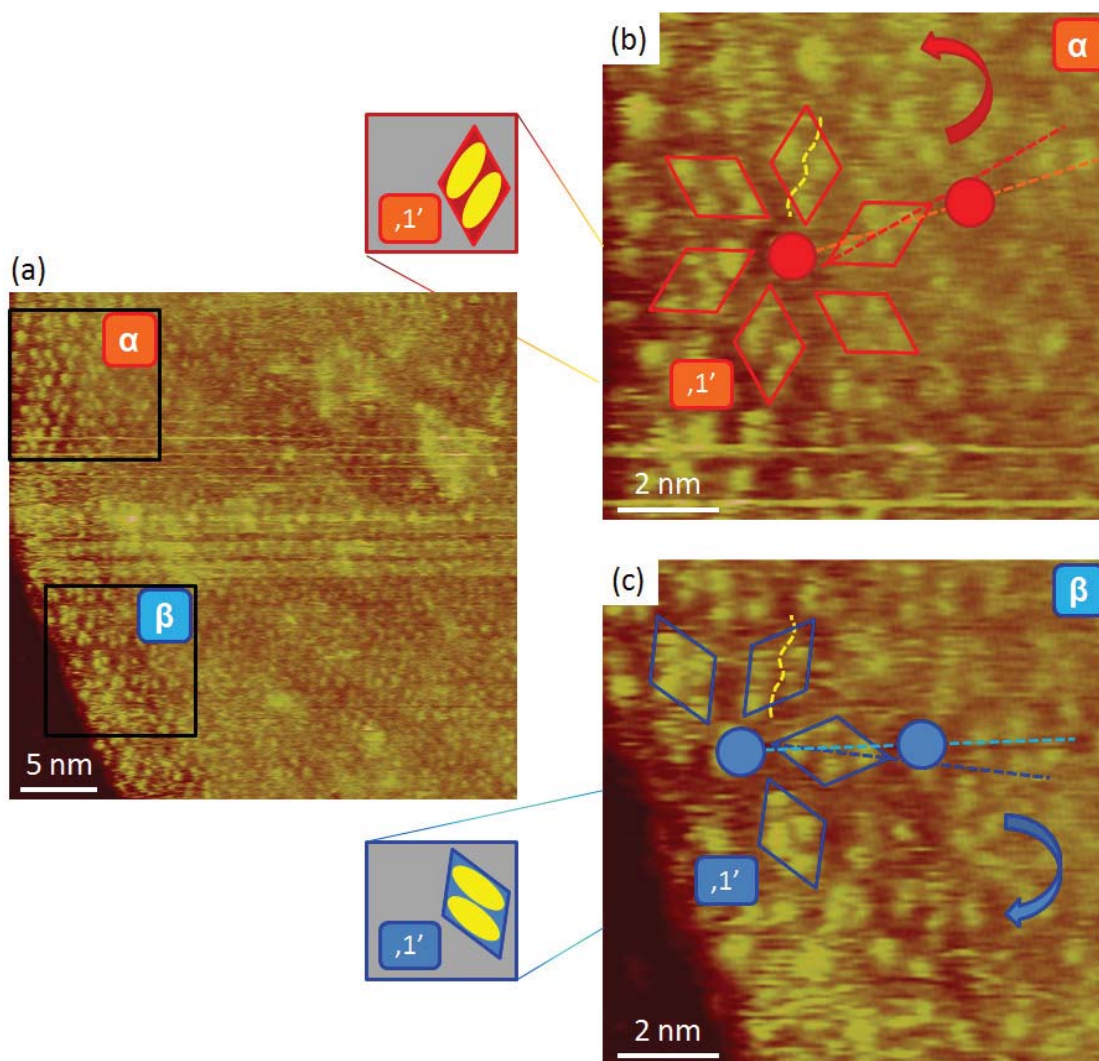


**Figure 4.10** STM images showing well-resolved central triphenylene moieties and azobenzene units in both domains. (b) and (c) represent close-ups of two regions of (a) with  $\alpha$ - and  $\beta$ -type domains, respectively. A pair of neighboring molecules at each of two close-ups is chosen and their central features are marked with discs. It is straightforward to see that the diamond feature in between is adopting one of two conformations. While in  $\alpha$ -type domains, the rhombus diagonal is rotated counter-clockwise with respect to molecular axis (orange dashed line), in  $\beta$ -type domains this rotation takes place in the opposite sense. The yellow dashed-line schematically separates the two constituents of the azo-dimer, for clarity of concept.  $I_t = 11$  pA,  $V_t = 250$  mV.

In addition to orientational duality of azobenzene dimeric features with respect to each molecular mesh, a detailed analysis of internodes areas within both types of domains enable us to state that in fact two kinds of dimers are present in the **C-12** monolayers. Although tunneling current contrast, as a reason of proximity of the constituents, makes these supramolecular adducts hardly individualizable, one may often discern which of the azobenzenes from a pair belongs to which of neighboring **C-12** molecules, as in the case of dimer-‘1’ highlighted on Figure 4.10(b), or occasionally

at the defect areas. This dimer, as shown by the inset of Figure 4.10(b) is arranged in a way that the right-hand side component is brought at a spot by each of **C-12** molecules, as a result we may name such dimer as ‘R-type’. The extensive analysis of areas of azobenzene dimers within  $\alpha$ -type domains resulted in consonance of structure, namely existence of ‘R-dimers’ only. Analogously, the ‘L-dimer’ present exclusively in  $\beta$ -type domains consists of two azobenzenes that schematically are the very picture of a left handshake, as demonstrated by Figure 4.10(c).

#### 4.3.5 Substrate-promoted assembling for the azobenzene/Au(111) system

If one considers two *trans*-azobenzene molecules forming a planar dimer related in shape to the collected STM data, geometrically there exist several configurations (some of them are presented in Figure 4.11). As stated by Wang *et al.*<sup>21</sup> the repulsion between positively charged hydrogen atoms renders the formation of azobenzene supramolecules of mixed RL/LR handedness unstable (Figure 4.11(a)). On contrary two types of dimers exist that remain stable: RR and LL, schematically shown by Figure 4.11(b). Both of the non-restricted dimers, being surface enantiomorphs, are characterized by the parallel orientation of the central -N=N- azo-bonds, and would give birth to the intermolecular interactions in either  $\alpha$ - or  $\beta$ -type domains, according to scheme on Figure 4.11(c).

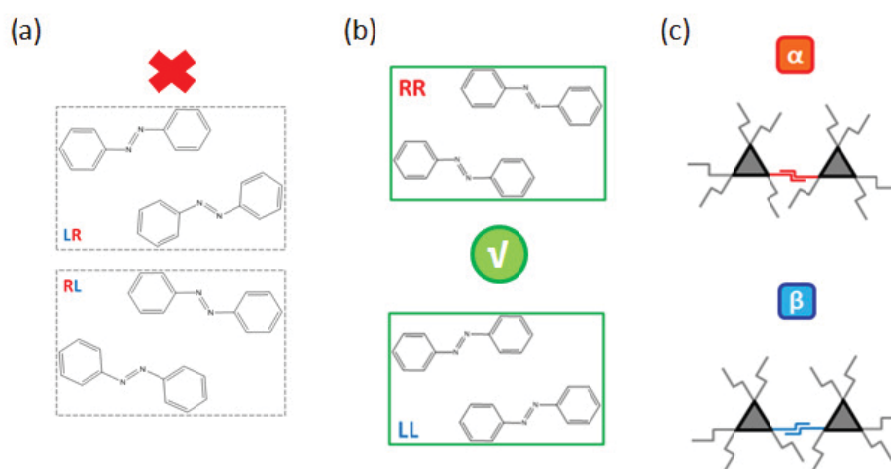


**Figure 4.11** Schematic representation of two unstable (a) and two stable (b) planar dimers of *trans*-azobenzenes. While the mixed LR/RL configurations are disfavored, the homogeneous RR and LL are well stabilized, according to Ref. 21. (c) Illustration of the ‘handedness’ of intermolecular interactions based on the dimeric structures from (b).

The RR/LL dimers may be the two specific low-energy configurations that owe their structure to dipolar interactions that are enhanced by hydrogen-like bonds. In fact, the orientational duality of azobenzene-azobenzene dimers is a manifestation of strong influence of the interfacial interactions

to the geometry of the studied system. This kind of interactions between azobenzenes has been evidenced already in the literature.<sup>21,33</sup> It is here supported by a rough estimation of the distances between facing hydrogen and nitrogen atoms, using the model presented on Figure 4.5(b). We find values between 0.3 and 0.35 nm, which is consistent with the expected values for hydrogen bonds.<sup>34</sup> This is in particular consistent with the values found for hydrogen bonds involving nitrogen atoms and leading to self-assembly for PTCDI molecules on Au(111).<sup>35</sup>

The proposed model of packing of  $\alpha$ - and  $\beta$ -domains of **C-12** on Au(111) is depicted by Figures 4.12(a) and (b), respectively, involving together with the commensurability of  $\alpha$ - and  $\beta$ -domains, the presence of clockwise R-azobenzene dimers and counter-clockwise L-azobenzene dimers in  $\alpha$ - and  $\beta$ -domains respectively.

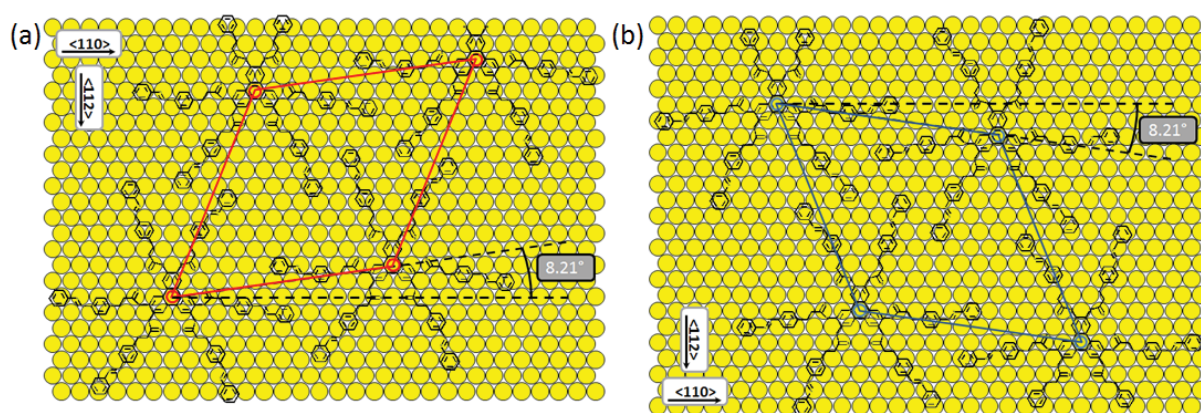


**Figure 4.12** Proposed model of molecular packing of **C-12** molecules on Au(111) associated with structures  $\alpha$  and  $\beta$ , (a) and (b) respectively. Both molecular meshes are rotated by  $\sim 8^\circ$  from Au<110>, either clockwise or counter-clockwise. These chiral molecular networks are expressed as a consequence of mirror-like interactions mediated by the Au(111), that specifically orient the monolayer and are thus at the origin of the twofold hexagonal symmetry observed for the case of **C-12**/Au(111) system.

The **C-12**/Au(111) system is not an isolated case of the appearance of chiral organization of coupled azobenzenes on Au(111). Kirakosian *et al.*<sup>33</sup> have studied coverage-dependent modifications in the architecture of the azobenzene adlayer on Au(111). For relatively small coverages (i.e. 0.5 ML) it was demonstrated that bare azobenzenes tend to aggregate in linear features (Figure 4.13(b)). Those linear supramolecular chains of specific surface orientation were assumed to originate from the dipolar interactions combined with hydrogen-like bonding between the unshared electron pair of a nitrogen atom of one azobenzene molecule and the net positive hydrogen atoms of the phenyl ring of another molecule (Figure 4.13(c)), which are expected to be very similar to interactions governing the **C-12**/Au(111) system.

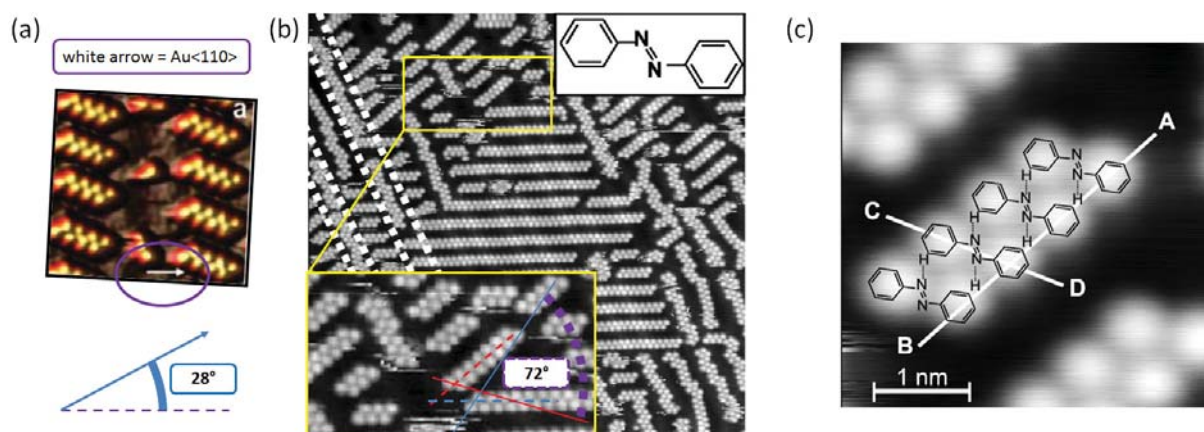


**Figure 4.13** STM images of azobenzene molecules self-assembled on Au(111). (a) Supramolecular tetramers of bare azobenzene physisorbed on Au(111). The blue arrow points the direction of orientation of a single azobenzene, which is rotated by ca  $28^\circ$  with respect to white arrow which symbolizes Au<110> direction (from Ref. 21). (b) STM images of 0.50 monolayer coverage of azobenzene on Au(111). The inset (yellow) shows mutual rotation of azobenzenes within two types of aggregates (blue/red), equal  $72^\circ$ . (c) Close-up STM image of a short chain of azobenzene molecules confined by the Au(111) substrate (from Ref. 33).

Figure 4.13(a) shows the STM image of azobenzene tetramers physisorbed at Au(111). The blue arrow points the direction of orientation of a single azobenzene which is rotated by ca  $28^\circ$  with respect to the Au<110> direction (white arrow).<sup>21</sup> Figures 4.13(b) and (c) represents images of 0.50 monolayer coverage of azobenzene on Au(111). A careful analysis of Figure 4.13(b) evidences two possible orientations of azobenzene units disoriented by roughly  $72^\circ$ . Both values found are obviously different from the one we observe in **C-12** network. Figure 4.10 evidences that only one single orientation is present with respect to Au<110> which is  $\pm 16^\circ$ . The origin of such difference is probability related to the imposed commensurability of **C-12** in the hexagonal network and suggest that several favorable orientations are possible for azobenzene units in interaction with Au(111).

#### 4.4 Specificity of the probed azobenzene interactions – STM of C-12/HOPG system

In order to validate the statement of the specific interactions of azobenzene coupling mediated by the Au(111) we have performed the analogical experiments of self-assembly of **C-12** molecules substrate other than gold. Figure 4.14 shows STM images of self-assemblies of **C-12** at the trichlorobenzene/HOPG interface.

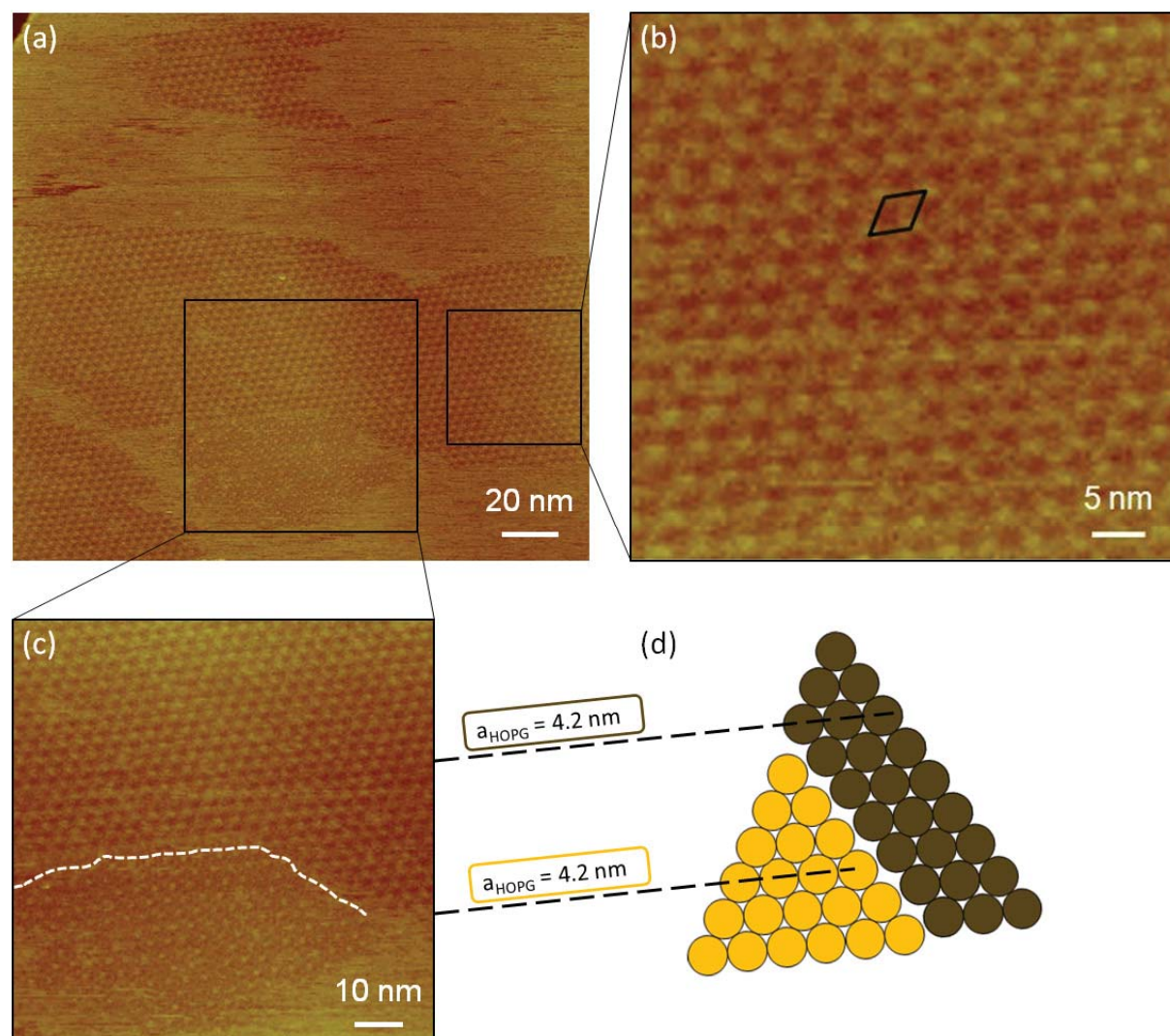


**Figure 4.14** STM constant current images of **C-12** self-assembled at the TCB/HOPG interface. (b) shows the homogenous **C-12** domain with the hexagonal symmetry of packing and the black diamond emphasizes the lattice parameter,  $a_{\text{HOPG}} = 4.2 \pm 0.1 \text{ nm}$ . (c) shows the interesting coexistence of two domains, which (despite of the difference in the tunneling contrast) possess similar orientation of molecular rows and similar unit cell sizes. The bottom-domain that is separated from the bigger top-domain by a white dashed-line, contains molecules that reside at different atomic site, what results in different tunneling contrast. (d) schematically shows the situation described. Closely-packed circles depict the hexagonally organized **C-12** molecules with the similar structure of both domains, that differ only by some minor translation on the Au(111) surface;  $I_t = 10 \text{ pA}$ ,  $V_t = 350 \text{ mV}$ .

A direct proof for the specificity of the molecule-substrate interactions in the case of **C-12**/Au(111) system is the fact that the **C-12**/TCB solution deposited onto highly-oriented pyrolytic graphite (HOPG) self-assembles only occasionally: the physisorbed self-assemblies remain visible at the interface for a few minutes only. From this we conclude that the **C-12** self-assemblies on HOPG are of decreased stability in comparison to those on Au(111). Figure 4.14 shows the STM images of **C-12** at the TCB/HOPG interface with several domains of hexagonal symmetry, that occasionally differ in contrast of lattice nodes. Figure 4.14(c) shows the close coexistence of two domains that differ in the tunneling contrast. The ‘bottom’-domain contains **C-12** molecules of higher apparent contrast at the center of each lattice node – in comparison with the ‘top’-domain. However, both domains contain hexagonally packed molecules with similar internode spacing and similarly oriented molecular rows. The most probable origin for the contrast difference between the two types of domains lies in different physisorption sites of the central triphenylene core on the HOPG surface. This, in turn would suggest a decreased specificity of physisorption (site) for **C-12**/HOPG system.

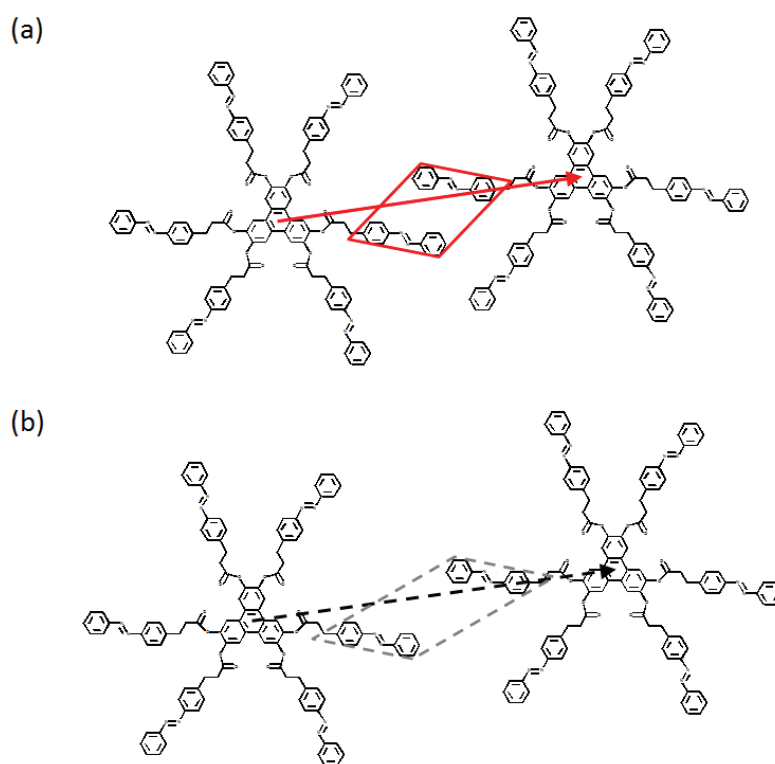


**Figure 4.15** Simplified geometrical representation of the dimer of **C-12** molecules on the basis of the lattice parameters on Au(111) and HOPG. (a) On Au(111), due to the influence of the substrate, system stabilizes a **C-12** dimer with an optimal nearest-neighbor distance by effective azobenzene coupling. (b) Increased lattice parameter of a **C-12** dimer on HOPG resulting in lack of analogical coupling, comes probably from the stronger affinity of terminal alkyl parts (here omitted) to interact with HOPG. All in all, the latter interactions do not drive to stable self-assemblies.

Furthermore, analysis of drift corrected images shows the modified lattice parameter ( $a_{\text{HOPG}} = 4.2 \pm 0.1$  nm), that absolutely excludes the azobenzene coupling between the neighboring molecules, even from purely geometrical point of view (Figure 4.15). Thus, **C-12** may be considered as a smart ensemble of azobenzenes, specific in interaction with the metallic Au(111) substrate.

#### 4.5 Conclusions

Comparing our observations to results from the literature, and comparing the structures formed on graphite and on Au(111), we propose that the interaction between neighboring azobenzenes is based on the hydrogen bonding, mediated by the Au(111) substrate. The estimated distances between azobenzene units are consistent with this hypothesis. The interaction occurring with six neighbors appears as a stabilizing factor. As a result, the formation of a hexagonal 2D network with a large period of 3.5 nm is observed. Moreover, dominating character of the more numerous azobenzene-azobenzene interactions is associated with an unfavorable orientation of the triphenylene core with respect to the substrate. This is established with the use of results from the preceding chapter. In addition, it means that three times the interaction between azobenzene units (half counted for one single molecule) may be of energy smaller than -0.26 eV, according to the preceding chapter, in agreement with the energy of hydrogen bonding, expected to range from 0.05 and 0.7 eV.<sup>34</sup> A large number of organic structures have already been demonstrated to be organized through hydrogen bonds in 2D on Au(111).<sup>35,36</sup> The new result is that this interaction appears specific to the Au(111) substrate, since it does not stabilize the network on graphite, suggesting not as strong interactions between neighboring azobenzenes on graphite. This specificity of Au(111) may be due to the selection of very specific orientations for the azo-benzene units, which may favor the formation of hydrogen bonds as well, the gain in energy being thus a combination between the adsorption energy of the azobenzene groups on one hand, and hydrogen bonding between neighbouring azobenzenes on the other hand. In turn, the formation of azobenzene dimers orients the entire crystallographic network. It is worth noticing that these interactions finally stabilize hexagonal networks with a very large period, which is quite unusual. For triphenylenes with unsubstituted aliphatic chains, hexagonal networks are not formed for molecules containing side-chains of 11 carbons. In turn, the row-like structures are formed.

The hydrogen bonding between azobenzenes finally appears at the origin of the ordered hexagonal network of **C-12** molecules on Au(111). In particular it creates a well-defined chirality in 2D. First, only one type of the molecular structure is adsorbed, the  $D_{3h}$  structure and not the  $C_{3v}$ , the more symmetric one, which is not observed in the ordered networks (see paragraph 4.2). Moreover, similar chiral molecular structures assemble together to form organizational chirality with either clockwise rotation in the first kind of network (network at  $+8^\circ$  from Au(111)) or counter-clockwise



rotation in the other one (network at  $-8^\circ$  from Au(111)). The selection of only two kinds of networks with opposite handedness is directly associated with the presence of the substrate and with the selection of precise azobenzene orientations.

In conclusion, the results presented in this chapter suggest that additional aromatic groups such as azobenzenes could be used, either for promoting the self-assembly of extended molecular systems or to preserve the hexagonal symmetry of packing on gold, which is often lost for discotic molecules with longer peripheral alkyl tails.<sup>37</sup> Often, as a result of Au(111)-surface reconstruction and in consequence losing of surface threefold symmetry, the self-assembly of molecules of threefold symmetry is blocked.<sup>38</sup> Azobenzene-bridging may possibly constitute an alternative for promoting the formation of monolayers of small organic molecules on Au(111), although we do not expect it could become as general a building motif as the interdigitation of alkenes, due to its structural complexity and dynamic (switching) potential.

## 4.6 Experimental section

### 4.6.1 Materials

**Analyte.** C-12 and the other azobenzene-substituted triphenylenes presented in this chapter were synthesized and characterized within the Department of Materials Chemistry, University of Ryukoku (Otsu, Japan).

**Solvent.** C-12 was dissolved in 1,2,4-trichlorobenzene (Sigma Aldrich, pure >99%, used as received) with a concentration of 1.0 mmol/L. Solution was heated up to  $\sim 70^\circ\text{C}$  for 15 min prior to deposition onto the substrate.

**Substrate.** The Au(111) substrates were purchased from Neyco (Structure Probe, Inc. supplier for France). The raw samples consisted of mica plates of thickness between 50 and 75  $\mu\text{m}$ , onto which thin ( $\sim 100$  nm) layer of gold has been evaporated. Details about the crystallographic structure of Au(111) will be presented in the another section.

**Probe.** The STM tip was mechanically cut from a Pt/Ir wire (90/10 wt%) that was purchased from Goodfellow S.A.R.L. During the measurement process the STM tip was immersed in the droplet of solution.

### 4.6.2 Sample preparation

A crucial step for ensuring the most favorable conditions for the self-assembly of molecules into the physisorption-driven monolayer is preparation of a high quality surface, i.e. composed of atomically flat terraces of large size (100s of nm in 2D). The procedure of preparing of Au(111) consist normally of short ( $\sim 1$  min) flame annealing in a hydrogen or propane gas flame. The latter one has been used for experiments described in this thesis. The gently heated ( $\sim 70^\circ\text{C}$ ) solution of H5T has been deposited onto freshly flamed Au/mica sample, straight after the flaming process was ceased.

### 4.6.3 Equipment: scanning tunneling microscope

The monolayers were investigated using a commercial STM equipped by low current head (Veeco, Digital Instruments, Inc. USA). For each monolayer, several STM-images recorded in constant current mode with current ranging from 1 to 100 pA and tip bias from  $\pm 100$  to  $\pm 1000$  mV were obtained with different samples and tips to check reproducibility and to ensure that results are free from artifacts. All STM images presented here were recorded under ambient conditions without any further image processing.

## 4.7 Acknowledgments

Prof. Kingo Uchida is gratefully acknowledged for the supplying the series of hexa-azobenzene substituted molecules of good purity. Dr. Alexandr Marchenko (Institute of Physics, National Academy of Science of Ukraine, Kiev, Ukraine) is acknowledged for many fruitful discussions on the obtained STM results.

## 4.8 References

1. Groszek, A. *Proc. R. Soc. Lon. Ser. A* **314**, 473-498 (1970).
2. Marchenko, A.; Cousty, J. & Van, L. P. *Langmuir* **18**, 1171–1175 (2002).
3. Marchenko, O. & Cousty, J. *Phys. Rev. Lett.* **84**, 5363-5366 (2000).
4. Yamada, R. & Uosaki, K. *J. Phys. Chem. B* **104**, 6021–6027 (2000).
5. Nägele, T.; Hoche, R.; Zinth, W. & Wachtveitl, J. *Chem. Phys. Lett.* **272**, 489–495 (1997).
6. Tamai, N. & Miyasaka, H. *Chem. Rev.* **100**, 1875–1890 (2000).
7. Feringa, B.L. *Molecular switches*, Wiley-VCH Verlag (2001).
8. Klajn, R. *Pure Appl. Chem.* **82**, 2247–2279 (2010).
9. Tegeder, P. *J. Phys.: Condens. Matter* **24**, 394001 (2012).
10. Morgenstern, K. *Prog. Surf. Sci.* **86**, 115–161 (2011).
11. Choi, B.-Y.; Kahng, S.-J.; Kim, S.; Kim, H.; Kim, H. W.; Song, Y. J.; Ihm, J. & Kuk, Y. *Phys. Rev. Lett.* **96**, 156106 (2006).
12. Alemani, M.; Peters, M. V.; Hecht, S.; Rieder, K.-H.; Moresco, F. & Grill, L. *J. Amer. Chem. Soc.* **128**, 14446–14447 (2006).
13. Comstock, M. J.; Cho, J.; Kirakosian, A. & Crommie, M. F. *Phys. Rev. B* **72**, 153414 (2005).
14. Mielke, J.; Selvanathan, S.; Peters, M.; Schwarz, J.; Hecht, S. & Grill, L. *J. Phys.: Condens. Matter* **24**, 394013 (2012).
15. Dri, C.; Peters, M.V.; Schwarz, J.; Hecht, S. & Grill, L. *Nat. Nanotechnol.* **3**, 649–653 (2008).
16. McNellis, E.; Mercurio, G.; Hagen, S.; Leyssner, F.; Meyer, J.; Soubatch, S.; Wolf, M.; Reuter, K.; Tegeder, P. & Tautz, F. S. *Chem. Phys. Lett.* **499**, 247–249 (2010).
17. Wolf, M. & Tegeder, P. *Surf. Sci.* **603**, 1506–1517 (2009).

18. Hagen, S.; Kate, P.; Leyssner, F.; Nandi, D.; Wolf, M. & Tegeder, P. *J. Chem. Phys.* **129**, 164102 (2008).
19. Comstock, M. J.; Levy, N.; Kirakosian, A.; Cho, J.; Lauterwasser, F.; Harvey, J. H.; Strubbe, D. A.; Frechet, J. M. J.; Trauner, D.; Louie, S. G. & Crommie, M. F. *Phys. Rev. Lett.* **99**, 038301 (2007).
20. Safiei, A.; Henzl, J. & Morgenstern, K. *Phys. Rev. Lett.* **104**, 216102 (2010).
21. Wang, Y.; Ge, X.; Schull, G.; Berndt, R.; Bornholdt, C. B.; Koehler, F. & Herges, R. *J. Amer. Chem. Soc.* **130**, 4218–4219 (2008).
22. Bléger, D.; Dokic, J.; Peters, M. V.; Grubert, L.; Saalfrank, P. & Hecht, S. *J. Phys. Chem. B* **115**, 9930–9940 (2011).
23. Tschierske, C. *J. Mater. Chem.* **11**, 2647–2671 (2001).
24. Barberá, J.; Donnio, B.; Gimenez, R.; Guillon, D.; Marcos, M.; Omenat, A. & Serrano, J. L. *J. Mater. Chem.* **11**, 2808–2813 (2001).
25. Kouwer, P. H. J. & Mehl, G. H. *J. Amer. Chem. Soc.* **125**, 11172–11173 (2003).
26. Kouwer, P. H. J. & Mehl, G. H. *Angew. Chem. Int. Ed.* **42**, 6015–6018 (2003).
27. Shimizu, Y.; Kurobe, A.; Monobe, H.; Terasawa, N.; Kiyohara, K. & Uchida, K. *Chem. Commun.* 1676–1677 (2003).
28. Tanaka, D.; Ishiguro, H.; Shimizu, Y. & Uchida, K. *J. Mater. Chem.* **22**, 25065–25071 (2012).
29. Fisher, A. J. & Blöchl, P. E. *Phys. Rev. Lett.* **70**, 3263–3266 (1993).
30. Cyr, D. M.; Venkataraman, B.; Flynn, G. W.; Black, A. & Whitesides, G. M. *J. Phys. Chem.* **100**, 13747–13759 (1996).
31. Venkataraman, B.; Flynn, G. W.; Wilbur, J. L.; Folkers, J. P. & Whitesides, G. M. *J. Phys. Chem.* **99**, 8684–8689 (1995).
32. Libuda, J. & Scoles, G. *J. Chem. Phys.* **112**, 1522–1530 (2000).
33. Kirakosian, A.; Comstock, M. J.; Cho, J. & Crommie, M. F. *Phys. Rev. B* **71**, 113409 (2005).
34. Barth, J. V. *Annu. Rev. Phys. Chem.* **58**, 375–407 (2007).
35. Mura, M.; Silly, F.; Briggs, G. A. D.; Castell, M. R. & Kantorovich, L. N. *J. Phys. Chem. C* **113**, 21840–21848 (2009)
36. Mura, M.; Silly, F.; Burlakov V.; Castell, M. R.; Briggs, G. A. D. & Kantorovich, L.N. *Phys. Rev. Lett.* **108**, 176103 (2012)
37. Katsonis, N.; Marchenko, A. & Fichou, D. *J. Amer. Chem. Soc.* **125**, 13682–13683 (2003).
38. Bléger, D.; Kreher, D.; Mathevet, F.; Attias, A.-J.; Schull, G.; Douillard, L.; Huard, A.; Fiorini-Debuisschert, & Charra, F. *Angew. Chem. Int. Ed.* **119**, 7548–7551 (2007).



## Chapter 5

### Self-assembly and dynamics in the self-assembled monolayers of C-12 at the TCB/Au(111) interface

Self-assembly in ambient conditions, and more specifically, at the liquid/solid interface, is inseparably connected to the increased mobility between the self-assembled monolayer and the surrounding liquid environment. This fact is usually manifested by dynamics that may be observed by scanning tunneling microscopy, as a sequence of scans. In this chapter, we perform a detailed analysis of dynamics of **C-12** monolayers on Au(111). At first, we evidence the difference in the interactions between azobenzene neighbors, between 'up'-'up'/'down'-'down' states and 'up'-'down' states of two neighboring **C-12** molecules. We then use this observation to interpret, the observed dynamics between 'up' and 'down' states of a given **C-12** molecule involved in an ordered network on Au(111). Most of those up/down 'contrast switching' events are shown to be associated with the influence of the molecules in close proximity. Moreover, the 'contrast switching' event is shown to happen more likely for molecules physisorbed at the domain borders, rather than for those from inside the domain. This observation is in good agreement with the increased intermolecular interaction potential inside the domains, compared to what happens at domain boundaries. The last part of this chapter is devoted to studies of homogeneity of hexagonal mesh coordinated by the azobenzene-group pairing. The previously presented non-correlation of two-fold orientation of **C-12** molecular mesh with the 'up'/'down' contrast of the central part of adsorbed molecules is shown as a spectrum of decreased concentration of the analyte.

## 5.1 Introduction

STM images with sub-molecular resolution of physisorbed molecular monolayers often give the impression that the molecules are 'frozen' at the interface and that only minor changes are occurring in the area that is being investigated. This impression is a direct consequence of the limited probing ability of the microscope in the z-direction and the non-instantaneous acquisition of data. The reality is usually quite different, and several spontaneous phenomena may often occur at the liquid/solid interface, starting from simple adsorption/desorption of molecules, their translational/rotational movement or the growth of the larger domains at the expense of smaller ones, referred to as the Ostwald ripening. The complexity of interactions involved in the formation of monolayers at the liquid/solid interface originates from (1) the interactions between the molecules of interest and the substrate, (2) intermolecular interactions between the molecules of the analyte, and (3) the influence of the solvent molecules. These interactions, as shown in previous chapters, dictate the appearance of monolayers by driving the self-assembly. Moreover, even in a relatively stable physisorbed system molecules diffusing around impact on the geometry of the monolayer, as demonstrated hereafter also. As a consequence distinguishable changes like desorption and re-adsorption should take place within the monolayer and the system could exhibit a dynamic behavior in the time-scale of the experiment. In addition, most low molecular weight compounds (i.e. *small* organic molecules) are too mobile to be visualized, except if they are trapped in a 2D (crystalline) matrix. Most of the observed dynamics at the solid/liquid interface has been proposed on graphite surfaces. An efficient route for example to obtain stable monolayers is a so-called multivalence approach.<sup>1,2</sup> The multivalency that due to the (high) effective concentration, leads to high affinity and to low dissociation rate, ensuring formation of thermodynamically and kinetically stable monolayers. One of the most eye-catching examples of dynamics in these self-assembled monolayers is the case of multivalent hexapod oligo(*p*-phenylene vinylene)-substituted hexaarylbenzene, which exhibited a multimode conformational dynamics mostly associated with desorption/adsorption of peripheral parts of the molecules. This dynamics was shown to be eventually promoted by the nearest neighbor interactions.<sup>2</sup> In addition, the translational motion of individual molecules was observed in porous systems. It occurred between neighboring voids. However, this kind of dynamics being fast, so it required high speed STM, which enabled to visualize hopping of small organic molecules from site to site (actually from void to void) within the molecular network (or molecular sieve).<sup>3,4</sup> In general, dynamic processes of organic molecules at the interfaces were shown previously by numerous studies evidencing the translational,<sup>5-7</sup> or rotational,<sup>8,9</sup> or finally conformational dynamics.<sup>2,10,11</sup>

In Chapter 4, we have established the organized network of **C-12** molecules at the Au(111) interface. It is a hexagonal 2D network of large period, stabilized by the interactions between the azobenzene units of neighboring molecules. These azobenzene units are symmetrically localized in the 6 peripheral chains of the **C-12** molecules. In the present chapter, we study the dynamics of this ordered network and relate it to the presence of these specific interactions, believed to be of hydrogen bonding type. We first show that the interactions between azobenzene units can be tuned by the molecular orientation. One state of the system (the homogenous one) has been presented in Chapter 4 as 'up'-'up' or 'down'-'down'. The other one (mixed) is described here and corresponds to 'up'-'down' orientation. In a second part of the chapter we describe the dynamics of changes between 'up' and 'down' states of one given molecule in the ordered network and interpret it in relation with the interactions between neighbors, confirming the hydrogen bonding nature of the interactions. In the last part of the chapter, we evidence the role of the interactions between neighboring azobenzene units in the growth of the ordered domains of **C-12** molecules. Surprisingly, we demonstrate that, for varying concentration of **C-12** solution used for deposition onto Au(111), the most stable (and most homogenous) structures, made of 'up'-'up' or 'down'-'down' types of conformations are formed for the highest concentration. Whereas the disorder, associated with the presence of mixed ('up'-'down') conformations increases when concentration is decreased. This highlights the fundamental difference between growth at the solid/liquid interface and growth under evaporation in UHV chambers.

## 5.2 Resolving the 'up-up' and 'down-down' C-12 dimer structure

In the previous chapter we have shown that **C-12** forms a self-assembled monolayer on Au(111), in which a determining role is played by the azobenzene moieties which, by effective coupling, define one of the two directions of the **C-12** molecular mesh. The central triphenylene core remains rather passive in determining the direction of **C-12** monolayer, as evidenced by its unfavorable orientation with respect to Au(111). We have also shown dual 'up'/'down' contrast of the central core is present in both types of domains and corresponds to a disorientation of the molecule by 60° which modifies the localization of the carbonyl oxygens of the carbonyl group linker between triphenylene and azobenzene moieties. This duality in triphenylene orientation, however, did not show any regularity or spatial periodicity. The schematic model of molecular packing for the compatible 'up'-'up' and 'down'-'down' pairs of interacting molecules was already shown in the previous chapter. Figures 5.1(a) and (b) are comparative demonstration of the change of intermolecular arrangement by rotating the central **C-12** molecule by 60°, from 'down' to 'up' state. It should be reminded that the



'up'/'down' stands for the tunneling contrast, which darker areas are a result of presence of carbonyl oxygens. Moreover, it does not correspond to a disorientation of the molecule by 180°, but to a 60° disorientation of the molecule. The background in both pictures (Figure 5.1(a) and (b)) contains the same STM image, and only the proposed model which is overlaid on the top is modified. The molecule in the middle of the hexagon (Figure 5.1(a)), that possess 'down' state, similarly to its neighbors, is rotated in Figure 5.1(b) to exhibit conformation change to 'up' state. As may be seen, no drastic changes are observed in the modified model and majority of interactions between azobenzene units are comparable. However, it appears from the comparison of the two blue rhombi (Figures 5.1(a) and (b)) that orientation and distance between interacting azobenzenes vary from 'down-down' to 'down-up' type of **C-12** dimer. A rough estimation of geometrical parameters connected with the model gives an idea of the geometrical changes in this particular case. The 'up'-'up' case, represented by Figure 5.1, exhibits the distance and orientation between two azobenzenes which could facilitate the hydrogen bonds. In particular, the nitrogen atoms are separated from the respective hydrogen atoms of a value  $0.32\div 0.36$  nm, which may be considered as a hydrogen-like bonding.<sup>12</sup> In addition, the symmetry axes of the two azobenzene units are rotated by 9°. After rotation of the central molecule (model only) the measured parameters for the same pair of **C-12** molecules are modified. The situation is illustrated on Figure 5.1(b). The distance between nitrogen atom and facing hydrogen atom coming from the phenyl ring of neighboring azobenzene equals  $0.44\div 0.46$  nm. It became larger and possibly out of the range for hydrogen-like bonding.<sup>12</sup> Even though the mutual orientation between azobenzenes is diminished to 6° and they are closer to be perfectly parallel, the azobenzene-azobenzene interactions could be lowered.

In addition, Figure 5.1 shows the probable mechanism of blocking of misorientation of **C-12** mesh. Supposing that molecule in the bottom left-corner is physisorbed and its future neighbor comes from the right-hand side – in theory it may choose two options to physisorb: either by normal right-handshake (Figure 5.1(c)), or by unusual coupling in pseudo right-handshake. The latter one, even though non-restricted by the azobenzene-azobenzene interactions is effectively blocked since the associated breaking of hexagonal symmetry in this case causes drop of the amount of azobenzene interactions. In particular, the coupling between the two **C-12** molecules lying at the shorter diagonal of the hexagonal cell does not happen. This possibly blocks the growth of the domains in the form depicted by Figure 5.1(d).

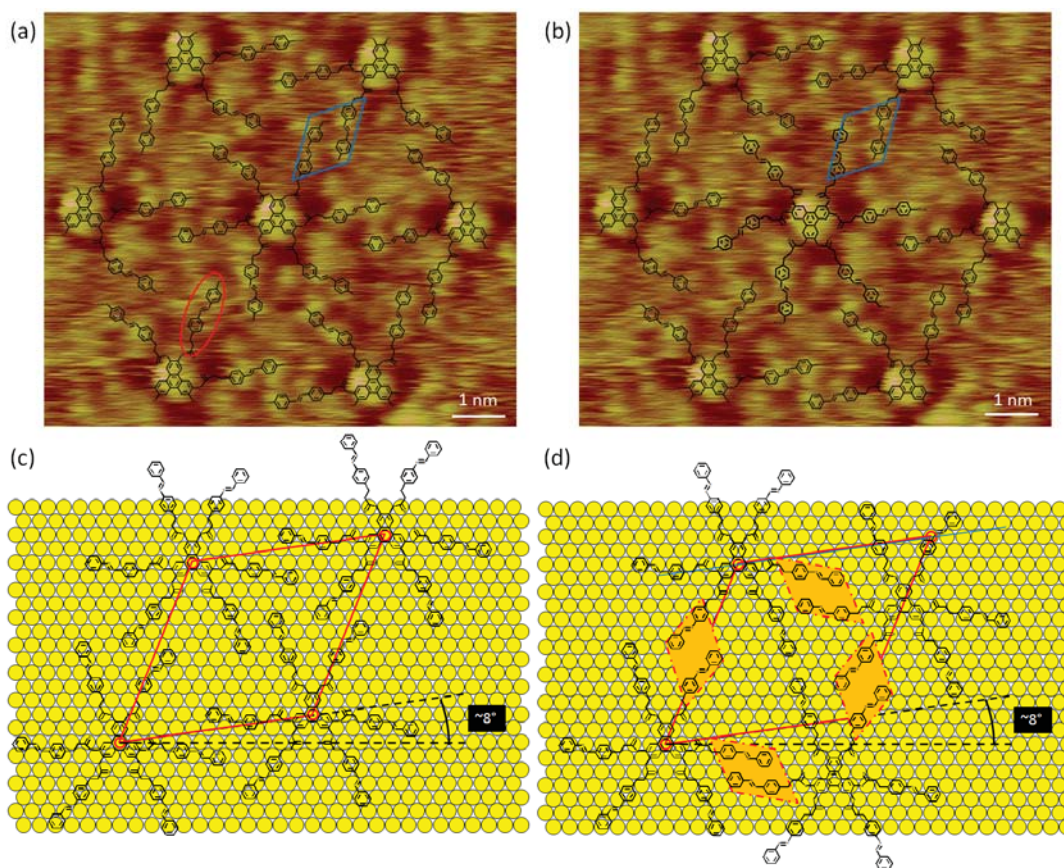


**Figure 5.1** (a) and (b) STM images with overlaid molecular packing that shows that rotation by  $60^\circ$  and introduction of non-uniform conformation does not change strongly the interactions between the neighboring molecules. (c) Schematic view on molecular packing of C-12 domain. Hypothetically a molecule in the bottom right corner instead of adsorbing at proper site may adsorb lower and thus may form the azobenzene coupling of another type (d). Even if such coupling is stable it will not be promoted because the total number of azobenzene interactions dropped from 5 to 4, since the coupling along the short diagonal is restricted.

### 5.3 STM observations of the local dynamic changes within C-12 monolayers

#### 5.3.1 Probing of 'up'/'down' contrast changes within C-12 monolayers

Figure 5.2 represents a sequence of STM images of C-12 monolayer taken at the rate of 28s per frame. The number in top-right corner of every image denotes the frame number and thus provides chronology for the observed changes. Among 12 (in some cases 14) molecules that are presented on each of the images, the most important one is the molecule in the top-left corner, which is highlighted by a circle around its center. On frames (1) and (2) the closest neighborhood of the lattice node creates a dark triangular shape in the 'down' state (grey circle). After two scanning cycles, the contrast around the discussed lattice node changes its *sign* from 'down' to 'up' (yellow

circle). After 5 additional scanning cycles (i.e. frame (7)), the contrast reverses back to the originally present 'down' conformation (frame 8), but after two additional frames the situation changes again. Thus we observe a sequence of 'up'/'down' contrast changes of a single molecular site, which is happening for similar tunneling conditions, i.e. constant tunneling current set-point and the applied voltage bias. The switching appears to occur only between the two states previously encountered in the hexagonally packed domains of **C-12**.

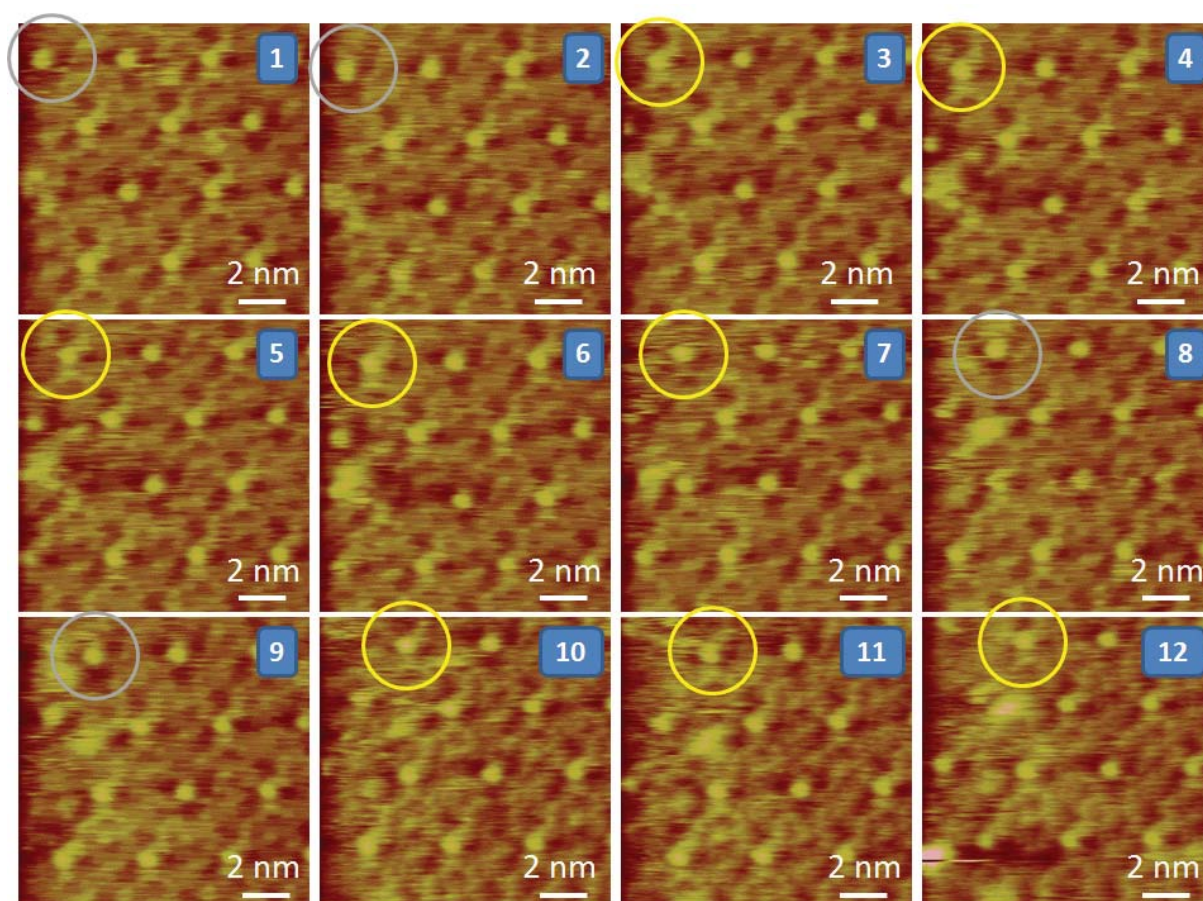


**Figure 5.2** Sequence of STM images showing the multiple 'up'/'down' contrast change of a single molecule of **C-12**;  $I_t = 9$  pA,  $V_t = 220$  mV. Grey circles correspond to the 'down' state whereas yellow circles highlight the 'up' state.

It needs to be underlined, that despite an extensive analysis of all STM data the only changes we could ever record are the 'up'/'down' dynamics. This is in agreement with the fact that there exist only two stable orientations of **C-12** molecules – driven by the azobenzene-azobenzene interactions. This observation remains consistent with the two alternative hypotheses, either rotation (by a multiple of  $60^\circ$ ) of the molecule, or desorption/re-absorption events - both too rapid to be recorded by our experimental setup.

Analogical situation of 'down' to 'up' contrast change of a single molecular site is depicted by Figure 5.3, with the only difference that due to the raster increase there is a time interval of 34s between each frames. One of the possibilities in this particular case is the fact of the presence of the step-edge at the left-hand side of the image. It often may cause the discontinuity of the monolayer and in consequence lower stability of the molecule at the boundary (decreased number of neighbors, and therefore the lower extent of stabilizing intermolecular interactions).

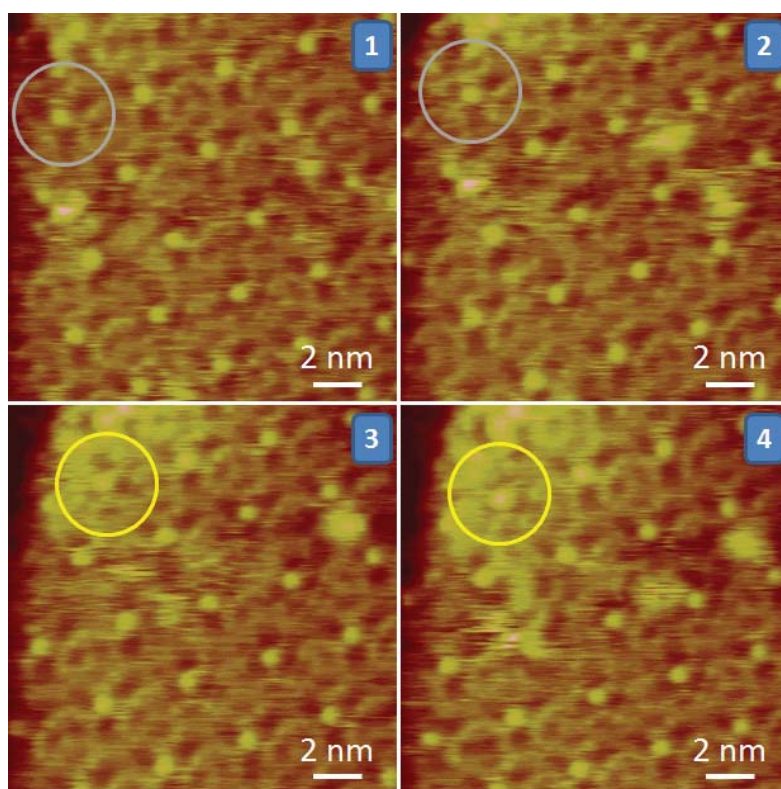


**Figure 5.3** Sequence of STM images showing the 'up'/'down' contrast change of a single molecule of C-12, possibly due to the fact that the adsorption site of the molecule is close to the step-edge, what may cause discontinuity of the domain. This may cause lower molecule stability on surface as a consequence of lacking of neighbors;  $I_t = 9$  pA,  $V_t = 220$  mV.

Figure 5.4 depicts another type of favorable circumstances for the observation of changes of the tunneling features. The molecule physisorbed in the top-left corner changes its contrast from 'down' to 'up', as a result of interaction with some diffusing molecule (either **C-12** or another chemical species), which presence is highlighted by the black arrow. The fuzzy area of occasionally bright contrast feature (see frames (3) and (8)), represents the molecule diffusing on the top of the physisorbed **C-12** monolayer. After residing in close proximity of the triphenylene core (frame (5)) the molecule diffuses away, and the clarity of the contrast is recovered. Finally, the physisorbed molecule, as a result of 'irritation' by the 'guest' molecule changes its contrast again (frame (9)).

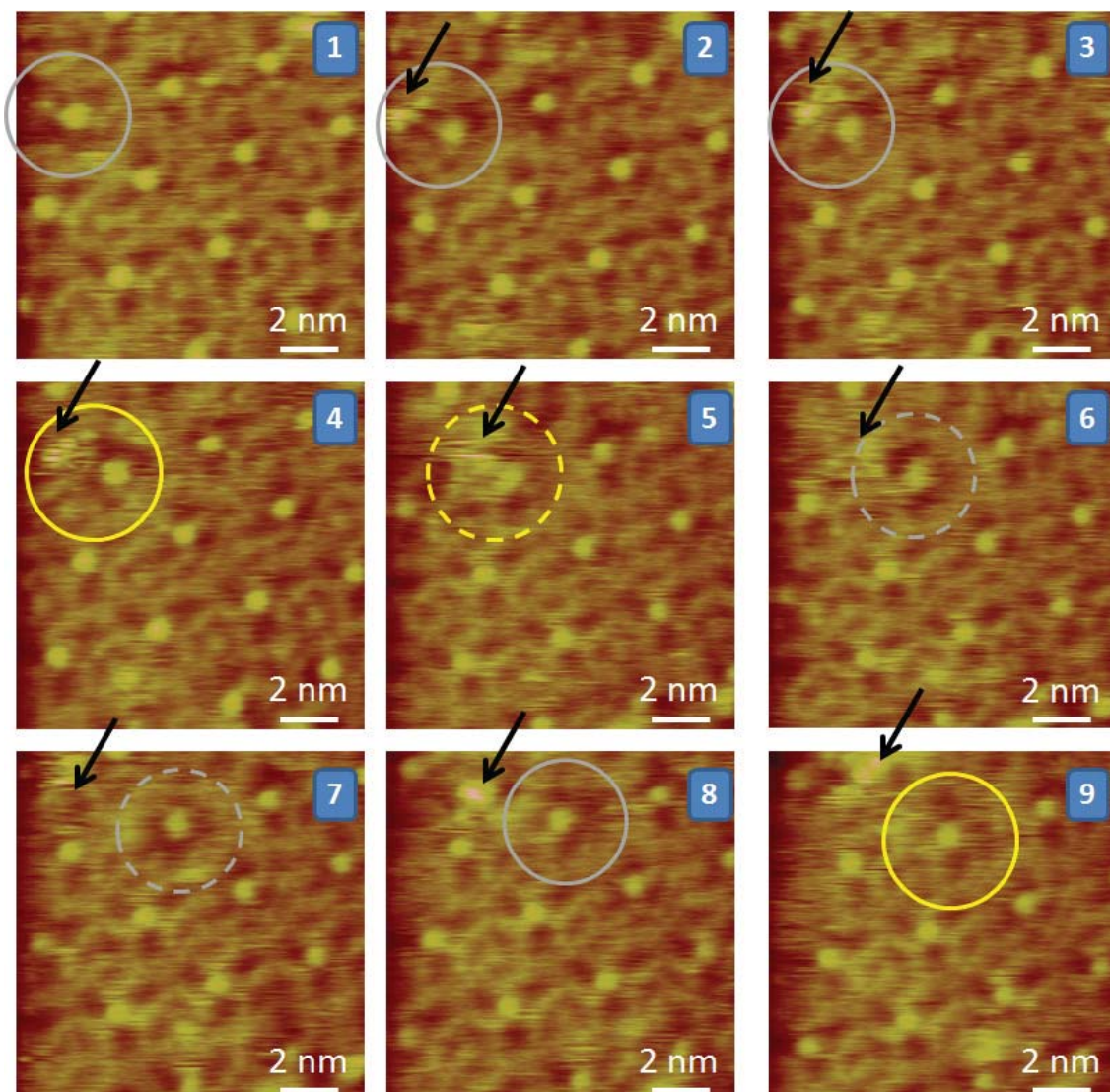


**Figure 5.4** Sequence of STM images showing the ‘up’/‘down’ contrast change of a single molecule of C-12 as a result of interactions with diffusing chemical species. After the intermediate period, when ‘up’/‘down’ contrast is ambiguous, the ‘guest’ molecule diffuses away;  $I_t = 10$  pA,  $V_t = 220$  mV.

### 5.3.2 Proposed mechanism of ‘up’/‘down’ contrast changes at the submolecular level

The previously discussed orientational changes of triangular features representing the central triphenylene core give a proof of the commonly known feature for the self-assembly at a liquid/solid interface, namely the inherent dynamics. The foregoing examples convey the message about the dynamics, but they do not decrypt it completely because the molecular motion in z-direction, e.g. desorption of a molecule from the monolayer into the solution and the adsorption of a molecule from the solution onto the same site, usually happens too fast to be noticed. Similarly any reorientation of the physisorbed molecule (translation or rotation) often occurs too fast to be captured by STM.

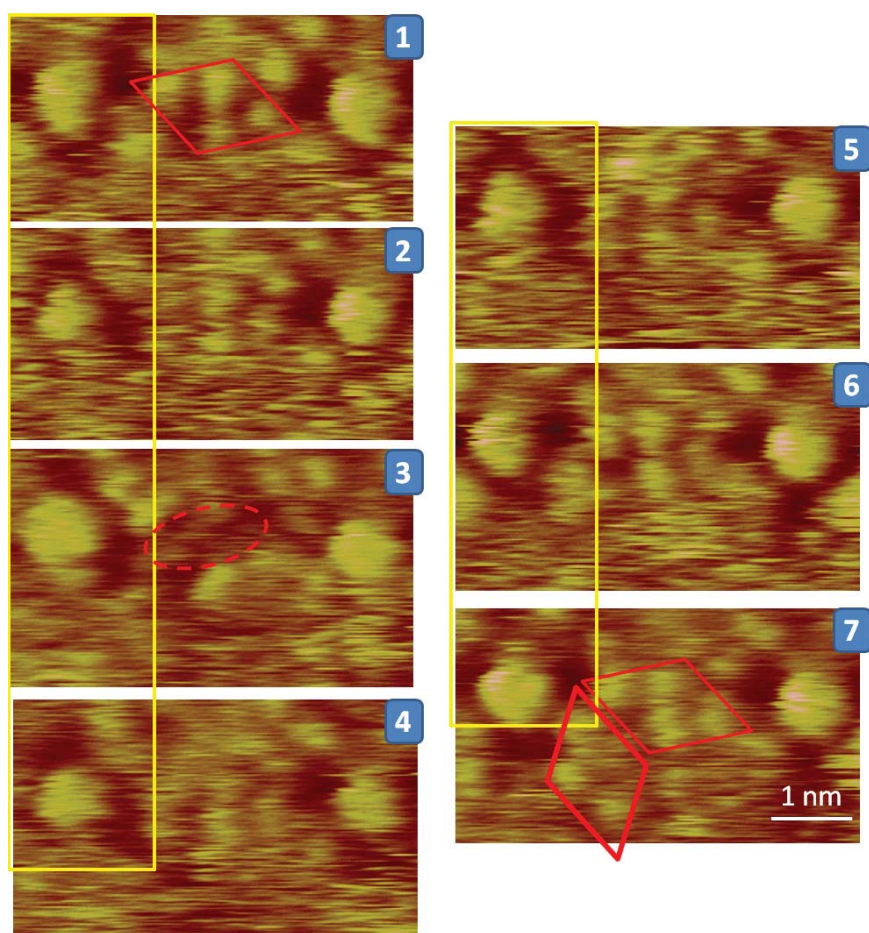


**Figure 5.5** Sequence of STM images showing the contrast changes of a single molecule of C-12 (left-hand side, highlighted in the yellow box) from ‘down’ to ‘up’ state and back. What shall be noticed is the blurring of the central area between two aromatic cores after the switching event, which is followed by disappearance of tunneling current features of the azobenzene group of switched molecule (*red-dashed oval* on frame (3)). Finally the system turns back to original state after the revert-switch - *red diamond* on frame (7). Time interval between subsequent images:  $\sim 15\text{s}$ ;  $I_t = 3.93\text{ pA}$ ,  $V_t = 315\text{ mV}$ .

Unlike the previous examples, Figure 5.5 shows a sequence of STM images with submolecular resolution, thus enabling a simultaneous observation of the dynamics of the triphenylene core and the tunneling contrast features originating from the azobenzene moieties. It should be underlined that, again, the dynamic behavior of the tunneling contrast occurs at the domain boundaries. Let us consider the molecule on the left-hand side (highlighted by a yellow frame). Its number of neighbors is smaller than for molecules inside the ordered domain, it is 4 which may be not sufficient to ensure the local stability of self-assembly. In contrast with previous examples the molecule is initially in ‘down’ state, being at the same time surrounded by molecules in ‘down’ state only. The interaction between two **C-12** molecules is well illustrated in frame (1). The cores of two molecules are aligned horizontally and they couple via well resolvable LL-type of azobenzene-azobenzene dimer, as

highlighted by the red parallelogram. The contrast features of the azobenzene groups and triphenylene cores are very clear and the latter show both 'down' state. Upon the scanning process the **C-12** molecule on the left-hand side changes the conformation of the central core, from 'down' to 'up'. The presence of both azobenzene moieties is still noticeable, so either the desorption/re-adsorption of 'new' molecule from the solution has happened, or the molecule that was originally residing the site has flipped by  $\pm 60^\circ$  forming a new antiparallel dimer. Clearly visible is the decrease of the smoothness of contrast in the inter-site area what suggests some local movements occurring. Frame (3) shows an interesting situation, since the resolution of the azobenzene dimer is evidently lost, and only the azobenzene group from the right-hand side molecule is imaged. The area occupied by the second azobenzene seems to be empty, as highlighted by the red oval shape, but the physical presence of the group cannot be excluded. However, a bright feature just on the left-hand side from the red oval suggests that the azobenzene is either decoupled from the surface or may have moved to the left, without desorption. During the two subsequent scans (frames (4) and (5)) coupling between left-hand side azobenzene and the right-hand side one takes place again, but still with some local movement, similarly to frame (2). It should be underlined that the observed movement occurs for the azobenzene units associated with the two interacting molecules, what suggests a decrease in the intermolecular interactions, and not a decrease of azobenzene-Au(111) interaction for the differently oriented azobenzenes. Following this reappearance of the azobenzene dimer, the **C-12** molecule on the left-hand side changes back its triphenylene core conformation from 'up' to 'down' (frame (6)). What finally happens on frame (7) is the reconstruction of the azobenzene coupling between both presented molecules associated with a well-defined STM contrast, suggesting strong immobilization of the dimer (red parallelogram). The additional interaction between the left-hand side **C-12** molecule and the neighbor residing below the investigated pair of **C-12** molecules becomes well-resolved as well (second red parallelogram). The neighborhood becomes better defined also if two molecules are both in down configuration as shown in frame (7) where, in addition, another azobenzene group is visualized and coupled with azobenzene moiety from below (vertical red rhombus). STM results suggest that the initial conformation of peripheral azobenzene groups (frame (1)) was possibly slightly disordered, avoiding accurate coupling between the **C-12** molecule and its neighbors. As a result, the molecule became more mobile, until efficient interactions with its neighbor could be finally established in frame (7). The final frame (7) contains no blurry regions, suggesting lack of the movement in the close proximity. This 'smooth' STM image and the stability of the structure suggest that the total of four azobenzene-azobenzene interactions may be sufficient for an average stabilization of **C-12** at the physisorption site for the homogeneous (all 'down' or all 'up') configurations with anyway some destabilization and induced dynamics being possible as shown in Figure 5.5.

We finally evidence that the azobenzene interactions tend to be more stable for two neighboring molecules in the 'up'-'up' or 'down'-'down' relation since they are observed to move less frequently. Moreover, lacking of 2 neighbors in the hexagonal mesh already allows for observation of dynamical behavior, contrary to e.g. case of six uniformly oriented (all-up/all-down) neighbors.

### 5.3.3 Conclusions on the dynamics of C-12 molecules on Au(111)

In conclusion, results from sections 5.2 and 5.3 demonstrate that dynamics has been observed between 'up' and 'down' states for **C-12** adsorbed on Au(111).

- This confirms that these two configurations are the stable ones, both associated with strong interactions between the neighboring molecules.
- The fact that dynamics has been observed for mixed domains ('up' and 'down' states) and in case of homogeneous domains for the molecules located at the domain boundaries, thus with a smaller number of neighbors, suggests that interactions between similarly oriented molecules is stronger ('up'-'up' or 'down'-'down') than for oppositely oriented molecules ('up'-'down'). This is confirmed by the intra-molecular observation of the lesser extent of movements for azobenzene dimers associated with similarly oriented molecules. Our results thus allow us to address the directionality of the hydrogen-like bonds between azobenzene units. We evidence a net decrease of interactions when the average angle between dipoles varies of an angle between 3 and 4°, and more importantly when the average distance between the N and H atoms establishing the hydrogen-like bond varies of a distance between 0.1 and 0.12 nm. It must be noticed that after an event leading to "up-down" interactions, the dimers may somewhat move (frames 4-5 of Figure 5.5), but look stabilized suggesting that strong enough interactions between neighboring azobenzene are preserved for distances of the order of 0.45 nm. This is also in agreement with the observations of stable networks with disordered 'up' and 'down' states (Chapter 4).
- Due to the scarcity of dynamics events, no statistical measurements are unfortunately available to estimate the corresponding energetically difference. We only show that in presence of 4 neighbors, the interactions between similarly oriented molecules become small enough to allow the energetical barrier associated with dynamics to be passed (Figure 5.5), similarly to the case of 6 neighbors with differently oriented molecules (Figure 5.2).
- All the presented observations of dynamic behavior of **C-12** do not allow to determine the nature of the molecular movements, desorption-adsorption of the molecule, or rotation by 60°. However, a number of previous observations of dynamics in 2D organic networks have been performed, but desorption has been evidenced for a part of the molecule only<sup>2</sup> and not for an entire, so large molecule, also in agreement with the expected large adsorption



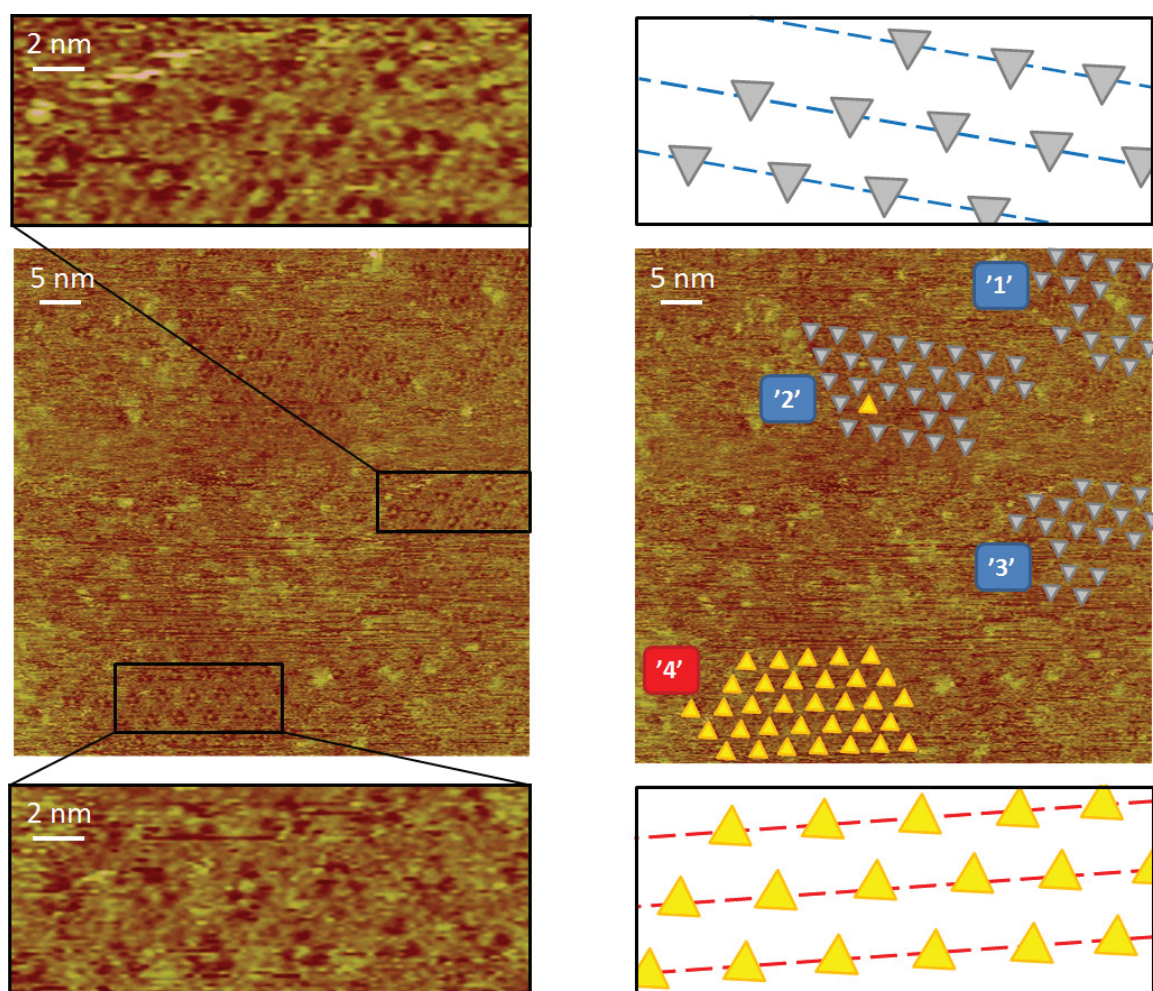
energy. Frame (3) of Figure 5.5 also evidences that after rotation of the molecule, desorption of the peripheral azobenzene is possible. On the other hand, displacement and/or rotation of molecules on graphite surface has been associated with confinement phenomena only<sup>2,3</sup>. We thus suspect surface confined phenomena as well for the **C-12** system and most probably simple rotation of the molecule by 60°. This kind of molecular rotation may appear difficult to the presence of the remaining peripheral parts of the molecules interacting with their neighbors. However, it appeared on graphite that this kind of movements of the entire molecules can occur despite the interactions with the neighbors, possibly due to intermittent desorption of the peripheral parts<sup>2,3</sup>.

#### **5.4 C-12 self-assemblies on Au(111) as a function of droplet concentration, role of inter-azobenzene interactions**

As already discussed in Chapter 4, the **C-12** molecules deposited onto Au(111) from the TCB solution form domains of hexagonal symmetry, which are oriented in two distinct directions with respect to the substrate crystallographic directions. The symmetrical deflection from Au<110> and thus mirror-like character has the origin in the formation of two types of *stable* azobenzene-dimers between the neighboring **C-12** molecules. In addition, the STM images that revealed the features of the central discotic motif – triphenylene – have evidenced that the inner part of the molecule is oriented similarly with respect to the substrate, regardless the molecular mesh orientation. Moreover the molecules in each domain are characterized by the interactions between neighbors, either ‘up’-‘up’ / ‘down’-‘down’, or ‘up’-‘down’. We now study the evolution of this last feature when the concentration of the droplet on top of the Au(111) has varied during the growth of the **C-12** molecular domains.

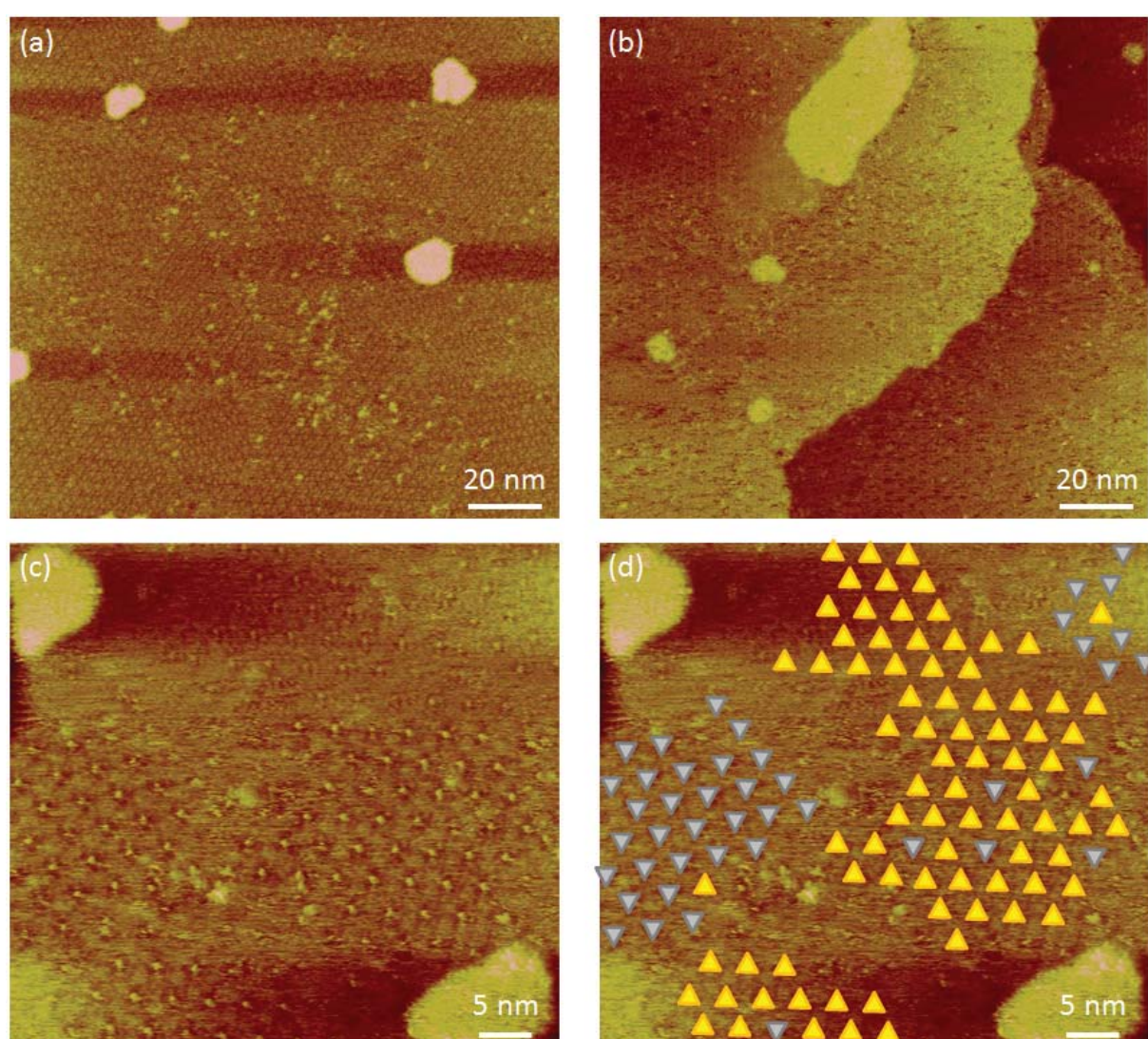
Figure 5.6 corresponds to the deposition of a droplet of **C-12** molecules at the TCB/Au(111) interface with the **C-12** concentration not precisely known but most probably higher than 1 mmol/L. The big image on the left-hand side shows the locally organized areas where the triangular features are clearly discernible. The three domains: ‘1’ in the top-right corner, ‘2’ in the central area of the upper half and ‘3’ on the right-hand side of the image consist of molecules in the ‘down’ state. The domain on the bottom consists of molecules in the ‘up’ state. For clarity reasons, the grey and yellow triangles are superimposed on image on the right-hand side. A straightforward observation is that the area of the sample depicted on the image is non-fully covered with the molecules of interest. This comes with the fact that the surface has been observed immediately after deposition. The four well-resolved domains are separated and do not form any boundaries. This gives an idea that most

possibly they were growing independently – starting from the respective 4 nucleation sites. The presented domains are small, however, they are all homogenous with respect to the orientation of the central core. The only small exception is one of the lattice nodes in the case of the domain '2' which represents the 'up' state, being surrounded by 'all-down' neighborhood. The depicted state where rather low surface coverage of **C-12** molecules takes place is often accompanied by the very high uniformity of orientation of molecules. As it will be shown in further part of this chapter, situation changes when certain experimental conditions are modified. For the larger self-assemblies of the molecules of **C-12** that normally consist of up to 50 molecules and still exhibit homogenous structures, occasionally only a single molecule-per-domain may be met in the opposite conformation. Statistically speaking we may say that (depending on the domain size), the homogeneity of structure is close to 1.00 and no values below 0.92 were found.



**Figure 5.6** (*left*) STM constant current images showing peculiar triangular contrast that originate from the double-bonded oxygen group of ester linker. Top and bottom close-ups show domains with 'all-down' and 'all-up' positions of physisorbed molecules, respectively. (*right*) The same image with grey and yellow triangles superimposed in the lattice nodes of each domain according to tunneling contrast. The insets show the respective packing of C-12 molecules in domains '3' and '4';  $I_t = 15$  pA,  $V_t = 250$  mV.

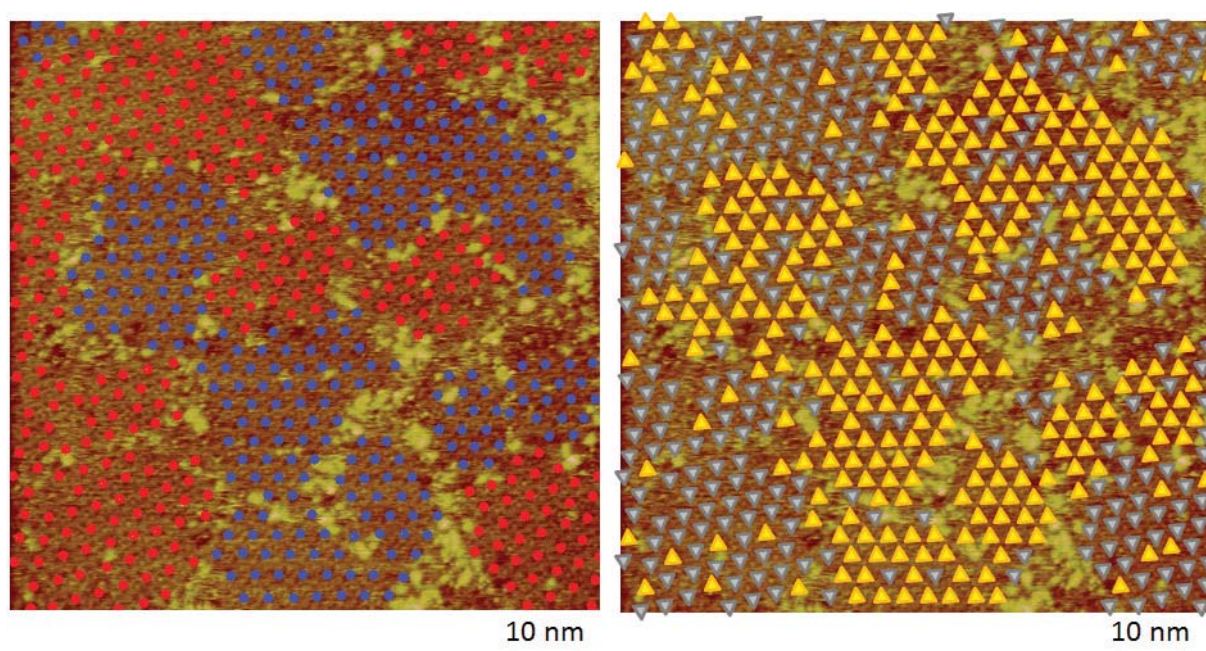
After preparation of a standard solution ( $C_1$ ) of **C-12** in TCB and following the regular procedures of the preparation of the Au(111) substrate and the solution deposition (please refer to the *Experimental section*), the resulting output of the self-assembly slightly changed. As may be seen on Figure 5.7, a more complete coverage of the scanned area was achieved – in comparison to the situation presented by Figure 5.6. Molecules tend to form self-assemblies extending on a single Au(111) terrace, as depicted by Figure 5.7(b). Even though the substrate contains more of the local imperfections (i.e. brighter islands) it is hard to find areas where the presence of hexagonal pattern is not manifested. It can be concluded that the prepared standard solution assures an optimal concentration of molecules to extensively cover the surface of the sample, for the deposition procedure applied.



**Figure 5.7** STM constant current images showing complete coverage of C-12 at the TCB/Au(111) interface, and remaining tendency to form rather uniform domains (homogeneity factor  $\sim 0.94$ ); (a)  $I_t = 17$  pA,  $V_t = 250$  mV; (b)  $I_t = 10$  pA,  $V_t = 250$  mV; (c) and (d)  $I_t = 18$  pA,  $V_t = 250$  mV.

Performing analogical analysis of the ‘up’/‘down’ states of physisorbed molecules, results in the average homogeneity within the domains on the level of  $0.94 \pm 0.01$ . This result suggests the presence of some point imperfections, however, uniformly oriented molecules are still observed, both: for small domains (less than 20 lattice nodes), but also for those intermediate (between 20 and 50 lattice nodes). Slightly bigger domains, i.e. those exceeding 50 molecules, give similar value of the average homogeneity degree. In overall, for analysed ca. 600 molecules from 3 different samples, the weighted average does differ slightly only from the arithmetic average – 0.9372 vs 0.94, what suggests that the size of the domain does not drastically influence the extent of the appearance of a site of ‘mistaken’ orientation within the self-assemblies of **C-12**.

Since concentration of chemical species is one of the primary parameters regarding the investigations of both kinetic and thermodynamic factors of the adsorption phenomena for a specific adsorbate-adsorbent system, we decided to dilute our standard solution by a factor of 5 (solution C<sub>2</sub>). The sample preparation and experimental conditions applied were similar in every respect to the previous experiments, however, deposition of the diluted solution has changed significantly the homogeneousness of resulting **C-12** self-assemblies.



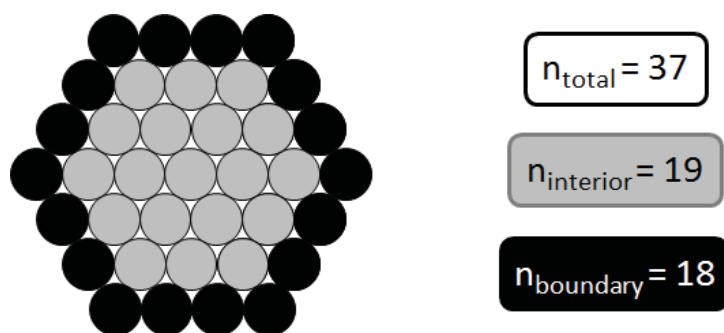
**Figure 5.8** STM image showing the decreased correlation between the domain orientation (*left*: red/blue colors in the lattice nodes) and the orientation of the core-part of the molecule (*right*: grey/yellow triangles pointing downwards or upwards, respectively). The mapping between the two properties results in the agreement of a factor of 0.8;  $I_t = 9 \text{ pA}$ ,  $V_t = 150 \text{ mV}$ .

Figure 5.8 is an illustrative example for the analysis of the conformational uniformity within the domains and the correlation between the mesh orientation (*left*) and the central core orientation (*right*). STM image on the left-hand side shows 18 domains, highlighted by red and blue colors to distinguish their different orientation with respect to the underlying Au(111). Those domains cover almost the whole STM image, locally only being separated by brighter irregular areas. The total amount of clearly resolved molecular sites equals 633 and 315 of that falls into red domains and 318 falls into blue domains. This again should support the equality of both types of domains and their mirror-like character.

When looking at the right-hand side image, easy to notice is the decrease in the uniformity of orientation within each domain, and the whole image appears less homogenous than the left one. In other words there is now a non-negligible number of 'up'-'down' neighbors in each ordered domains. Surprisingly, extensive analysis of the image suggest, that it is almost equally likely (0.47 vs 0.53) for the counter-oriented triphenylene core to occupy the interior of the domain, and the domain boundary site, where the influence of the neighboring domains may play a role. Let us make a few simple assumptions to evidence that in fact the presence of 'up'/'down' interactions does not depend strongly on the closest lateral environment. In other words we would like to show that it does not play a role if the molecule occupies a lattice node at the boundary or at the interior of the 2-D crystal. First of all, taking into account the average domain size for presented experimental data, which equals  $>35.2$  molecular sites,<sup>1</sup> one may construct a hexagonal mesh related in number of lattice nodes to this average value. Figure 5.9 depicts the simplest possibility, where symmetric 2-D crystal contain in total 37 lattice nodes, out of which 18 are the boundary nodes and the remaining 19 are the interior sites - depicted by black and grey circles, respectively. Presented shape is the only one where the number of interior sites exceeds the number of boundary sites, and consequently any change in shape of the domain containing this fixed number of lattice nodes creates a situation where boundary sites become majority. Thus, assuming numerous smaller domains ( $n_{\text{total}} < 37$ ) and bigger domains of elongated or irregular shape – for which  $n_{\text{interior}} < n_{\text{boundary}}$ , we would expect to observe significantly more 'up'/'down' interactions at the domain boundaries. Since our analysis suggests that it is not the case, we may deduce that the inhomogeneity in the 'up'/'down' state is probably not dependent on the adsorption site.

---

<sup>1</sup> In fact it is slightly bigger than this value, since some of the domains are not fully depicted.



**Figure 5.9** Schematic representation of the most symmetrical packing of hexagonal mesh, related in size to the average domain size.

Another dilution by a factor of 5 (i.e. dilution of the standard solution by  $5^2 = 25$ , solution  $C_3$ ) results in further decrease of homogeneity of orientation of triphenylene cores within the physisorbed domains. Situation is well depicted by the Figure 5.10, which presents the STM image with the superimposed color-coded symbols, analogically to the previous –  $C_2$  case.

Figure 5.10 shows the area of size comparable to the previous sample, i.e. the one prepared from drop casting of  $C_2$  solution (Figure 5.8). The number of characterized domains is equal to 20 (vs 18 in the  $C_2$  case), and the total number of characterized lattice nodes is also approximate, 618 (vs 633 in the  $C_2$  case). Likewise, partition between the two types of domain orientations (red and blue colors) is close to be identical (0.49 and 0.51 for blue and red domains, respectively). However, what really differs is the extent of ‘up’/‘down’ interactions within the domains of **C-12**. While for the more concentrated samples the analysis of the ‘up’/‘down’ interactions resulted in values as high as 0.94 for ‘up’-‘up’ of ‘down’-‘down’ (in the case of standard  $C_1$  solution) and 0.8 (for the  $C_2$  solution diluted in the ratio 1:5), further dilution by 1:5 ratio results in decreasing at the level of 0.67. It simply means that statistically 1 over 3 molecules within each domain adapts the neighboring orientation opposite to the remaining two molecules. As in the previous cases, weighted value gives similar result, since there does not exist a monotonic trend relating the homogeneity factor to the number of molecules within 2-D crystal (in the studied range of domain sizes). A more global view on the intra-domain homogeneity as a function of domain size is shown on Figure 5.11. For each of the three concentrations under study one may find a set of rather non-monotonic data, oscillating in the range of  $\langle \text{average value} \rangle \pm 0.1$ .

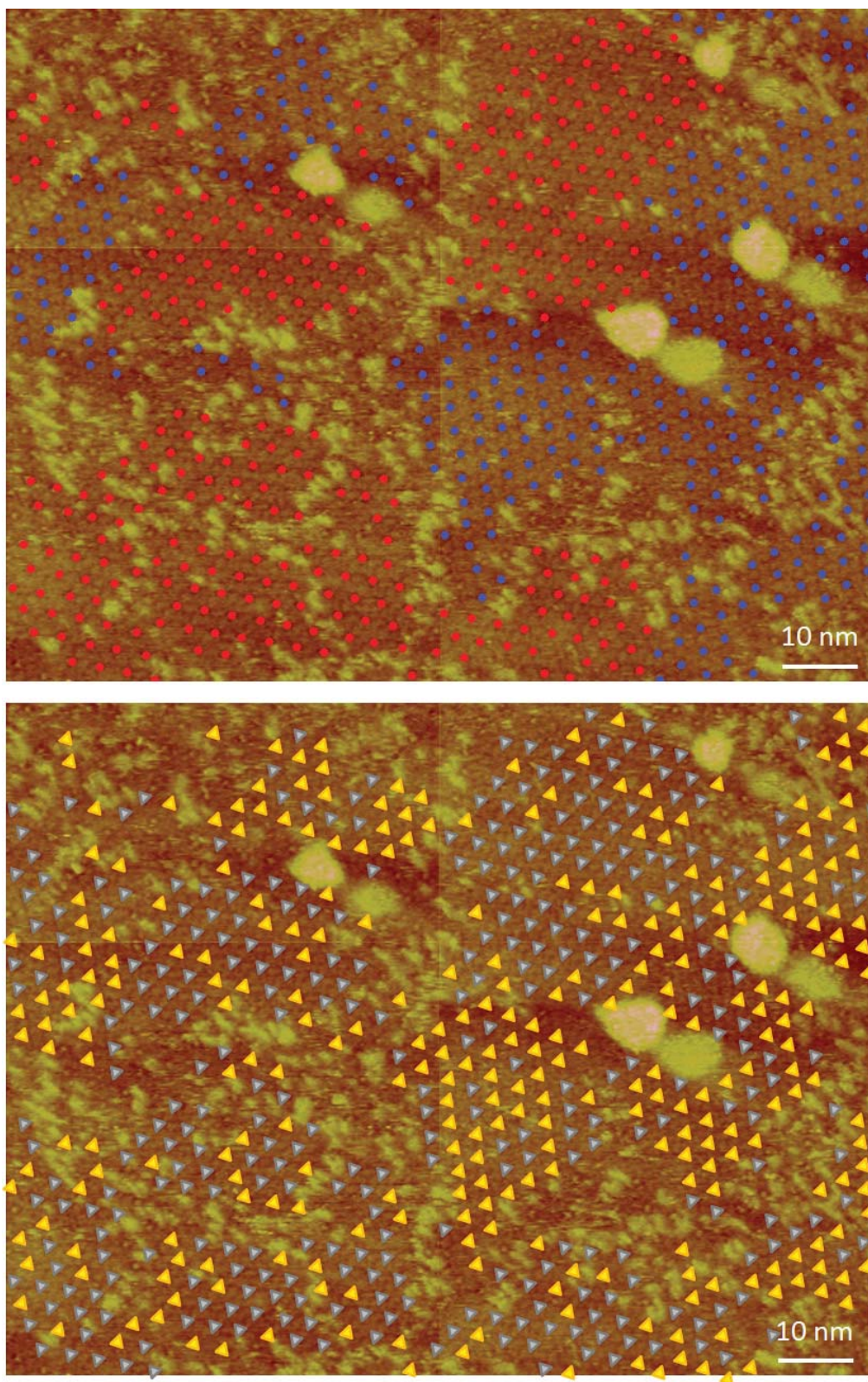


**Figure 5.10** STM image showing further decrease in correlation between the domain orientation (*top*: red/blue dots in the lattice nodes) and the orientation of the core-part of the molecule (*bottom*: grey/yellow triangles pointing downwards or upwards, respectively). The mapping between the two properties results in the agreement of a factor of 0.67;  $I_t = 11$  pA,  $V_t = 250$  mV.

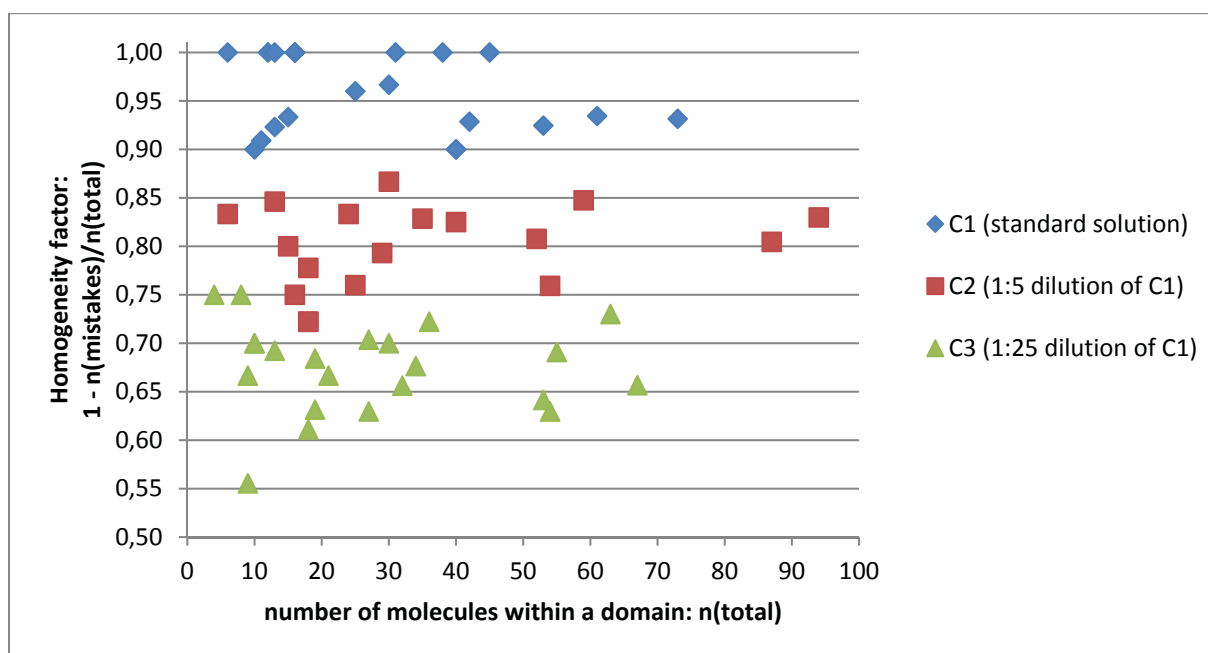


**Figure 5.11** The plot showing the relation between homogeneity of the domain (in terms of number of ‘up’-‘up’ or ‘down’-‘down’ orientations) and its size, for a series of concentrations of **C-12**. The three horizontal regions may be distinguished that correspond to the most concentrated (blue data points), intermediate (red data points) and least concentrated (green data points) solutions.

When the three sets of data points are combined, as on the Figure 5.11, it is straightforward to notice that each of them covers some limited region in y-range, which is weakly (if at all) dependent on the domain size. Moreover, the overall set of data suggests invariant behavior of the system in the studied concentration range. Picking any x-value (domain size) and drawing a vertical line upwards, one would always find a sequence of data points of monotonically increasing concentration of **C-12**. We may conclude, that decreasing the concentration of the molecules of interest, results in the formation of self-assemblies of less uniform internal structure. However, this statement cannot be generalized at this point, because of the limited range of domain sizes that we investigated (up to 100 lattice nodes).

## 5.5 Conclusions

In conclusion, our results confirm what we observed in Chapter 4 already, i.e. the energetical differences between the situation where interacting **C-12** molecules display similar molecular orientations (‘up’-‘up’ or ‘down’-‘down’), compared to the situation where interacting **C-12** molecules display the opposite orientations (‘up’-‘down’). The size of the average domain is not



modified when the concentration of the **C-12** solution is changed, and the distribution between  $\alpha$  and  $\beta$  domains remains similar as well. The only difference is the change in the local order. The number of 'up'-'down' interaction increases with respect to the 'up'-'up' or the 'down'-'down' ones when the concentration decreases. This effect of the concentration has an influence on the growth of the domains, which means that with this specific **C-12**/Au(111) system we can study how an ordered network is built, when two intermolecular interactions are possible, which are slightly only different in terms of the energy.

We can first observe that the size of the domains is very small and definitely smaller than the size of the domains formed by triphenylene molecules such as H5T (see Chapter 3). The small size of the domains suggests that, once adsorbed, the **C-12** molecules move to a smaller extent than H5T ones, which is in agreement with their larger size and with a larger interaction with the substrate. If we consider the droplet concentration as playing the same role than a molecular flux during UHV experiments, our results are surprising. We would indeed expect a more disordered state with large concentration than with small concentrations, whereas the contrary is observed. Our results can finally be associated with a characteristic distance on the substrate corresponding to the mobility of the molecules when they become adsorbed. It would be of the order of the average size of domain, in other words 17 nm (square root of the average domain size, 286 nm<sup>2</sup>). We thus don't expect a variation of this mobility with the droplet concentration. On the other hand, our results also suggest that a characteristic time of mobility for adsorbed molecules, once adsorbed and in intermolecular interaction, could be defined and associated with the rotational mobility of the molecules. Since a larger number of molecules are expected to be adsorbed by unit of time for higher concentrations, the ordered orientation leading to a more stable structure could be found for large concentration and not for small concentrations. This reasoning would imply that, in order to create ordered networks, the coordinated mobility of all the molecules together would be necessary. It would be achieved for large concentrations and not for small concentrations.

In order to test these ideas and to obtain quantitative values of the relevant parameters, in particular regarding differences between the two possible intermolecular interactions compared here, it would be useful to confront a theoretical model to our experimental data. It is thus one of the perspectives of this work. Obtaining the evolution of the interaction energy for azobenzenes of varying orientation would indeed be useful in order to more completely describe the specific interaction, namely the hydrogen bonding between azobenzene dimers, these interactions being possibly involved in a number of other 2D structures.

## 5.6 Experimental section

### 5.6.1 Materials

**Analyte.** C-12 and was synthesized and characterized by Prof. Kingo Uchida and his team within the Department of Materials Chemistry, University of Ryukoku (Otsu, Japan).

**Solvent.** The standard solution was prepared by dissolving of C-12 in 1,2,4-trichlorobenzene (Sigma Aldrich, pure >99%, used as received) with a concentration of 1.0 mmol/L. Solution was heated up to  $\sim 70^\circ\text{C}$  for 15 min prior to deposition onto the substrate.

**Substrate.** The Au(111) substrates were purchased from Neyco (Structure Probe, Inc. supplier for France). The raw samples consisted of mica plates of thickness between 50 and 75  $\mu\text{m}$ , onto which thin ( $\sim 100$  nm) layer of gold has been evaporated.

**Probe.** The STM tip was mechanically cut from a Pt/Ir wire (90/10 wt%) that was purchased from Goodfellow SARL. During the measurements the STM tip was immersed in the droplet of solution.

### 5.6.2 Sample preparation

A crucial step for ensuring the most favorable conditions for the self-assembly of molecules into the physisorption-driven monolayer is preparation of a high quality surface, i.e. composed of atomically flat terraces of large size (1000's of  $\text{nm}^2$ ). The procedure of preparing of Au(111) consist normally of short ( $\sim 1$  min) flame annealing in a hydrogen or propane gas flame. The latter one has been used for experiments described in this thesis. The gently heated ( $\sim 70^\circ\text{C}$ ) solution of H5T has been deposited onto freshly flamed Au/mica sample, straight after the flaming process was ceased.

### 5.6.3 Equipment: scanning tunneling microscope

The monolayers were investigated using a commercial STM equipped with a low current head (Veeco, Digital Instruments, Inc. USA). For each monolayer, several STM-images recorded in constant current mode with current ranging from 1 to 100 pA and tip bias from  $\pm 100$  to  $\pm 1000$  mV were obtained with different samples and tips to check reproducibility and to ensure that results are free from artifacts. All STM images presented here were recorded under ambient conditions without any further image processing.

## 5.7 Acknowledgments

Prof. Kingo Uchida, (Ryukoku University, Japan), is gratefully acknowledged for the supplying of C-12 material of good purity. Dr. Alexandr Marchenko (Institute of Physics, National Academy of Science of Ukraine, Kiev, Ukraine) is acknowledged for many fruitful discussions on the STM data.

## 5.8 References

1. Mulder, A.; Huskens, J. & Reinhoudt, D. N. *Org. Biomol. Chem.* **2**, 3409–3424 (2004).
2. Xu, H.; Minoia, A.; Tomovic, Z.; Lazzaroni, R.; Meijer, E. W.; Schenning, A. P. H. J. & De Feyter, S. *ACS Nano* **3**, 1016–1024 (2009).
3. Schull, G.; Douillard, L.; Fiorini-Debuisschert, C.; Charra, F.; Mathevet, F.; Kreher, D. & Attias, A.-J. *Nano Lett.* **6**, 1360–1363 (2006).
4. Schull, G.; Douillard, L.; Fiorini-Debuisschert, C.; Charra, F.; Mathevet, F.; Kreher, D. & Attias, A.-J. *et al. Adv. Mater* **18**, 2954–2957 (2006).
5. Miwa, J. A.; Weigelt, S.; Gersen, H.; Besenbacher, F.; Rosei, F. & Linderoth, T. R. *J. Amer. Chem. Soc.* **128**, 3164–3165 (2006).
6. Weckesser, J.; Barth, J. V. & Kern, K. *J. Chem. Phys.* **110**, 5351–5354 (1999).
7. Berner, S.; Brunner, M.; Ramoino, L.; Suzuki, H.; Guntherodt, H.-J. & Jung, T. A. *Chem. Phys. Lett.* **348**, 175–181 (2001).
8. Wintjes, N.; Bonifazi, D.; Cheng, F.; Kiebele, A.; Stöhr, M.; Jung, T.; Spillmann, H. & Diederich, F. *Angew. Chem. Int. Ed.* **119**, 4167–4170 (2007).
9. Wahl, M.; Stöhr, M.; Spillmann, H.; Jung, T. A. & Gade, L. H. *Chem. Commun.* 1349–1351 (2007).
10. Lingenfelder, M.; Tomba, G.; Costantini, G.; Colombi Ciacchi, L.; De Vita, A. & Kern, K. *Angew. Chem. Int. Ed.* **46**, 4492–4495 (2007).
11. Scherer, L. J.; Merz, L.; Constable, E. C.; Housecroft, C. E.; Neuburger, M. & Hermann, B. A. *J. Amer. Chem. Soc.* **127**, 4033–4041 (2005).
12. Barth, J. V. *Annu. Rev. Phys. Chem.* **58**, 375–407 (2007).

## Chapter 6

### Cholesteric liquid crystal droplets: three-dimensional confinement of chirality

This chapter provides a brief introduction to the subject of dispersions of calamitic (rod-like) liquid crystals, where in particular a thermotropic liquid crystal plays the role of the dispersed phase. As it is presented by extensive literature synopsis, recent years have shown a significant increase of interest in the liquid crystals dispersions. Starting from the simplest confined systems, namely nematic liquid crystal droplets, the following steps constitute of differentiating the effects of varying boundary conditions and the influence of external electric and magnetic fields. A special attention is focused on the cholesteric (chiral nematic) liquid crystal droplets and the different expressions of chirality in those confined systems, depending on the *geometrical confinement* parameter. The macroscopically detected expression of chirality, as a main foundation for the subsequent chapter, is described for previously studied systems both at the equilibrium and where the cholesteric pitch is varied, e.g. as a result of temperature changes. The presented basic research examples should stimulate the research in the newborn area of *soft photonics*.

## 6.1 Introduction to thermotropic liquid crystals of rod-like molecules

In Chapters 2 to 5, the main subject of interest were monolayers of different discotic molecules, which in bulk exhibit a tendency to form mesophases (e.g. columnar mesophases). The molecular shape of those building blocks is a reason why they are normally called discotic liquid crystals. However, the group of discotic molecules possessing mesomorphic properties is rather small in comparison to the totality of mesogenic materials. In fact, the discovery of liquid crystals and majority of research down to the present day is connected with mesophases which constitute of molecular building blocks of elongated (rod-like) shape. Also the most numerous group of thermotropic liquid crystals is represented by the molecules of rod-like shape, which are alternatively called *calamitic* mesogens. According to nomenclature proposed by Friedel<sup>1</sup> they are classified in three subgroups: nematic, cholesteric and smectic liquid crystals.

The nematic liquid crystals exhibit high degree of long-range orientational order of the mesogens, but no long-range translational order. The difference between nematic phases and isotropic liquid is that the former case the molecules are spontaneously oriented with their long axes approximately parallel (i.e. pointing the direction of a pseudovector – *director n*). The preferred direction that the molecules long-axis points varies locally in the medium, but a uniformly aligned specimen is optically uniaxial, positive and strongly birefringent.

The cholesteric mesophase is the special type of nematic liquid crystal, formed exclusively by optically active molecules. As a consequence the structure acquires a spontaneous twist about an axis normal to the preferred molecular directions. The twist may be right-handed or left-handed depending on the molecular conformation, and is the origin of the other name for cholesterics - chiral nematics. Optically inactive species or racemic mixtures result in a helix of infinite pitch which corresponds to the true nematic.

The smectic state is another distinct type of mesophase of liquid crystal substances. Molecules in smectic phase show a degree of translational order not present in nematics. In the smectic state, the molecules maintain general orientation order of nematics, but additionally align themselves in layers or planes. Motion is restricted to occur within these planes, and separate planes are observed to flow past each other. Hence this mesophase has fluid properties, though it is much more viscous than the nematic, and such enhanced 'solid-like' behavior is a result of increased self-organization. Interesting remains the fact, that many compounds are observed to form more than one type of smectic phase, of which as many as 12 have been identified. Some of them (e.g.  $S_B$ ,  $S_E$ ,  $S_G$ ,  $S_H$ ,  $S_J$  and  $S_K$ ) have a three-dimensional long-range positional order as in a crystal, though with very weak interlayer forces and hence energetically weak interlayer ordering, while some others, referred to as hexatic phases, have three-dimensional long-range bond-orientational order, but without any long-range positional order.

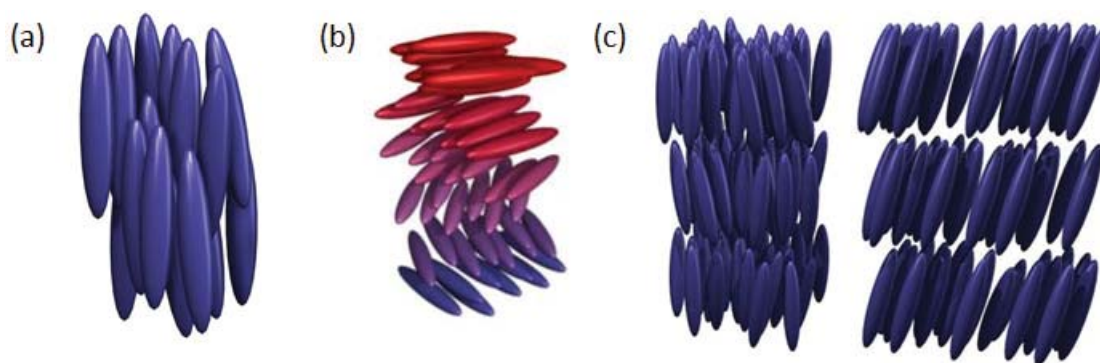


**Figure 6.1** Representation of (a) nematic mesophase, (b) cholesteric (chiral nematic) mesophase and (c) smectic A and C mesophases - the mesophases formed most often by calamitic mesogens.

Liquid crystals in general possess two inherent, but rather contradictory features: structural order (that is mostly of orientational type) and dynamics (i.e. fluidity). The first feature that is a reason of birefringence gives the opportunity of observing beautiful liquid crystalline textures under the Polarized Light Microscope (PLM), alternatively named Polarizing Optical Microscope (POM). Most of the previous experimental investigations on liquid crystals presented in this chapter and in the next chapter were done with the use of PLM.

### 6.1.1 Chirality induction in nematic liquid crystals by doping with chiral dopants

Almost one century ago Friedel have proved that addition of a small amount of chiral non-racemic solute converts a nematic liquid crystal into a cholesteric liquid crystal.<sup>1</sup> The chiral dopant needs to be soluble in the nematic matrix, in order to be able to induce a twist distortion which leads to the appearance of the helical structure. The twist distortion depends on the chemical structure and absolute configuration of the dopant molecule. At low dopant concentrations, the reciprocal of cholesteric pitch increases linearly with the amount of enantiomerically pure dopant. The rate of change between those two properties determines a specific value for each dopant/nematic host system. Qualitatively speaking, effective induction of cholesteric twist is characterized by the parameter called the ‘helical twisting power’ ( $\beta_M$ ), which describes the ability of a chiral dopant to twist a nematic host, and is expressed by the following formula:

$$\beta_M = \frac{1}{P c ee} \quad (1)$$

where  $P$  is the pitch induced by the chiral dopant,  $c$  is its concentration and  $ee$  its enantiomeric excess. The sign of HTP is positive for a right handed cholesteric helix and negative for a left-handed one.

### 6.1.2 Photo-responsive chiral liquid crystals

One possibility to create a chiral liquid crystal system that is stimuli-responsive is to dope a nematic liquid crystal with a molecular photochromic switch. Photochromic switches are molecules that can be interconverted reversibly between two distinguishable states by light, often one of them is a metastable state. The incorporation of photochromic switches in the liquid crystalline host offers the possibility of controlling the supramolecular chirality of the liquid crystal using light. A very interesting property of some photo-responsive liquid crystals is the possibility of undergoing the helix inversion. The necessary condition for the occurrence of helix inversion is the existence of two states of the photochromic dopant that induce the opposite cholesteric helices. Moreover, the photostationary state needs to be in favor of the unstable isomer to let it express its presence.

Numerous investigations based on doping nematic liquid crystals with chiral photo-responsive dopants have evidenced the controllable pitch modifications in cholesteric liquid crystals.<sup>2</sup> For example, overcrowded alkenes are chiral and photo-responsive molecules promoting photo-inversion of the cholesteric helix when used as dopants: the helical twisting powers of their stable and *meta*-stable forms have opposite signs, which results in the opposite handednesses of the cholesteric helix at the stable state and at the photostationary state. In addition, the overcrowded alkenes often exhibit high values of helical twisting power of both isomeric forms, what ensures a large photoinduced variation of the cholesteric pitch even at low dopant concentration. More details about those compounds, including the schematic helix inversion will be presented at the beginning of Chapter 7, which is devoted to studies of CLC droplets doped with overcrowded alkenes.

Due to the fact, that synthesis and purification of overcrowded alkenes is not an easy task, researchers have investigated the possibility of using other classes of chemical compounds as photo-switchable chiral dopants. In fact, switching mechanism of most of those molecules is based on the *cis-trans* isomerization. Some of the examples of molecular structures are presented on Figure 6.2. The symmetrical and non-symmetrical molecular switches shown on panels (a) and (b) represent the binol-based azobenzene chiral dopants, that were shown to provoke light-induced helix inversion of respective CLC mixtures in E7 and ZLI-2359 nematic hosts.<sup>3,4</sup> The  $\alpha,\beta$ -unsaturated ketone molecule presented on Figure 6.2(c) was reported to drive a photoinduced cholesteric helix inversion in the liquid crystal 5CB.<sup>5</sup> The same host was used to dope with a chiral azobenzophenone derivative (panel (d)), in order to show a reversible helix inversion.<sup>6</sup> However, a drawback of azobenzene derivatives is generally pointed in the current literature and lies in their lack of thermal stability.<sup>7</sup> As a result, the research in the area of synthesizing of new chiral and photo-switchable dopants allowing helix inversion, especially possessing high helical twisting powers, remains an ongoing challenge.

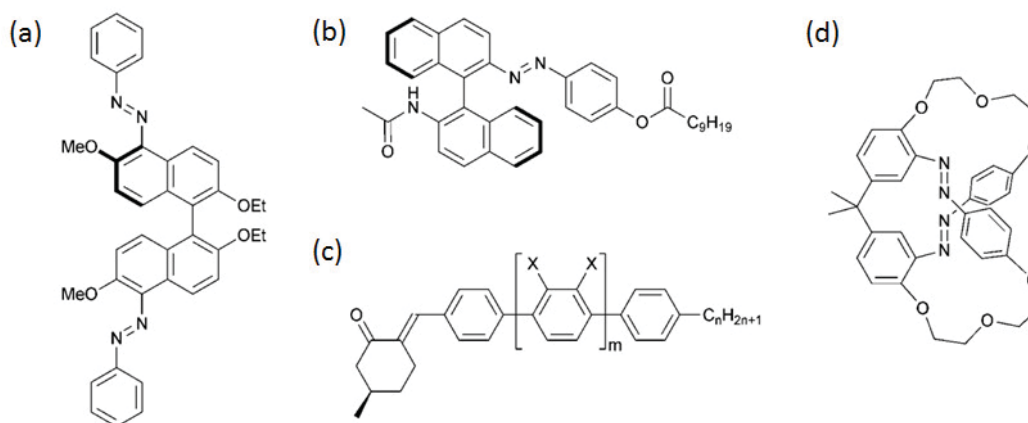


**Figure 6.2** Examples of photo-responsive azobenzene-based dopants promoting helix inversion in cholesteric liquid crystals (from Ref. 7).

### 6.1.3 Polarized Light Microscopy (PLM)

Polarized Light Microscopy (PLM) is said to be one of the 3 basic techniques for scientist dealing with liquid crystals.<sup>8</sup> The remaining two are: Differential Scanning Calorimetry (DSC) and X-ray diffraction (XRD). While the DSC merely provides information on phase transition temperatures, the X-ray studies help to determine the actual structure of the phase of the sample. Polarized Light Microscopy on the other hand can give information of both: phase transition temperatures and phase type. This is achieved by temperature dependent texture investigations between crossed polarizers.

In general, Liquid Crystals are optically anisotropic media, what simply means that their optical properties depend on the direction within the medium. The optical properties of a material can be visualized using a geometrical representation of the dielectric tensor, known as the index ellipsoid. The intercepts of the ellipsoid surface with its three principal axes give the principal refractive indices of the medium. This index ellipsoid would become a sphere for an isotropic system, so one in which the properties are independent on the direction (e.g. 'regular' isotropic liquid).

Most commonly, liquid-crystalline phases are optically uniaxial (in other words: they have one optic axis), what means that they have two principal refractive indices: the ordinary and the extraordinary refractive index, denoted  $n_o$  and  $n_e$ , respectively. The index ellipsoid in this case is an ellipsoid of evolution. Both cases are depicted by Figure 6.3. An anisotropic uniaxial material can be either uniaxial positive or uniaxial negative. The former case occurs when the value of  $n_o$  (the refractive index of the light propagating along the optic axis) is lower than that of  $n_e$  (the refractive index of the light propagating perpendicular, but with polarization parallel, to the optic axis). The



latter case, met very often in discotic LC phases like nematic and columnar, is characterized by  $n_o > n_e$ , which makes the index ellipsoid oblate. This feature gave the first commercial application of discotic liquid crystals, as films for the optical compensation of LC displays.<sup>9</sup>

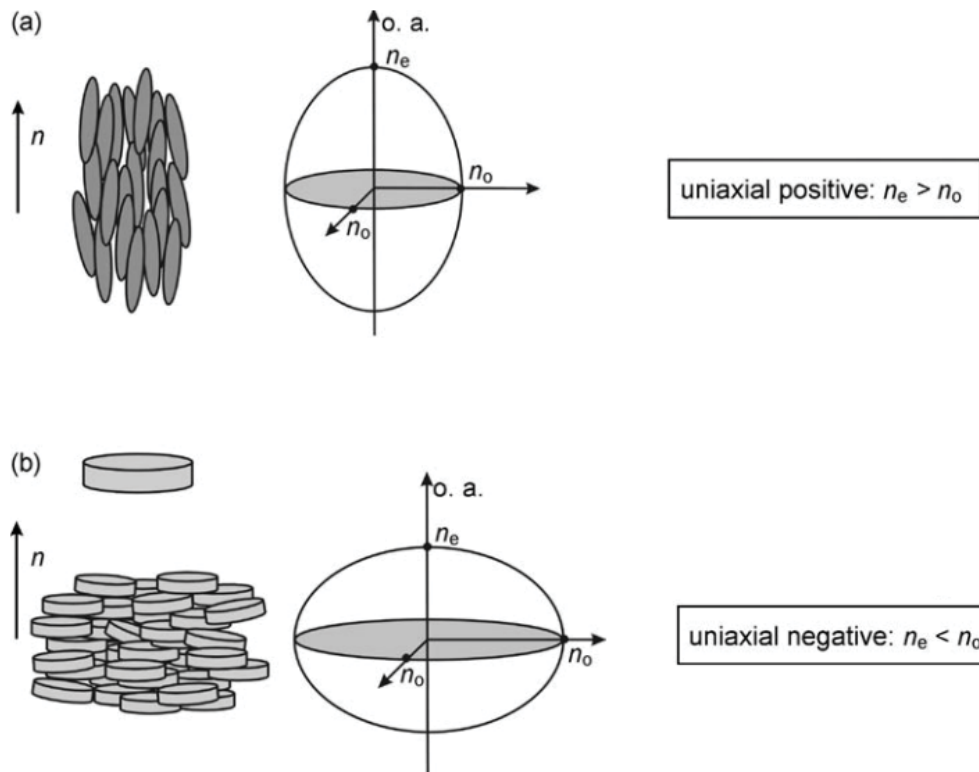


**Figure 6.3** Index ellipsoids for uniaxial positive (a) and negative (b) liquid crystals (from Ref. 10).

A typical Polarized Light Microscope is shown on Figure 6.4. The setup consists of a light source - generally a halogen light bulb emitting white light. The light is reflected upwards by a mirror, passes through a lens, and is linearly polarized by a polarizer, which can often be rotated by  $360^\circ$ . Optionally, having a white light as source, an optical filter may be inserted in this place, if wavelength dependent experiments will be performed. Then the light enters the condenser that collects the light from the source and assures uniform illumination of the sample. Transmitted light passes into an objective and follows to the analyzer - a second polarizer that is often rotatable. Afterwards image is usually splitted on a prism to be observed by charge-coupled device (CCD) camera mounted or by the ocular. For the texture studies the analyzer is oriented at right angle to the polarizer, so that if no birefringent sample is present the field of view is black.

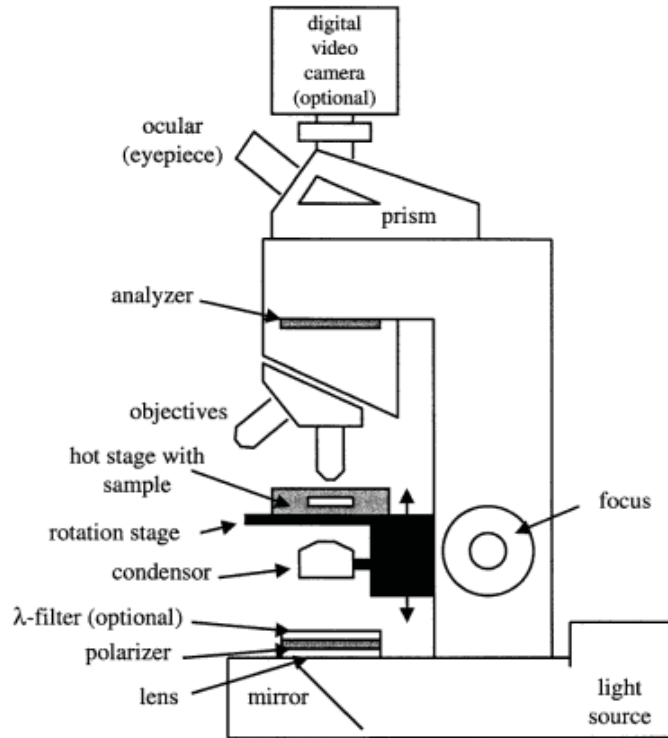


Figure 6.4 Schematic view of Polarized Light Microscope (from Ref. 8).

#### 6.1.4 Bulk elasticity of nematic and cholesteric liquid crystals

If we assume  $F_0$  to be a free energy of a uniformly aligned nematic liquid crystal, then any deformations of a director field (mechanical, caused by external electric or magnetic fields, etc.) would increase the resulting free energy,  $F$ . In the case of liquid crystals what is meant by deformation is rather the change in orientation between neighboring building blocks than any changes of the positions of neighboring points (typical for solid materials). The resulting formula of perturbed free energy will be as follows:

$$F = F_0 + K_{11}(\nabla \cdot \mathbf{n})^2 + K_{22}(\mathbf{n} \cdot \nabla \times \mathbf{n} - q_0)^2 + K_{33}(\mathbf{n} \times \nabla \times \mathbf{n})^2, \quad (1)$$

where  $K_{11}$ ,  $K_{22}$  and  $K_{33}$  are elastic constants for the three different basic deformation modes of director field: *splay*, *twist* and *bend*, respectively (see Figure 6.5). For simplicity, often the so-called 'one-constant approximation' is used with:  $K_{11} = K_{22} = K_{33} = K > 0$ .<sup>11</sup> The term  $q_0$  represents the helical wavevector related to the cholesteric pitch,  $P_0$  (i.e. length at which the director  $\mathbf{n}$  turns for  $2\pi$ ) as follows:  $q_0 = 2\pi/P_0$ . It should be mentioned that  $q_0 > 0$  for right-handed twist and  $q_0 < 0$  for left-handed twist and vanishes in the nematic.

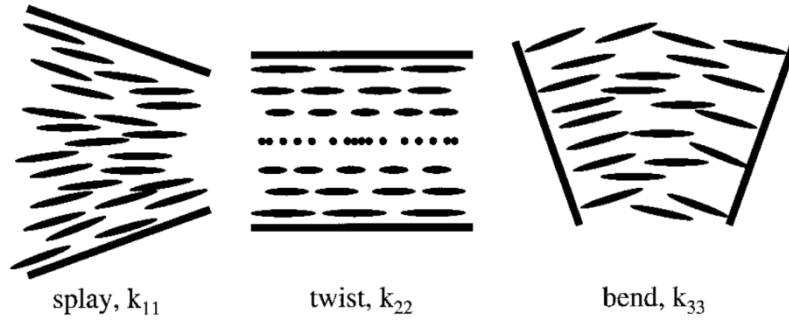


**Figure 6.5** Three fundamental bulk distortions of a nematic liquid crystal: splay, twist, and bend (from Ref. 8).

### 6.1.5 Surface anchoring in nematic liquid crystals

In the case of anisotropic media, like liquid crystals, the surface energy per unit area ( $\sigma$ ) is not constant and depends on the orientation of the interface with respect to the director (i.e. symmetry axes of the molecules). Moreover, presence of the interface implies the distortion of the order parameter both in bulk and at the surface. Surface orientation of the director is characterized by two angles: a polar angle  $\theta$  and an azimuthal angle  $\varphi$ . The particular direction  $(\theta_0, \varphi_0)$  that minimizes the function  $\sigma(\theta, \varphi)$  is called the *easy axis*. Thus,  $\sigma(\theta, \varphi)$  can be presented as a sum of the surface tension  $\sigma_0(\theta_0, \varphi_0)$  at equilibrium orientation and the anchoring energy function  $w(\theta, \varphi)$  that depends on the molecular interactions at the interface:<sup>6</sup>

$$\sigma(\theta, \varphi) = \sigma_0(\theta_0, \varphi_0) + w(\theta - \theta_0, \varphi - \varphi_0), \quad (2)$$

The anchoring determines a stable direction of the director orientation with respect to the surface/interface. The strength of anchoring is usually described by polar ( $w_\theta$ ) and azimuthal ( $w_\varphi$ ) anchoring coefficients which simply measure the work (per unit area) needed to deflect the director from the *easy axis*  $(\theta_0, \varphi_0)$ . One of the most commonly used models for surface anchoring energy, especially for the polar part, is the Rapini-Papoular anchoring potential:<sup>7</sup>

$$w = \frac{1}{2} w_\theta \sin^2(\theta - \theta_0), \quad (3)$$

Figure 6.6 depicts some general types of anchoring modes for a flat interface. Anchoring is said to be perpendicular, or more often called *homeotropic*, when the director  $\mathbf{n}$  is normal to the interface (polar angle,  $\theta_0 = 0$ ). When the director is tangent to the surface (i.e. polar angle,  $\theta_0 = \frac{\pi}{2}$ ), the anchoring is called *planar*. The intermediate case ( $0 < \theta_0 < \frac{\pi}{2}$ ) is called *tilted*.

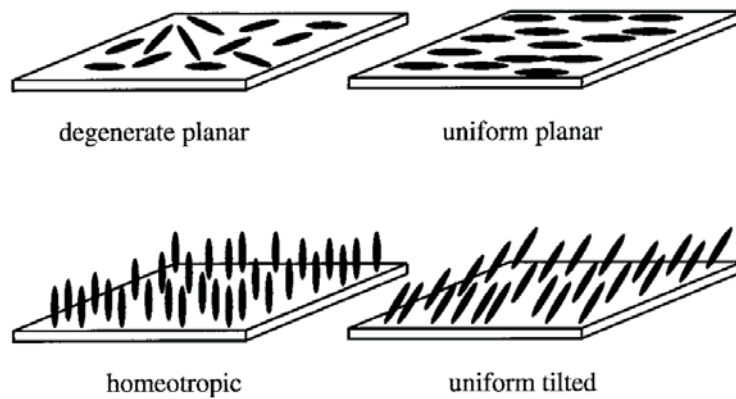


Figure 6.6 Schematic illustration of different anchoring modes (from Ref. 8).

## 6.2 Studies of dispersed systems of liquid crystals

In fact dispersions of liquid crystals have been experimentally investigated from the very beginning of the research in the field of liquid crystals. Even though they were produced intentionally at the end of XIX<sup>th</sup> century by the German physicist Otto Lehmann who was dealing with dispersed LC systems of *para*-azoxyanisole,<sup>14</sup> liquid crystal droplets were quickly forgotten. Recently, the studies of liquid crystals in various confined geometries have been of great interest.<sup>15</sup> In addition to the technologically-driven research, like development of Polymer-Dispersed Liquid Crystals (PDLC) as electro-optic medium,<sup>16</sup> a lot of basic research have been conducted in the field of liquid crystals dispersions. The fact that the ground state of a liquid crystal is an outcome of the elasticity of material and the surface anchoring, gives a lot of interesting possibilities for physicists and mathematicians to realize and examine their geometrical and topological ideas in the field of materials science.<sup>15</sup>

### 6.2.1 Droplets of nematic liquid crystals

If one considers a liquid crystalline droplet, e.g. a nematic droplet, its structure is determined by the balance of anisotropic surface tension and internal elasticity. Moreover, unlike for solids and isotropic liquids – in the case of liquid crystals both surface and bulk terms of the minimum free energy functional should be considered.<sup>6</sup> The anisotropic surface energy depends on the surface orientation of molecules and it scales with the square of the droplets size,  $F_{surface} \sim \sigma R^2$ , where  $R$  stands for radius of the droplet. Since the director is defined by molecular orientation, any boundary conditions applied – depending on the systems geometry – may impose director gradients, which cost the elastic energy. The latter one is dependent on the elastic constant,  $K$ , and interestingly it exhibits a linear dependence with the droplets size  $F_{elastic} \sim KR$ .<sup>17</sup> As a consequence, for the droplets of

anisotropic materials like nematic liquid crystal, the surface energies outweigh the bulk elastic energy for large enough  $R$ . Considering the typical values of surface free energy per unit area (including ‘anchoring energy’  $w_\theta$  - which is angular-dependent part) and the elastic constants ( $K$ ), nematic droplets: (1) remain spherical shape, and (2) their internal structure is highly dependent on their size (for a given anchoring conditions, i.e. type of a surrounding isotropic matrix). As illustrated on Figure 6.7, droplets with normal surface anchoring may exhibit significantly different director fields. For example, smaller droplets, with size  $R \ll K/w_\theta$  (i.e. radius much smaller than the ratio of bulk elastic constant and the anchoring energy) tend to preserve a spatially uniform director field at the expense of violated boundary conditions.

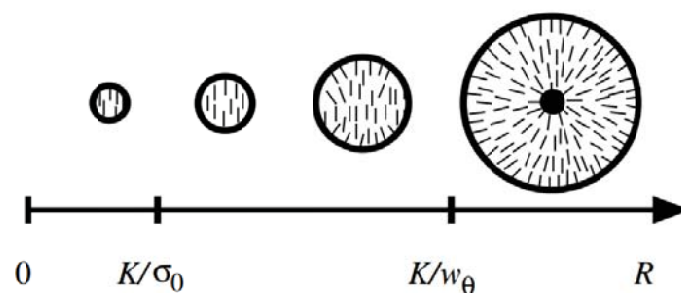


**Figure 6.7** Schematic representation director configurations of nematic droplets with normal surface anchoring. While for small droplets ( $R \ll K/w_\theta$ ) the director orientation tends to be uniform, large droplets ( $R \gg K/w_\theta$ ) in ground state contain topological defects - here depicted by the black spot in the center of a droplet (from Ref. 12).

While increasing the size of the nematic droplet the surface term, which scales with the square of the radius  $R$ , progressively becomes more substantial. Ultimately, for droplet of radius exceeding the characteristic anchoring length,  $R \gg L_w = K/w_\theta$ , a concentric director field would be observed, with a stable topological defect called a hedgehog, located in the center of a droplet. In fact stable topological defects are the inherent feature of liquid crystal dispersions for droplets of supramicron size. As stated before, for sufficiently big droplet the surface anchoring plays a predominant role in determining a director field configuration.

An illustrative example is provided by Figure 6.8(a). Initially observed textures of three nematic droplets ( $R$  for the biggest droplet equals  $20 \mu\text{m}$ ) evidence the bipolar configuration of the director field for the case of each droplet. It may be encountered from the two darker areas at *the north and south poles* of each droplet, which correspond to the two topological defects called boojums.

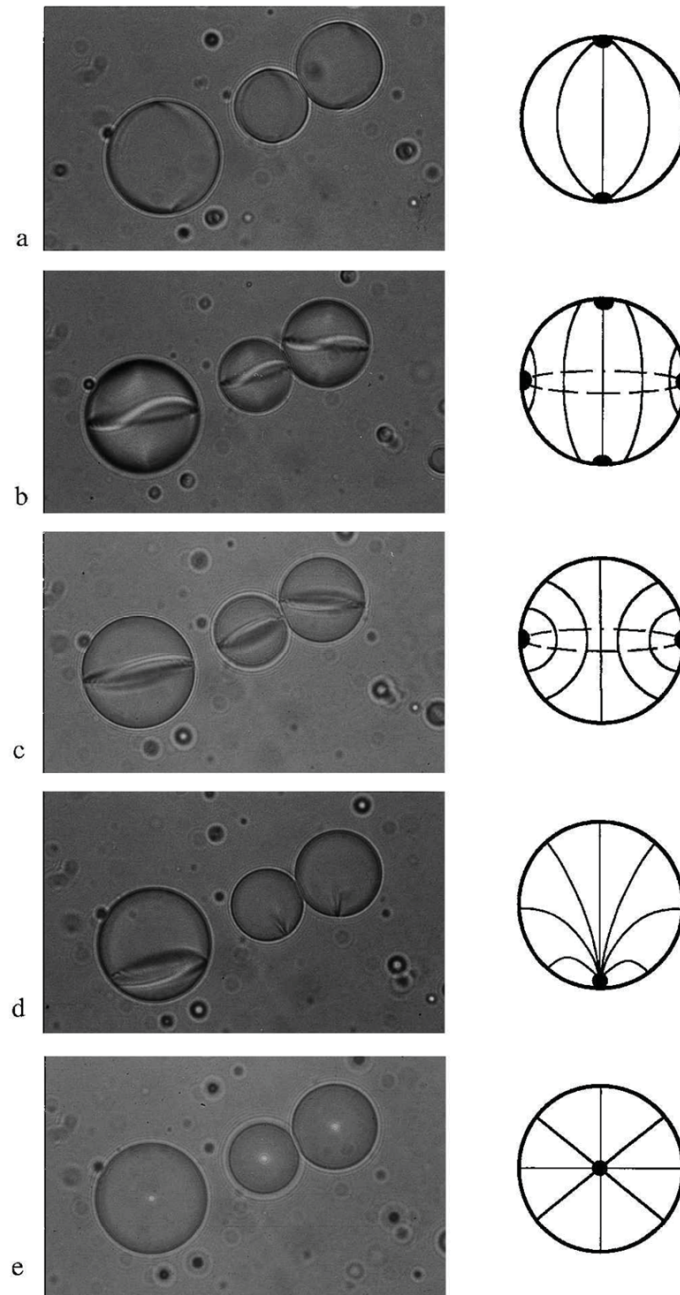


**Figure 6.8** Sequence of microphotographs of textures of three nematic droplets (*left*) and the respective schematic representation of the director orientation (*right*). (a) represents the *bipolar* droplet configuration with two defects at the *north* and *south poles* of each droplet. Those defects, called boojums, are the result of the strictly tangential boundary conditions imposed by the surrounding glycerin matrix. Subsequent images show the appearance of an equatorial disclination line (b), followed by fading out of boojums (c). The disclination line shrinks into a surface hedgehog (d), which changes its position from *the south pole* to the center of the droplet, resulting in *radial* configuration (e). The overall process of transformation of two surface defects (*boojums*) into a single bulk defect (*hedgehog*) is fully reversible, and results from the temperature-driven change of boundary conditions from strictly tangential to strictly normal (from Ref. 17).

Those defects are surface defects (contrary to the previously mentioned bulk hedgehog defect) and they appear as a consequence of a strictly tangential boundary conditions imposed by the surrounding glycerin matrix. The director configuration for each droplet is schematically shown by the scheme on the right panel. Subsequent images show the evolution of textures as a result of temperature-driven activation of a lecithin surface agent which changes the boundary conditions from strictly tangential (Figure 6.8(a)) to the strictly normal (Figure 6.8(e)). Figure 6.8(b) shows that at first an equatorial disclination line is formed (bright/dark sinusoidal curve), which is followed by the gradual disappearance of boojums (Figure 6.8(c)) and the shrinkage of the disclination into a surface hedgehog at the proximity of the *south pole* (Figure 6.8(d)). Ultimately the hedgehog undergoes the relocation from surface to the bulk of each droplet, what is presented on Figure 6.8(e) and results in the radial structure, already shown on Figure 6.7. The sequence of discussed micrographs clearly evidences the transformation of topological defects of one kind (pair of boojums) into a defect of another kind (hedgehog).

Worth to underline is that the presented dynamic evolution of topological defects in nematic droplets (stimulated by accommodation of modified boundary conditions) proceeds in agreement with the conservation of the overall topological charge for each droplet. Moreover, as described in details by Volovik and Lavrentovich<sup>18</sup> it is a fully reversible process.

After an extensive description of defects in the condensed matter physics with the use of topological approach,<sup>19</sup> studies of the topological defects and their evolution became one of the most prominent subjects in physics of liquid crystals.<sup>20,21</sup> Notion of the topological charge provides an appropriate classification of topological defects in condensed media and enables to study stability of defects, which is governed by conservation of the overall topological charge of a system (here: nematic droplet). Analogically to the laws of conservation of e.g. electric charges, the law of conservation of topological charges regulates processes like creation, annihilation and transformation of this kind of charges.

## 6.2.2 Appearance of chirality: twisted bipolar droplets from achiral nematic LCs

The radial and bipolar types of droplets of a nematic liquid crystal presented above are one of the most commonly found objects during experimental studies of LC dispersions. Nevertheless, currently a number of other director configurations within liquid crystal droplets are known.<sup>15</sup> As shown for the previous cases, a decisive factor for the structure of director field for spherically bounded LC system may be the surface anchoring. Moreover, not only the boundary conditions may determine the observed structure, but also the ratio of elastic constants, the size and form of droplet as well as external fields. A somehow classical example of this kind appears when:

$$K_{11} \geq K_{22} + 0.431K_{33} \quad (3)$$

$K_{11}$ ,  $K_{22}$  and  $K_{33}$  being the elastic constants corresponding to bend, twist and splay deformations, respectively. Such stability criterion was postulated by Williams,<sup>22</sup> who predicted that a twisted bipolar structure would spontaneously form if the additional condition would be fulfilled. Namely, that the droplet is big enough, and the bulk effects dominate the surface effects. In such case, the bipolar structure which contains only two types of deformations: bend and splay, would be no more the most stable droplet configuration. The structure of a twisted bipolar nematic droplet and the polarized microscopy image are presented on Figure 6.9.

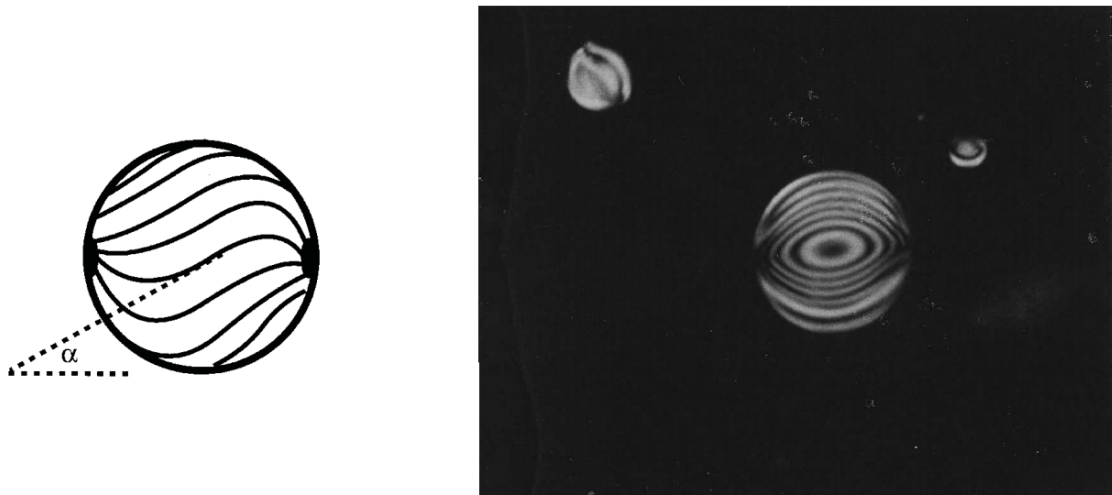
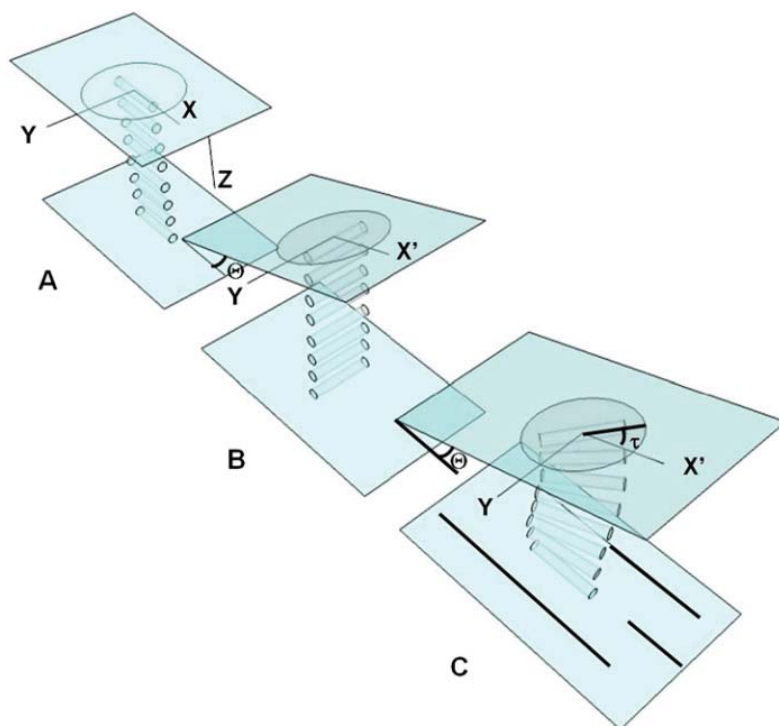


**Figure 6.9** Schematic representation of a director field for a twisted bipolar structure. The angle  $\alpha$  is defined by the angle of the director field on the droplet surface relative to the droplet symmetry axis (*left*). The twist vanishes as the director approached the diameter of the droplet joining two surface defects. Twisted bipolar droplet suspended in glycerine ( $R = 31 \mu\text{m}$ ) examined under crossed polarizers with symmetry axis along polarizer (*right*) (from Ref. 23).



The theoretical predictions by Williams - about the phase transition between untwisted structure and twisted one - were confirmed by the experimental results reported by Volovik and Lavrentovich.<sup>18</sup> Moreover, the existence of similar transitions has been demonstrated for droplets with homeotropic anchoring containing point defects of hedgehog type.<sup>24</sup> According to Lavrentovich and Sergan, who studied more deeply the occurring phase transitions, the untwisted-twisted transitions proceed due to the temperature-induced changes of the elastic constants.<sup>25</sup> Both (untwisted and twisted) states of the droplets differ only with respect to the structural symmetry, neither phase state of nematic itself, nor boundary conditions. A detailed work of Drzaic summarized the previously reported results on the appearance of twisted bipolar structures as generally favored for systems of high splay energy, i.e. for which  $K_{33}/K_{11} < 0.93$ .<sup>23</sup> Moreover, it was also shown that the nematic liquid crystals confined to spheres (and also cylinders) represent a general class of structures in which achiral molecules can form chiral structures due to the combination of external boundary conditions and the minimization of the free energy near defect structures.<sup>23</sup> Prinsen and van der Schoot<sup>26</sup> have calculated more recently that escaping to twisted configuration is preferable for spindle-shaped nematic droplets (tactoids) if the twist and bend elastic constants are small enough compared to the splay elastic constant. Accordingly, they have generalized Williams' criterion to bipolar droplets of an arbitrary aspect ratio, showing that the more elongated the droplet is - the less likely a twisted-bipolar director configuration appears.

The more pictorial example which may be considered as a rather simple pathway of macroscopic chirality induction in an organic system with no molecular chirality was presented by Tortora and Lavrentovich.<sup>27</sup> The chiral symmetry breaking observed for tactoidal droplets of lyotropic chromonic liquid crystals (LCLC), was explained by the authors as a result of replacement of energetically costly splay packing of the LCLC aggregates within the curved bipolar tactoidal shape - with twisted packing. In other words the observed chirality breaking requires a medium with certain anisotropy of elastic properties sandwiched between one oriented (e.g. rubbed) interface, and another of non-planar geometry. Analogically, the geometrical anchoring related to the thickness gradient was previously reported to induce a director twist in the nematic liquid crystal aligned in planar way.<sup>28</sup> In the case of LCLC tactoid droplets, authors estimate that the twist deformation would reduce the overall elastic energy of the system when the following condition is fulfilled:  $K_{22}/K_{11} < \Theta^2$ , (where  $\Theta$  is the tilt angle between the local curvature of the tactoid droplet and the plane of the surface underneath). The geometric interpretation of the mechanism of described phenomena is depicted by Figure 6.10.



(A) Two parallel surfaces result in a degenerate in-plane orientation of  $\mathbf{n}$ .

(B) Tilting of the top plate by an angle  $\Theta$  around the  $y$ -axis in absence of in-plane physical anchoring produces uniform orientation of  $\mathbf{n}$  along the  $y$ -axis.

(C) The balance between the geometrical anchoring imposed by the surface tilt and the physical anchoring along the  $x$ -axis at the bottom substrate results in a twisted structure (from Ref. 27).

**Figure 6.10** Schematic view of the N structure along the  $z$ -axis, confined between two surfaces imposing tangential orientation on  $\mathbf{n}$ .

### 6.2.3 Droplets of cholesteric liquid crystals

The literature examples highlighted in the previous section evidenced the appearance of chirality of structure (manifested by optical activity of nematic droplets of twisted bipolar director configuration) in system composed of achiral components. In the following section the dispersions with the inherent (bulk) chirality will be discussed. First of all, the characteristic feature of a cholesteric (chiral nematic –  $N^*$ ) liquid crystal is the helical structure which is a manifestation of helical distortion of material. This distortion may be found e.g. in cholesterol esters, which are pure chiral systems, but also appear after addition of a small amount of chiral molecule (dopant) to the regular nematic liquid crystal. Nematics and cholesterics appear to some extent as two subclasses of the same family.<sup>5</sup> Leaving aside the fact of obviously different optical properties (e.g. Bragg reflections in the case of cholesterics), there are circumstances that normally chiral nematic and nematic may be treated similarly. What clearly distincts the chiral nematics from the regular nematics is the finite value of the cholesteric pitch ( $P_0$ ). And this is the geometrical scale of the system related to the value of the pitch that enables us to consider (or not) the chiral and non-chiral nematic as affined.

#### 6.2.4 Geometrical factor determining the structure of cholesteric droplets

While describing the nematic droplets it was pointed out that the anchoring type (and strength) may be crucial for the director spatial arrangement of the system. In particular, the characteristic anchoring length parameter,  $L_w$ , was mentioned, which was furthermore equated to the droplets size – in order to estimate the potential structure of the droplet. In cholesteric droplets the decisive relation is not the  $L_w$  vs  $R$ , but the  $L_w$  vs  $P_0$ .<sup>29</sup> For a nematic drop, the anchoring is strong when  $L_w \ll R$ . On the contrary, in a chiral nematic drop with  $P_0 < R$ , the important length is the pitch and consequently the anchoring is strong for  $L_w \ll P_0$ . This implies, that the type of anchoring (weak or strong) in large chiral nematic droplets ( $P_0 < R$ ) is independent of the size of the droplet, unlike the case of nematics. This is a first fundamental difference. In consequence, the important geometrical factor which determines the structure of the cholesteric droplet is the relation between the droplets radius ( $R$ ) and the cholesteric pitch of the CLC mixture forming the droplet ( $P_0$ ). Before we describe quantitatively the influence of  $R/P_0$  ratio on the director configuration within a cholesteric droplet, first let us introduce some of the most commonly met structures, basing on the theoretical and experimental investigations.

#### 6.2.5 Cholesteric droplets of planar anchoring – theoretical approach

Bearing in mind a manifold nature of nematic droplets and the fact that the cholesteric liquid crystals possess the inherent twist one would expect the increase in complexity of structures in the case of cholesteric droplets. Mainly three structures are found in literature that concern the cholesteric droplets with planar degenerate anchoring:<sup>30,31</sup> (i) radial spherical structure (RSS), (ii) diametrical spherical structure (DSS), and (iii) twisted bipolar structure, analogical to the one appearing for nematic droplets of certain elastic properties. In experiments, most commonly the radial spherical structure is observed, alternatively called the *spherulitic texture* or the *Frank-Pryce model*.<sup>32</sup> For low chirality and generally smaller droplets, the twisted bipolar director structure becomes energetically more favorable than the planar bipolar structure.<sup>31</sup> Similarly to the case of nematic droplets, their cholesteric counterparts reveal the appearance of topological defects in their ground states. For example, in the radial spherical structure, the predicted +2 disclination shows an interesting analogy to the magnetic monopoles - Dirac monopoles.<sup>20,33</sup>

Zumer and co-workers have performed extensive theoretical studies on chiral nematic droplets.<sup>29,30,34</sup> Figure 6.11 illustrates the structural details of the three different configurations of such systems. Panel on the top (a) represents the radial spherical structure, middle panel (b) shows characteristics of the diametrical spherical structure, and the one on the bottom (c) depicts features

of the planar bipolar structure. Left part of the panel shows the topological defects (here:  $\chi$ -disclination lines) for respective structures. In addition, their topological strengths are depicted (denoted  $s$ ). It should be mentioned, that in the case of radial spherical and diametrical spherical structures those lines appear in bulk. In the case of planar bipolar structure, the disclination line lies at the surface of the droplet (forming a spiral). The three sketches at the central part of the image show the cross-sections of each droplet together with the cholesteric surfaces, which are concentric in two first cases, and planar in the third case. The three sketches on the right-hand side schematically show director fields on three different cholesteric spheres/planes. In other words they illustrate the director fields in the consecutive cholesteric surfaces, which are either spherical (a) and (b), or planar (c).

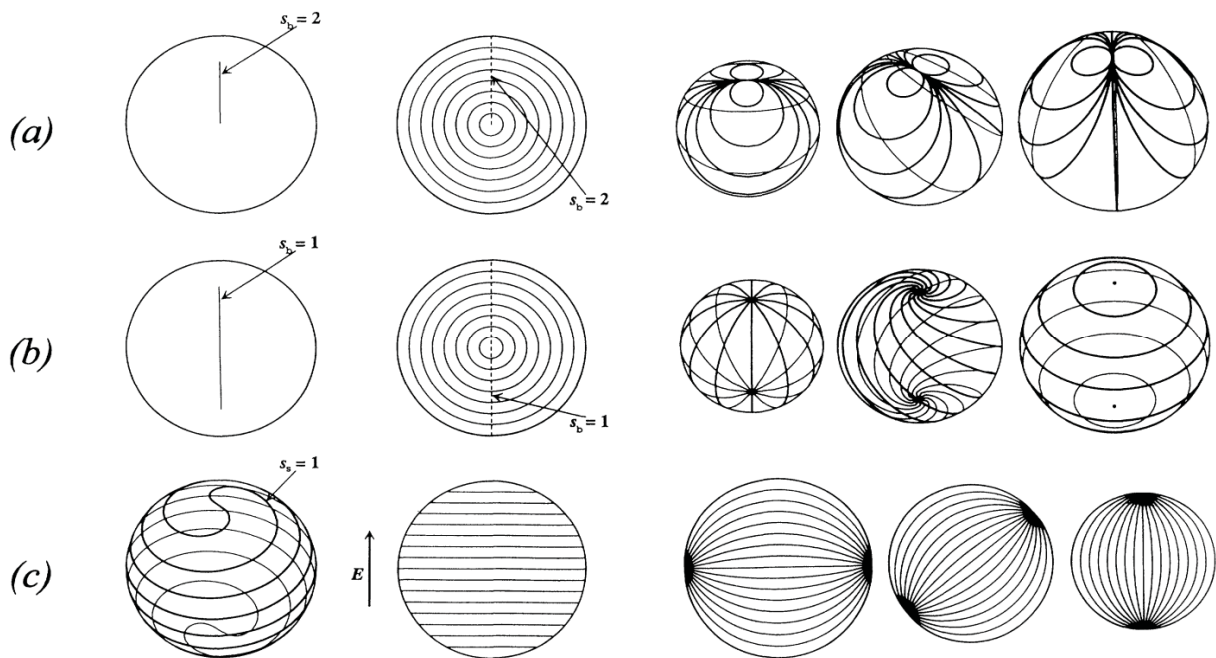


**Figure 6.11** Schematic view of: (a) radial spherical structure (RSS), (b) diametrical spherical structure (DSS), and (c) planar bipolar structure (PBS). The sketches on the left panel show a 3D view of  $\chi$ -disclination lines with their bulk strengths  $s$ . These lines are bulk lines for spherical structures (a), (b) and surface lines for planar bipolar structure (c). The middle sketches show cross sections of the droplets. The  $N^*$  surfaces are concentric spheres for the cases (a) and (b), and planes in the case of (c). The middle sketches also show bulk  $\chi$  lines (a), (b). On the right panel the director fields on several  $N$  spheres (a), (b) and  $N^*$  planes (c) are shown. Radial configuration of helical axes in spherical structures (a), (b) results in the relative rotation of director configuration on successive  $N$  spheres. On the other hand, the helical axes are parallel to the  $z$  axis in planar bipolar structure (c) and this results in the relative rotation of director configuration on successive  $N^*$  circles along the  $z$  axis (from Ref. 30).

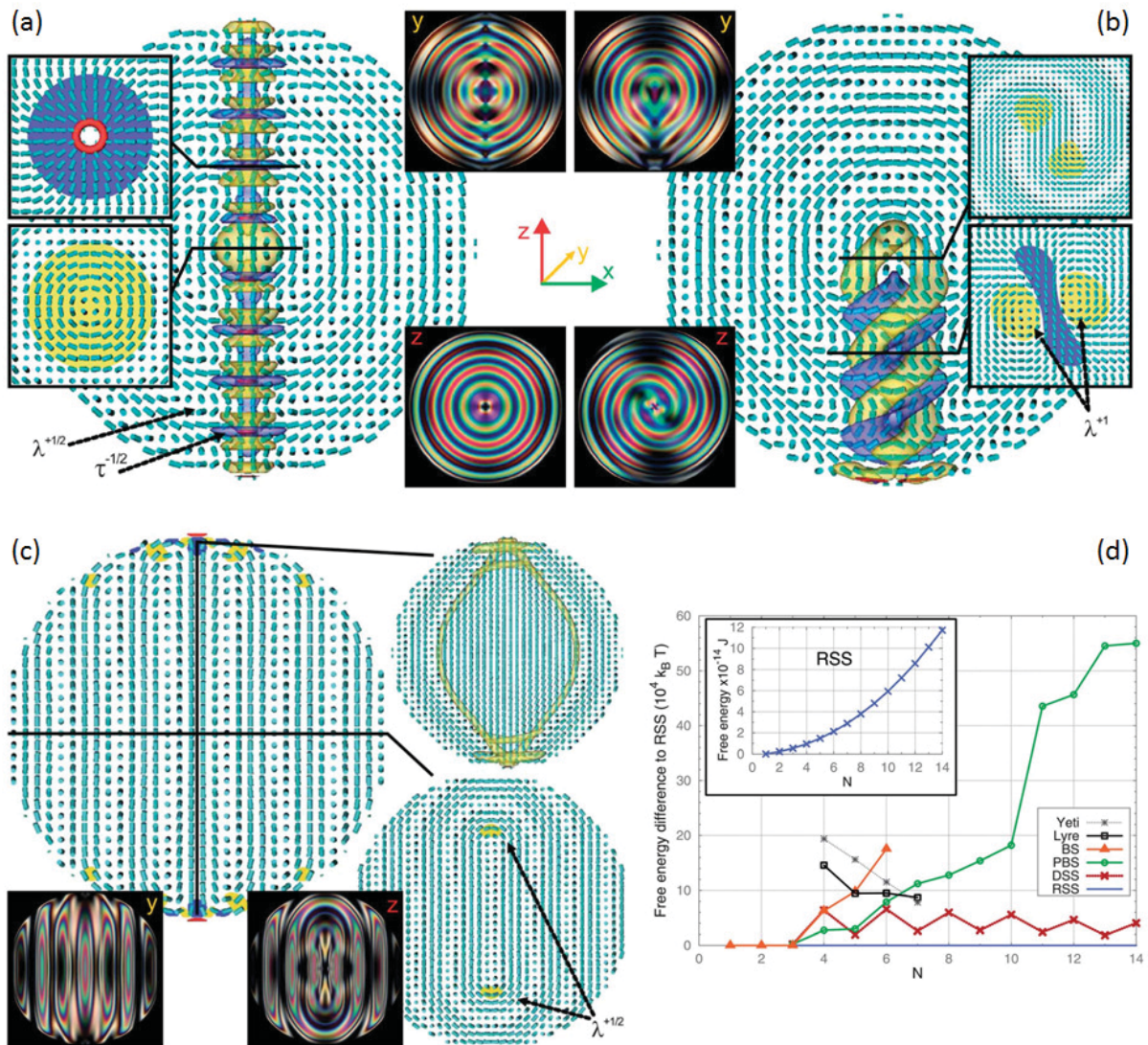


**Figure 6.12** Simulated director configurations in the case of (a) radial spherical ( $N = 10$ ), (b) diametrical spherical ( $N = 10$ ) and (c) planar bipolar ( $N = 8$ ) droplets. The insets show the director field at marked cross-sections and the simulated polarization micrographs (for details please refer to Sec *et al.*<sup>35</sup>). (d) Stability of the structures in cholesteric droplets. Free energy differences relative to the stable radial spherical structure (RSS) are calculated for: diametrical structure (DSS, in red crosses), planar bipolar structure (PBS, in green circles) and other (metastable) structures. Note the oscillation of the free energy difference for DSS for odd and even  $N$ . The Lyre and Yeti structures have much higher free energy than the other structures. Inset shows the total free energy for the RSS structure for varying  $N$  (i.e. varying the cholesteric pitch at fixed droplet size) (from Ref. 35).

More recent studies on structures of spherical cholesteric droplets with degenerate planar anchoring were performed by Sec *et al.*, using a mesoscopic numerical modeling. The total free energy of the droplets was calculated using the Landau-de Gennes free energy approach in order to fully characterize the director fields, including the defect regions. To provide a relevant measure of the relative size of the droplet with respect to the chiral pitch, the pitch was presented in units of the droplet diameter. For that, a relation:  $P_0 = 4R/N$ , was used, where  $N$  corresponds to the number of  $\pi$  turns the director would make in a non-confined cholesteric along the distance equal to the droplet diameter  $2R$ . After minimization of energy six (meta)stable orientational profiles were found, each characterized by its specific configuration of the director profile and the topological defects. The general features of three of the presented structures (RSS, DSS and PBS)<sup>30</sup> were in agreement with previous studies, moreover some new – metastable structures were found.

Stability of the obtained structures of cholesteric droplets was further examined as a function of pitch-to-droplet radius parameter:  $N = 4R/P_0$ . Relative free energy plot, together with complete configurations of director profiles for RSS, DSS and PBS structures are presented on Figure 6.12.

From the presented results of stability studies we may conclude several important facts:

- since free energy differences between the structures are high (of the order of  $\sim 10^4 k_B T$ ) the thermal fluctuations should not provoke the transitions between the structures;
- radial spherical structure to be the stable structure for spherical droplets with  $N > 3$ , which is also in good agreement with experiments;<sup>31,36</sup>
- at a chosen droplet size, the free energy difference between RSS and DSS structure decreases with increasing  $N$  (i.e shorter pitch);
- interestingly, the free energy difference between the DSS and RSS structures oscillates for even  $N$  or odd  $N$ . This corresponds to the DSS structure always having an even number of  $\tau^{-1/2}$  ring defects (see Figure 6.12(a)) either for odd  $N$  (favorable) or even  $N$  when it is frustrated;
- the planar bipolar structure (PBS) emerges energetically more favorable (but still metastable) than the DSS structure for  $N \leq 6$ , whereas for larger  $N$  it has the highest free energy. Moreover, for  $N > 10$  the free energy difference becomes substantial and thus PBS is not expected to be observed in experiments (not even as metastable).

## 6.2.6 Cholesteric droplets of planar anchoring – experimental validation

In order to verify theoretical results Xu and Crooker reported experimental study of behavior of chiral nematic droplets with parallel boundary conditions for varying two parameters: (1) radius-to-pitch ratio and (2) droplet size. Experiments based on recording of polarized microscopy images which were further compared with simulated images coming from theoretically proposed director fields.<sup>31</sup> Figure 6.13 presents three polarized microscopy images that are representative for the three regimes reported by Xu and Crooker. The authors show, that for low chirality regime (which they define as:  $P_0 > R$ ) texture is twisted bipolar, as depicted by Figure 6.13(a). For high chirality regime (i.e.  $P_0 < R$ ) droplet exhibits the radial spherical texture (*Frank-Pryce model*, Figure 6.11(a)). Figure 6.13(b) shows the radial spherical droplet that possesses the characteristic concentric features, i.e. radial period. It is also suggested, that the third regime appears for  $P_0 \ll R$ , and although the texture of the droplet looks much different, the structure is still radial spherical.

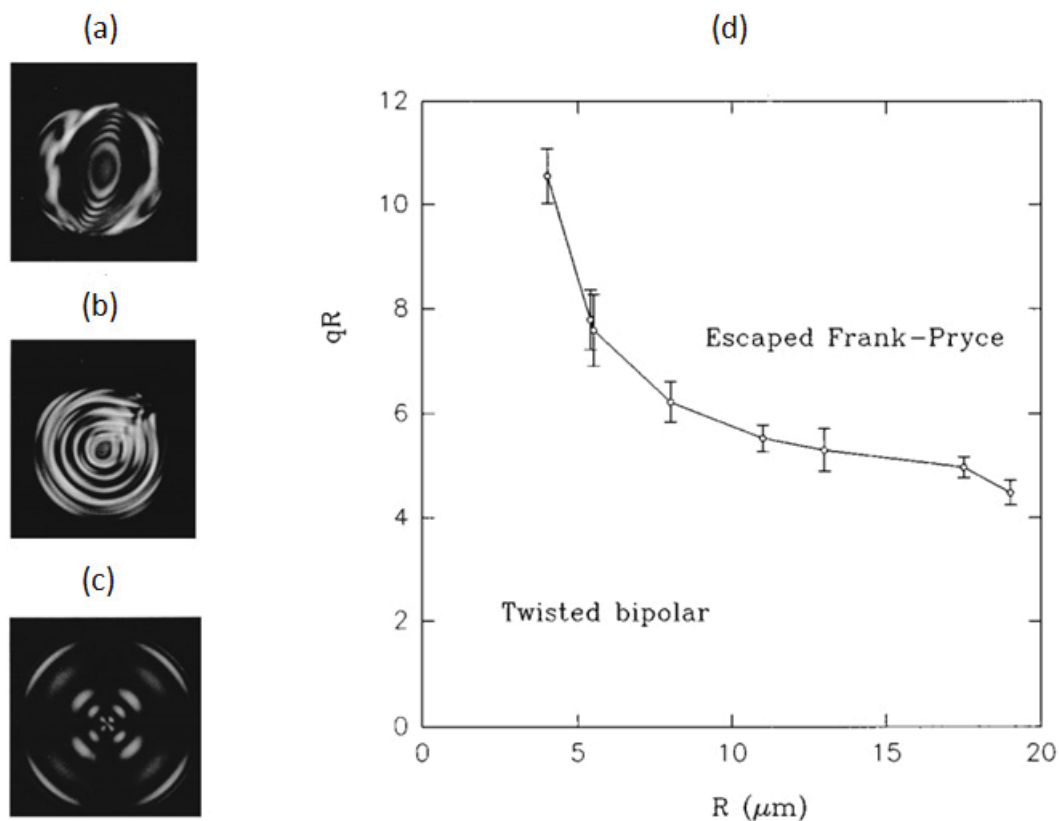


**Figure 6.13** Polarized microscopy images of different textures of cholesteric droplets. Examples of droplets with (a) low chirality  $P_0 > R$ , (b) high chirality  $P_0 < R$ , and (c) very high chirality  $P_0 \ll R$ . (d) represents the phase stability diagram in the  $R/P_0$  vs  $R$  plane. Error flags shows the region where droplets may be either Frank-Pryce (i.e. radial spherical) or twisted bipolar (from Ref. 31).

By analyzing different cholesteric dispersions, i.e. varying the cholesteric pitch, the authors investigated the stability of existence of twisted bipolar and radial spherical droplets. Figure 6.13(d) is the phase stability diagram which shows the relation of  $R/P_0$  vs  $R$ . It is easily noticed that for the droplets of radius  $\sim 10 \mu\text{m}$  or higher, the  $R/P_0$  ratio does not vary much, in agreement with the theoretically predicted  $R/P_0 = \text{const}$ . On the contrary, as  $R$  becomes smaller  $R/P_0$  parameter increases dramatically. The last fact is explained by the authors as a consequence of non-negligible surface extrapolation length ( $\xi$ ), i.e. violation of  $\xi \ll R$  condition for  $R < 5 \mu\text{m}$ . In other words, it means that for such small droplets influence of surface anchoring is non-ideal. In general, as the  $R/P_0$  ratio is reduced, a structural transition takes place from the radial spherical to the twisted bipolar structure. Although the previously quoted theoretical calculations assume the diametrical structure as the most stable, Xu and Crooker did not report on any evidence of DSS droplets during their experiments.

The authors also described a mechanism of transition between two topologically different states, namely the radial spherical to twisted bipolar transition. In order to perform those dynamical studies, a temperature-induced change of cholesteric pitch was calibrated to ensure the conditions of slow pitch variation. Figure 6.14 shows the sequence of images depicting the transition for increasing cholesteric pitch. Shortly after increase of temperature of the sample the surface defect (positioned at 12 o'clock) split into two surface defects (Figure 6.14(a)), which then move apart (Figures 6.14(b) and (c)). Then one of the surface defects combines with the bulk defect to form the twisted bipolar structure (Figure 6.14(d)).

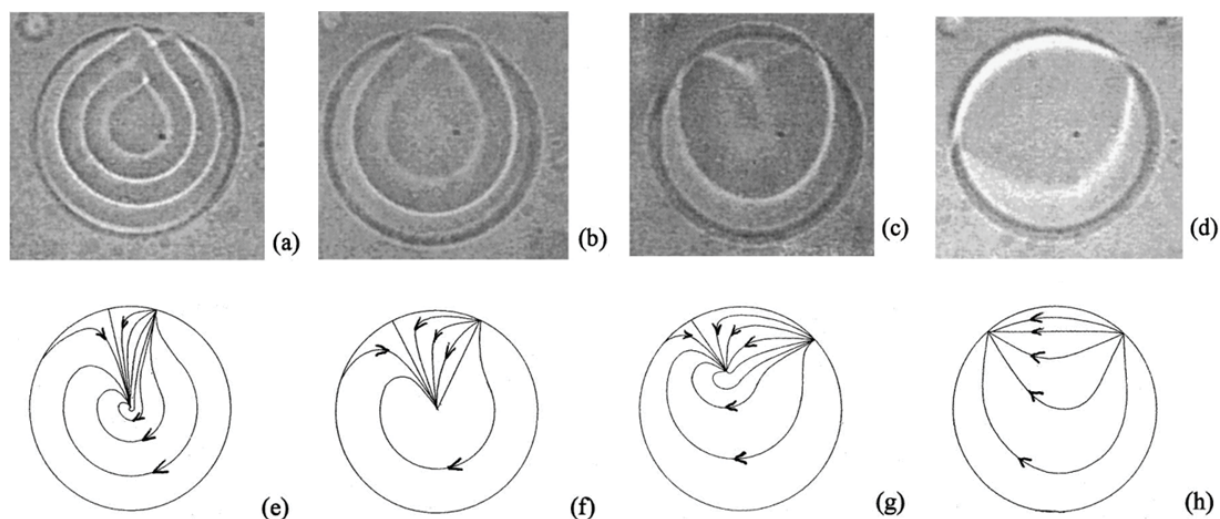


**Figure 6.14** Details of the bipolar–Frank-Pryce transition for decreasing chirality of the droplet. (a) Surface defect splits into two surface defects. (b) Two surface defects move apart, and the number of fringes becomes smaller. (c) Central defect moves toward one surface defect and merges in (d). (e)–(h) Schematic models for stages (a)–(d) (from Ref. 31).



### 6.2.7 Negative-to-positive monopole transitions in cholesteric droplets

A very important report from the point of view of future studies of compensated cholesteric liquid crystal mixtures was published by Kurik and Lavrentovich.<sup>33</sup> They have studied a compensated liquid crystal mixture, where the helicity of the system may be influenced by temperature. Frame (a) from the left panel of on the Figure 6.15 shows the radial texture, and its evolution to the bipolar texture (d). Authors follow a detailed description on the topological defects present at every stage. The frame (a) contains texture with a radial defect which is pointed with white arrow. For decreasing of temperature, authors observe the helix unwinding, and enlargement of the radial period, that for the ratio  $R/P$  achieving 1 decomposes into two points on the surface of the droplet (frame (b)). Further decrease of temperature is manifested by the continuous separation of both points – towards the poles of the drop (frame (c)). Ultimately the bipolar droplet with two diametrically opposite point surface singularities is established. For further decrease of temperature (results not shown) authors report on the reappearance of radial spherical texture, thus a thermally induced helix inversion for the droplets with planar anchoring.

Kurik and Lavrentovich have performed analogous studies for the case of the droplet with homeotropic anchoring. To vary the anchoring mode at the droplets surface they used the mixture of glycerine with a small amount (~1 wt%) of lecithin which provokes the change of anchoring from planar to homeotropic as a result of temperature decrease. The right side of the panel on Figure 6.15 represents the transition of cholesteric droplet textures. For high values of  $R/P$  ratio, i.e.  $> 10$  textures again represent the radial spherical structure (frame (a)), since for such big droplets the surface do not change the distance of packing between the layers (as discussed in point 6.2.4). During the decrease of temperature, and lowering the  $R/P$  ratio (up to  $< 5$ ), additional defect appears, namely an equatorial disclination (frame (b)). Further decrease in temperature, and reaching the  $R/P < 1$  results in the relaxation of the disclination into a point surface defect (frame (c)). Continuation of the cooling process results in the helix inversion of the structure (not shown). In summary Kurik and Lavrentovich evidenced the thermally driven helix inversion in the cholesteric liquid crystal droplets for both cases of surface anchoring, and they point the existence of additional surface defect appearing for the case of homeotropic droplet anchoring.<sup>33</sup>

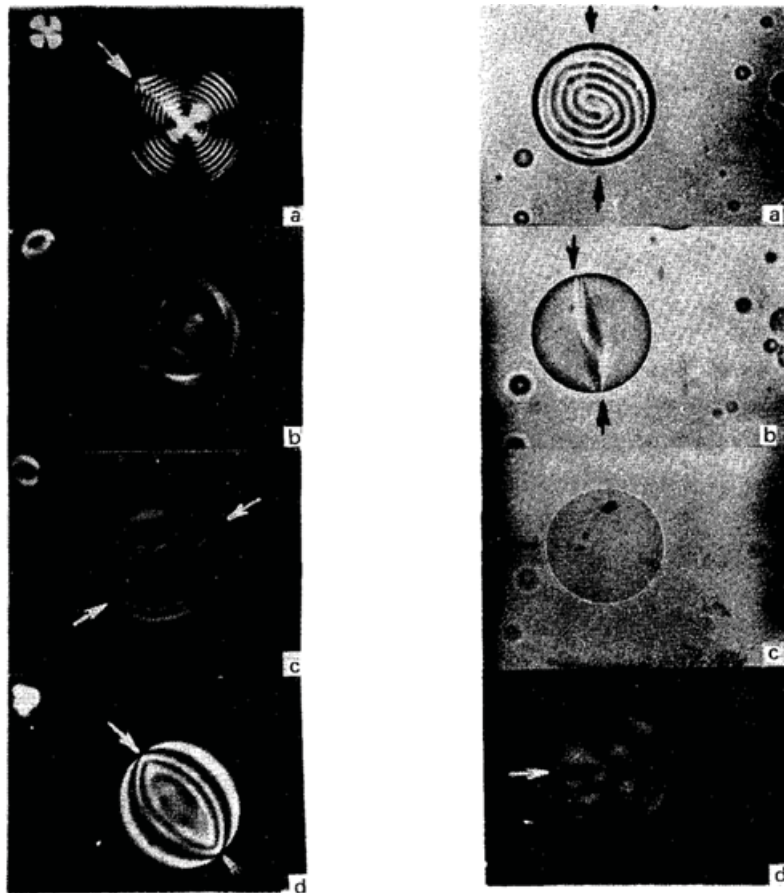


**Figure 6.15** (*left*) Vertically arranged sequence of 4 images shows the transition between the radial texture (a) and bipolar texture (d) in the case of CLC drop  $R = 35 \mu\text{m}$  in planar anchoring conditions. (*right*) Vertically arranged sequence of 4 images shows the transition between the radial texture (a) and bipolar texture (d) in the case of CLC drop  $R = 38 \mu\text{m}$  in glycerine/lecithin mixture inducing a planar to homeotropic conditions change. Authors underline the additional topological defect appearing for the case of homeotropic anchoring, namely an equatorial disclination (from Ref. 33).

### 6.3 Conclusions

In summary, presented literature should evidence a reader that investigations of dispersed liquid crystal systems are the active field of both theoretical and experimental research. Several peculiarities, coming from the non-compatibility of spherical boundary and anisotropy of the mesophases arise. First, it was shown that it is common for both nematic and cholesteric droplet to contain topological defects. It was shown that by imposing the change in the boundary conditions in the case of nematic droplets, a change between different textures may be seen, which is accompanied by the transformation of topological defects – specific for the two structures. Later, basing on the example of cholesteric droplets suspended in an isotropic matrix it was proven that the spatial confinement of ordered structures may impose certain restrictions on the configurations of the order parameter that in consequence requires the appearance of topological defects in the ground state. Identification of those defects and observation of their evolution during the studies of dynamic processes opens new possibilities, where topological methods may be helpful for the structure analysis.

It was also shown that the spatial confinement – together with the relative smallness of the twist elastic constant, may lead to twisted structures – even for the mesophases composed of nonchiral molecules. In other words, the specific feature of soft matter is that it does not always require the presence of chiral centers in the molecules constituting the mesophase – to exhibit chirality.

Moreover, textures of cholesteric droplets were shown to be highly dependent by the extent of geometrical confinement: the radius-to-pitch ratio, resulting in multiple possibilities of cholesteric droplet textures appearing. A temperature-driven change of the cholesteric pitch, enabled to steer between the two limiting cases of stable cholesteric droplets: radial spherical (high  $R/P$ ) and twisted bipolar (small  $R/P$ ). Ultimately, it was shown, that a helix inversion in cholesteric droplets may be induced by the temperature. Understanding this process and resolving the subsequent steps is an important point for the studies contained in the Chapter 7, where photo-induced changes of cholesteric droplet textures are provoked.

## 6.4 References

1. Friedel, G. *Ann. Phys.* **18**, 273–474 (1922).
2. Eelkema, R. & Feringa, B. L. *Org. Biomol. Chem.* **4**, 3729–3745 (2006).
3. van Delden, R. A.; Mecca, T.; Rosini, C. & Feringa, B. L. *Chem. Eur. J.* **10**, 61–70 (2004).
4. Pierraccini, S.; Gottarelli, G.; Labruto, R.; Masiero, S.; Pandoli, O. & Spada, G. P. *Chem. Eur. J.* **10**, 5632–5639 (2004).
5. Krivoshey, A. I.; Shkolnikova, N. I.; Chepeleva, L. V.; Kutulya, L. A. & Pivnenko, N. S. *Funct. Mater.* **11**, 76–81 (2004).
6. Mathews, M. & Tamaoki, N. *Chem. Commun.* 3609–3611 (2009).
7. Katsonis, N., Lacaze, E. & Ferrarini, A. *J. Mater. Chem.* **22**, 7088–7097 (2012).
8. Dierking, I. *Textures of liquid crystals*, John Wiley & Sons (2006).
9. Kawata, K. *Chem. Rec.* **2**, 59–80 (2002).
10. Laschat, S.; Baro, A.; Steinke, N.; Giesselmann, F.; Hagele, C.; Scalia, G.; Judele, R.; Kapatsina, E.; Sauer, S.; Schreivogel, A. & Tosoni, M. *Angew. Chem. Int. Ed.* **46**, 4832–4887 (2007)
11. De Gennes, P.-G. & Prost, J. *The Physics of Liquid Crystals*, Oxford University Press (1993).
12. Kleman, M. & Lavrentovich, O. D. *Soft matter physics: an introduction*, Springer (2003).
13. Rapini, A. & Papoular, M. *J. Phys. Colloq.* **30**, C4–54–C4–56 (1969).
14. Lehmann, O. *Z. Phys. Chem.* **5**, 427–435 (1904).
15. Crawford, G. P. & Zumer, S. *Liquid Crystals in Complex Geometries*, Taylor & Francis, London (1996).
16. Crooker, P. & Yang, D. *Appl. Phys. Lett.* **57**, 2529–2531 (1990).
17. Lavrentovich, O. D. *Liq. Cryst.* **24**, 117–126 (1998).
18. Volovik, G. E. & Lavrentovich, O. D. *Zh. Eksp. Teor. Fiz.* **85**, 1997–2010 (1983).
19. Mermin, N. D. *Rev. Mod. Phys.* **51**, 591–648 (1979).
20. Volovik, G. & Mineev, V. *JETP* **45**, 1186–1196 (1977).
21. Kleman, M. & Lavrentovich, O. D. *Phil. Mag.* **86**, 4117–4137 (2006).
22. Williams, R. *J. Phys. A* **19**, 3211–3222 (1986).

23. Drzaic, P. S. *Liq. Cryst.* **26**, 623–627 (1999).
24. Lavrentovich, O. D. & Terentjev, E. M. *JETP* **64**, 1237–1244 (1986).
25. Lavrentovich, O. D. & Sergan, V. V. *Nuovo Cimento D* **12**, 1219–1222 (1990).
26. Prinsen, P. & van der Schoot, P. J. *Phys.: Condens. Matter* **16**, 8835–8850 (2004).
27. Tortora, L. & Lavrentovich, O. D. *Proc. Natl. Acad. Sci. U.S.A.* **108**, 5163–5168 (2011).
28. Lavrentovich, O. D. *Phys. Rev. A* **46**, R722–R725 (1992).
29. Bajc, J.; Crooker, P. & Zumer, S. *Liq. Cryst. Today* **7**, 1–6 (1997).
30. Bajc, J.; Bezic, J. & Zumer, S. *Phys. Rev. E* **51**, 2176–2189 (1995).
31. Xu, F. & Crooker, P. *Phys. Rev. E* **56**, 6853–6860 (1997).
32. Robinson, C.; Ward, J. & Beevers, R. *Farad. Discuss.* **25**, 29–42 (1958).
33. Kurik, M. V. & Lavrentovich, O. D. *JETP Lett.* **35**, 444–447 (1982).
34. Bajc, J. & Zumer, S. *Phys. Rev. E* **55**, 2925–2937 (1997).
35. Sec, D.; Porenta, T.; Ravnik, M. & Zumer, S. *Soft Mat.* **8**, 11982–11988 (2012).
36. Humar, M. & Musevic, I. *Opt. Express* **18**, 26995–27003 (2010).

## Chapter 7

### Photo-switching the structures of cholesteric liquid crystal droplets with planar surface anchoring

This chapter is dedicated to studying experimentally droplets of photo-controllable cholesteric liquid crystals (CLCs), where the chiral dopant is an overcrowded alkene-based molecular motor. Since the droplets of cholesteric liquid crystal are known to exhibit different configurations of director field, depending on the extent of their geometrical confinement, a brief static description is provided at the beginning of the chapter. The subsequent section is related to studying the dynamic behavior of frustrated systems, and the influence of the extent of geometrical confinement on the expression of chirality. Upon the irradiation by ultraviolet light, a stable form of molecular motor is photo-isomerized into a form that has a different helical twisting power, and induces a cholesteric helix having an opposite helicity. This property of molecular motors allows photocontrolling the cholesteric pitch, up to helix inversion, simply by adjusting the irradiation conditions. We study the induced structural variations.

## 7.1 Introduction

The emerging area of soft photonics has attracted a lot of interest during the last decade.<sup>1-4</sup> Thermotropic liquid crystals (LCs) play a major role in this field because, as a consequence of birefringence and specific configurations of the director field. Their optical properties are often different from the optical properties of solids and isotropic materials. Humar *et al.*<sup>5</sup> have shown recently that a nematic LC droplet can confine light by total internal reflection and thus support whispering-gallery modes. Moreover, they have shown that their chiral counterparts, cholesteric liquid crystal droplets act as spherical Bragg onion microcavities as a result of periodic modulation of the refractive index in the radial direction. When fluorescent dye molecules are introduced in the material, these cholesteric droplets have been shown to isotropically emit coherent light, thus constituting the first omnidirectional microlaser.<sup>6</sup> The main advantage of using LCs as a gain medium comes from the enhanced tunability of the spectral properties, which has been achieved by using electric field<sup>5</sup> and temperature.<sup>6</sup>

However, temperature and electric field are not the only parameters that can steer effectively the director field of a chiral liquid crystal, thereby controlling its structure and determining its optical properties. One alternative possibility is to use a photo-responsive chiral dopant: as discussed in Chapter 6 (6.1.2). Under irradiation, this chiral dopant changes its molecular form, and the chirality of the LC in which the chiral motor is embedded varies. This chapter reports on studies of cholesteric liquid crystal (CLC) droplets in which chirality is introduced by a chiral molecular motor, used as a dopant (Figure 7.1). The special property of the overcrowded alkene-based molecular motor used for the studies is, that under irradiation the dopant, which has high twisting power, is converted into an isomer with comparatively high twisting ability – but with opposite sign. Therefore, photo-isomerization process causes unwinding and subsequent rewinding of the cholesteric helix, in the opposite sense. Monitoring the texture modifications in cholesteric liquid crystal droplets, as a result of irradiation with light gives an opportunity to understand more completely the behavior of chiral dispersions and in particular to probe the expression of chirality in frustrated systems, in the presented system also for the case of helical twist inversion.

Results presented here are devoted to studies performed in a transparent matrix that induces planar anchoring of liquid crystal molecules: when the radius-to-pitch ratio is sufficiently high, the cholesteric droplets display a radial texture.<sup>7-9</sup> The beginning of the chapter contains the detailed description of the system just after the preparation of samples. Structural analysis of droplets, depending on the droplet size, is a starting point for understanding the dynamic processes induced by light. Subsequently, the second part of the chapter is devoted to monitoring and qualitative description of the transitions of structures under irradiation.

### 7.1.1 Overcrowded alkenes – molecular motors as dopants for photo-responsive cholesteric liquid crystals

Structure of molecular motor used in the frame of this chapter is presented in Figure 7.1(a). A motor molecule consists of a rotor part that dictates the direction of rotation, a central carbon–carbon double bond that functions as an axle, and a fluorene stator part that resembles the liquid crystal host.<sup>10</sup> The three molecules shown on the panel (a) differ by a substituent in the rotor part, which is either a methyl group, an *iso*-propyl group or a phenyl group. Upon irradiation of motor molecule with ultraviolet light of  $\lambda = 365$  nm, a photochemical isomerization around the central double bond occurs that results in the helix inversion. A subsequent thermal step, again involving helix inversion, occurs readily at 20 °C (with a reaction-time half-life of 9.9 min in toluene).<sup>11</sup> Two photochemical steps, each followed by a thermal step, add up to a full 360° rotary cycle, which is depicted by the Figure 7.1(b).

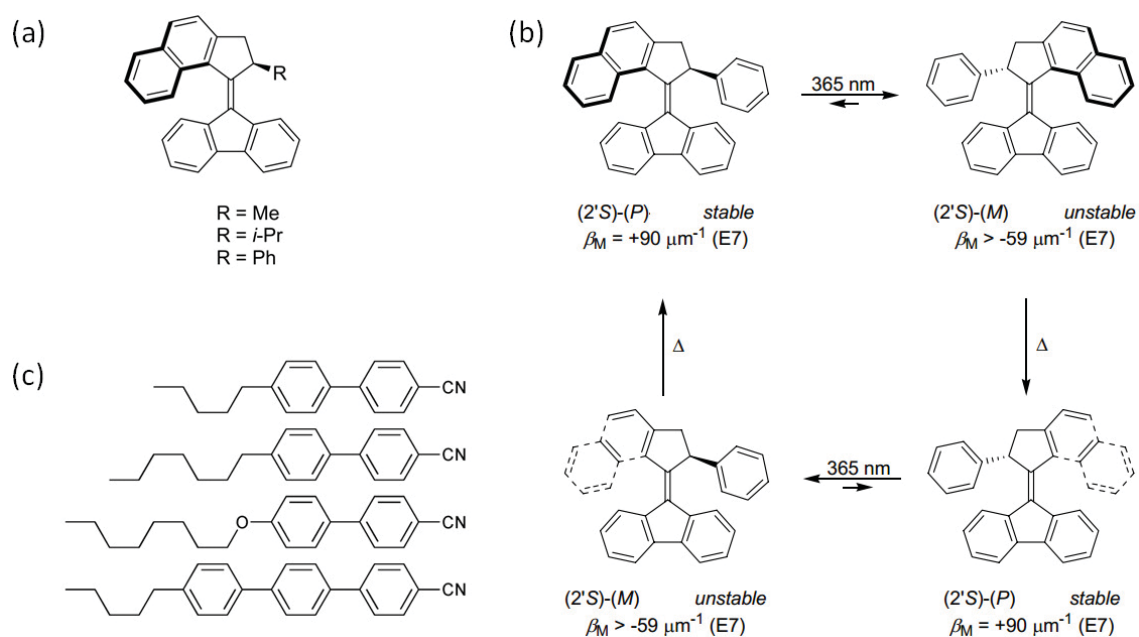


**Figure 7.1** (a) Chemical structures of three molecular motors of the overcrowded alkene homologues. (b) Light-driven unidirectional rotation of molecular motor and the helical twisting powers ( $\beta_M$ ) associated with the four structures during the rotary process. (c) E7 which is an eutectic liquid crystal mixture of cyanobiphenyls, used as host nematic liquid crystal (from Ref. 12).

E7 is a commonly used mixture of cyanobiphenyls, which we use as a nematic liquid crystal host. It is important to mention since helical twisting power of a dopant is actually a property of a dopant-liquid crystal pair, and results from complex interaction between the chiral molecule and the molecules of the host matrix.<sup>13</sup> For the studies presented in this chapter different concentrations of ‘Methyl motor’ molecule in E7 were used, dispersed in PVP/glycerol (25/75 wt%) matrix.



### 7.1.2 Determination of the cholesteric pitch

Pitch determination for all of the mixtures has been performed by the Grandjean-Cano method. By using the wedge cell of known geometry, like one schematically presented on Figure 7.2(a), we are able to localize the disclination lines and to measure the distance between them (denoted on the Figure 7.2.(a) by 'R') which is related to the cholesteric pitch of the prepared mixture. A polarized microscopy image of one of the samples is shown on Figure 7.2(b) with the disclination lines in the vertical direction.

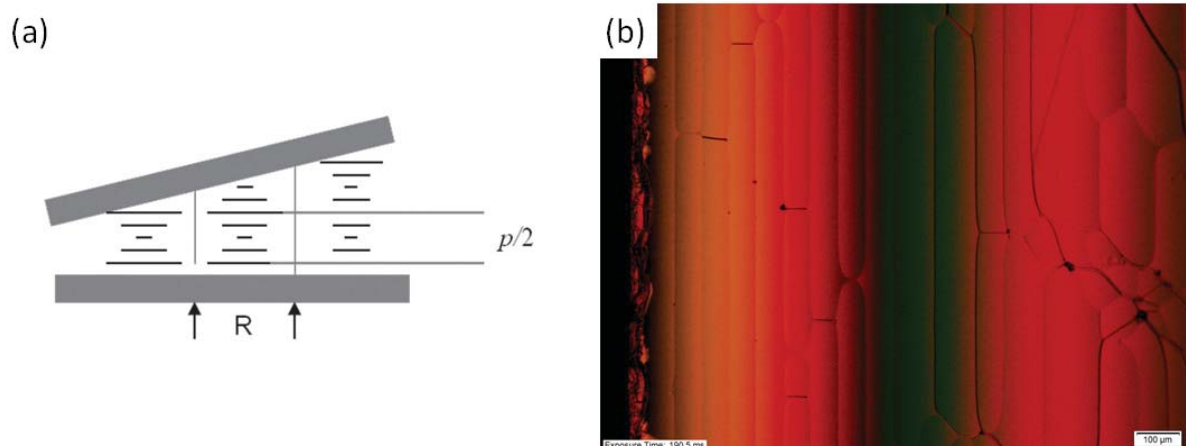


**Figure 7.2** (a) Schematic illustration of a Grandjean-Cano wedge cell for determination of the cholesteric pitch of a CLC mixture doped with the chiral molecule of known helical twisting power. Disclination lines are pointed out with arrows and the thickness change between two domains is marked as  $p/2$  (from Ref. 14). (b) Polarized microscopy image of the wedge cell sample of one of the CLC/E7 mixtures.

In order to perform studies with different droplet size-to-pitch ratio four mixtures of 'Methyl motor' ( $R = Me$ , Figure 7.1(a)) in E7 have been prepared, with a dopant concentration ranging from 0.5 to 1.5 wt%. Chiral dopants inducing helicity of both handednesses have been used to compare the behavior of cholesteric liquid crystals having opposite twist directions. Samples are designated as '1x' and '2x', where '1' and '2' denotes *R*- and *S*-enantiomers of the molecular motor, respectively. The following pitch ( $P_w$ ) values were obtained, in agreement with a  $\beta_M = 43.33 [\mu\text{m}^{-1}]$ :<sup>15</sup>

Sample	$P_w$ pitch [ $\mu\text{m}$ ]
1a	10,12
1b	1,95
1c	2,46
2a	2,27

Three liquid crystals (**1b**, **1c** and **2a**) display a small initial pitch ( $P_w$ ), and one (**1a**) possesses a large  $P_w$  value. Since the second part of this chapter involves dynamic studies of cholesteric droplets a behavior of non-confined cholesteric pitch under irradiation is needed as a reference. All wedge samples were irradiated in similar conditions and the evolution of the pitch was determined from the changing distances between the disclination lines. The results are summarized on Figure 7.3.

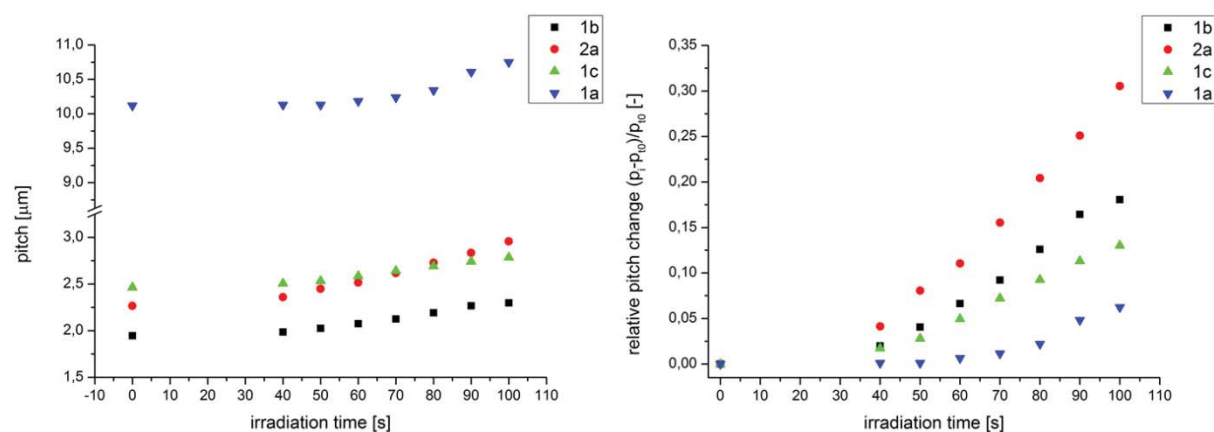


**Figure 7.3** Evolution of the cholesteric pitch in time, for 'Methyl motor'/E7 mixtures under irradiation with UV light ( $\lambda = 365$  nm).

As expected, we observe an increase of the pitch, that we attribute to helix unwinding. Assuming similar irradiation conditions and an identical cell geometry, surprisingly sample **2a** exhibits a larger pitch modification than the other photo-responsive CLCs (relative to its initial value). Behavior of **1x** samples of *R*-enantiomer shows a tendency, that for increasing pitch (**1b** < **1c** < **1a**) the relative pitch modification measured after 100 s,  $(^{100}P_w - ^0P_w)/^0P_w$  decreases, in agreement with the fact that the dopant concentration is lower when the pitch  $P_w$  is larger.

	1b	1c	1a
$^0P_w$ [μm]	1.95	2.46	10.12
$(^{100}P_w - ^0P_w)/^0P_w$ [-]	0.18	0.13	0.06

During the irradiation of the wedge cell, cholesteric pitch of the irradiated CLC mixture increases, what is manifested by increasing the distance between the disclination lines. Since for the wedge cell used for the studies all of the disclination lines disappeared from the monitored area, determination of the resulting pitch was not possible anymore. However, since molecular motor exhibits a helix

inversion, the chirality of the mixture should be re-gained for the longer irradiation times, when the photostationary state is reached. All of the CLC mixtures were irradiated for a period of 10 and 20 minutes, but none of them displayed cholesteric helix inversion, manifested by re-appearance of the disclination lines, i.e. the pitch. However, knowing the cholesteric pitch of all of the prepared CLC mixtures we are able to calculate the actual content of the chiral dopant in each of CLC mixtures. Then, possessing the value of helical twisting power at the photostationary state,  ${}^{\text{PSS}}\beta_{\text{M}} = -17.33 [\mu\text{m}^{-1}]$ ,<sup>15</sup> we are able to determine the expected values of cholesteric pitch at the photostationary state ( ${}^{\text{PSS}}P_{\text{w}}$ ), presented in Table 7.1. It should be underlined that this estimation may be true only under assumption that the same composition at PSS has been reached, what requires exactly similar experimental conditions.

**Table 7.1** Calculated cholesteric pitch values for studied CLC mixtures at the photostationary state. Also indicated are values of  $R_{\text{critical}}$ , i.e. minimal values of  $R$  that support expressing of radial spherical texture.

Sample	${}^{\text{PSS}}P_{\text{w}}$ pitch [ $\mu\text{m}$ ]	$R_{\text{critical}}$ [ $\mu\text{m}$ ]
1a	25.30	32.89
1b	4.88	13.16
1c	6.15	16.61
2a	5.68	15.32

Then possessing the values of helical twisting power at the photostationary state we are able to determine the limit value of  $R$  which would support the expressing of chirality by a radial texture. The additional assumption is that the estimation of  $R/{}^{\text{PSS}}P_{\text{w}} > 2$  and of  $R/{}^{\text{PSS}}P_{\text{w}} > 2.75$  holds for **1a** and (**1b**, **1c**, **2a**) CLC mixtures.

## 7.2 Droplets of photo-responsive cholesteric liquid crystals in a glycerol matrix

### 7.2.1 Low concentration of chiral dopant

Figure 7.4 shows polarized microscopy images of droplets from the cholesteric liquid crystal **1a**, dispersed in the glycerol matrix. As may be noticed from the left panel, the large droplets ( $R > 12.7 \mu\text{m}$ ) contain spiral concentric features that are typical for a radial spherical structure, whereas the smaller droplets, presented on the right panel, are lacking this feature and display a bipolar texture. These two structures are presented in Chapter 6 (Figure 6.11(a) and Figure 6.9, respectively). The presence of both types of textures is in agreement with the boundary conditions imposed by the matrix, which is a planar anchoring.<sup>7</sup> The concentric feature for radial spherical droplets leads to periods approximately equal to half the pitch value ( $P_w$  value,  $10.12 \mu\text{m}$ ).<sup>16</sup> The transition between the two structures corresponds  $R/P_w = 1.3$ , which is a much lower value than found in the literature, namely  $R/P_w = 6$ .<sup>9</sup>

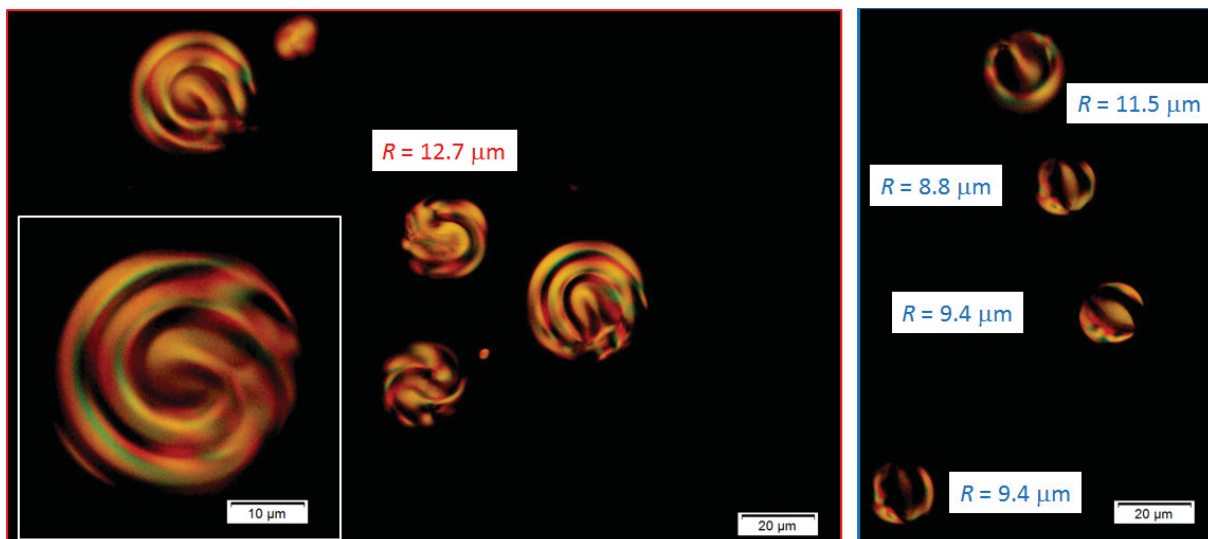


**Figure 7.4** Polarized microscopy images of **1a**/E7 droplets. Droplets in the left panel represent the radial spherical texture and droplets on the right represent the twisted bipolar texture. There is a clear relation of structure presented by the droplet and its size. The droplets of diameter  $P = 11.5 \mu\text{m}$  or smaller represent bipolar structure. Bigger droplets possess visible concentric onion-like feature which is a manifestation of radial structure. Some intermediate cases, like droplet in the center of the image ( $R = 12.7 \mu\text{m}$ ) are also observed.

## 7.2.2 High concentration of chiral dopant

Figure 7.5 shows a polarized microscopy image of droplets of CLC of high concentration of dopant (**1b**) dispersed in PVP/glycerol (25/75 wt%) matrix. Vast amount of droplets exhibit textures with periodic concentric rings of alternating light-dark colors. The stripes are observed because of the modulation of the refractive index, their periodicity corresponding to half of the pitch. The cholesteric helix is pointing from the center of the droplet in all directions outwards to the surface. As shown in the model and included images on Figure 6.12(b) the texture may appear two-folds, either as an 'onion-like' with a visible linear *radial* defect pointing from the center of the droplet, or like a 'spiral', when the defect is pointing perpendicularly to the image plane. The difference with the (**1a**) sample is visible at first glance, since the droplets exhibiting the radial spherical texture possess a much smaller radial period, related to the smaller value of cholesteric pitch, than previously observed. Moreover, for this chiral mixture the droplets of the other structures, the bipolar ones are hardly found since they may correspond to droplets of very small sizes, like the ones highlighted by the blue squares on Figure 7.5.

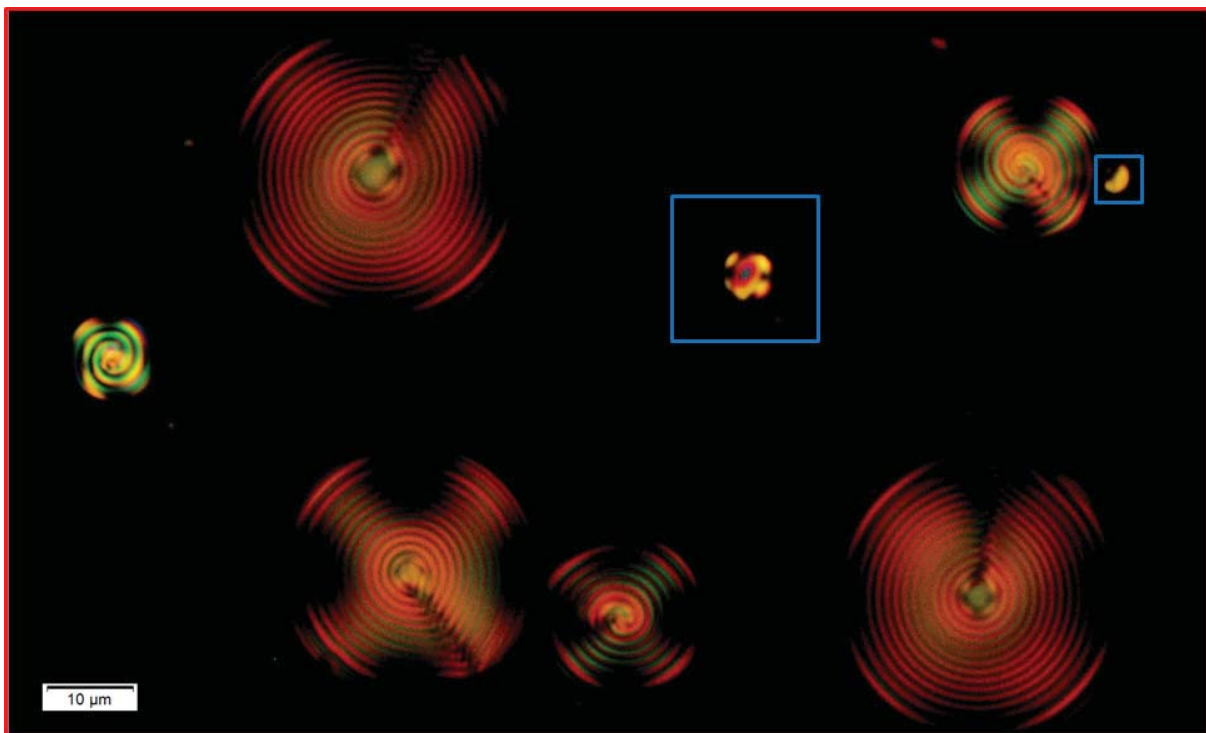


**Figure 7.5** Polarized microscopy images of **1b**/E7 droplets. Majority of droplets exhibit the onion-like textures, i.e. radial spherical textures, and few small ( $D < 5 \mu\text{m}$ ) droplets resemble the bipolar textures. For the former case the perfect structures with nearly concentric shells are clearly visible. Occasionally visible (if not out of focus) are also the defect lines which go from the center of droplet to the surface there is a defect line.

### 7.3 Effect of geometrical confinement on the cholesteric textures

What may be further noticed from Figure 7.5 is that the period of the smaller green-colored droplet on the left-hand side of the image appears slightly larger than the period found in bigger droplets. This tendency may be seen more explicitly on Figure 7.6.

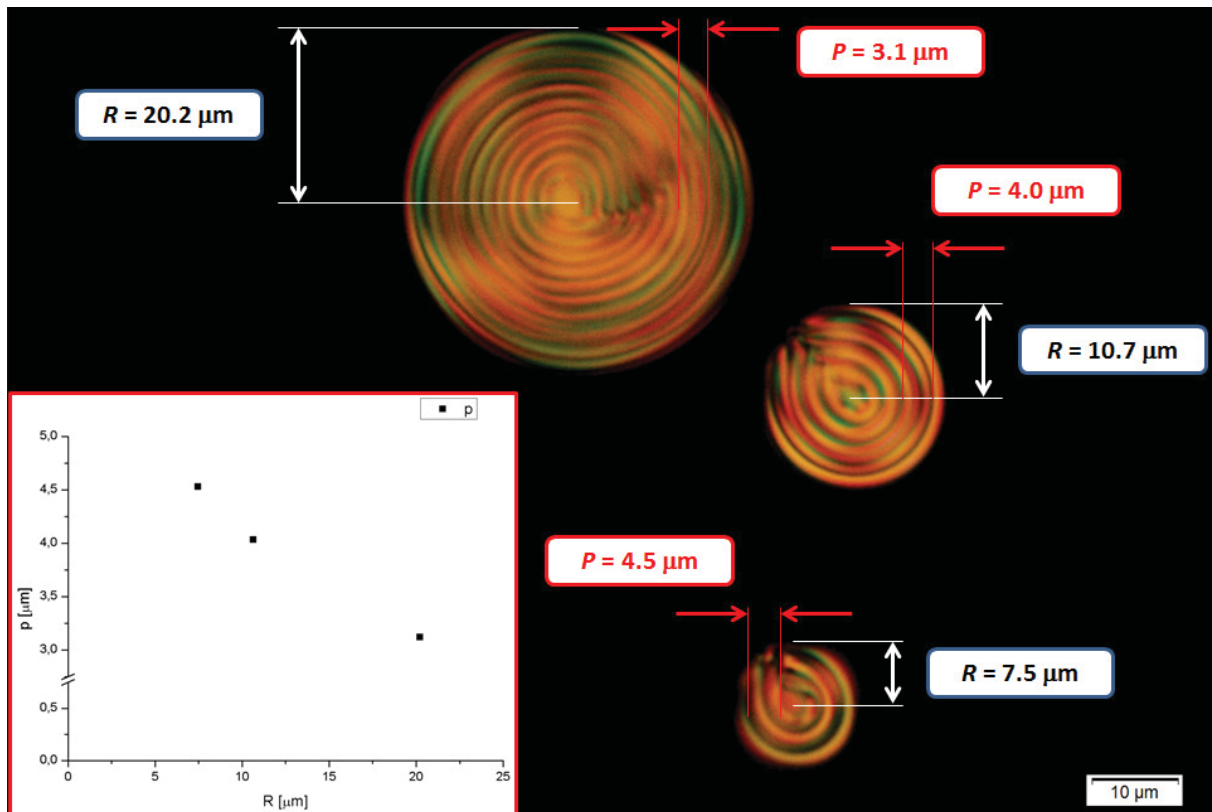


**Figure 7.6** Polarized microscopy images of **1b**/E7 droplets. The three radial spherical droplets show an increase in the value of radial period as the droplet size decreases. The tendency is shown by the  $P$  vs  $R$  plot (*inset*).

Figure 7.6 shows polarized microscopy images of three droplets of different sizes:  $R = 20.2 \mu\text{m}$ ,  $R = 10.7 \mu\text{m}$  and  $R = 7.5 \mu\text{m}$ . We observe that  $P$ , the period of the radial texture increases when the size of the droplet decreases:  $P = 3.1 \mu\text{m}$ ,  $P = 4.0 \mu\text{m}$  and  $P = 4.5 \mu\text{m}$ , respectively. A detailed examination of samples with a measurement of the size of the droplet and respective radial period for large amount of droplets could help in finding any relation between the measured period (which may be considered as an apparent pitch value) and the radius ( $R$ ) of the droplets. These results are presented on Figure 7.7. For clarity, the data extracted from CLC mixture of lower content of chiral dopant (**1a**) where  $P_w$  is roughly five times bigger, are shown separately (*top*). Horizontal dashed-lines represent the value of the cholesteric pitch for each of the cholesteric liquid crystals.

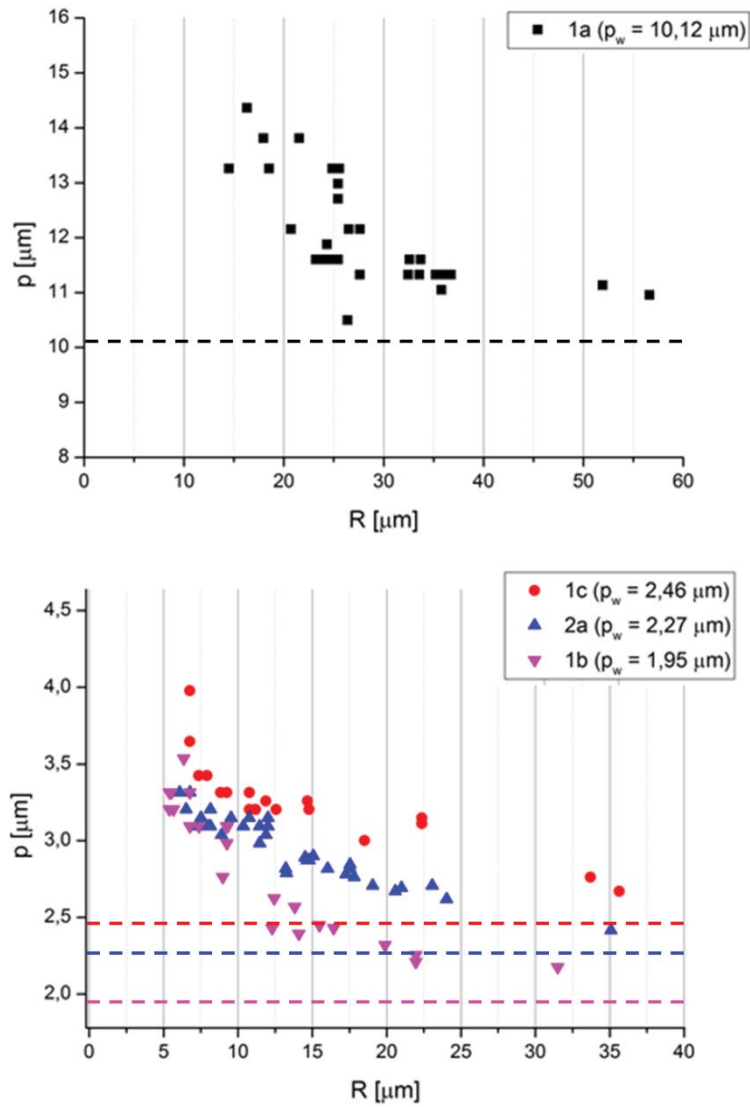


**Figure 7.7** Plots showing the dependence of the radial period of the radial spherical droplets as a function of droplets radius. Results are divided into two plots representing mixture of a low concentration of chiral dopant (*top*) and mixtures of high concentration of chiral dopant (*bottom*). In both cases a similar trend is visible: that the measured value of period (apparent pitch) becomes larger, as the droplet size reaches ca.  $R = 15 \mu\text{m}$ , and  $R = 5 \mu\text{m}$ , for droplets of low and high concentration of dopant, respectively. Horizontal dashed-lines represent the cholesteric pitch values for respective cholesteric liquid crystals under investigations.

A general trend may be noticed, namely, the radial period diminishes when the radius of the droplet increases, and asymptotically tends to the  $P_w$  values obtained on the basis of the wedge cell measurements. The smallest values of radial period found for each sample, which normally stand for the biggest radial spherical droplets, were 8% to 12% bigger than the respective  $P_w$ :

Sample	$P_w$ [ $\mu\text{m}$ ]	$P_d$ for $R_{\text{max}}$ [ $\mu\text{m}$ ]	Relative ( $P_d/P_w$ )
1b	1.95	2.18	1.12
2a	2.27	2.42	1.07
1c	2.45	2.67	1.09
1a	10.12	10.96	1.08

Also, for the three samples of pitch around 2  $\mu\text{m}$ , an asymptotic behavior for high pitch values is found for droplets reaching size of  $R \sim 6 \mu\text{m}$ . Similar tendency is found for the samples of low concentration of dopant, for which analogical behavior is observed for  $R$  reaching 15  $\mu\text{m}$ .

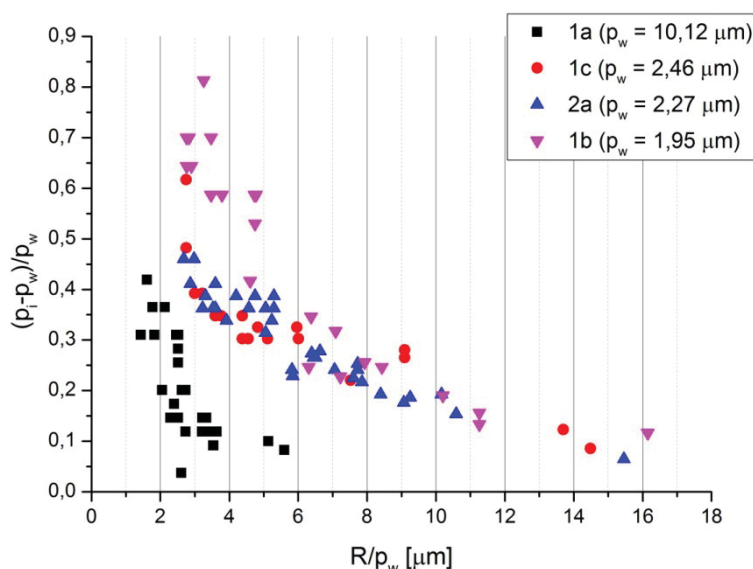


**Figure 7.8** Relative period change  $(P-P_w)/P_w$  vs  $R/P_w$  for the different  $P_w$  values. One should notice that the black squares that represent the CLC mixture of low dopant concentration enables to access the radial structure for the relatively lower size, considering the geometrical confinement.

If one wants to take into consideration the geometrical confinement, we need to scale each system relative to its confinement parameter,  $R/P_w$ . Then the relative change of the pitch for each droplet with respect to the confinement, namely:  $(P-P_w)/P_w$  @ y-axis vs  $R/P_w$  @ x-axis, is depicted on Figure 7.8. We evidence:

- A smaller chirality strain, for CLC mixtures of low dopant concentration ( $P_w = 10.12 \mu\text{m}$ ) with respect to the mixtures of high dopant concentration. The  $(P-P_w)/P_w$  values are substantially smaller for equal confinement parameter,  $R/P_w$ ;



- The vertical asymptotic behavior for diminishing  $R/P_w$  values correspond to the transition from radial texture to bipolar texture. The transition  $R/P_w$  values appear smaller ( $R/P_w < 2$ ), for CLC mixtures of low dopant concentration, in contrast with samples of highly-doped CLC mixtures, for which minimal  $R/P_w \sim 2.75$ . This difference may be connected with the lower constraints coming from the elastic forces in the first case since radius at transition is significantly larger ( $R = 14.5 \mu\text{m}$ , with respect to  $R = 5.4 \mu\text{m}$ ). This difference may account as well for the different slopes of the curves shown on Figure 7.8, between large (**1a**) and small (**1b, 1c, 2a**)  $P_w$  values.

Concerning the transition between radial and bipolar textures, Xu and Crooker,<sup>9</sup> have reported that  $R/P_w$ , associated with this transition, increases as  $R$  becomes smaller than a few micrometers. Analogical situation for our system is presented on Figure 7.9. The plot shows the transition values of  $R/P_w$  for 4 studied CLC solutions, together with a linear fit. The situation presented here looks analogical to the case described by Xu and Crooker. Although Xu and Crooker studied a more extended spectrum of chiral solutions, the general trend of increase of  $R/P_w$  for smaller droplets is preserved. Moreover, decrease of  $R/P_w$  along  $R = 6 \mu\text{m}$  and  $R = 14 \mu\text{m}$  is comparable to the decrease in the analogous part of the Xu and Crooker plot (Figure 6.12(d)). However, it is understandable that the  $R/P_w$  values should be different, smaller in our case, since both the chiral dopant and the nematic host are different than in the cited literature.<sup>9</sup>

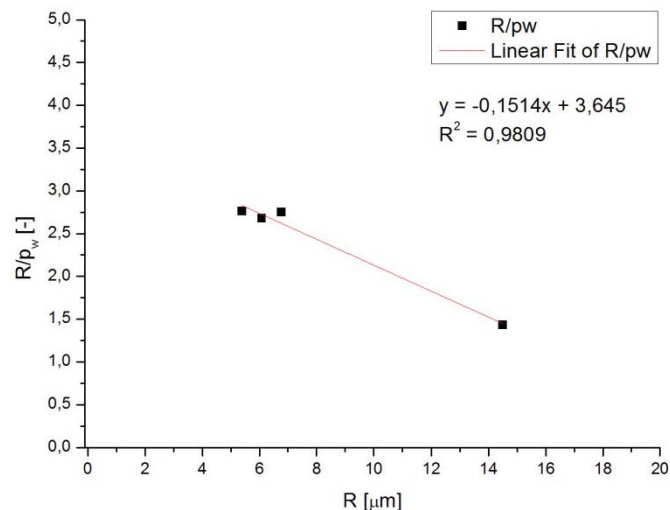


**Figure 7.9** Critical  $R/P_w$  values for the four studied concentrations of chiral dopant. In accordance with previous studies,<sup>9</sup> the accessible  $R/P_w$  value for radial spherical structure appearance is higher for the three CLC mixtures of higher concentration of chiral dopant (see three data points on the left).

To exclude the possibility of overlooking of the smaller than listed radial droplets of highly-doped CLC mixtures (**1c**, **1b** and **2a**), an additional analysis has been performed which aimed at finding the cholesteric liquid crystal droplets of bipolar textures. The result is depicted on Figure 7.10, where black and red symbols denote radial spherical and twisted bipolar structures, respectively. The plot on the right panel is the zoomed area of the transition-region for all four cholesteric liquid crystals. What should be noticed is that the transition between the two textures cases occurs rather sharply in all cases.

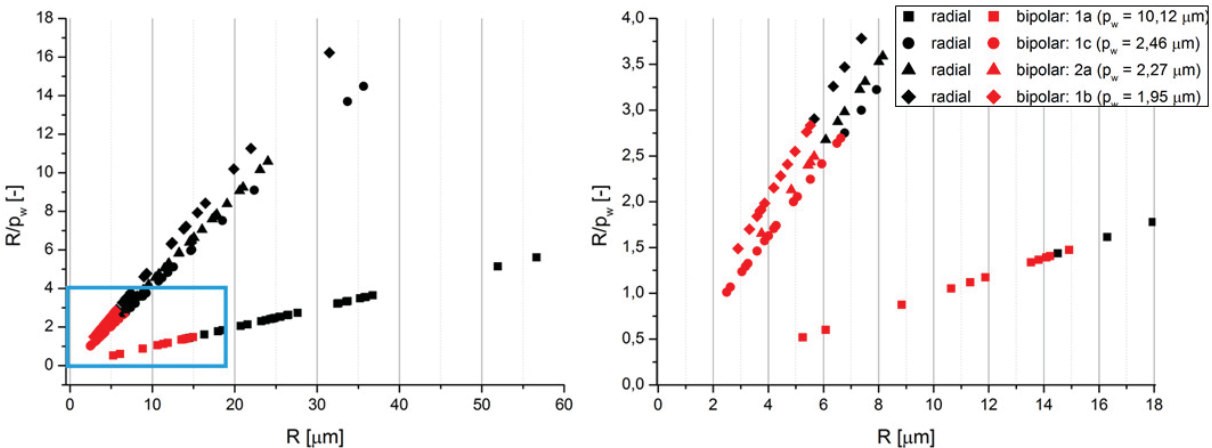


**Figure 7.10** Phase transition from the radial spherical structure (*black data points*) to the twisted bipolar structure (*red data points*) for the four studied concentrations of chiral dopant. The plot on the right-hand side is a zoomed area of smaller  $R/P_w$  values, highlighted by a blue box.

## 7.4 Photo-induced structural changes in the cholesteric droplets

We have observed that the texture of the droplets undergoes a sharp transition from radial to bipolar, when the  $R/P_w$  ratio decreases. We consequently sought to visualize the details of this transition, in relation with the cholesteric variations measured in film (Figure 7.3) and compare its dynamics with texture transitions driven by other stimuli, e.g. by temperature.<sup>9</sup> In order to trigger texture modifications the droplets were irradiated at  $\lambda = 365$  nm. Figure 7.11 presents a sequence of frames extracted from the corresponding movie. Frame (a) presents a single cholesteric droplet of mixture **2a**, of radius equal  $19.6 \mu\text{m}$ . The resulting  $R/P_w$  ratio equals 8.6. The value of the initial radial period  $P$ , extracted from this picture equals  $2.56 \mu\text{m}$ . Moreover, the spiral center of the droplet, together with the symmetric character of the image suggest that the radial defect is oriented parallel to the image plane (see lower image on the Figure 6.12(b)).

Frame (b) shows that immediately after irradiation is started the concentric feature begins to enlarge, which is a manifestation of the isomerization of the motor and what results in an overall decreasing helical twisting power. During the whole process the droplet retains its spherical shape with a constant radius and central symmetry of the radial period. It takes approximately 2.5 minutes for the spiral to unwind, which results in the formation of a twisted bipolar structure, depicted at frame (d). Proceeding with irradiation results in the appearance of another concentric feature (frame (e)) close to the surface of the droplet and turning inversely with respect to frame (c), in agreement with an inverse rewinding of the cholesteric pitch. However, this new texture is not complete since it covers only half of the droplets perimeter. It takes approximately 8 minutes for this process to stop. At this point, further irradiation has no positive feedback in formation of the complete radial period of the droplet, and actually the spiral starts disappearing, frame (f). After 20 minutes of irradiation the droplet has not well defined texture, obviously not one resembling a radial spherical texture. At this point the UV irradiation is stopped.

Immediately after stopping the irradiation with UV light, i.e. when the photochemical reaction leading to the metastable isomer is stopped, the droplet starts to relax back. Again through the twisted bipolar state, it takes approximately 1 minute that droplet regains its concentric feature, that is well depicted by frame (g). This process is continued and the new concentric rings are appearing from the center of the droplet, pushing the 'older' ones outwards, to the droplets perimeter. In consequence the period start to squeeze and the radial texture is progressively smaller, frame (h). In addition the radial defect clearly appears, after less than 4 minutes (frame (i)). Frame (j) evidences that after about 10 minutes of relaxation the droplet attains its original radial period value. The only noticeable difference is the reorientation of the radial defect which, originally pointing in direction perpendicular to the image – now is oriented in the position 5 o'clock.

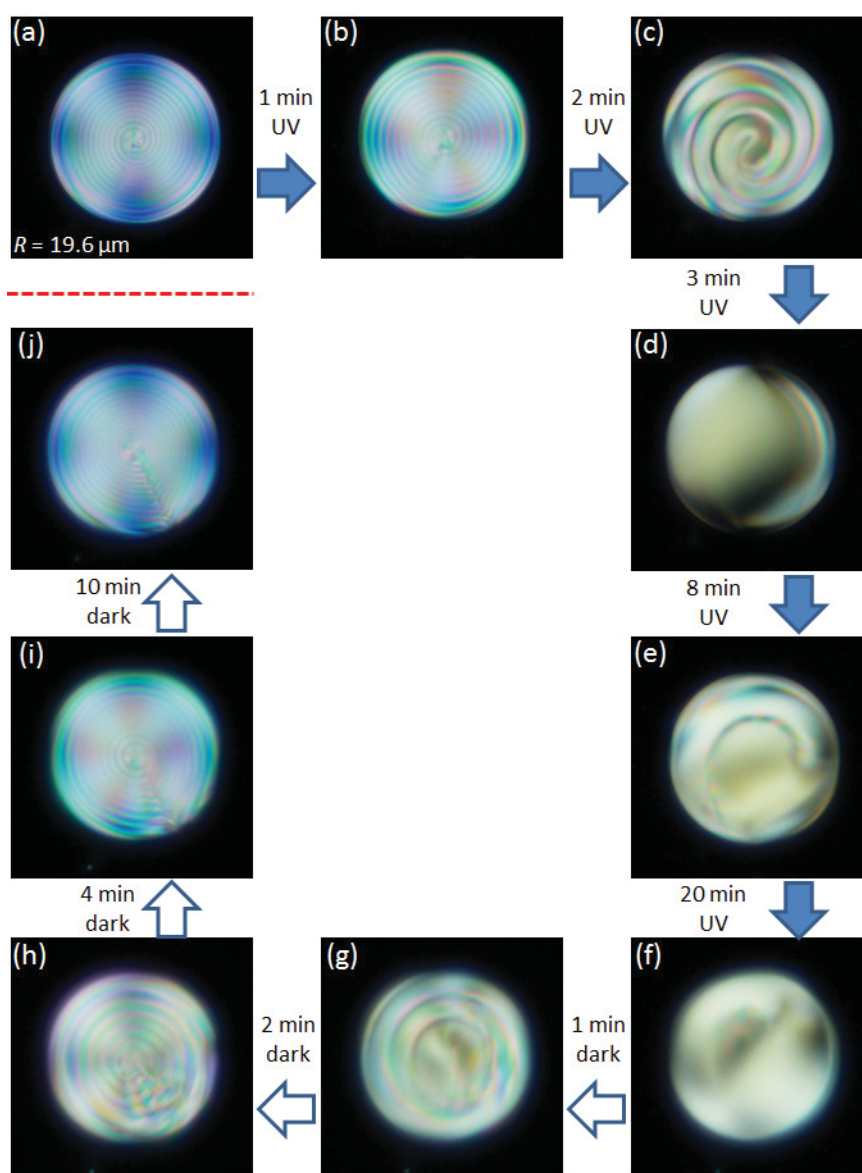


**Figure 7.11** Sequence of polarized microscopy patterns (transmission mode) showing the evolution of the texture of droplet (**2a**) under the irradiation with UV. (a) to (e) evolution of  $R = 19.6 \mu\text{m}$  droplet texture during the irradiation. Frames (a) to (c) show the unwinding of radial structure that leads to a bipolar structure, (d), followed by initial stage of formation of helix of reverse handedness, (e). The result of last step (e) ceases with time, (f). Frames (f) to (j) depict the relaxation process starting immediately after irradiation of the sample has been stopped. Original size of the period of the radial texture is restored after ca. 10 mins, (j). However, although the original size of the radial period is restored, there is a visible difference in the orientation of the radial defect. The originally pointing to the plane of the Figure, (a), now it is in the 5 o'clock position, (j).

These results thus evidence a continuous unwinding of the presented droplet, but without a complete reversal rewinding. This may be due to the expected high values of the pitch at the photostationary state ( $P_w^{PSS}$ ), displayed on Table 7.1. According to the value for **2a**, a photostationary critical radius to obtain radial texture for **2a** CLC would be around  $15.3 \mu\text{m}$  ( $R/P_w^{PSS}$  of the order of 2.7), the same order of magnitude than the presented droplet which is slightly larger, in agreement with the observation of (partial) rewinding. It must be noticed that rewinding is observed after 8 minutes, whereas it has never been observed in the wedge cells.

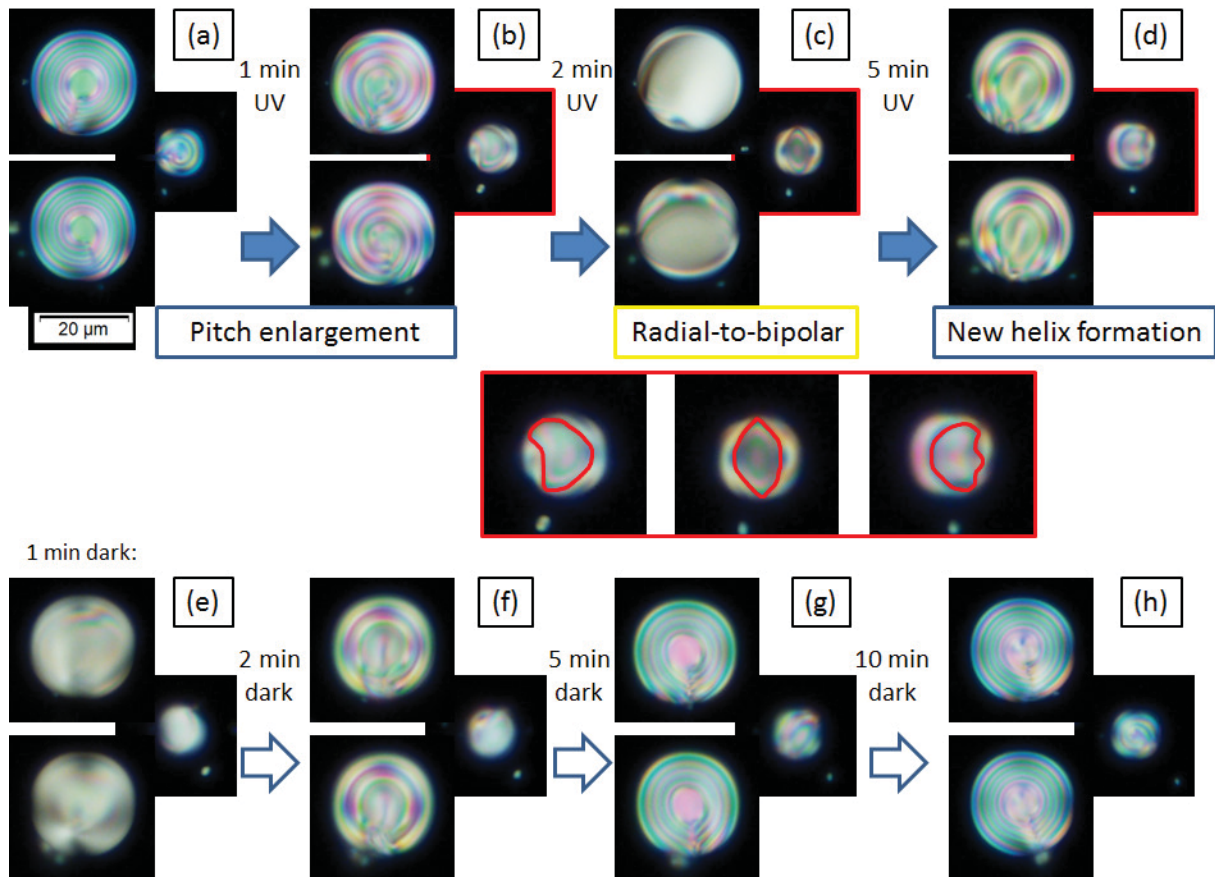


**Figure 7.12** Sequence of polarized microscopy patterns (transmission mode) showing the evolution of textures of three droplets (**1b**) under the irradiation with UV. The two droplets on the left part of each panel have similar radius equal  $11.9 \mu\text{m}$  and the smaller droplet has radius equal  $5.6 \mu\text{m}$ .

Figure 7.12 presents the sequence of frames extracted from another movie. Each frame presents three cholesteric droplets of mixture **1b**, of which radii are equal to:  $11.9$ ,  $11.9$  and  $5.6 \mu\text{m}$ . The respective  $R/P_w$  values are:  $6.1$ ,  $6.1$  and  $2.87$ . Values of size of radial period are estimated to be  $2.53 \mu\text{m}$  for the two bigger droplets, and the radial period is not measurable in the case of the smaller droplet. Since the two droplets on the left part of each panel have similar size and radial period it will

be important to examine their behavior – whether it is the same – and compare it with the behavior of the smaller droplet. Since all the three droplets were well focused at one time, they must lie in one horizontal plane, and thus we may assume identical irradiation conditions. After starting of irradiation, the concentric radial periods in all of the droplets start to enlarge, as in the previous case depicted by Figure 7.11. However, complete disappearance of the radial period seems to happen faster, than previously. Already after 1 minute of irradiation the period of the small droplet has almost completely disappeared. The analogous situation for bigger droplets happens after less than 2 minutes, which is again a shorter time than the first presented dynamical study. So there is a radial-to-bipolar texture transition in between frames (b) and (c). The middle panel (red box) underlines the evolution of the bipolar texture of the small droplet close to the helix inversion. Initially deflected to the left, the defect becomes symmetric (bipolar) and then a change of the deflection to the right is observed. This may be a chirality manifestation, demonstrating that, similarly to homeotropic sessile droplets, even if the defect is a nematic defect, optically, the droplet remains chiral and changes of chirality during the irradiation.<sup>17</sup> After 3 minutes of irradiation the first signs of reappearance of the radial period may be noticed. Frame (d) evidences that after 5 minutes the helix of inverse twist is readily visible, but at this point process is slowed down and stopped.

Small droplet on the right part of the panel is hardly perceived as a radial texture remaining rather bipolar after reversal of handedness. This is in agreement with a large value of the cholesteric pitch in the photostationary state with respect to the initial one. The results of Figure 7.12 finally mean that the droplets presented on Figure 7.12 achieve the following steps of unwinding and helix inversion generally faster, than for the Figure 7.11. This may be in relation with their smaller initial  $R/P_w$  ratios, i.e. 6.1 and 2.87 versus 8.6. On the other hand, for **1b** mixture, we expect a photostationary pitch  $^{PSS}P_w = 4.88 \mu\text{m}$ . So the calculated photostationary confinement is  $R/^{PSS}P_w = 2.44$  for the large droplets on Figure 7.12. It is of the order of magnitude of 2.7, which may explain why we indeed observe it. The reason that we observe it more evidently than on the Figure 7.11 may be due to the fact that rewinding is faster for smaller droplets, similarly to unwinding.

The bottom panels also show the relaxation process. From textures on the frames (e) and (f) it may be concluded that the three presented droplets need less than one minute to transform into bipolar texture, and less than 2 minutes to re-gain first signs of the radial spherical texture. In total, system needs less than 10 minutes to restore its original properties. Interestingly one of the two equal-sized droplets (*bottom*) restores its original orientation of radial defect, while the other one (*top*) does not. As it was shown, both of the droplets undergo transitions of textures in a similar rate. The smaller one proceeds faster, especially for the steps that involve escaping from the radial structure, e.g. (a)-to-(b), in agreement with the also faster process for Figure 7.12 with respect to Figure 7.11.

The analysis of droplets prepared from the mixtures of high dopant concentration resulted in manifestation of the helix inversion, although possibly incomplete in some cases (Figure 7.11). A comparison with the behavior of CLC mixture of low dopant concentration (**1a**) will be discussed now. Figure 7.13 presents two droplets of CLC mixture of low dopant concentration, with  $R$  values equal to  $22.5\ \mu\text{m}$  and  $17\ \mu\text{m}$ .

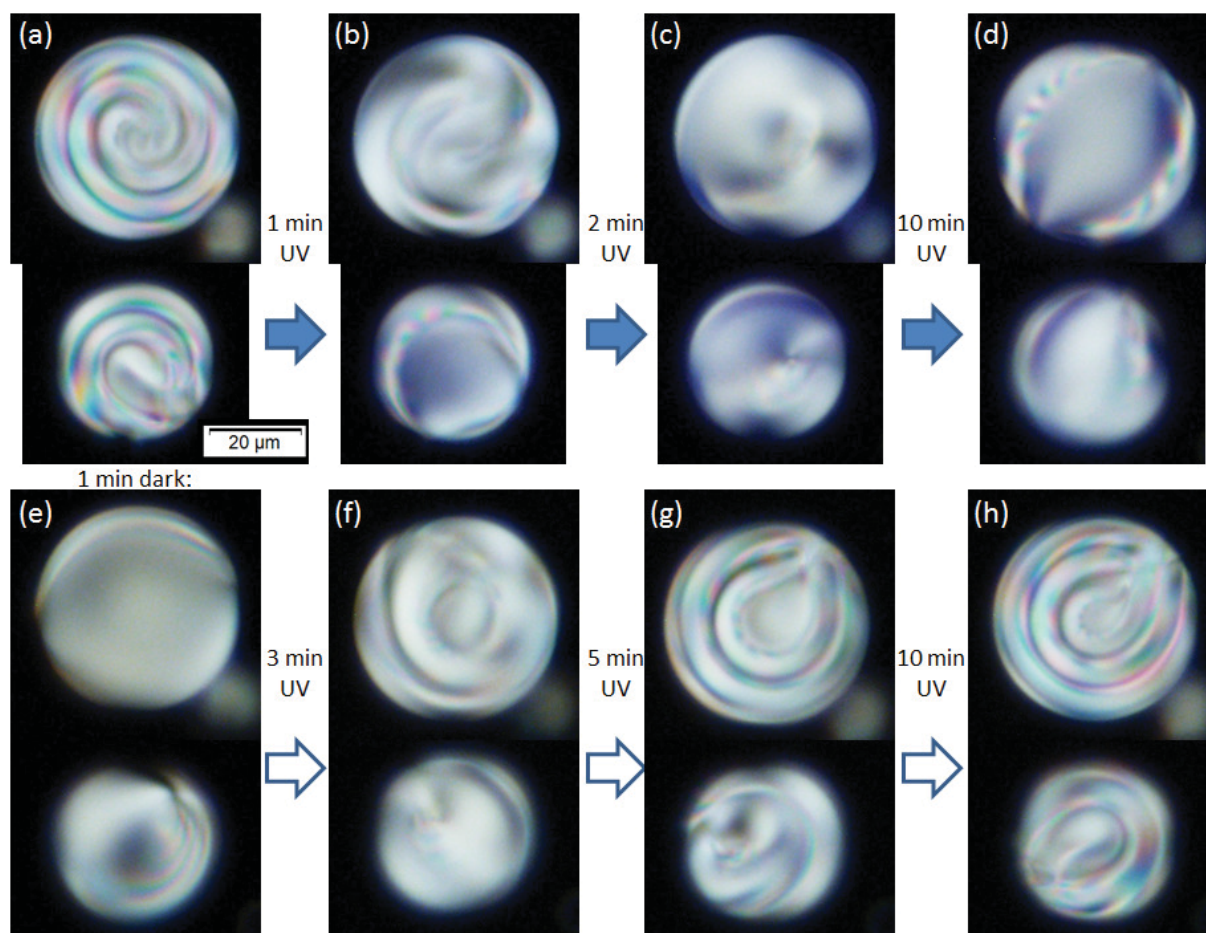


**Figure 7.13** Sequence of polarized microscopy patterns (transmission mode) showing the evolution of textures of two droplets of CLC mixture of low dopant concentration (**1a**) under the irradiation with UV. The radius of bigger droplet (*top*) is equal to  $22.5\ \mu\text{m}$  and the radius of smaller droplet (*bottom*) is equal to  $17\ \mu\text{m}$ .

Although the textures somehow resemble the radial texture it is difficult to determine the value of radial period, at least for sure for the smaller droplet. The respective  $R/P_w$  values are: 2.23 and 1.68. Under the irradiation, no texture following the bipolar texture is seen (frames (c) and (d)). In other words – there is no manifestation of helix inversion, because the droplets are too small to express chirality at the photostationary state. The helical twisting power at the photostationary state is lower in magnitude in comparison to the initial state leading, as already observed in the previous

measurements, to a larger inverse pitch. As shown in the Table 7.1, we expect a photostationary pitch  $P_w^{PSS} = 32.9 \mu\text{m}$ , clearly too large with respect to the droplet size ( $22.5 \mu\text{m}$  and  $17 \mu\text{m}$ ) to allow for rewinding. As in the previous cases, the relaxation process takes pace just after terminating the irradiation. Moreover, similarly to the cases of highly-doped CLCs, this process goes through the analogous states obtained during irradiation. Frame (h) shows the radial texture with the size of the period restored to the initial values (frame (a)). Again reorientation of textures of droplets is noticeable. The radial defect of the bigger droplet originally pointing out of the image plane (frame (a)) after the relaxation is oriented in the position 2 o'clock (frame (h)). Also the texture of the smaller droplet is oriented differently at the initial and final stages of the process.

We have compared droplets of different sizes in two kinds of cholesteric mixtures: possessing larger and smaller cholesteric pitch. Now it would be interesting to find two droplets, possibly one from the CLC mixture of low dopant concentration and the other one from the CLC mixture of high dopant concentration which will possess similar values of  $R/P_w$  ratio, and compare their behavior. Such situation is presented on Figure 7.14. The two droplets from **2a** and **1a** mixtures were chosen, of  $R/P_w$  equal to 3.8 and 3.7, respectively (a). As previously noticed, already before irradiation there is a visible difference in relative difference of radial period with respect the cholesteric pitch ( $(P - P_w)/P_w$ ). If one compares two dashed horizontal lines on Figure 7.14(b), it may be noticed, that for small droplet (black squares) relative difference between the period and pitch equals 0.38, and for bigger droplet (red circles) this value is smaller and equal 0.11, accordingly to Figure 7.8.

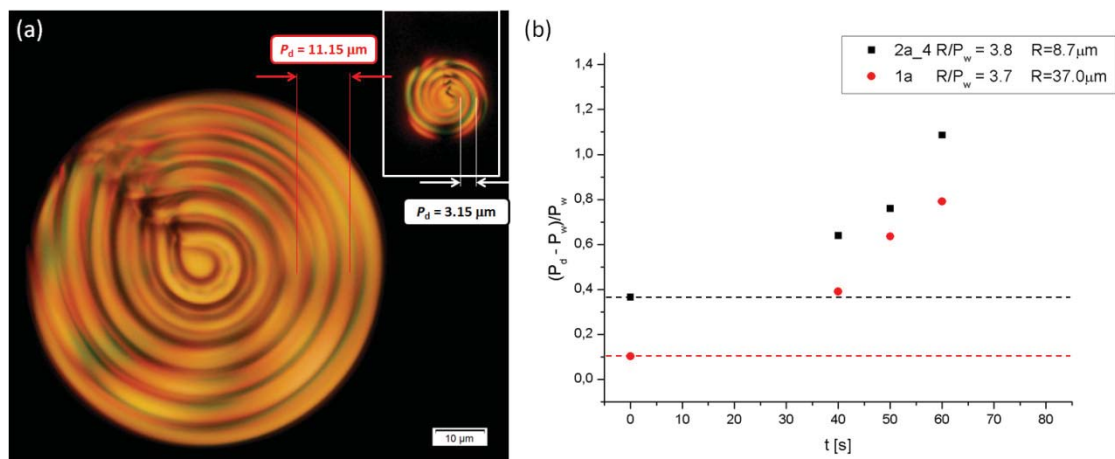


**Figure 7.14** (a) Polarized microscopy image of two droplets of  $R/P_w$  equal to 3.8 and 3.7. (b) Temporal evolution of a relative difference of radial period to cholesteric pitch change  $(P - P_w)/P_w$  under UV irradiation for low initial  $R/P_w$ . Although initial difference ( $t = 0$ ) is noticeable (0.38 vs 0.11), the dynamic behavior is very similar.



What may be further seen on Figure 7.14 is that both droplets, although significantly differing in size ( $R = 8.7 \mu\text{m}$  and  $R = 37 \mu\text{m}$ ) unwind with similar rate. This actually means that despite the different initial conditions, and starting  $R/P_w$ , the effective unwinding – with respect to each cholesteric pitch - is similar and depends only on the confinement parameter  $R/P_w$ .

Figure 7.15 shows the relative change of the period-to-pitch in time, for droplets of **1b** CLC mixture (*left*) and one droplet of **1a** mixture (*right*), related to the change of respective pitch (black squares on both plots).

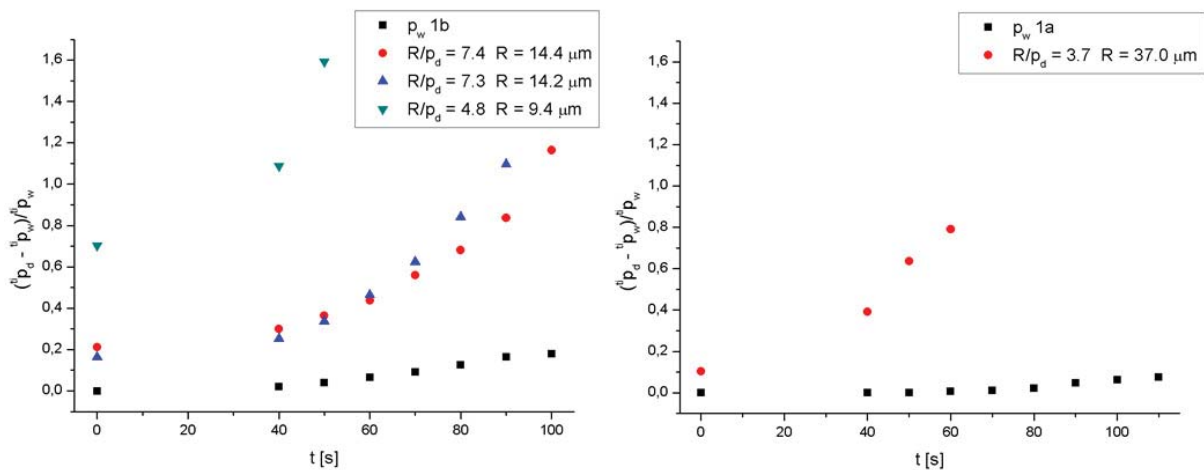


**Figure 7.15** Temporal evolution of a relative period change  $(P - P_w)/P_w$  under UV irradiation for **1b** (*left*) and **1a** (*right*) samples, representing shortest pitch 1.95  $\mu\text{m}$  and longest pitch 10.12  $\mu\text{m}$ , respectively.

It is observed for all of the samples that the droplets response is much faster, i.e. the change of period is faster in comparison to the cholesteric pitch evolution. This is clearly seen on Figure 7.15, together with the role of the confinement parameter. The evolution of the period for droplets of different sizes is shown for CLC mixtures **1b** (*left*) and **1a** (*right*) with respect to the evolution of the cholesteric pitch (black squares) under irradiation. A faster evolution is observed when the confinement  $R/P_w$  decreases, what is manifested by steeper slope for the set of green data-points than e.g. the slope of set of red data-points (both on the left panel). This confirms the dominant role of the confinement and shows that the process of divergence between the speed of cholesteric pitch change and the period change rises when the confinement increases.

## 7.5 Discussion and conclusions

The results presented in this chapter confirm many features that were observed before in other cholesteric liquid crystal droplets. Preparing these droplets in an environment inducing planar anchoring resulted in the creation of dispersions in which chirality is expressed differently – depending on the extent of geometrical confinement. The crucial parameter, namely the relation between the native cholesteric pitch ( $P_w$ ) and the size of the droplet has been shown to determine similar textures of droplets in comparison to the cases where other chiral (but non-photoactive) dopants were used. The main two structures that are evidenced: radial spherical structure and twisted bipolar structure, were shown to appear in cholesteric liquid crystals having both large or small initial pitch. However, it is also shown here that, for the lower concentration of chiral dopant (**1a**), the radial spherical structure is stabilized for  $R/P_w$  values larger than approximately  $R/P_w = 1.3$  and for the larger concentration of dopants (**1b**, **2a**), it is stabilized for  $R/P_w$  larger than 2.7. In other words for two droplets of similar  $R/P_w$ , i.e. approaching value of 2, we may find also different expressions of the chirality depending on the absolute pitch value. It means that the overall geometrical confinement conditions, both surface and bulk elasticity make droplets of mixture of high dopant concentration unstable in the radial configuration. We find decreasing transition confinement ratios (below which a twisted bipolar state is induced) when the pitch increases, in agreement with the evolution also evidenced in literature<sup>9</sup>. However the absolute values of the transition confinement ratios are different. This underlines the role of the chemical structure of the liquid crystals on the establishment of the cholesteric structures.

Using a molecular motor dopant enabled us to photo-induce the helicity of both signs. This is due to the fact that, upon the irradiation, photochemically induced change of enantiomeric excess results in the continuous increase of the size of the radial period until a bipolar (in other words ‘pseudonematic’) state followed by a rewinding of radial period with inverse helicity. Such change was previously shown for the temperature induced change in chirality only.<sup>9</sup> Under irradiation, we now evidence continuous structural changes, from unwinding of the radial structure, transition to the twisted bipolar state and its disorientation through very transitory bipolar state (manifestation of the other sign of the twist) and rewinding of helix of a reverse handedness. These dynamic features appear in droplets considerably more rapidly than in films. We finally evidence the rewinding with a reverse handedness in the droplets, whereas irradiation of wedge cells with similar parameters of irradiation did not result in evidence of helix inversion.

It was shown, that for both types of mixtures (i.e. CLCs of low and high dopant concentrations), two droplets of similar  $R/P_w$  ratio, although evidencing different initial conditions (i.e. the period related to the actual pitch), undergo a continuous change of comparable dynamics. In other words, for similar starting  $R/P_w$  ratio it takes the same amount of time to 'unwind' the radial spherical texture. Such size-dependent dynamic analysis was never shown for thermally induced changes of chirality for the dispersed cholesteric liquid crystals. This observation evidences that the relevant parameter is the confinement with respect to the pitch and not the intrinsic size of the droplet, so not the nematic elastic deformations within the droplet.

It was shown for all of the cases, that the rate of change of the droplet period for the confined systems (both large and small cholesteric pitch), is much faster than the photo-induced change of the cholesteric pitch in the wedge cell. In addition, for the group of droplets within one sample (differing in size) there is a clear trend of the more steep increase of change of the period-to-pitch, for the smaller initial  $R/P_w$  values. This would mean that the closer the initial state of the droplet to the transition  $R/P_w$  value, the fastest the tendency in change. Exact and quantitative analysis is rather uncertain, but from the studied samples we may conclude that there is a positive effect of confinement on the helix unwinding, even more for the smaller droplets, which are virtually closer to the transition to bipolar texture.

Upon continuation of irradiation and passing to the twisted bipolar structure, which resembles the texture encountered for the nematic droplet we were able to reach a situation where the contribution of each of the motor isomers cancelled out. Moreover, the special property of the motor molecule, that is the helix inversion, enabled us to manifest the change of twisting in the bipolar state. In a second step, it manifests the reappearance of the radial spherical structure, but with a different handedness. This reappearance however occurs to a different extent. Since the helical twisting power in the photostationary state (PSS) is not the same than in the initial state, a radial texture may or may not appear, in relation with a larger pitch in the PSS state. For sufficiently big droplets, for which  $R/P_w^{PSS}$  value at PSS is bigger than a critical value, one observe reappearance of a radial spherical structure which is an evidence of the helix inversion within the confined cholesteric mixture. Such an event was previously studied and manifested in droplets, for a compensated mixture of liquid crystals with the temperature increase again serving as a stimulus for the transition between the structures.<sup>7</sup> In addition, a transition between different textures of sessile CLC droplets has been controlled by photo-switching of molecular motors.<sup>17</sup> However, it has never been shown to provoke a helix inversion in the spherical droplets for a single chiral dopant system.

Finally our results evidence the possibility to continuously vary cholesteric droplets under UV-illumination. In particular we are able to continuously vary the period of the radial texture. This observation is promising for future applications. As explained in Chapter 6 a cholesteric droplet of radial texture can be viewed as a spherical Bragg microcavity.<sup>1</sup> These onion-like structures are particularly interesting because of their perfect rotational symmetry in 3D and resulting, if doped with molecules of organic dye, omnidirectional lasing action. Optical manipulation of the period presented in this chapter is a proof of principle. However, it should be said that in order to apply the photo-tunability of radial period for lasing in the visible part of spectrum, one should demonstrate this principle in for much smaller values of period (i.e. submicron periods, which are not resolvable by regular optical microscopy). Tuning of the spherical Bragg resonator with light is an interesting alternative for the temperature-driven modulation of its photonic bandgap, since the latter cannot be always applied.

## 7.6 Experimental section

**Molecular motor.** Molecular motors used for the studies included in this chapter was synthesized and characterized by Supitchaya Iamsaard.

**Preparation of CLC mixtures.** Enantiomerically pure amounts of motor and E7 were weighed in separate vials. A few droplets of dichloromethane (Sigma Aldrich, HPLC grade – used as received) were then added to E7 and the solution was added to the vial containing the motor. The resulting solution was heated on a hot-stage (60 °C) for about 30 minutes to evaporate the dichloromethane.

**Preparation of PVP/glycerol matrix.** Glycerol is known to impose planar boundary condition (anchoring) to a variety of nematic liquid crystals. A small amount of polyvinylpyrrolidone (PVP) was added to this glycerol matrix in a mass ratio 1:3, in order to make the matrix thicker. The PVP and glycerol were purchased from Sigma Aldrich and used as received. The PVP/glycerol mixture was heated at 130 °C for about 1 hour. The mixture was stirred well prior to use.

**Substrates.** Regular microscopy glass slides were used as substrates for the samples. Prior to the deposition they were examined for presence of mechanical defects and flushed with a stream of nitrogen gas.

**Ultraviolet light source.** A Spectroline pencil lamp was used for irradiation at  $\lambda = 365$  nm, with a nominal intensity of  $1 \text{ mW cm}^{-2}$  at 2.5 cm.

**Sample preparation.** A drop of freshly prepared PVP/glycerol mixture was transferred onto a clean microscope glass slide. Subsequently a small drop of liquid crystal was mechanically transferred onto the PVP/glycerol drop, and the droplets were formed by mechanical shearing. This procedure yields large amounts of CLC droplets. The droplets formed by the liquid crystal in the glycerol matrix are polydispersed, with sizes ranging from few  $\mu\text{m}$  to few tens of  $\mu\text{m}$ . Because of surface tension they have almost perfect spherical shape and smooth surface.

## 7.7 Acknowledgments

Dr. Benjamin Matt is acknowledged for the sample preparation and Supitchaya Iamsaard is acknowledged for synthesizing of molecular motors.

## 7.8 References

1. Cao, W.; Muñoz, A.; Palffy-Muhoray, P. & Taheri, B. *Nat. Mater.* **1**, 111–113 (2002).
2. Coles, H. & Morris, S. *Nature Photon.* **4**, 676–685 (2010).
3. Musevic, I. *Liq. Cryst.* **41**, 418–429 (2014).
4. Musevic, I.; Skarabot, M. & Humar, M. *J. Phys.: Condens. Matter* **23**, 284112 (2011).
5. Humar, M.; Ravnik, M.; Pajk, S. & Musevic, I. *Nature Photon.* **3**, 595–600 (2009).
6. Humar, M. & Musevic, I. *Opt. Express* **18**, 26995–27003 (2010).
7. Kurik, M. V. & Lavrentovich, O. D. *JETP Lett* **35**, 444–447 (1982).
8. Sec, D.; Porenta, T.; Ravnik, M. & Zumer, S. *Soft Mat.* **8**, 11982–11988 (2012).
9. Xu, F. & Crooker, P. *Phys. Rev. E* **56**, 6853–6860 (1997).
10. Koumura, N.; Geertsema, E. M.; Meetsma, A. & Feringa, B. L. *J. Amer. Chem. Soc.* **122**, 12005–12006 (2000).
11. Eelkema, R.; Pollard, M. M.; Vicario, J.; Katsonis, N.; Ramon, B. S.; Bastiaansen, C. W. M.; Broer, D. J. & Feringa, B. L. *Nature* **440**, 163–163 (2006).
12. Eelkema, R. & Feringa, B. L. *Org. Biomol. Chem.* **4**, 3729–3745 (2006).
13. Bosco, A.; Jongejan, M. G. M.; Eelkema, R.; Katsonis, N.; Lacaze, E.; Ferrarini, A. & Feringa, B. L. *J. Amer. Chem. Soc.* **130**, 14615–14624 (2008).
14. Wang, Y. & Li, Q. *Adv. Mater.* **24**, 1926–1945 (2012).
15. Jongejan, M. G. M., PhD Thesis, University of Groningen (2010).
16. Robinson, C. *Farad. Discuss.* **52**, 571–592 (1956).
17. Chen, J.; Lacaze, E.; Brasselet, E.; Harutyunyan, S. R.; Katsonis, N. & Feringa, B. L. *J. Mater. Chem. C* **2**, 8137–8141 (2014).



## Summary and perspectives

Liquid crystals are special type of materials which retaining to some extent the order of molecular organization also gain the dynamic properties. One of the main issues in liquid crystals research and also in the area of nanoscience and nanotechnology are studies of the interfaces with the liquid crystal. Such interfaces, including the organic/inorganic interfaces, are particularly important for the development of devices, like light-emitting diodes or photovoltaic cells, in which the active layer is composed of liquid crystal molecules. The understanding of behavior of mesogenic molecules under the influence of a metallic substrate (i.e. 2D confinement) is crucial for the design and evaluation of more developed systems which, due to the presence of specific functional groups may be controllable, e.g. by light. This in perspective would lead to the so-called *smart materials*. Another issue investigated here is the influence of a 3D confinement on the behavior of cholesteric liquid crystals, and in particular on the dynamic behavior of the photo-responsive CLC mixtures under the UV irradiation.

In the first part of the thesis (Chapters 3-5), the research is aimed at the deepening of knowledge about the self-assembled monolayers of discotic liquid crystals by the STM measurements at the liquid/solid interface. It has been shown, by combining experimental and theoretical methods that under the influence of the solid substrate, combination of intermolecular and interfacial interactions may lead to the appearance of chirality. For the case of a model H5T molecule the self-assembled monolayers have shown the appearance of both: point and organizational types of chirality, despite of the fact that neither the molecule nor the substrate was chiral. For another molecular system, C-12 - a triphenylene peripherally substituted with azobenzene moieties self-assemblies bearing the chiral nature were also evidenced. In the corresponding hexagonal network formed by the physisorbed molecules, six dimers of azobenzene subunits coming from the neighboring molecules formed "rosettes" which displayed clockwise or counter-clockwise rotation. The two stable configurations of the azobenzene-dimers also defined the two types of adsorbed domains. For the H5T, the chirality was mediated by classical van der Waals interactions between molecules and between molecules and substrate, the substrate selecting only two of many possible chiral self-assemblies. In the case of C-12 it has been shown that the origin of the self-assembly comes from the intermolecular hydrogen bonds between the azobenzene moieties of neighboring molecules, which are substrate-mediated.



In summary, the results described in this thesis demonstrate the complex relation between the geometrical confinement of molecules possessing mesogenic properties and the property of chirality. It was already known that the multimodal chirality may arise in the non-chiral systems as a consequence of 2D confinement. Here, we tried to unravel the specific influence of the balance of intermolecular/molecular-substrate interactions. H5T molecule was shown to form on Au(111) domains expressing two types of surface chirality. On the one hand, the *point* chirality which is connected with a rotation of molecular symmetry axes with respect to the molecular rows and to the substrate symmetry axes. It was determined by the maximizing of molecular surface density, the interfacial interactions coming from both: the central polyaromatic core and the peripheral alkyl chains. On the other hand, the organizational type of chirality was manifested by the rotation of the molecular rows of H5T with respect to the substrate symmetry axes. This latter type of self-assemblies originated from the optimal orientation of the central part of the molecule only. The study of H5T/Au(111) system finally evidenced the dual origin of both H5T domains on Au(111), driven by specific interactions of the substrate with either the polyaromatic core or the alkoxy chains. Moreover, the observation of density-driven symmetry breaking with simple symmetric molecules suggests that a large number of physisorbed molecules are likely to present a similar behavior. However this demonstration was possible only through the combination of the STM experiments and theoretical models which have taken into account the van der Waals and the steric interactions.

Another important issue raised in this thesis is the relation between chirality and specific intermolecular interactions, hydrogen bonding between the azobenzene moieties of neighboring C-12 molecules. Those interactions, evidenced specifically on Au(111) substrate should be the subject of more detailed studies, including other metallic substrates since they do not appear on graphite. It was shown that the directionality of the two mirror-image domains characterizing the ordered C-12 networks on Au(111) is determined by the orientation of one of the two stable azobenzene dimers created between neighboring molecules, with respect to Au(111). It was thus established that the C-12/Au(111) system is dominated by those interactions. Now, it would be interesting to investigate if this azobenzene pairing is capable to dominate other molecular systems, e.g. by studying molecules that consist of different polyaromatic core decorated with azobenzenes. Another question arises: is it possible to build an azobenzene-containing system which, due to the symmetry of the core, would promote appearance of both types of (chiral) azobenzene interactions and thus would remain non-chiral as a whole molecular entity?

The origin of 2D chirality for organic molecules which do not contain any chiral center is a subject of ongoing studies. It was thus important to unravel some of the relations between interactions and induced chirality. However it would be now important to understand how to select only one kind of chirality to obtain chiral 2D systems at a macroscopic scale as well. Among the parameters that are continuously explored for this purpose remain the effects of chiral solvents or chiral auxiliaries. There are still a lot of mysteries on the subtle balance of molecule-molecule and molecule-substrate interactions to become unraveled which could possibly allow for obtaining chirality at the macroscopic scale. The use of chiral substrates like vicinal single crystals also appears promising.

The main subject of study in the second part of the thesis was investigation of the influence of the 3D confinement on the chirality of the photoactive cholesteric droplets. The results presented in Chapter 7 are devoted to both static description of the system and dynamic studies. Due to the photo-responsive character of a chiral dopant we were able to modify the cholesteric pitch of the CLC mixture and thus to map the expression of chirality for a varying geometrical confinement parameter: radius-to-pitch. We evidenced a successful control of the cholesteric droplets structure by UV irradiation and we studied the induced structural variations. In particular, the 3D confinement of a photo-responsive CLC mixture was shown to positively support the helix inversion within the cholesteric droplets, the unwinding of the cholesteric droplets being faster for smaller radius-to-pitch ratio.

The cholesteric droplets were already shown to play a promising role of the spherical Bragg microcavities which, thanks to the property of the nematic host, remain tunable. Very interesting from the fundamental point of view would be the observation of the response of the system for the action of more than one stimulus, i.e. temperature and light. The successful demonstration of the variation of cholesteric droplets under UV-irradiation appears particularly promising for their future applications as controllable omnidirectional lasers, based on the spherical onion microresonators. An optimal engineering of the microcavity for achieving the lasing action and the desired spectral tunability should be another issue for future works. Since the emission is normally originated at the center of the CLC droplet and it is attenuated while traversing radially, the organic dye molecules or other emitters may be concentrated in this area only. This, in longer perspective opens a way to possible hybrid structures, where e.g. an emitter like a single quantum dot is embedded in the center of CLC droplet/shell.



## Samenvatting en perspectieven

Een liquid crystal ofwel een vloeibaar kristal is een speciaal soort materiaal dat zich in een aggregatietoestand bevindt, welke eigenschappen van zowel kristallijne als vloeibare fasen in zich verenigt. Een van de belangrijkste kwesties in het onderzoek naar vloeibare kristallen en zeker ook in de nanotechnologie, zijn studies op het gebied van interfaces met vloeibare kristallen. Dergelijke interfaces, zowel organische als anorganische, zijn belangrijk voor de ontwikkeling van apparaten, zoals lichtgevende diodes of zonnecellen. Hierbij is de actieve laag voornamelijk samengesteld uit vloeibare kristalmoleculen.

Moleculen die aanleiding geven tot vloeibaar kristallijn gedrag, worden mesogenen genoemd. Het gedrag van deze mesogenen, welke zich in de nabijheid van een metaal substraat bevinden (d.w.z. 2D beperking), is van groot belang wanneer een component wordt ontworpen. Zeker wanneer functionele groepen worden geïntroduceerd in het mesogeen, die het gedrag van mesogenen zelf kunnen veranderen door stimuli van buitenaf. Kennis van deze interactie kan leiden tot zogenoemde *smart-materialen*.

Daarnaast is er gekeken naar wat de bulk eigenschappen (3D beperking) zijn van cholesterische vloeibare kristallen (CLK). Hierbij is in het bijzonder aandacht geschonken aan de dynamische eigenschappen van de fotogevoelige CLK mengsels onder invloed van UV-radiatie.

In het eerste deel van het proefschrift (Hoofdstukken 3-5), is het onderzoek gericht op de verdieping van de kennis over de zelf-geassembleerde monolagen van discotische vloeibare kristallen op substraten. Hierbij is gebruik gemaakt van STM metingen aan het vloeï-/vaste stof grensvlak. Door middel van deze metingen is experimenteel en theoretisch aangetoond dat de combinatie van het vaste substraat, intermoleculaire interacties en het grensvlak kan leiden tot geïnduceerde chiraliteit. Monolagen van het goed bestudeerde H5T molecuul leiden op deze manier zelfs tot dubbele chiraliteit; punt en organisatorische chiraliteit. Dit, desondanks dat noch het molecuul, noch het substraat, onafhankelijk van elkaar chiraliteit vertoont. Een tweede bestudeerd moleculair systeem is C-12, welke ook zelf-assembleren op een Au(111) substraat, waarna ze chiraliteit vertonen. Dit molecuul bestaat uit trifenyleen met perifeer gesubstitueerde azobenzeen eenheden. De drijvende kracht voor zelf-assemblage, in het C-12 systeem, is de intermoleculaire interactie tussen aangrenzende azobenzeen eenheden, waarna ze dimeren vormen. Zes van deze azobenzeen sub-eenheden vormen een rozet, welke optisch gezien met of tegen de klok in draaien. Azobenzeen-

dimeren kennen twee stabiele configuraties, welke ook de twee types van geabsorbeerde domeinen zijn. Voor het H5T molecuul werd chiraliteit geïnduceerd door klassieke van der Waals interacties tussen moleculen onderling en moleculen en substraat, waarbij het substraat slechts twee selectieve vormen van zelf-assemblage toe laat, die ook chiraliteit vertonen. In het geval van C-12 is aangetoond dat de oorzaak van zelf-assemblage alleen wordt veroorzaakt door intermoleculaire waterstofbindingen tussen de azobenzeen eenheden van naburige moleculen.

De resultaten van deze thesis laten duidelijk het complexe verband zien tussen ruimtelijk begrenzings van mesogenen en de daar bijhorende (geïnduceerde) chiraliteit. Zeker voor non-chirale systemen, waar d.m.v. monolagen toch chiraliteit geïntroduceerd kan worden. Er is specifiek gekeken naar wat de invloed op chiraliteit van het systeem is, als de ratio tussen (inter)moleculaire en substraat interacties wordt aangepast. H5T moleculen op Au(111) vormen domeinen waar zelfs twee types van oppervlakte chiraliteit zijn gemeten, namelijk punt en organisatorisch chiraliteit. Punt chiraliteit is de rotatie rondom de symmetrie as van het molecuul met respect tot de substraat symmetrie assen. Deze vorm van chiraliteit werd vastgesteld door het maximaliseren van oppervlaktedichtheid. Organisatorische chiraliteit is de rotatie van moleculaire rijen van H5T molecuul ten opzichte van substraat symmetrie assen. Door het H5T/Au(111) systeem te bestuderen kon worden geconcludeerd en aangetoond dat de dubbele oorsprong van de beide, hierboven besproken, H5T domeinen op Au(111), vooral komt door specifieke interacties tussen het substraat met de polyaromatische kern of de perifere alkoxy ketens. Eveneens het resultaat van symmetriebreking door de dichtheid aan te passen, met eenvoudige symmetrische moleculen, suggereert dat een groot aantal fysisorbeerde moleculen waarschijnlijk een soortgelijk gedrag vertonen.

Een ander issue dat is besproken in deze thesis, is de relatie tussen chiraliteit en specifieke intermoleculaire interacties, en specifiek de relatie tussen waterstofbruggen en de azobenzeen groepen van naburige C-12 moleculen. Deze interacties zijn in het bijzonder geobserveerd op Au(111) substraten, maar het zou ook in detail moeten worden onderzocht op andere metallische substraten, aangezien de interacties niet zijn gevonden op grafeen substraten. In dit proefschrift is o.a. aangetoond dat karakteristieke directionele ordening van C-12 op Au(111) voortkomt uit de oriëntatie van één van de twee stabiele azobenzeen dimeren gevormd tussen naburige moleculen op Au(111). Het zou dus interessant zijn om te onderzoeken of deze azobenzeen koppelingen ook andere moleculaire systemen kan domineren. Dit zou gedaan kunnen worden door het bestuderen van moleculen die bestaan uit verschillende polycyclische aromatische kernen met azobenzeen schillen. Een tweede onderzoeksvraag kan als volgt geformuleerd worden; is het mogelijk om een ander azobenzeen systeem te ontwikkelen dat door de symmetrie van de kern, ook kan leiden tot beide typen (chirale) azobenzeen interacties, maar niet in bulk?

De oorsprong van chiraliteit door middel van 2D beperkingen, voor organische moleculen, die zelf geen chiraal centrum bevatten, is een onderwerp van veel lopende studies. Het was dus van belang om een aantal relaties, die bestaan tussen interface interacties en geïnduceerde chiraliteit, te ontrafelen. Op dit punt is het belangrijk om te begrijpen hoe je slechts één soort chiraliteit kan selecteren om zo ook 2D macroscopische chirale systemen te krijgen. Onder de vele parameters die continu onderzocht worden, blijven de effecten van chirale oplosmiddelen of hulpstoffen belangrijk. Er zijn nog vele mysteries op het gebied van de subtiele balans tussen molecuul-molecuul en molecuul-substraat interacties om ontrafeld te worden, welke mogelijk kunnen leiden tot het verkrijgen van chiraliteit op de macroscopische schaal. Hierin lijkt het gebruik van chirale substraten zoals vicinaal enkelkristallen ook veelbelovend.

Het belangrijkste onderwerp van het tweede deel van dit proefschrift was onderzoek naar de invloed van de bulk eigenschappen op de chiraliteit van de foto-actieve cholesterisch druppels. De resultaten in Hoofdstuk 7 zijn zowel gewijd aan een statische, dan wel een dynamische beschrijving van het systeem. Door het fotogevoelige karakter van een chirale doteerstof was het mogelijk de cholesterische rotatie van het vloeibare kristallische mengsel te beïnvloeden. Hierdoor was het mogelijk een expressie van chiraliteit te maken voor een variërende geometrische parameter, namelijk; radius t.o.v. de afstand. We hebben bewezen dat er een succesvolle controle over de cholesterische structuur druppels door UV-bestraling is en de geïnduceerde structurele variaties zijn onderzocht. Vooral de bulk eigenschappen van een fotogevoelig CLK mengsel bleek een helix inversie in de cholesterische druppels, het ontwikkelen van de cholesterische druppels wordt sneller bij een kleinere radius tot afstand verhouding.

Het is al aangetoond dat cholesterisch druppels een belangrijke rol spelen bij van de sferische Bragg microholtes, die dankzij het eigendom van de nematische host, aanpasbaar blijven. Deze druppels worden slechts door één stimulus veranderd. Nu zou het, vanuit een fundamenteel oogpunt, erg interessant zijn om een chiraal systeem te ontwerpen die reageert op meer dan één stimulus, bijv. licht én temperatuur . De succesvolle demonstratie van de chirale verandering van cholesterische druppels onder UV-bestraling lijkt veelbelovend voor de toekomstige toepassingen in o.a. regelbare omnidirectionele lasers, gebaseerd op de sferische ui-vormige microresonators. De optimale vorm van een microcavity, voor het bereiken van de, zo genoemde, lasing actie en de gewenste spectrale aanpassing is een ander probleem voor de toekomst. Aangezien de emissie normaal ontstaat in het centrum van de cholesterisch druppel en wordt verzwakt terwijl het licht de druppel radiaal doorkruist. Dit zorgt op langere termijn voor eventuele hybride structuren, waar, bijvoorbeeld, een emitter als een enkele quantum dot is ingebed in het centrum van cholesterisch druppel/omhulsel structuur.



## Résumé et perspectives

La compréhension du comportement de molécules mésogéniques sous l'influence d'une surface métallique (par un confinement 2D) est cruciale dans la mise au point et la caractérisation de systèmes plus complexes qui, par le biais de groupes fonctionnels spécifiques, pourraient être contrôlables par la lumière par exemple.

Les travaux présentés dans une première partie de la thèse (Chapitres 3 à 5) visent à approfondir les connaissances sur les auto-assemblages de cristaux liquides discotiques. Il a été démontré, par des méthodes expérimentales et théoriques, que sous l'influence d'un substrat solide, la combinaison des interactions intermoléculaires et interfaciales peut mener à l'apparition de la chiralité. De plus, dans le cas de molécules modèles H5T, la couche auto-assemblée a montré l'apparition de deux types de chiralités (la chiralité ponctuelle et la chiralité au niveau organisationnel) alors que ni les molécules, ni le substrat ne sont chiraux. Un autre système moléculaire, C-12 – un triphénylène symétriquement substitué avec des groupements azobenzène – a également été montré comme susceptible de former des couches auto-assemblées chirales. Dans le cas du C-12, il a été déterminé que l'auto-assemblage provient des liaisons hydrogène entre les groupements azobenzène de molécules voisines, et sont influencées par le substrat.

Les résultats décrits dans cette thèse démontrent qu'il existe une relation complexe entre le confinement géométrique de molécules à 2D et les propriétés de chiralité. En particulier, il a été démontré qu'une chiralité multimodale peut être observée pour des systèmes non chiraux par le biais du confinement 2D. Les molécules H5T forment, sur Au(111), des domaines pour lesquels deux types de chiralité peuvent être observés. D'une part, la chiralité ponctuelle liée aux axes de symétrie de la molécule par rapport aux axes de symétrie du substrat a été mise en évidence. Elle provient en même temps de la maximisation de la densité moléculaire surfacique et des interactions interfaciales associées aux chaînes alkyles périphériques. D'autre part, la chiralité au niveau organisationnel se manifeste par une rotation entre les rangées d'H5T et les axes de symétrie du substrat. Ce dernier type d'auto-assemblage provient d'une orientation optimale de la partie centrale de la molécule uniquement. En règle générale, les études sur le système H5T/Au(111) ont prouvé que des interactions simples, de type van der Waals sont susceptibles de créer des chiralités complexes, ce qui donne un caractère générique à ce type de phénomène. Par ailleurs, pour les molécules de type triphénylène le caractère dual des interactions molécule-substrat a été mis en évidence, soit étant dominé par les cœurs aromatiques des molécules, soit par les parties aliphatiques.



Une autre question importante est l'apparition des domaines chiraux induits par des interactions intermoléculaires spécifiques, avec en particulier, les liaisons hydrogène entre les groupements azobenzènes de molécules voisines. Ces interactions, mises en évidence avec des substrats d'Au(111), pourraient faire l'objet d'études approfondies incluant d'autres substrats métalliques. L'orientation des deux domaines chiraux est déterminée par l'orientation de l'un des deux dimères d'azobenzène stable par rapport à l'Au(111). Il a par conséquent été déduit que l'organisation du système C-12/Au(111) est déterminée par ces liaisons hydrogène. A présent, il pourrait être très intéressant d'étudier si le couplage d'azobenzène est capable de dominer également d'autres systèmes moléculaires. D'autres questions restent en suspens : est-il était possible de construire un système contenant des azobenzènes qui, grâce à la symétrie du cœur, pourrait promouvoir l'apparition des deux types d'interactions entre azobenzène au sein d'une même molécule. Nous obtiendrions alors une molécule dont l'ensemble reste non-chiral.

L'origine de la chiralité 2D pour les molécules n'ayant aucun centre chiral est un sujet qui fait l'objet de nombreuses études actuellement. Parmi les paramètres systématiquement examinés, l'un des plus importants après la nature du substrat, est l'utilisation d'un solvant chiral ou l'addition des auxiliaires chiraux. Cela permet de créer des chiralités à l'échelle macroscopique.

La seconde partie de la thèse est principalement dédiée à l'étude de l'influence du confinement 3D sur la chiralité de gouttes de cristal liquide cholestérique (CLC). Les résultats présentés dans le Chapitre 7 concernent la description de la statique et de la dynamique de ces systèmes. Grâce à la nature photo-sensible du dopant chiral utilisé, nous avons été capables de modifier le pas cholestérique du mélange de CLC et par conséquent de déterminer l'expression de la chiralité pour un ratio *rayon/pas cholestérique* variable. Nous sommes parvenus à contrôler le pas cholestérique au sein de gouttes par irradiation UV et nous avons étudié les variations structurelles que l'irradiation induit. Nous avons notamment observé que le confinement 3D d'un mélange de CLC photo-sensible a une influence positive sur l'inversion de l'hélice dans la goutte et que la paramètre clef pour contrôler la vitesse de débobinage de l'hélice est la ratio *rayon/pas cholestérique*.

Les gouttes cholestériques s'avèrent prometteuses pour mettre au point des microcavités de Bragg sphériques. Nous avons démontré que sous l'irradiation UV nous pouvons modifier de façon contrôlée les périodes des résonateurs de Bragg. Cela laisse envisager la mise au point de microlasers de longueur d'onde contrôlable. L'optimisation de la conception des microcavités dans le but de parvenir à l'émission stimulée d'une part, et l'ajustement des propriétés spectrales des microcavités d'autre part est un des principaux enjeux maintenant dans le domaine des microrésonateurs sphériques 3D. Comme l'émission provient du centre du résonateur il est important de parvenir à concentrer les molécules émettrices au centre de la goutte. Ceci ouvre la voie à des structures hybrides avec par exemple une boîte quantique unique disposée au centre de la goutte CLC.

## Acknowledgements

After more than four years of my PhD it is finally the moment when I may express my gratitude to the number of people that enabled me to start the 'PhD period' and helped me each time I needed it on my way to here - where I am now.

I need to start with person who found me, believed in me and guided me through a research area of surface science which was a new discipline for me, not mastered in the laboratory during my Master studies. **Emmanuelle**, I would like to thank you for all this time, for all your energy and enthusiasm. I need to say that I really admire you being still active in the laboratory, while having so many collaborations and projects. Several times the passion with which you were depicting our goal motivated me so strongly that it was finally achieved, even though the beginnings were hard. I have a feeling that I've learnt a lot from you about the scientific process: from its very beginning till the communication based on the solid knowledge. Thanks to your collaboration with **Nathalie** I was able to explore a bit another country on my map: the Netherlands. I would like to thank Nathalie for enabling me to start my PhD by visit in Groningen, where I had a good opportunity to get familiar with the STM technique which was crucial for majority of my PhD period. Moreover, this time was an excellent opportunity for me to see how the top level science is made by chemists, who design and synthesize molecules that make unbelievable things.<sup>1</sup> In addition I would like to say that I am really impressed on how scientifically active you are despite of the fact that your family has enlarged since the moment we've met for the first time. In addition, thanks to your mobility I was lucky to live for one year in another place and to interact with another group of (bio)chemists, this time in Enschede. I would like to thank you and **Jeroen** for this opportunity and for enabling me to work in a place with such good conditions.

I would like to thank Prof. **Steven De Feyter**, Dr. **Fabrice Charra**, Prof. **Christophe Petit**, Prof. **Jacco Snoeijer** and Prof. **Harold Zandvliet** for accepting of being the part of my Graduation Committee. It is a pleasure for me, since many of your works inspired me strongly.

---

<sup>1</sup> I would like to thank here all of the members of **Prof. Feringa group** at that time, especially the subgroup of 'Smart surfaces & systems': **Wesley, Greg, Hella, Johan, Jort, Oleksii, Thom, Tom, Xiaoyan**. Moreover, the 'Tuesday-football' subgroup and the others around: **Anthony, Arjen, Apu, Artem, Ashoka, Celine, Danny, Erik, Felix, Francesca, Giuseppe, Hans, Hilda, Jiaobing, Jochem, Johannes, Lachlan, Massimo, Mathieu, Nop, Pat, Pieter, Robby, Syuzi, Takeshi, Wiktor** and the non-chemists (*Mamio* football-mates): **Andrey, Bas, Elmer, Giuseppe, Jin, Johan, Juan, Julien, Kostas, Lotsi, Manfred, Philip, Sergii, Tano** and **Vili**.

During my stay in Paris I was not only lucky to explore the beautiful and special (to my opinion) city. I was also lucky to work within the extremely nice group of people. I would like to thank **Sergey**, who has shown me the experimental setup, and with whom I spent a lot of time on discussion of our results while travelling by RER to the far city of Orsay. I would like to thank **Bernard**, who taught me a lot concerning the theoretical approach to the problems I was facing. Moreover, his smile and sense of humor had extremely positive influence on me in numerous moments. He had spent with me many afternoons explaining some peculiarities of French grammar and word-formation, sometimes correcting my letters written in 'French', at least I was sure that it was French... In other words: invaluable contribution to my socialization.

Another person with a great input in scientific projects I have conducted at that time is **Sasha Marchenko**, who has spent a lot of time with me during his visits in Paris. Thank you for all those discussions we had. I really appreciate your time, and I was very happy to visit you in Ukraine.

I should thank **Delphine** for helping me so many times when I did not understand hundreds of e-mails I was receiving in French each week. She was always there to remind me about most important issues regarding meetings, conferences or ... lunchtime. I was happy to see you finishing and defending your thesis last year. I wish you good luck for the future! **Axel**, thanks for helping me with the translation of the summary part into French. Of course many thanks for the rest of our group at INSP: **Ahmed, Geoffroy, Habib, Ieva, Iryna, Jean-Noël, Joël, Laurent, Louis, Marie-Claude, Michel, Nadine, Olivier, Rana, Romain, Sébastien, Sophie, Xianbin, Yves** and **Zineb**. Moreover, I owe a special thanks to **Denis**, who shared with me his knowledge on mechanics, what in consequence made me possible to use on a daily basis my old-Peugeot-bike as a means of transportation.

I would like to thank people not affiliated to our group, especially **Jean-Louis** for sharing his knowledge on the charge transport properties of organic semiconductors and enabling me to use the time-of-flight setup. I would like to acknowledge **Fabrice** for our collaboration. Many thanks to all other PhD students at INSP: **Amaury, Cherif, Clotilde, Francisco, Hong, Hugo, Nico, Leszek** and **Raphael**, I also shouldn't forget to mention people whose work enabled me to concentrate on science: **Elisabeth, Isabelle, Lucdivine, Myriam, Natalia** and **Stephanie**.

The last year of my PhD I have spent in Enschede, where everything was a bit more calm and quiet. I have met many new people very enthusiastic about their work. I was impressed by the quality of work and deepness in understanding of supramolecular chemistry by many students guided by **Juriaan** and **Pascal**. **Wim**, I would like to thank you for a very interesting discussion in Lunteren. I am very grateful to **Tibor**, who has actually introduced me to STM during my stay in Groningen and have pointed me out several interesting remarks regarding my results. I wish you also good luck and a happy life with your family. **Melissa**, I will remember you spending so much time in the lab, that many of PhD students should be embarrassed 😊. Of course, I do not mean BNT people.

When I started a new project, quite different to the ones I conducted before I came to Enschede it was **Ben** who has introduced me to the topic of cholesteric droplets. *Merci!* It was good to have opportunity to chat with you, and thanks to you I have not forgotten all of my French. I wish you a lot of success. **Sarah, Rianne, Supitch** – you were always very helpful to show me where-is-what in the chemistry lab where I was normally on a status of a guest. It was really nice to have such kind people around me. Sarah, thanks for some fruitful discussions regarding my last project.

**Rajesh**, I remember us talking so many times about approaching to the end of the thesis. The time has finally come. I know you are defending a week after me. Good luck and take care - wherever you go. I really liked your positive spirit. **Roberto**, thanks for accepting to be my paranymph in this busy period for you. I wish you good luck with completing your thesis, just like I wish the same to the other PhDs in the lab. **Aijie, Alejandro, Andrea, Anne, Bettina, Carlo, Carmen, Emanuela, Eugenio, Gavin, Gülistan, He, Janneke, Jasper, Jenny, Jens, Jiguang, Laura, Maarten, Mark, Martijn, Melanie, Nicole, Raquel, Rik, Rindia, Shirish, Stan, Sven, Tegger, Tom, Tushar, Wies** and **Ye**, thank you for the nice (& loud 😊 – Raquel) atmosphere in the ‘chicken-farm’ and at the coffee corner. I am sure the ways of some of us will cross at some point in the future. **Nicole** and **Izabel**, thank you for all your help. Whenever I had an administrative question your response was fast and clear. That was very efficient and it helped me a lot. **Bianca, Marcel, Regine** – the BNT/MnF cluster is really lucky having you over there. **Richard**, besides your big knowledge I need to say that I remember some interesting chats with you at the coffee corner. Thanks to you I know a bit more about the Netherlands, thank you once more. Special thanks for **Rick** and **Wouter**, who have helped me with the translation of the summary of my thesis to Dutch.

**Bugra**, my flatmate – thanks a lot for all your help, including mail, etc. Some more people outside the lab: **Barry** I am really happy I know you. It is always nice to meet someone who speaks your language a bit and knows about your culture, cuisine, etc. I appreciate it and I will try to bring you some ‘Ptasie mleczko’ when I am back in Enschede. **Bijoy**, I even cannot say how many times you’ve helped me. Thank you for being so friendly and open-minded. It was a pleasure to play with you in one team. I am very happy that you have agreed to be my paranymph and I wish you all the best, in your private and professional life. I liked the way you were motivating us before the games. Of course the other members of Drienerlo 4 team: **Alfredo, Arian, Daniel, David, Edo, Eelco, Enrique, Felix, Guillaume, Hendrik, Islam, Jelle, Mario, Martin, Matthias, Mauricio, Maurits, Milos, Murat, Sam**, and **Victor** – it was a pleasure to train and play with all of you. Thanks to you I had a nice break from the lab and office work. We were really an international team (the international level will come, I am sure 😊). Even though we were not playing in the Eredivisie I think we made a huge progress during that season. Good luck guys! And no injuries, please.

Nie mogę zapomnieć o wszystkich, którzy znajdowali czas na to, żeby spotkać się ze mną podczas tych krótkich weekendów które spędzałem od czasu do czasu w Polsce. Ktoś z Was zawsze znalazł czas żeby odebrać mnie z lotniska, czy (co gorsza) zawieść na nie o 4 rano. Wielokrotnie korzystałem z Waszej nieocenionej pomocy i nieograniczonej gościnności. **Grzegorz, Mateusz, Tomek, Krzysiu** - serdeczne dzięki za niejednokrotne wsparcie i podpytywanie jak mi idzie. O wiele łatwiej było mi się zmobilizować myśląc, że w pewnym stopniu Was to również obchodzi. Tak samo mocno dziękuję **Awkowi, Łukaszowi, Staszкови, Gogłowi, Maćkowi, Wojtkowi K.** Dzięki Wam wszystkim cały czas lubiłem wracać do kraju. Ciesze się, że Was mam i że mamy kontakt pomimo faktu, że podczas ostatnich 7-miu lat większość czasu spędziłem zagranicą (podobnie jak **Piotrek H.** – cieszę się, że tak trzęsiesz 'biznesem'!). Osobne pozdrowienia dla Waszych żon/partnerek i rodzin ☺. Dużo zdrowia i do zobaczenia.

Równie często wsparcie otrzymywałem od mojej rodziny. **Babciu**, uwielbiam jak pytasz kiedy 'wybywam' i kiedy znów wrócę. Właśnie teraz wracam kolejny raz. Nie wiem na jak długo, nie wiem kiedy i gdzie znów wyjadę, ale dziękuję Ci za wszystko co dla mnie zrobiłaś. Nigdy Ci tego nie zapomnę. **Ciociu-mamo**, Tobie również dziękuję za wszystkie niedziele (i nie tylko) i za zawsze ciepłe słowa. Możesz być taka dumna ze swoich dzieci. **Aga, Adam, Artur** – fajnie widzieć jak wspaniale sobie radzicie. Właściwie zakładacie (albo założyliście) już Wasze własne rodziny. Cieszę się ogromnie patrząc na to (od czasu do czasu) i wiem, że należy się Wam szczęście. Trzymam za Was wszystkich kciuki. **Marcin**, za Ciebie również trzymam, najmocniej. Dobrze mieć takiego brata jak Ty. Mam nadzieję, że wszystkie (Twoje/Wasze z **Milena**) plany się spełnią i że będziesz żył tak jak chcesz. Nie będę oryginalny jeżeli napiszę, że do niczego bym nie doszedł gdyby nie **Rodzice. Mamo, Tato** – to Wy wspieraliście mnie najmocniej i najczęściej. Dziękuję za wszystko i kocham Was. Najważniejsze podziękowania zostawiłem na koniec: **Aniu** dziękuję Ci za to, że wytrzymałaś ponad rok ciągłych rozstań, a później cierpliwie znosiłaś ciągnące się tygodnie, które spędzałem przed komputerem. Choć niewiele o tym wszystkim mówiłem, to musisz wiedzieć, że bardzo mi pomogłaś i bez Ciebie na pewno byłoby mi o wiele trudniej. Dziękuję za to, że jesteś.

## Curriculum Vitae

Piotr Ślęczkowski was born in Knurów, Poland, on May 5<sup>th</sup>, 1984. He studied Industrial and Engineering Chemistry at the Silesian University of Technology (Silesian University of Technology, Gliwice, Poland), where he received his MScEng degree in December 2010. His master project, entitled 'Liquid Crystalline materials with insight into discotic mesogens' was carried out in the Department of Physical Chemistry and Technology of Polymers (Faculty of Chemistry, SUT) under supervision of prof. Jerzy Żak, PhD, DScEng.

In addition, in September 2007 he was accepted for a two-year interdisciplinary Erasmus Mundus Master's Course: 'MONABIPHOT: Molecular nano- and bio-photonics for telecommunications and biotechnologies', organized by the international consortium of 4 European universities and coordinated by Institut d'Alembert (ENS Cachan, France). During the final year, he has performed a research project at the Institut des NanoSciences de Paris (University Paris 6, France), and after defending master thesis, entitled 'Time-of-flight measurements of new semi-conducting liquid crystalline materials' in July 2009, he has obtained MSc in Physics from ENS Cachan, and MScEng degree from Wrocław University of Technology.

Since March 2010, he is a PhD candidate, jointly: in the 'Physico-chemistry and Dynamics of Surfaces' group at the Institut des NanoSciences de Paris (University Paris 6, France) under the supervision of Dr. Emmanuelle Lacaze, and in the 'Biomolecular Nanotechnology' group at the University of Twente, under the supervision of Dr. Nathalie Katsonis. The aim of his project is the investigation of various modes of chirality under different conditions of confinement. The results of this research are described in this thesis.

## List of Publications

4. P. Ślęczkowski, B. Matt, S. Iamsaard, E. Lacaze and N. Katsonis.  
Towards all-optical 3D-microlaser: Exploration of Cholesteric LCs under Geometrical Confinement.  
*Manuscript in preparation.*
3. P. Ślęczkowski, N. Katsonis, K. Uchida, A. Marchenko, B. Croset and E. Lacaze.  
Controlling the 2D Self-assembly of Discotic Liquid Crystals: A New Role for Azobenzenes.  
*Manuscript in preparation.*
2. P. Ślęczkowski, N. Katsonis, O. Kapitanchuk, A. Marchenko, F. Mathevet, B. Croset and E. Lacaze.  
Emergence of Chirality in Hexagonally Packed Monolayers of Hexapentyloxytriphenylene on Au(111): A Joint Experimental and Theoretical Study.  
*Langmuir*, **2014**, *accepted for publication.*
1. P. Ślęczkowski, N. Katsonis, A. Marchenko and E. Lacaze.  
Twofold Orientation of Triphenylene-Based Discotic Liquid Crystals on Gold.  
*Mol. Cryst. Liq. Cryst.*, **2012**, *558*, 102-108.